UNIVERSIDAD NACIONAL AUTÓNOMA DE MÉXICO

POSGRADO EN CIENCIAS DE LA TIERRA

INSTITUTO DE GEOLOGÍA

ESTUDIO TERMOTECTÓNICO Y DE PROCEDENCIA DE SEDIMENTOS DE LA SIERRA DE CHIAPAS MEDIANTE TRAZAS DE FISIÓN Y GEOQUÍMICA EN APATITOS

T E S I S

QUE PARA OPTAR POR EL GRADO DE:

DOCTOR EN CIENCIAS DE LA TIERRA

PRESENTA

Fanis Abdullin

TUTOR

Dr. Jesús Solé-Viñas (Instituto de Geología, UNAM)

COMITÉ TUTOR

Dr. Gilberto Silva Romo (Facultad de Ingeniería, UNAM)

Dr. Javier de Jesús Meneses-Rocha (PEMEX)

Dr. Juan Rogelio Román-Ramos (PEMEX)

México D.F., Febrero, 2016

COMITÉ DE ADMISIÓN

Dr. Mario Villalobos Peñalosa

Dr. Peter Schaaf

Dr. Antonio Camprubí i Cano

COMITÉ PREDOCTORAL

Dr. Jesús Solé

Dr. Luigi Solari

Dr. Peter Schaaf

Dr. Thierry Calmus

COMITÉ DE EXAMEN DE GRADO

Dr. Jesús Solé

Dr. Luigi Solari

Dr. Peter Schaaf

Dr. Thierry Calmus

Dr. Javier J. Meneses-Rocha

Fanis Abdullin

Universidad Nacional Autónoma de México,

Posgrado en Ciencias de la Tierra, México D.F.

fanisius@yandex.ru

Esta tesis se la dedico a mi familia,

a Valentina y Vadim que son los “satélites” de mi vida. Gracias por su paciencia y por confiar en mí.

AGRADECIMIENTOS

Quiero agradecer en primer lugar a mi asesor, al Dr. Jesús Solé por su compromiso y motivación así como por enseñarme a pensar de una forma no convencional y siempre buscar alternativas. También a los Doctores Luigi Solari y Carlos Ortega por su apoyo en las mediciones con LA-ICP-MS. De la misma forma, quiero dar gracias a los Maestros Jaime Díaz y Consuelo Macías por su gran ayuda en la preparación de muestras para los análisis geoquímicos. Me gustaría expresar mi agradecimiento a María Luisa, Gloria y Araceli así como al Dr. Gustavo Tolson por ayudarme a resolver varios asuntos burocráticos y económicos. Me gustaría agradecer también a los expertos en termocronología, los Doctores Thierry Calmus y Peter Schaaf por ser parte del Jurado de mi examen de grado.

Agradezco a mis camaradas del Posgrado, Alekz, David y Caro, Bernardo y Bethania, Beto y Elisa, Roberto, Memo, Daniel, Gerardo, por su sincera amistad.

Gracias a la Universidad Nacional Autónoma de México y al Consejo Nacional de Ciencia y Tecnología por darme la oportunidad de realizar mis estudios de doctorado.

Este estudio fue financiado por el proyecto de PAPIIT No. IN111414 otorgado al Dr. Jesús Solé.

Finalmente, quiero agradecer atentamente al Dr. Javier Meneses-Rocha por compartir conmigo su gran experiencia y guiarme durante mi investigación. Fue un gran honor colaborar con uno de los geólogos más importantes de México.

R E S U M E N

La Sierra de Chiapas, que se localiza en el sur de México como una parte del Bloque Maya, representa una región tectónicamente compleja. Este estudio se enfoca en la identificación de las edades de los eventos termo-tectónicos y magmáticos que ocurrieron en la Sierra de Chiapas. Las rocas del basamento (Macizo de Chiapas) así como las areniscas del Jurásico–Cretácico inferior (Formaciones Todos Santos y San Ricardo) y del Eoceno (Formación El Bosque) se dataron por el método de trazas de fisión en apatitos mediante LA-ICP-MS, con el fin de resolver los objetivos centrales de este estudio. En todos los cristales de apatito analizados, se obtuvieron también las concentraciones de elementos trazas y REE, las cuales se utilizaron para determinar áreas fuente para los sedimentos del Jurásico–Cretácico inferior y del Eoceno.

Los resultados obtenidos en este trabajo indican que los apatitos detríticos de la Formación Todos Santos (Toarciano–Oxfordiano) se resetearon parcialmente para el termocronómetro de trazas de fisión, debido a un sepultamiento suficiente durante el desarrollo de la plataforma del Cretácico. Las historias térmicas modeladas para las rocas de esta unidad muestran un periodo de levantamiento (con tasas de enfriamiento menores de 3°C/Ma) durante el Cretácico superior–Eoceno inferior (~83–51 Ma), lo cual se puede correlacionar con la Orogenia Laramide. Las muestras del basamento tienen edades de trazas de fisión en apatitos que varían en un rango bastante amplio,

de ~45 a ~23 Ma, sin una correlación clara entre la elevación de las muestras y sus edades. Estos apatitos muestran unas longitudes promedio de trazas confinadas de 12 a 12.5 μm. Estos resultados implican que el Macizo de Chiapas no sufrió ningún tipo de levantamiento significativo en el periodo comprendido entre el Eoceno inferior y el Mioceno inferior. Este periodo de quiescencia tectónica relativa se identificó también usando las curvas de enfriamiento construidas para las muestras de la Formación Todos Santos. Los datos de trazas de fisión en apatitos, particularmente las historias térmicas de la Formación Todos Santos, detectaron también un evento tectónico del Mioceno medio–superior, lo cual corresponde al evento Chiapaneco. Los apatitos detríticos del miembro arenoso (Berriasiano–Aptiano) de la Formación San Ricardo no se resetearon para el sistema de trazas de fisión, ya que éstos tienen unos picos de edades de 222 ± 9 y 175 ± 8 Ma. Estas edades obtenidas son las edades de enfriamiento de sus rocas fuente, las cuales son contemporáneas respectivamente con el evento Pérmico–Triásico y con un volcanismo de arco del Jurásico inferior–medio que afectaron al Macizo de Chiapas. Los apatitos detríticos de las areniscas micáceas de la Formación El Bosque (Ypresiano–Luteciano) también muestran unas edades que son mayores o iguales a su edad de depósito.

Los estudios de procedencia de sedimentos basados en la química de apatitos indican claramente que los sedimentos del Jurásico–Cretácico inferior provienen del Macizo de Chiapas. Un cambio fuerte en el área fuente se detectó entre el Mesozoico y el Eoceno. Los materiales siliciclásticos de la Formación El Bosque definitivamente no proceden del Macizo de Chiapas. Estos sedimentos provienen principalmente de

una cadena montañosa al norte y al centro de Guatemala, como sugieren las composiciones geoquímicas determinadas en apatitos detríticos.

Los resultados termocronológicos y geoquímicos obtenidos en este estudio y algunos datos reportados previamente permiten detectar, como mínimo, cinco etapas principales post-Pérmicas en la evolución termo-tectónica y tectono-magmática de la Sierra de Chiapas: (1) el evento Permo–Triásico que tuvo lugar en el Macizo de Chiapas; (2) un volcanismo de arco del Jurásico inferior–medio, el cual afectó al área del Macizo de Chiapas; (3) la Orogenia Laramide (~83–51 Ma); (4) un evento termo-tectónico del Mioceno medio–superior (la Orogenia Chiapaneca); y (5) un nuevo volcanismo del Plioceno al reciente. Los resultados de este estudio pueden ser útiles para un mejor entendimiento de la evolución tectónica y paleogeográfica del sur de México. Se propuso también una reconstrucción paleogeográfica para el área de estudio, desde el Cretácico hasta el Plioceno. Es evidente que la Sierra de Chiapas se tiene que considerar como una yuxtaposición de distintos dominios paleogeográficos.

Palabras clave:

apatitos; termocronología por trazas de fisión; procedencia de sedimentos; evolución termo-tectónica; paleogeografía; sur de México; Sierra de Chiapas

A B S T R A C T

The Sierra de Chiapas, which is located in southern Mexico as part of the Maya Block, represents a tectonically complex region. This study is focused on the timing of thermo-tectonic and tectono-magmatic events that occurred in the Sierra de Chiapas. Basement rock samples from the Chiapas Massif as well as sandstones from Jurassic to early Cretaceous (Todos Santos and San Ricardo Formations) and Eocene units (the El Bosque Formation) were dated using LA-ICP-MS-based apatite fission-track technique, to resolve the main goals proposed. Trace-element and REE concentrations were also obtained in all the apatites analyzed, which were then used to identify the source areas for Jurassic–early Cretaceous and Eocene sediments.

The results obtained in this work indicate that detrital apatite grains from the Todos Santos Formation (Toarcian–Oxfordian) were partially reset for the fission-track thermochronometer, owing to its burial-related heating during the development of the Cretaceous platform. The thermal histories modelled for rock samples from this unit show that a period of exhumation (with cooling rates of less than 3°C/Ma) occurred during the late Cretaceous–early Eocene (~83–51 Ma), which can likely be correlated with the Laramide orogeny. Most basement samples yield apatite fission-track ages from ~45 Ma to ~23 Ma, without clear relationship between the ages and the elevations of samples. These apatite crystals are characterized by mean confined

track lengths of 12–12.5 μm. These results imply that the Chiapas Massif has not experienced any significant tectonic uplift during the early Eocene–early Miocene. This period of relative tectonic quiescence was also observed using cooling curves constructed for the Todos Santos Formation sandstone samples. Apatite fission-track results, particularly from this Formation, also detected a middle–late Miocene event, which corresponds to the Chiapanecan thermo-tectonic event.

Apatites from the sandy member (Berriasian to Aptian) from the San Ricardo Formation were not reset for the fission-track system, since these yielded age peaks at 222 ± 9 Ma and 175 ± 8 Ma. These obtained ages are the cooling ages of their source rocks, which are respectively coeval with the Permo–Triassic event and an early–middle Jurassic arc volcanism that affected the Chiapas Massif area. Detrital apatites from micaceous sandstones from the El Bosque Formation (Ypresian–Lutetian) also have ages that are greater than or equal to its stratum age.

Sediment provenance studies based on apatite geochemistry strongly indicate that Jurassic to early Cretaceous sediments were mainly derived from the Chiapas Massif. A significant change in provenance was observed from Mesozoic to Eocene stratigraphic units. Siliciclastic materials of the El Bosque Formation were definitely not derived from the Chiapas Massif region. These sediments were predominantly derived from northern and central Guatemala, as suggested by apatite geochemistry.

The thermochronological and geochemical results obtained in this study, as well as previously published geological data, indicate that the Sierra de Chiapas has experienced a multi-episodic thermo-tectonic and magmatic evolution, with a least

five main post-Permian stages: (1) the late Permian–Triassic event that formed the Chiapas Massif; (2) an early–middle Jurassic arc volcanism that affected the Chiapas Massif region; (3) Laramide orogeny (~83–51 Ma); (4) the Chiapanecan thermo-tectonic event (middle to late Miocene); and (5) a new recent volcanism (Pliocene to present). The results of this study can be useful towards a better understanding of the thermo-tectonic and paleogeographic history of southern Mexico. A paleogeographic reconstruction was also proposed for the Cretaceous to Pliocene period. It is evident that the Sierra de Chiapas should be considered as a juxtaposition of distinct paleogeographic domains.

Keywords:

apatite; fission-track thermochronology; sedimentary provenance; thermo-tectonic evolution; paleogeography; southern Mexico; Sierra de Chiapas

ÍNDICE GENERAL

1. INTRODUCCIÓN

El análisis de trazas de fisión en apatitos es un importante termocronómetro de baja temperatura (60–120 °C) que permite investigar las historias térmicas de muchos tipos de rocas y que se puede aplicar para resolver varios problemas geológicos en un rango amplio de ambientes tectónicos. Hasta ahora, en México existen pocos estudios relacionados con la termocronología de baja temperatura tales como trazas de fisión y (U–Th)/He (*e.g.*, Ortega-Rivera *et al.*, 1997; Kowallis *et al.*, 1998; Calmus *et al.*, 1999, 2015; Ortega-Rivera, 2003; Ducea *et al.*, 2004; Pi *et al.*, 2005; Solé y Pi, 2005; Ratschbacher *et al.*, 2009; Witt *et al.*, 2012; Abdullin *et al.*, 2014, 2016a). Desarrollar e implementar estos métodos radioisotópicos debe ser de interés nacional ya que abre nuevos campos de estudio y aplicación. Este trabajo de tesis se enfoca principalmente en la participación del desarrollo del método de trazas de fisión alternativo (medición *in-situ* de la concentración del ^{238}U), el cual no requiere la irradiación de las muestras con neutrones térmicos en un reactor nuclear. Además, este método novedoso permite obtener las concentraciones del U y Th al mismo tiempo que las de otros elementos traza (*e.g.*, Y, Sr) y REE (*Rare Earth Elements*), lo que puede ser útil no solo para los estudios geocronológicos sino que también para los estudios petrogenéticos así como para la procedencia de sedimentos clásticos (Abdullin *et al.*, 2014, 2016a, 2016b).

Esta tesis se enfoca también en la aplicación del método mencionado para los estudios termocronológicos y geoquímicos de rocas del basamento cristalino (Macizo

de Chiapas) y de rocas siliciclásticas (Mesozoico y Cenozoico), con el fin de entender mejor la evolución geológica de la Sierra de Chiapas (*i.e.*, parte del Bloque Maya, Sur de México). La mayoría de estudios geocronológicos previos se habían enfocado para investigar la evolución del Macizo de Chiapas usando los métodos radioisotópicos de temperaturas media y alta tales como K–Ar, Rb–Sr y U–Pb (*e.g.*, Damon *et al.*, 1981; Schaaf *et al.*, 2002; Weber *et al.*, 2005, 2007, 2008; Estrada-Carmona *et al.*, 2009, 2012). Estos estudios fueron importantes para entender la evolución geodinámica del Macizo de Chiapas desde el Paleozoico hasta el Triásico–Jurásico. Sin embargo, en la Sierra de Chiapas se han realizado muy pocos estudios de termocronología usando los métodos de baja temperatura (Ratschbacher *et al.*, 2009; Witt *et al.*, 2012). Estos dos estudios permitieron detectar un evento tectónico del Mioceno, el cual se correlaciona con el evento Chiapaneco (ver Sánchez-Montes de Oca, 1979, 2006; Carfantan, 1981; Meneses-Rocha, 1985, 1991, 2001; Guzmán-Speziale, 2010).

El estudio presente aporta nuevos datos de edades de trazas de fisión así como las composiciones geoquímicas de apatitos obtenidas en varias rocas de Chiapas. Los resultados de esta tesis y algunos datos previamente publicados señalan que la Sierra de Chiapas experimentó una evolución tectónica con múltiples episodios. Esta tesis es un trabajo de investigación acumulativo que consiste de tres artículos publicados, los cuales conforman tres capítulos principales (ver los capítulos 4, 5 y 6). Los resultados obtenidos en este estudio se usaron para la reconstrucción paleogeográfica de Chiapas para un rango de tiempo geológico desde el Cretácico hasta el Plioceno (capítulo 7).

2. MARCO GEOLÓGICO

La Sierra de Chiapas forma parte del Bloque Maya (Figura 2.1) y representa una región geodinámicamente compleja, la cual está controlada por la interacción de las placas tectónicas Norteamericana, del Caribe y de Cocos (ver Ratschbacher *et al*., 2009; Guzmán-Speziale, 2010; Witt *et al*., 2012; Molina-Garza *et al*., 2015). Algunos geólogos (Sánchez-Montes de Oca, 1979, 2006; Meneses-Rocha, 1985, 2001) dividen la Sierra de Chiapas en cinco subprovincias tectónicas generales (Figura 2.2), a saber, el Macizo de Chiapas, la Sierra Monoclinal, el Anticlinorio del Chicomuselo y las subprovincias de Fallas de Transcurrencia y de Fallas Inversas.

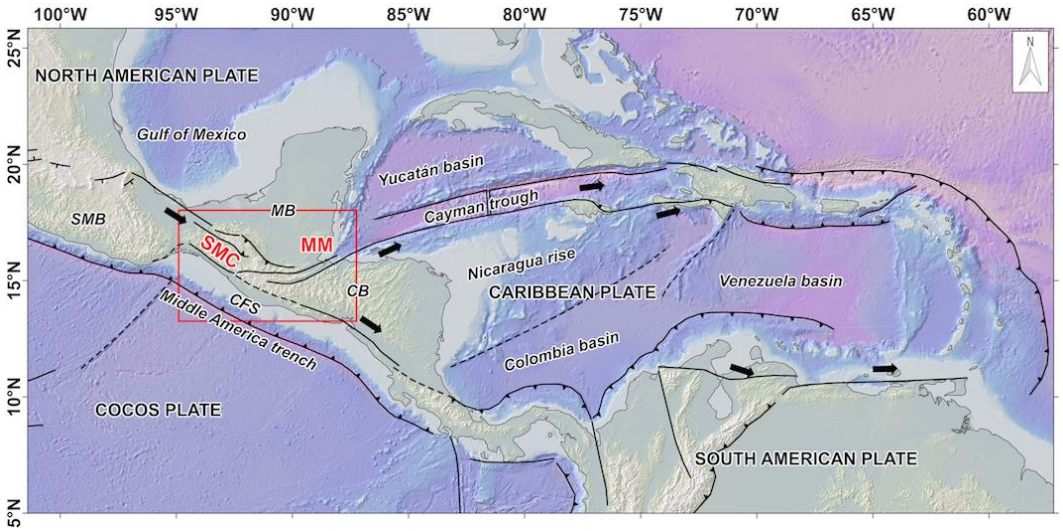

Figura 2.1. Mapa regional que muestra los límites entre las placas Norteamericana, Caribe y Cocos (tomado de Andreani y Gloaguen, 2016). MB – Bloque Maya, CB – Bloque Chortís, MM – Montañas Maya y SMC – Sierra de Chiapas. El rectángulo con líneas rojas corresponde a la Figura 2.3.

El basamento cristalino de la Sierra de Chiapas y de la porción sur del Bloque Maya es el Macizo de Chiapas, el cual aflora en la porción occidental de Chiapas (ver Figuras 2.2 y 2.3). Este basamento se compone principalmente de rocas plutónicas de diferentes composiciones (desde gabros hasta granitos y pegmatitas), algunas de las cuales están deformadas y metamorfoseadas (Schaaf *et al*., 2002; Weber *et al*., 2005, 2007, 2008; Estrada-Carmona *et al*., 2009). Los primeros resultados geocronológicos aceptables fueron reportados por Damon *et al*. (1981) quienes obtuvieron una edad de 256 ± 10 Ma (isócrona de Rb–Sr para diez muestras de roca). Las edades de Rb–Sr en pares de mica–roca total varían entre 244 ± 12 y 214 ± 11 Ma (Schaaf *et al*., 2002), lo que señala que el Macizo de Chiapas fue afectado por un evento tectono-magmático durante el Triásico. Este evento Permo–Triásico (~260–220 Ma) que tuvo lugar en el Macizo de Chiapas se puede relacionar a un metamorfismo con anatexia asociada así como a la intrusión de voluminosos plutones dentro de rocas pre-batolíticas de edades Paleozoicas tales como gneises, metabasitas y rocas calcosilicatadas (*e.g*., Weber *et al*., 2008; Estrada-Carmona *et al*., 2009). En la actualidad se sabe bien que el Macizo de Chiapas incluye también componentes Grenvillianos (Weber *et al*., 2015), lo que había sido previamente propuesto por Schaaf *et al*. (2002) en base a edades modelo de Sm–Nd. Unos granitoides del Ordovícico también se reportaron en este basamento (Estrada-Carmona *et al*., 2012). Durante el Mioceno medio y superior, una actividad ígnea afectó al Macizo de Chiapas (*e.g*., Molina-Garza *et al*., 2015) y generó muchas intrusiones graníticas a lo largo de la Zona de Cizalla de Tonalá (Figuras 2.2 y 2.3).

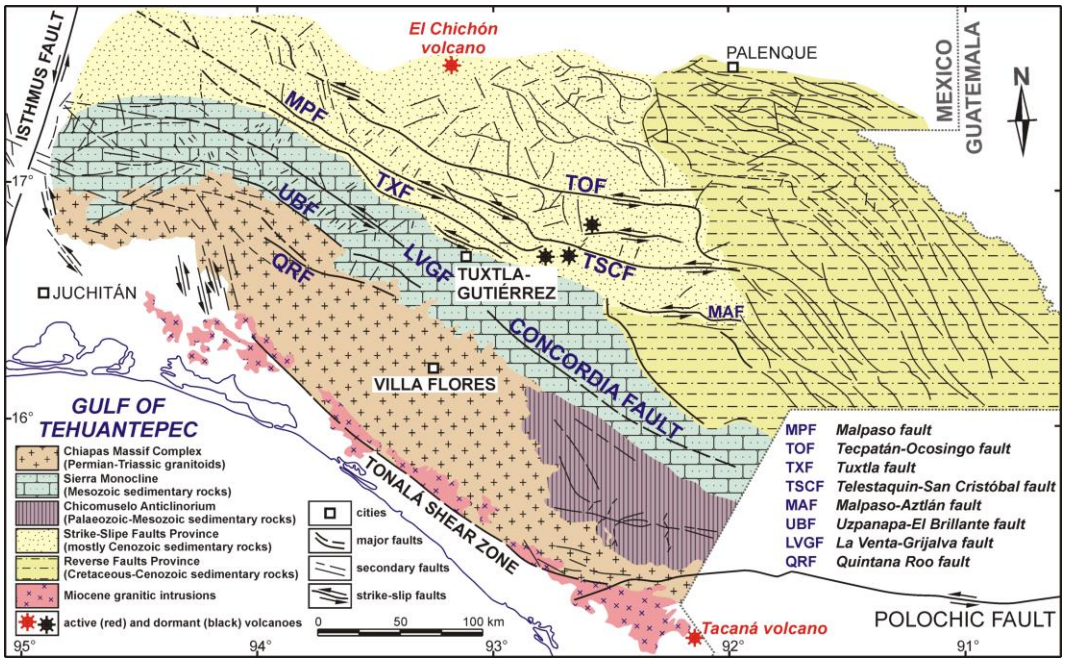

Figura 2.2. Mapa tectónico de la Sierra de Chiapas (modificado de Meneses-Rocha, 1985, 2001). Las descripciones de las subprovincias de Chiapas se pueden consultar en Meneses-Roca (2001) y también en los capítulos 5 y 6 de esta tesis (ver en Abdullin *et al*., 2016a, 2016b).

El Jurásico inferior–medio de la columna estratigráfica de la Sierra de Chiapas está formado por depósitos volcanoclásticos de las Formaciones La Silla y Andesitas Pueblo Viejo (Meneses-Rocha, 2001; Sánchez-Montes de Oca, 2006; Godinez-Urban *et al*., 2011), los que se depositaron en un ambiente pre-*rift* y/o *rift* durante la apertura del Golfo de México. El volcanismo del Jurásico inferior a medio se puede relacionar con el arco volcánico Nazas (de acuerdo con la hipótesis propuesta en Godinez-Urban *et al*., 2011). Durante el Toarciano al Oxfordiano se depositaron los lechos rojos (*red*

beds) de la Formación Todos Santos (Blair, 1987; Godinez-Urban *et al*., 2011; Witt *et al*., 2012) en un ambiente de *rift* controlado por la apertura del Golfo de México.

El mar del Jurásico invadió un continente que ocupaba el territorio de Chiapas y la Plataforma de Yucatán. Entre estos elementos se formó la Cuenca del Sureste, en la cual se registró una transgresión Jurásica que culminó con la instalación de la plataforma Cretácica (*e.g*., Meneses-Rocha, 1985, 2001; Padilla y Sánchez, 2007). En la Sierra de Chiapas, la exposición de la columna transgresiva se encuentra en la parte norte de la Sierra Monoclinal, en donde sobre la Formación Todos Santos descansa concordantemente, mediante una secuencia transicional, la Formación San Ricardo. La Formación San Ricardo, de acuerdo con algunos estudios paleontológicos (*e.g*., Quezada-Muñetón, 1983, 1987; Mandujano Velásquez, 1996; Sánchez *et al*., 2004), tiene las siguientes edades de depósito para sus tres miembros distintos: miembro basal calcáreo (Oxfordiano al Kimmeridgiano), miembro margoso (del Tithoniano) y miembro superior arenoso (del Berrisiano al Aptiano). Su análogo es la Formación Jericó que aflora en la porción sur de la subprovincia Sierra Monoclinal y está representada principalmente por rocas siliciclásticas de origen continental (Quezada-Muñetón, 1983; Meneses-Rocha, 1985, 2001; Ham-Wong, 2007; Godinez-Urban *et al*., 2011). Es evidente que los sedimentos del Jurásico (*i.e*., las Formaciones La Silla, Todos Santos, San Ricardo y Jericó) provienen principalmente de rocas fuente ígneas y metamórficas del Macizo de Chiapas (Meneses-Rocha, 1985, 1991, 2001; Sánchez-Montes de Oca, 2006), lo cual fue confirmado en base a estudios de procedencia de sedimentos usando métodos radioisotópicos (*i.e*., U–Pb en zircones detríticos y trazas

de fisión en apatitos detríticos) así como métodos geoquímicos (*e.g.*, ver los estudios realizados por Godinez-Urban *et al.*, 2011 y Abdullin *et al.*, 2016a, 2016b).

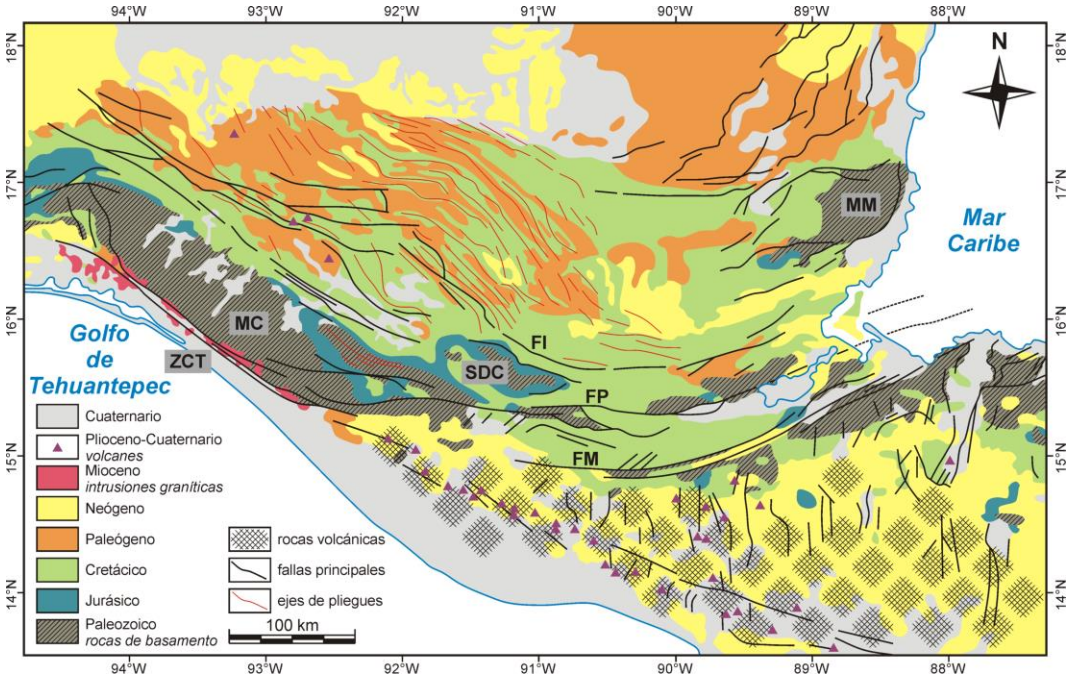

Figura 2.3. Mapa geológico simplificado de la Sierra de Chiapas, de las Montañas Maya y del norte de Guatemala (tomado de Andreani y Gloaguen, 2016). MC – Macizo de Chiapas, ZCT – Zona de Cizalla de Tonalá; SDC – Sierra de los Cuchumatanes; MM – Montañas Maya; FP – Falla de Polochic; FM – Falla de Motagua; FI – Falla de Ixcán.

El periodo Albiano–Santoniano está representado por la Formación Sierra Madre, la cual está constituida por unas potentes capas de carbonatos (con un espesor total de 1000–2500 m; Rosales-Domínguez *et al.*, 1997; Rosales-Domínguez, 1998). La Formación (o Grupo) Sierra Madre evidentemente se depositó en una plataforma durante la etapa post-*rift* (estabilidad tectónica) en la evolución tectónica del Golfo de

México (Rosales-Domínguez, 1998; Meneses-Rocha, 2001; Sánchez *et al*., 2004). En el Campaniano–Maastrichtiano tuvo lugar un cambio fuerte en la sedimentación. Las unidades de este periodo se componen de una mezcla de sedimentos siliciclásticos y carbonatos (Figura 2.4). Por ejemplo, la Formación Ocozocoautla, que se formó en un ambiente costero, contiene gravas, areniscas de grano grueso–medio a fino, así como lutitas, margas y calizas (Quezada-Muñetón, 1987; Rosales-Domínguez *et al*., 1997). La composición mineralógica de los depósitos clásticos de esta Formación señala que estos representan un reciclaje de areniscas de la Formación Todos Santos (Meneses-Rocha, 1985, 2001; Sánchez-Montes de Oca, 2006; Ham-Wong, 2007).

La columna litoestratigráfica del Cenozoico de la Sierra de Chiapas (ver en la Figura 2.4) consiste principalmente de rocas terrígenas (Meneses-Rocha, 1985, 2001; Quezada-Muñetón, 1987; Sánchez *et al*., 2004; Sánchez-Montes de Oca, 2006; Ham-Wong, 2007). El Paleoceno marca el final de la transición de la sedimentación marina a la sedimentación siliciclástica (Figura 2.4). Las unidades del Paleoceno consisten de sedimentos de plataforma somera, turbiditas (*e.g*., la Formación Lutitas Nanchital con un espesor variable de 300–1100 m) así como de depósitos de cuenca profunda (*e.g*., la Formación Soyaló con un espesor de ~900 m), las cuales afloran principalmente en la provincia de Fallas de Transcurrencia (Quezada-Muñetón, 1987; Meneses-Rocha, 2001; Sánchez *et al*., 2004). Las Formaciones del Eoceno–Oligoceno incluyen rocas siliciclásticas continentales (*e.g*., la Formación El Bosque) y unos pocos depósitos de plataforma somera localmente asociados con carbonatos (las Formaciones Lomut y Mompuyil con unos espesores de ~500–900 m y de 500–1400 m, respectivamente),

las cuales afloran en las provincias de Fallas de Transcurrencia y de Fallas Inversas (*e.g.*, Meneses-Rocha, 2001; Sánchez-Montes de Oca, 2006; Ham-Wong, 2007; Witt *et al*., 2012; Abdullin *et al*., 2016a, 2016b). Las secuencias del Oligoceno y Mioceno muestran un incremento significativo en la sedimentación terrígena (las Formaciones La Laja, Depósito, Encanto e Ixtapa). La porción superior de la columna estratigráfica (Plioceno y Cuaternario) de la Sierra de Chiapas se presenta por sedimentos recientes y por depósitos volcanoclásticos los cuales se derivaron de rocas volcánicas formadas en la Sierra de Chiapas desde el Plioceno hasta reciente (*e.g.*, Mora *et al*., 2012).

Los primeros estudios detallados de procedencia de sedimentos realizados por Witt *et al*. (2012) demostraron que la mayoría de sedimentos del Paleoceno y Eoceno curiosamente no proviene del Macizo de Chiapas. Previamente se había sugerido que estos sedimentos siliciclásticos principalmente provienen de rocas fuente ubicadas en Guatemala (Meneses-Rocha, 1991, 2001). La hipótesis propuesta por Meneses-Rocha (1985, 1991, 2001) parece confirmarse en base a un análisis de procedencia de estos sedimentos (ver Abdullin *et al*., 2016b en el capítulo 6 de esta tesis). Por el contrario, los sedimentos de rocas siliciclásticas del Oligoceno–Mioceno parece que provienen de rocas fuente del Macizo de Chiapas y de areniscas recicladas de las Formaciones Jurásicas (*e.g.*, Meneses-Rocha, 1991, 2001; Witt *et al*., 2012).

La Figura 2.4 muestra la columna litoestratigráfica sintetizada de Chiapas. Los detalles de la descripción de las unidades de la Sierra de Chiapas se pueden consultar en Meneses-Rocha (2001). La descripción de algunas de las Formaciones de Chiapas

así como de las unidades muestreadas se puede encontrar también en los capítulos 5 y 6 de esta tesis (ver los trabajos de Abdullin *et al*., 2016a, 2016b).

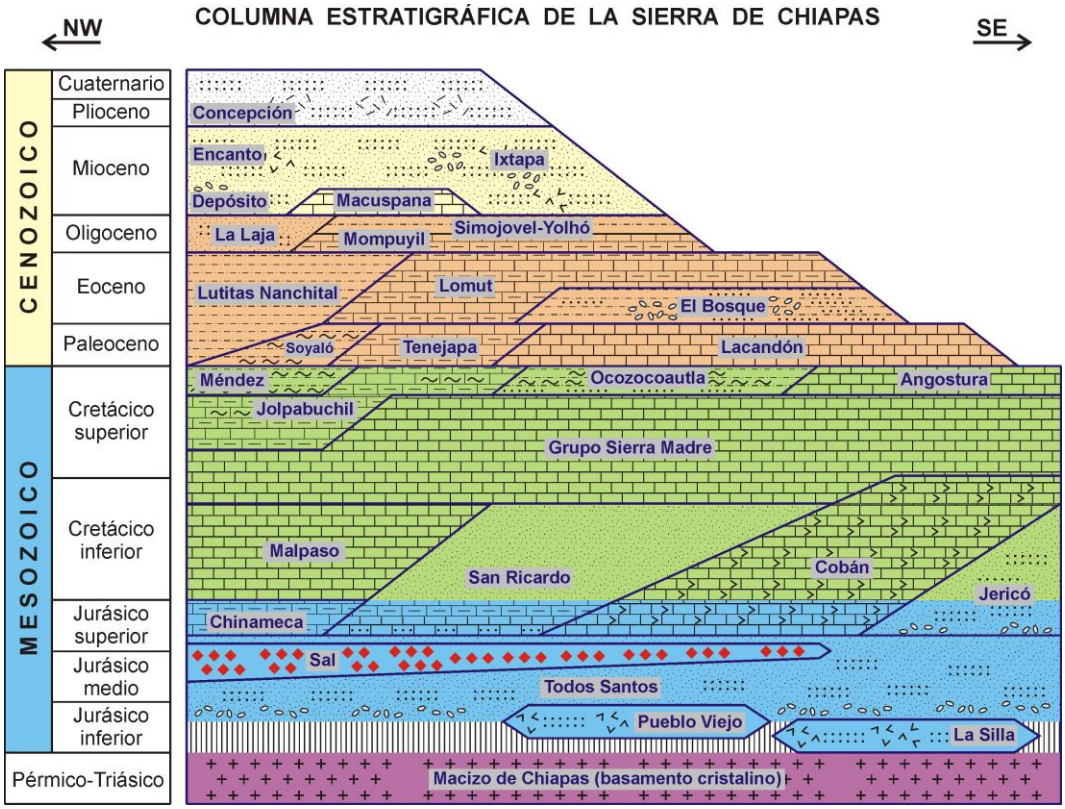

Figura 2.4. Columna litoestratigráfica de la Sierra de Chiapas que muestra las Formaciones principales (modificado de Ham-Wong, 2007). Las edades de las unidades estratigráficas se sintetizaron de varias publicaciones (Quezada-Muñetón, 1983, 1987; Meneses-Rocha, 1985, 2001; Mandujano Velásquez, 1996; Rosales-Domínguez *et al*., 1997; Rosales-Domínguez, 1998; Sánchez *et al*., 2004; Sánchez-Montes de Oca, 2006; Ham-Wong, 2007; Godinez-Urban *et al*., 2011).

3. OBJETIVOS PRINCIPALES

(1) Participar en el desarrollo del método de trazas de fisión alternativo, el cual se basa en las mediciones *in-situ* del contenido del isótopo ^{238}U usando LA-ICP-MS (*Laser Ablation Inductively Coupled Plasma Mass Spectrometry*).

(2) Demostrar las ventajas y desventajas del método novedoso comparándolo con el método convencional EDM (*External Detector Method*).

(3) En base a los nuevos datos termocronológicos (edades por trazas de fisión) y geoquímicos (elementos trazas y REE) obtenidos en apatitos durante el trabajo presente, estudiar la evolución geológica de la Sierra de Chiapas la cual forma parte del Bloque Maya, Sur de México.

(4) Diferenciar los eventos termo-tectónicos y tectono-magmáticos ocurridos en la Sierra de Chiapas, usando los resultados de este estudio así como los datos geológicos previamente publicados.

(5) Usar los resultados obtenidos para las reconstrucciones paleogeográficas de la Sierra de Chiapas, desde el Cretácico hasta el Plioceno.

4. METODOLOGÍA ANALÍTICA

La fisión nuclear espontánea es una forma de desintegración radioactiva de los isótopos pesados (*i.e.*, con masas atómicas mayores a 230 u; *e.g.*, ^{232}Th, ^{235}U, ^{238}U) que ocurre sin excitación externa, *i.e.*, es un proceso natural (Flerov y Petrzhak, 1940; Holden y Hoffman, 2000). En geocronología, la datación por el método de trazas de fisión del ^{238}U se utilizó por primera vez a inicios de la década del 1960 (ver Price y Walker, 1962, 1963; Fleischer *et al*., 1965). La fisión espontánea de un núcleo de ^{238}U produce dos núcleos nuevos (con unas masas de ~145 ± 5 y ~90 ± 5 u) que son expulsados en sentido contrario generando un defecto aproximadamente lineal (*i.e.*, traza de fisión; Figuras 4.1 y 4.2) en la estructura cristalina de ciertos minerales (*e.g.*, apatito, zircón, titanita, monacita, micas, granate, algunos vidrios volcánicos, fluorita, epidotas) los cuales deben tener una concentración medible de U en su composición geoquímica (Fleischer *et al*., 1975; Wagner y Van den Haute, 1992; Donelick *et al*., 2005). Por lo general, las trazas de fisión en minerales tienen direcciones aleatorias (Figura 4.3). Según la IUPAC (*International Union of Pure and Applied Chemistry*, ver Holden y Hoffman, 2000), la vida media de la fisión espontanea del ^{238}U es de $(8.2 \pm 0.1)\times10^{15}$ a. Eso significa que la constante del decaimiento por la fisión espontánea (λ_f) del isótopo ^{238}U es igual a $(8.45 \pm 0.1)\times10^{-17}$ a^{-1}. Este es el valor más usado para determinar las edades de diferentes minerales con la técnica de trazas de fisión (*e.g.*, Wagner y Van den Haute, 1992; Bernet *et al*., 2004; Hasebe *et al*., 2004,

2009; Bernet y Garver, 2005; Hadler *et al*., 2009; Curvo *et al*., 2013; Abdullin *et al*., 2014, 2016a; Gleadow *et al*., 2015). Los experimentos más recientes realizados por medio de distintos métodos (Guedes *et al*., 2003; Yoshioka *et al*., 2005) muestran que λ_f es de $(8.3–8.6)\times10^{-17}$ a^{-1}, lo que es igual al valor recomendado por la IUPAC.

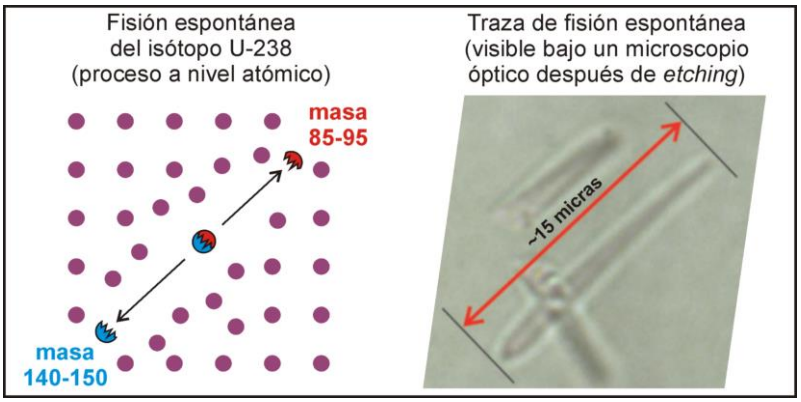

Figura 4.1. Se muestra de forma sencilla como se generan las trazas de fisión espontánea en minerales.

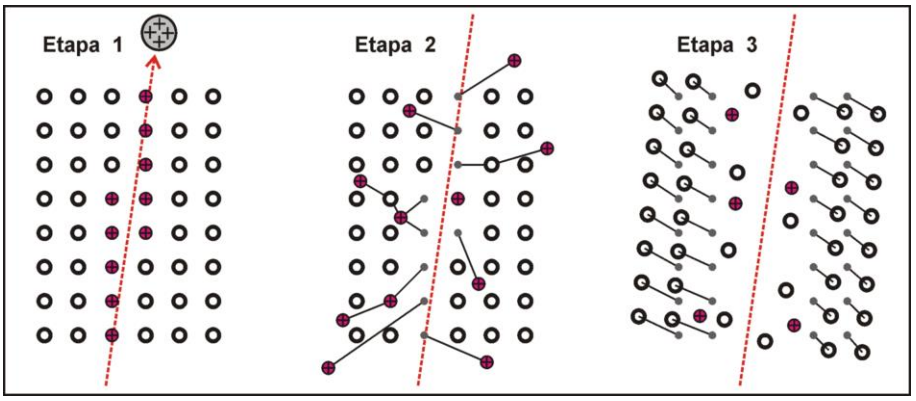

Figura 4.2. Tres etapas esquemáticas de la formación de trazas de fisión espontánea: (1) ionización de los átomos en la estructura cristalina por el movimiento de partículas cargadas (*i.e*., estado inestable); (2) desplazamiento electrostático de los átomos desde sus posiciones iniciales; (3) relajación y tensión elástica. Modificado de Fleischer *et al*. (1965, 1975).

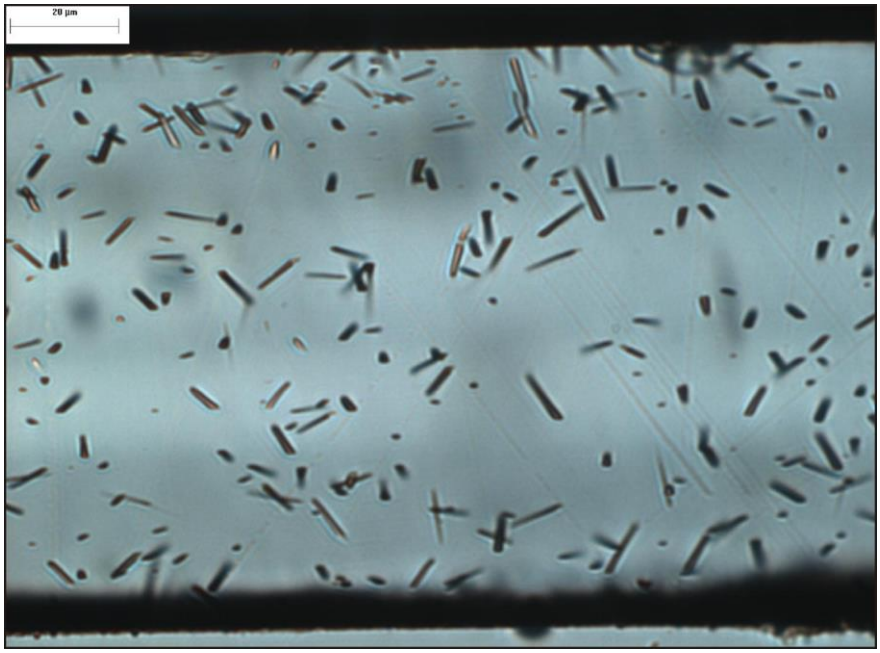

Figura 4.3. Un ejemplo de apatito con trazas de fisión espontánea visibles bajo el microscopio después de realizar el ataque químico (*etching*). La escala corresponde a 20 micras.

Se sabe que para determinar las edades de minerales con el método de trazas de fisión se requiere conocer la concentración del isótopo ^{238}U (*i.e.*, isótopo "padre") y la densidad de trazas de fisión espontánea (*i.e.*, productos del viaje de los isótopos "hijo"). Es cada vez más frecuente el uso de la datación mediante trazas de fisión usando una metodología reciente (*e.g.*, ver Hasebe *et al.*, 2004, 2009; Donelick *et al.*, 2005; Hadler *et al.*, 2009; Chew y Donelick, 2012; Abdullin *et al.*, 2014, 2016a; Liu *et al.*, 2014) que consiste principalmente en el conteo de trazas espontáneas (*i.e.*, el número de trazas por cm^2) y la determinación directa de la concentración de ^{238}U con LA-ICP-MS (*Laser Ablation Inductively Coupled Plasma Mass Spectrometry*). Los

dos pasos fundamentales de esta metodología se muestran en la Figura 4.4. Algunos ejemplos de apatitos en los cuales se realizó el conteo de trazas de fisión espontánea se muestran en la Figura 4.5. Es muy importante mencionar que la técnica de trazas de fisión, a diferencia de otros métodos radiométricos clásicos (*i.e.*, K–Ar, Ar–Ar, U–Pb, Rb–Sr), es un método relativamente subjetivo (*i.e.*, la calidad del conteo de trazas de fisión depende principalmente de la calidad de preparación de muestras así como de la experiencia del operador). Algunos apatitos no se pueden fechar con la técnica alternativa (*i.e.*, usando LA-ICP-MS). Por ejemplo, los apatitos de eclogitas pueden tener unas concentraciones de U menores de 0.5–1 ppm (Sassi *et al.*, 2000; Hermann, 2002; Spandler *et al.*, 2003; Guo *et al.*, 2013), lo que implica que estos apatitos tendrán muy pocas trazas de fisión generadas o no tendrán ninguna traza que se pueda observar bajo el microscopio (esto depende también de la edad del apatito por trazas de fisión). Asimismo, la técnica alternativa es difícilmente aplicable a apatitos que pueden presentar zonaciones fuertes de U (*i.e.*, zonaciones notables de la densidad de trazas) o que contienen mucho U (Figura 4.6), lo cual impide hacer un conteo de trazas adecuado. Muchas inclusiones de minerales enriquecidos en U (*e.g.*, monacita, zircón, magnetita) pueden mostrar alto contenido de U y consecuentemente generar edades de apatitos anormalmente jóvenes, mientras que la zonación significativa de U puede producir una sobreestimación de la edad del grano individual (Hasebe y Arai, 2007; Abdullin *et al.*, 2014, 2016a; Liu *et al.*, 2014). Es obligatorio tomar en cuenta lo mencionado anteriormente, sobre todo en el caso de los fechamientos de apatitos detríticos (Abdullin *et al.*, 2014, 2016a).

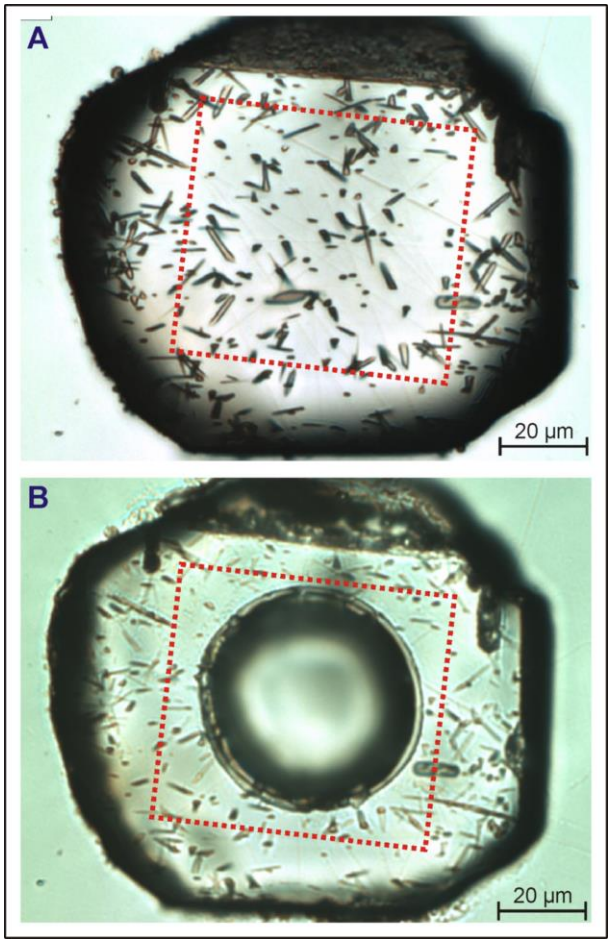

Figura 4.4. Un ejemplo de apatito detrítico (Formación Todos Santos) fechado con el método de trazas de fisión por medio de LA-ICP-MS (Fig. 3 en Abdullin *et al*., 2016a). (A) Microfotografía que muestra la superficie de apatito pulido y atacado químicamente. El área con líneas rojas punteadas corresponde al dominio dentro del cual se realizó el conteo de trazas de fisión espontánea del isótopo ^{238}U. (B) La misma microfotografía que muestra el cráter de la ablación láser generado durante la medición de los elementos trazas (incluyendo U) y REE con LA-ICP-MS. El diámetro del cráter es aproximadamente de 50 micras. Nótese que el micro-muestreo con láser se realizó dentro del mismo campo para el cual se determinó previamente la densidad de trazas. La escala en ambas microfotografías es de 20 micras.

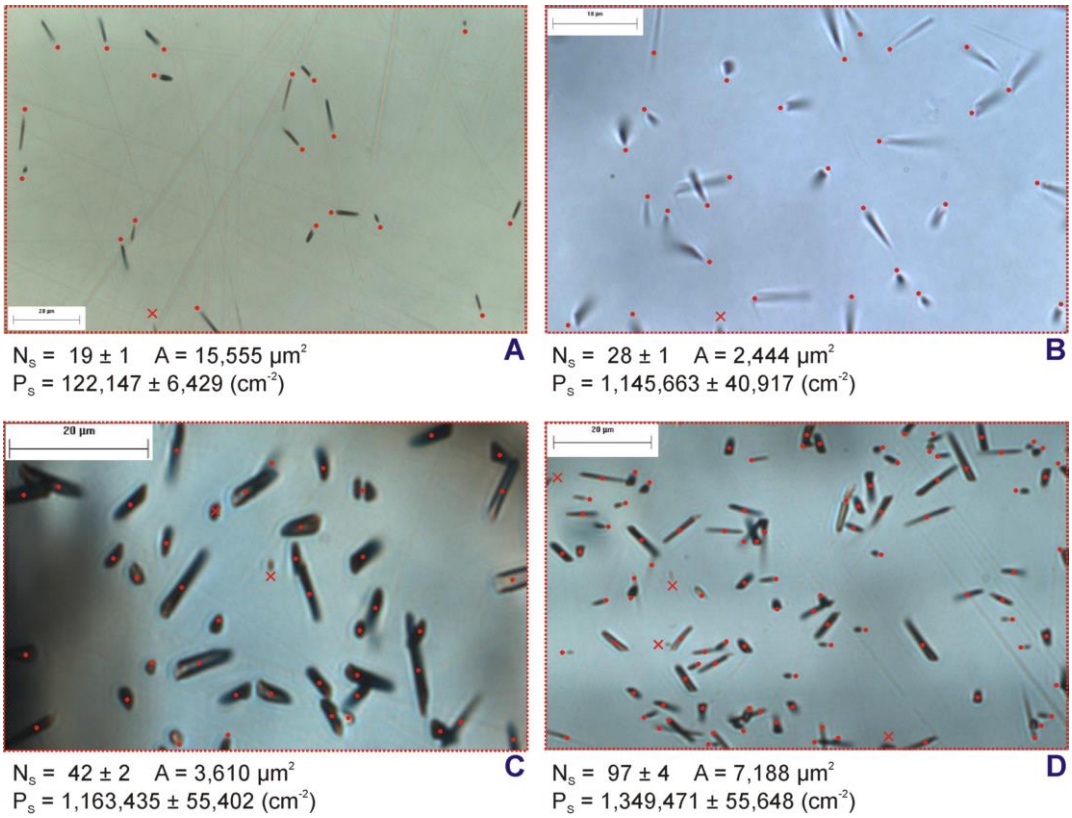

Figura 4.5. Algunos ejemplos de cristales de apatito que se utilizaron para el conteo de trazas de fisión espontánea. N_S significa número de trazas registradas (puntos rojos) en el área de conteo A (se muestra con líneas rojas punteadas). P_S es la densidad de trazas de fisión (*i.e.*, número de trazas por cm^2).

Prácticamente en todos los minerales la temperatura de cierre es función de la tasa de enfriamiento, pues el concepto de la temperatura de cierre se basa en la teoría de difusión de los átomos a través de un sólido (Dodson, 1973). Sin embargo, se sabe también que las trazas en apatitos con alto contenido de cloro (≥3% en peso) son más resistentes al borrado térmico que las trazas en apatitos con contenidos de cloro entre 0 y 1% en peso (Ketcham *et al*., 1999; Barbarand *et al*., 2003; Donelick *et al*., 2005). Los apatitos comunes (F-apatitos) tienen unas temperaturas de cierre efectivas para el

sistema de trazas de fisión de 90 °C a 120 °C, dependiendo de la tasa de enfriamiento (*e.g.*, Gleadow *et al*., 1986; Gallagher, 1995; Donelick *et al*., 2005). En el caso de Cl-apatitos, la temperatura de cierre no está determinada exactamente hasta ahora. Sin embargo, de acuerdo con Ketcham *et al*. (1999) y Donelick *et al*. (2005), los Cl-apatitos pueden tener una temperatura de cierre de ~140–160 °C o hasta un rango más elevado. La Figura 4.7 muestra las temperaturas de cierre de algunos geocronómetros, incluyendo algunos de los termocronómetros de baja temperatura más aplicados para resolver diversos problemas geológicos en un rango amplio de ambientes geológicos.

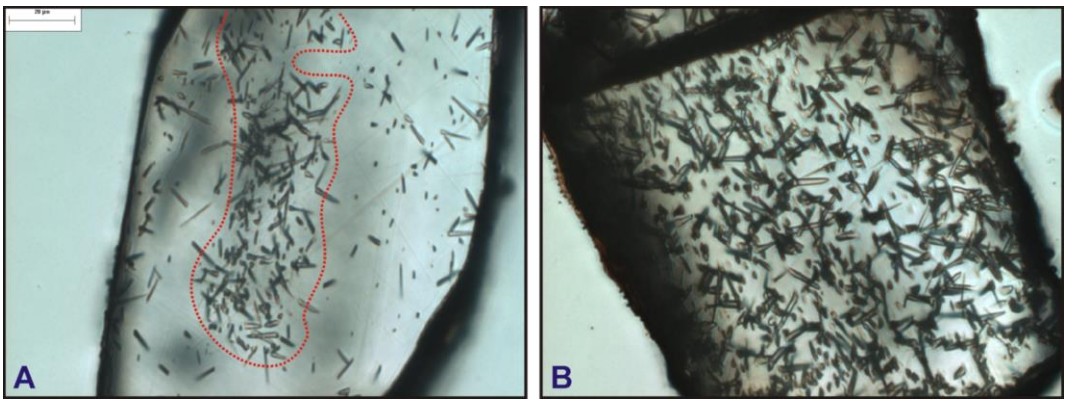

Figura 4.6. Ejemplos de apatitos que son bastante difíciles de datar con el método de trazas de fisión alternativo. (A) Apatito con una zonación notable de U (el centro del grano es enriquecido en U ya que contiene muchas trazas espontáneas, comparando con los bordes del grano). (B) Apatito con mucho U y que muestra una densidad de trazas incontable (en este grano de apatito en particular se obtuvo una concentración de U más de 260 ppm usando LA-ICP-MS, lo que no es común para los apatitos).

Los detalles de la preparación de muestras para los análisis de trazas de fisión, de los estudios microscópicos, mediciones de elementos trazas y de REE (*Rare Earth*

Elements) con LA-ICP-MS así como el cálculo de las edades de apatitos y de errores se pueden consultar en Hasebe *et al*. (2004, 2009) y Donelick *et al*. (2005), así como en los capítulos 4, 5 y 6 de esta tesis (ver Abdullin *et al*., 2014, 2016a, 2016b).

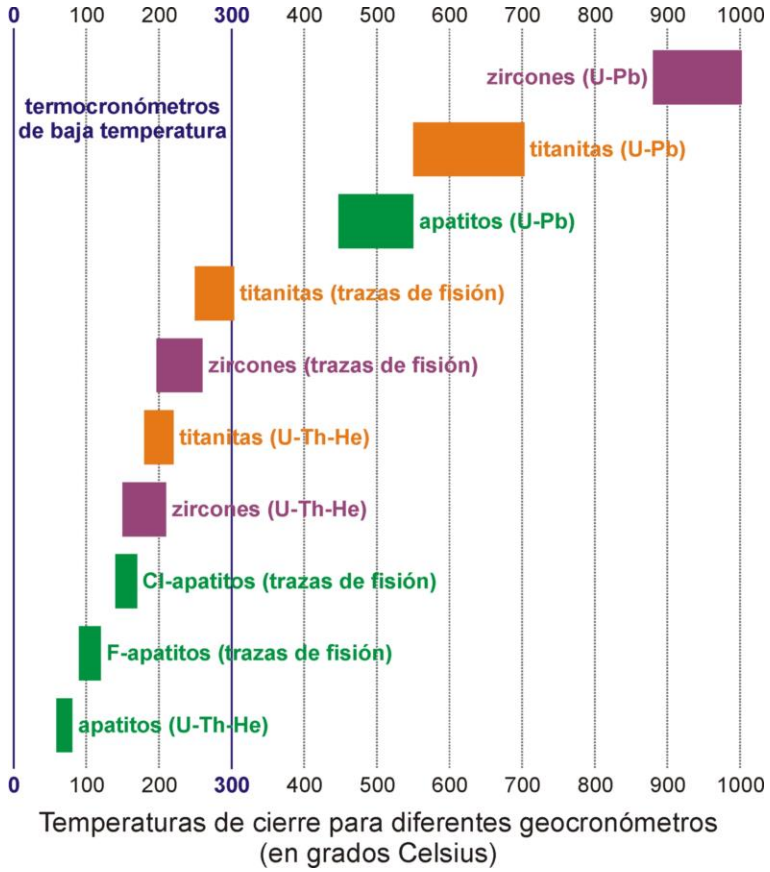

Figura 4.7. Temperaturas de cierre efectivas de apatitos, zircones y titanitas para (U–Th)/He, trazas de fisión y U–Pb (compilado de Lee *et al*., 1997; Coyle y Wagner, 1998; Ketcham *et al*., 1999; Farley, 2002; Donelick *et al*., 2005; Reiners, 2005; Schoene y Bowring, 2007; Bernet, 2009; Cochrane *et al*., 2014). En el caso de Cl-apatitos la temperatura de cierre para trazas de fisión es empírica.

Para poder realizar las dataciones de apatitos por trazas de fisión en forma rutinaria, se realizaron dataciones experimentales del F-apatito del Cerro de Mercado (Durango, México). Este apatito es un mineral estándar a nivel internacional y se puede usar para varios métodos de datación (trazas de fisión, datación por He, U–Pb) así como para estudios geoquímicos, ya que éste es un mineral suficientemente homogéneo. Hasta la fecha su edad estándar se considera de 31.4 ± 0.5 (1σ) Ma.

Los resultados de este experimento se presentan en el siguiente artículo:

Abdullin, F., Solé, J., y Solari, L., (2014).

Datación mediante trazas de fisión y análisis multielemental con LA-ICP-MS del fluorapatito de Cerro de Mercado (Durango, México): *Revista Mexicana de Ciencias Geológicas*, v. 31 (3), p. 395–406.

Datación mediante trazas de fisión y análisis multielemental con LA-ICP-MS del fluorapatito de Cerro de Mercado (Durango, México)

Fanis Abdullin[1,*], Jesús Solé[2] y Luigi Solari[3]

[1] *Posgrado en Ciencias de la Tierra, Instituto de Geología, Universidad Nacional Autónoma de México, Ciudad Universitaria, 04510 Coyoacán, México D.F., México.*
[2] *Instituto de Geología, Universidad Nacional Autónoma de México, Ciudad Universitaria, 04510 Coyoacán, México D.F., México.*
[3] *Centro de Geociencias, Universidad Nacional Autónoma de México, Campus Juriquilla, Apartado Postal 1-742, 76001 Querétaro, Qro., México.*
** fanisius@yandex.ru*

RESUMEN

Este artículo describe la datación mediante trazas de fisión y el análisis multielemental del fluorapatito de Cerro de Mercado (Durango, México) por medio de ablación láser asociada con un espectrómetro de masas con fuente de plasma de acoplamiento inductivo (LA-ICP-MS). Para este apatito se obtuvo una edad promedio de 31.2 ± 0.2 Ma (1σ) utilizando 104 edades de trazas de fisión determinadas en 12 fragmentos diferentes, lo que concuerda perfectamente con el valor aceptado de 31.4 ± 0.5 Ma (1σ). Se realizó una revisión de la literatura sobre la composición química y edad del apatito de Durango, y los resultados obtenidos a lo largo de este estudio (elementos traza, las Tierras Raras y edades de trazas de fisión) son coincidentes con algunos datos publicados. En este trabajo se presenta también una ecuación nueva para calcular la incertidumbre de las edades de trazas de fisión tomando en cuenta todos los errores analíticos. Los resultados obtenidos validan el procedimiento utilizado y permiten que esta metodología pueda ser usada rutinariamente en otros apatitos.

Palabras clave: ablación láser, Tierras Raras, elementos traza, trazas de fisión, apatito, Durango.

ABSTRACT

This paper presents the fission track age and multielemental analysis of the Durango fluorapatite (Cerro de Mercado, Durango, Mexico) performed by laser ablation-inductively coupled plasma-mass spectrometry (LA-ICP-MS). A mean age of 31.2 ± 0.2 Ma (1σ) was obtained from 104 fission-track ages determined in 12 different fragments, which is in close agreement with the accepted value of 31.4 ± 0.5 Ma (1σ). The literature about the chemical composition and age of the Durango apatite was also reviewed and the results obtained in this study (REE, trace elements and fission-track ages) are consistent with the published data. This study also presents a new equation for calculating the uncertainty of fission-track ages taking into account all analytical errors. These results validate the procedure used and allow this methodology to be used routinely in other apatites.

Key words: laser ablation, Rare Earth elements, trace elements, fission-track, apatite, Durango.

INTRODUCCIÓN

El análisis de trazas de fisión (TF) en apatitos es un importante termocronómetro de baja temperatura (60 – 120 °C) que permite investigar las historias térmicas de rocas ígneas, metamórficas o sedimentarias y que se puede usar para resolver diversos problemas geológicos en un rango amplio de ambientes geológicos (*e.g.*, Gleadow *et al.*, 1986; Green *et al.*, 1986; Gallagher, 1995; Calmus *et al.*, 1999; Yan *et al.*, 2003; Green y Duddy, 2006; Shen *et al.*, 2009; Zhang *et al.*, 2009; Bermúdez *et al.*, 2010; Witt *et al.*, 2012; Qiu *et al.*, 2012; Liu *et al.*, 2014). Por ejemplo, es uno de los pocos métodos isotópicos aplicado para reconstruir la evolución termo-tectónica de cuencas sedimentarias (Shen *et al.*, 2009; Witt *et al.*, 2012). El análisis de TF en apatitos permite también reconstruir la historia térmica de una roca incluso en el caso de un sepultamiento y una exhumación adicionales a su exhumación inicial (Zhang *et al.*, 2009). Además, la técnica TF en apatitos se puede usar para estudiar la historia tectónica de regiones geodinámicamente muy complejas (Bermúdez *et al.*, 2010). La datación de apatitos detríticos por TF tiene potencial para determinar la edad estratigráfica y procedencia de sedimentos (Yan *et al.*, 2003). El análisis de TF en apatitos tiene también aplicaciones prácticas para la exploración minera (Liu *et al.*, 2014) y de hidrocarburos (Qiu *et al.*, 2012).

En México hay pocos estudios relacionados con la termocronología de baja temperatura, es decir, TF y (U-Th)/He (*e.g.*, Kowallis *et al.*, 1998; Calmus *et al.*, 1999, 2012; Ducea *et al.*, 2004; Solé y Pi, 2005; Pi *et al.*, 2005; Ratschbacher *et al.*, 2009; Witt *et al.*, 2012). Desarrollar e implementar estos métodos abre nuevos campos de estudio y aplicación a nivel nacional e internacional. Es cada vez más frecuente el uso de la datación mediante TF usando una metodología reciente (*e.g.*, Hasebe

Abdullin, F., Solé, J., Solari, L., 2014, Datación mediante trazas de fisión y análisis multielemental con LA-ICP-MS del fluorapatito de Cerro de Mercado (Durango, México): Revista Mexicana de Ciencias Geológicas, v. 31, núm. 3, p. 395-406.

et al., 2004), que consiste en el conteo de trazas espontáneas (*i.e*., densidad por cm^2) y la determinación directa de la concentración del isótopo ^{238}U con LA-ICP-MS (ablación láser asociada con un espectrómetro de masas con fuente de plasma inductivamente acoplado). La nueva técnica evidentemente tiene algunas ventajas si se compara con el método convencional, el cual requiere más esfuerzo y tiempo debido a la necesidad de irradiar las muestras. Además, la técnica de TF LA-ICP-MS permite al mismo tiempo obtener las concentraciones de otros elementos traza y de elementos de las Tierras Raras (REE).

Este trabajo describe el método alternativo, incluyendo los aspectos de preparación de las muestras, realización de los análisis, una ecuación nueva para calcular los errores de edades TF, así como su aplicación al fluorapatito estándar de Cerro de Mercado (Durango, México). Se comparan los resultados obtenidos (composición química y edad) con datos publicados y se explica la importancia del análisis multielemental en apatitos por medio de LA-ICP-MS.

TEORÍA

Apatitos

El grupo de los apatitos tiene una composición química general $A_5[PO_4]_3Z$, en la cual los cationes (A) son Ca^{2+}, Pb^{2+} y como impurezas isomórficas también pueden ser REE^{3+}, Y^{3+}, Mn^{2+} y Sr^{2+}. Los aniones adicionales (Z) son F^-, Cl^-, $[OH]^-$, O^{2-} y $[CO_3]^{2-}$. En algunos casos, el anión complejo $[PO_4]^{3-}$ puede ser sustituido parcialmente por el anión más débil $[SiO_4]^{4-}$, pero con la combinación del anión más fuerte $[SO_4]^{2-}$. El apatito es el mineral más común del grupo de los fosfatos en la corteza terrestre y su fórmula química general es $Ca_5(PO_4)_3[F,Cl,OH]$. Los aniones adicionales de F, Cl y OH definen los tres tipos de apatito: fluorapatito, clorapatito e hidroxiapatito, respectivamente. El F-apatito es el que se encuentra más comúnmente en la naturaleza (Betekhtin, 1956).

El contenido promedio de elementos mayores en los F-apatitos es de (% en peso): CaO (55.5), P_2O_5 (42.3), F (3.8), y en los Cl-apatitos: CaO (53.8), P_2O_5 (41.0), Cl (6.8) (Lesnov, 2012). El apatito puede ser de color verde, amarillo, azul, blanco, violeta o transparente. Tiene una dureza de 5 en la escala de Mohs y su densidad varía de 3.15 a 3.23 $g{\cdot}cm^{-3}$. Los cristales de apatito por lo general tienen forma de prisma hexagonal bipiramidal o pinacoidal y en rocas metamórficas y sedimentarias se pueden encontrar en formas euhédricas o anhédricas. De los circones se distinguen fácilmente utilizando un microscopio con luz polarizada, ya que los circones tienen colores de interferencia y relieve más altos que los apatitos. En lámina delgada estándar los apatitos aparecen con colores del primer orden y tienen un relieve más alto que el cuarzo. En los ácidos fuertes (*e.g*., HNO_3, HCl y H_2SO_4) los apatitos se disuelven, sin embargo, en la naturaleza son suficientemente resistentes al intemperismo físicoquímico y pueden sobrevivir en la superficie terrestre y durante la diagénesis (Betekhtin, 1956; Belousova *et al*., 2002; Morton y Yaxley, 2007; Lesnov, 2012; Jafarzadeh *et al*., 2014). Las siguientes características del apatito permiten que sea un mineral excelente para los estudios geoquímicos y las dataciones mediante TF, (U-Th)/He y U-Pb: (1) muchas rocas ígneas, metamórficas y sedimentarias siliciclásticas contienen este mineral en su composición; (2) presencia de los elementos traza y REE, en particular U y Th; (3) estabilidad química en las superficie terrestre; (4) capacidad de conservar los elementos traza y REE durante la diagénesis.

Datación por trazas de fisión

La fisión espontánea es una forma de la desintegración radioactiva de isótopos pesados que ocurre sin excitación externa, es decir, es un proceso natural (Flerov y Petrzhak, 1940). En geología, la datación con TF se utilizó por primera vez a inicios de la década de 1960 (Price y Walker, 1962, 1963; Fleischer *et al*., 1965). La fisión espontánea de un núcleo del ^{238}U produce dos nuevos núcleos que son expulsados en sentido contrario generando un defecto aproximadamente lineal (traza de fisión) en la estructura cristalina. Las trazas de fisión en minerales tienen direcciones aleatorias. La vida media de la fisión espontánea del ^{238}U es de $(8.2 \pm 0.1)\times10^{15}$ a (Holden y Hoffman, 2000). Atacando químicamente (*etching*) los cristales pulidos de apatito u otro mineral, las trazas se revelan y alcanzan un tamaño visible en el microscopio óptico. En los minerales, la zona con defectos producidos por la fisión se mantiene después de que los núcleos se hayan detenido, sin embargo, un incremento de la temperatura puede hacer que estos defectos desaparezcan ya que los átomos desplazados vuelven a su posición inicial en la red cristalina. A este proceso de acortamiento de trazas se le llama borrado térmico o *annealing* (*e.g*., Wagner y Van den Haute, 1992). Para los apatitos comunes (*i.e*., F-apatitos), la zona entre los 60 y 120 °C es la zona en la que las trazas sufren un borrado térmico parcial y tienen longitudes variables (menos de 16 ± 1 µm) que se conoce como PAZ (*Partial Annealing Zone*, *e.g*., Gleadow *et al*., 1986; Green *et al*., 1986). Eso significa que el borrado parcial reduce las edades aparentes y acorta las longitudes de las trazas, mientras que el borrado total (más de 120 °C) reinicializa la edad TF de apatito hasta ~0 Ma. En otras palabras, la temperatura efectiva de cierre para los apatitos es igual a 110 ± 10 °C (Gleadow *et al*., 1986; Green *et al*., 1986; Gallagher, 1995). A diferencia de los apatitos, los circones que se utilizan también comúnmente para las dataciones por TF tienen una temperatura de cierre de ~240 ± 30 °C (Brandon *et al*., 1998; Bernet y Garver, 2005) y se aplican por lo general para la termocronología de rocas ígneas o metamórficas y para determinar la procedencia y edad estratigráfica de sedimentos (*e.g*., Bernet *et al*., 2004; Bernet y Garver, 2005; Solov'ev y Rogov, 2010).

En todos los minerales la temperatura de cierre es función de la tasa de enfriamiento, pues el concepto de la temperatura de cierre se basa en la teoría de difusión de los átomos a través de un sólido (Dodson, 1973). Se sabe también que los apatitos con alto contenido de cloro (≥ 3 % en peso) son más resistentes al borrado térmico que los apatitos con contenidos de cloro entre 0 y 1% en peso (*e.g*., Ketcham *et al*., 1999). Como alternativa para no tener que determinar la concentración de cloro en apatito, se puede calibrar la temperatura de cierre con otro parámetro, llamado D_{par} (Donelick *et al*., 2005). Los valores de D_{par} se miden utilizando un microscopio óptico (luz reflejada) y son iguales a la longitud de las figuras de corrosión (*etch pits*) que se forman en la superficie pulida de los apatitos después de atacarlos químicamente. Estas figuras de corrosión representan figuras geométricas formadas por la intersección del microagujero del ataque químico con la superficie pulida del apatito y son de formas hexagonales alargadas que tienen la misma dirección que el eje C cristalográfico. Entre D_{par} y la concentración de cloro existe una correlación positiva y D_{par} se puede utilizar como una herramienta semicuantitativa para determinar la concentración del cloro (Ketcham *et al*., 1999; Donelick *et al*., 2005), por lo tanto cualquier de los dos parámetros cinéticos se puede usar para determinar la temperatura de cierre de apatitos y las características del borrado parcial de las trazas. Los apatitos con D_{par} ~1.50 µm y Cl < 1 % en peso tienen una temperatura de cierre de ~110 °C (suponiendo una tasa de enfriamiento de 10 °C/Ma), mientras que para los apatitos con $D_{par} \geq 3.00$ µm y/o Cl ≥ 3 % en peso la temperatura de cierre puede aumentar hasta los 150 °C o más (Ketcham *et al*., 1999; Donelick *et al*., 2005). Esto significa también que en teoría los Cl-apatitos deben tener una PAZ con temperaturas más elevadas en comparación con los F-apatitos, probablemente alrededor de 90 – 160 °C. Es muy importante, sobre todo para los apatitos detríticos, separarlos en diferentes poblaciones según las concentraciones de cloro (microsonda electró-

nica de barrido, EPMA) o los valores de D_{par} (microscopia óptica).

Las trazas espontáneas en un mineral se generan durante el tiempo geológico (proceso natural), mientras que las trazas inducidas se forman por la fisión del ^{235}U por la irradiación de las muestras con neutrones térmicos en un reactor (proceso artificial, Gleadow *et al*., 1986; Green *et al*., 1986; Wagner y Van den Haute, 1992; Gallagher, 1995). La cantidad de trazas espontáneas principalmente depende del contenido de uranio en el cristal, y del tiempo durante el cual este cristal ha estado a una temperatura suficientemente baja para que sus trazas se preserven. La cantidad de trazas inducidas sirve para calcular la concentración del ^{235}U en el cristal, que está relacionada directamente con la concentración del ^{238}U ($^{238}U/^{235}U$ = 137.88; Steiger y Jäger, 1977). La edad obtenida por TF indica el tiempo mínimo durante el cual se han acumulado las trazas observables hoy en un mineral (*e.g*., Gallagher, 1995). Para calcular la edad TF con el método convencional es necesario obtener las densidades de los dos tipos de trazas (ρ_S – espontáneas y ρ_i – inducidas). Las trazas inducidas después de la irradiación de la muestra se registran en un detector externo (muscovita con un contenido del uranio <1 ppm), el cual, al igual que la muestra, debe ser atacado químicamente. Este método se denomina de detector externo (EDM – *External Detector Method*, *e.g*., Gleadow *et al*., 1986; Green *et al*., 1986; Wagner y Van den Haute, 1992; Gallagher, 1995; Jonckheere *et al*., 1993; Jonckheere y Van den Haute, 1996). A través de las densidades de trazas espontáneas e inducidas en un mineral se puede obtener la concentración del uranio en este mineral. Entonces, sabiendo la densidad de las trazas espontáneas y las constantes del decaimiento total del ^{238}U (λ_D) y por la fisión espontánea del ^{238}U (λ_f), y la concentración del ^{238}U, es posible obtener la edad del mineral.

En comparación con la técnica EDM, es relativamente fácil medir la concentración del ^{238}U en los apatitos con LA-ICP-MS (usando las relaciones $^{238}U/^{43}Ca$ o $^{238}U/^{44}Ca$). Las primeras dataciones de apatitos y circones con el método alternativo (LA-ICP-MS) fueron obtenidas por Cox *et al*. (2000) y Svojtka y Košler (2002). Resultó que las edades obtenidas con los métodos convencional y alternativo son prácticamente iguales. Por ejemplo, en dos grupos de circones analizados con el método EDM se obtuvieron edades de 231 ± 13 (1σ) Ma y 218 ± 15 (1σ) Ma, mientras que con el método TF LA-ICP-MS los mismos circones se dataron en 238 ± 12 (1σ) Ma y 214 ± 9 (1σ) Ma, respectivamente (Svojtka y Košler, 2002). Más tarde, Hasebe *et al*. (2004) y Donelick *et al*. (2005) desarrollaron la metodología alternativa usando LA-ICP-MS.

MATERIAL DE REFERENCIA

La selección de un mineral de referencia es un punto muy importante para dataciones y análisis químicos. En este trabajo se escogió el fluorapatito de Cerro de Mercado (Durango, México). Los cristales de este mineral son de color amarillo y son muy transparentes. Sus tamaños pueden ser de 1 – 3 cm, por lo que son fáciles de colectar para utilizarlos en los experimentos de laboratorio. El apatito de Durango (DUR) no es un mineral de referencia ideal, pues algunos cristales pueden tener inclusiones y zonación de algunos elementos químicos (*e.g*., Boyce y Hodges, 2005). Sin embargo, es suficientemente homogéneo y su composición química no es muy variable, lo que permite que sea un mineral de referencia confiable internacionalmente para análisis químicos y dataciones mediante TF, (U-Th)/He y U-Pb. Goldoff *et al*. (2012) analizaron los elementos mayores en el fluorapatito DUR con EPMA y proponen la siguiente composición promedio en % en peso (± 1σ): CaO (54.5 ± 0.3), P_2O_5 (41.6 ± 0.3), F (3.4 ± 0.1) y Cl (0.43), dando un total de 100%. De acuerdo con Young *et al*. (1969), los granos enteros del DUR tienen de 9.7 a 12.3 ppm de U y de 167 a 238 ppm de Th. Solé y Pi (2005) determinaron mediante ICP-MS (en solución) las concentraciones promedio de U (13.5 ppm) y Th (255.5 ppm) y las de otros elementos traza y REE. Los análisis puntuales con LA-ICP-MS indican que las concentraciones del U y Th en el DUR normalmente varían en los rangos 10 – 15 ppm y 200 – 330 ppm, respectivamente (Belousova *et al*., 2002; Hasebe *et al*., 2004; Boyce y Hodges, 2005).

Los apatitos DUR se encuentran en depósitos de hierro asociados con rocas volcánicas que tienen una edad K/Ar de 31.4 ± 0.5 (1σ) Ma (Naeser y Fleischer, 1975), recalculada por Green (1985) usando las constantes de decaimiento de Steiger y Jäger (1977). De acuerdo con los datos de (U-Th)/He de Farley (2002) la edad del DUR es de 32 ± 1 (1σ) Ma. Las rocas volcánicas del Cerro de Mercado fueron fechadas también mediante $^{40}Ar/^{39}Ar$ y los resultados indican una edad de 31.4 ± 0.1 (1σ) Ma (McDowell *et al*., 2005). Para el apatito DUR, Solé y Pi (2005) obtuvieron la misma edad de 31.4 ± 1.0 (1σ) Ma mediante el sistema (U-Th)/He. Jonckheere *et al*. (1993), usando las densidades de trazas obtenidas por distintos operadores, fecharon el fluorapatito DUR por TF convencional en diferentes cortes de cristal (basal y prismático) y determinaron que las edades varían en un rango de 29 – 33 Ma, dando una edad promedio de 31.4 ± 0.5 (1σ) Ma. Hasebe *et al*. (2004) determinaron las concentraciones de ^{238}U con LA-ICP-MS en 11 *spots* para el fluorapatito DUR y por primera vez reportaron una edad aceptable de 29.7 ± 1.9 (1σ) Ma usando el método TF alternativo. Chew y Donelick (2012) con TF LA-ICP-MS (más de 500 *spots*) y usando directamente las relaciones corregidas de $^{238}U_{cps}/^{43}Ca_{cps}$ para este apatito obtuvieron una edad de 31.4 ± 0.7 (1σ) Ma. Recientemente, Chew *et al*. (2014) dataron el fluorapatito DUR con el método U-Pb LA-ICP-MS y proponen una edad de 31.8 ± 0.2 (1σ) Ma. En general, las edades reportadas mediante diferentes métodos isotópicos para las rocas volcánicas y el fluorapatito DUR son coincidentes dentro de los márgenes de incertidumbre y se puede resumir que hasta la fecha la edad estándar para el apatito DUR se sigue tomando como 31.4 ± 0.5 (1σ) Ma.

EXPERIMENTOS Y METODOLOGÍA

Preparación de muestras y estudios ópticos

Para los experimentos se seleccionaron más de 15 fragmentos del apatito DUR con tamaños de 500 a 1500 μm en diámetro, procedentes de un único cristal de unos 2 cm de longitud. Observando bajo un microscopio binocular y usando unas pinzas de acero, los fragmentos fueron adheridos con cinta de doble cara a una base dentro de un aro de plástico de 2.5 cm de diámetro, el cual se rellenó con resina epóxica (EpoFix), en una proporción preestablecida de resina/catalizador (7/1). El tiempo de solidificación completa de la mezcla es de 12 horas. Luego, la cara de la probeta con los cristales montados se pulió primero con lijas húmedas de número P1500/2500 (12.6/8.3 μm de carburo de silicio) para desbastar. El pulido se terminó gradualmente usando suspensiones de alúmina de 5, 1, 0.25 y 0.05 μm. Todo el proceso se realizó manualmente y cada vez, al cambiar el paño y el abrasivo, la probeta se limpió con agua destilada en un baño ultrasónico durante ~10 min. Al final, la probeta se limpió con alcohol y se secó al aire libre (30 min). Durante todo el proceso de preparación de la probeta es necesario controlar la calidad del pulido bajo un microscopio óptico con luz reflejada. El pulido debe ser lo más perfecto posible (el equivalente a un pulido para microsonda electrónica o mejor), de lo contrario será complicado observar las trazas espontáneas después de la reacción química. Todos los pasos de la preparación de muestra se realizaron en el Laboratorio de Separación de Minerales del Instituto de Geología, UNAM. El ataque químico (*etching*) se realizó usando la metodología convencional, con 5.5 M HNO_3 (20 ± 0.5 s; 21 ± 1 °C, *e.g*., Donelick *et al*., 2005). Al terminar el ataque

químico, la probeta se limpió inmediatamente con agua destilada y se secó al aire libre.

Después del ataque químico, el análisis TF empieza con la observación de las trazas espontáneas bajo un microscopio óptico de luz transmitida. En este estudio se usó un Olympus BX51 instalado en el Instituto de Geología, UNAM. Se utilizó un *software* general de tratamiento de imágenes (ImageProPlus) para mediciones de áreas, *etc*., el cual permite también realizar un conteo semiautomático de trazas espontáneas. La escala de medición del *software* se calibró para los objetivos usando una lámina micrométrica. La datación por TF LA-ICP-MS requiere muestreos puntuales con láser dentro de los mismos campos para los cuales se calcularon las densidades de trazas espontáneas (Hasebe *et al*., 2004; Donelick *et al*., 2005; Chew y Donelick, 2012). La selección del área para el conteo de trazas depende principalmente del tamaño de cristal y de la homogeneidad de la distribución de trazas. Para el conteo de trazas se usaron oculares 15× y objetivos 40× y 100× con un aumento total de 600× y 1500×, respectivamente. La observación detallada de los apatitos montados permitió seleccionar 12 fragmentos sin inclusiones visibles y con una distribución de trazas aparentemente homogénea. En los primeros nueve fragmento de DUR se escogió un campo con área (*S*) de 150×200 μm^2 para el conteo de trazas. Partiendo de la superficie analizada *S* (30,000 μm^2) y del número de trazas espontáneas registradas (N_S) se obtuvieron las densidades de trazas (p_S) para cada fragmento contando los dos tipos de trazas, superficiales y confinadas. Los valores de p_S se expresaron en número por cm^2. En los últimos tres fragmentos las densidades se obtuvieron en áreas más grandes (47,040, 89,340 y 87,750 μm^2).

Mediciones de elementos con LA-ICP-MS

Las mediciones de las concentraciones de elementos traza y REE se realizaron en el Laboratorio de Estudios Isotópicos (LEI) del Centro de Geociencias, UNAM, utilizando un sistema de ablación láser de excímeros Resonetics M050 193 nm ArF, acoplado a un espectrómetro de masas cuadrupolar con fuente de plasma inductivamente acoplado (ICP-MS). Para la ablación se usó una fluencia de 6 J·cm^{-2}, un *spot* de ablación de 44 μm de diámetro y una frecuencia de 5 Hz. De acuerdo con mediciones previas (Solari *et al*., 2010), la tasa de penetración es de 0.15 μm por cada disparo. En un tiempo de ablación de 30 segundos, la penetración corresponde a unos 22 μm. Los isótopos y elementos medidos son ^{43}Ca, ^{44}Ca, Mn, Sr, Y, REE, Th y ^{238}U. Por cada 10 *spots* en DUR se realizaron 1 – 2 *spots* en el vidrio NIST612 de composición elemental conocida. Los resultados obtenidos usando NIST612 fueron normalizados al estándar interno de ^{43}Ca tomando un promedio de CaO para DUR de 54.5% (Goldoff *et al*., 2012). Se analizaron un total de 104 *spots* en 12 fragmentos de DUR, en los dominios en los cuales se contaron previamente las trazas espontáneas (Figuras 1a y 1b). Los elementos de las primeras 54 ablaciones se midieron con un ICP-MS Thermo Xseries II y los otros 50 *spots* se analizaron con un Thermo iCAP Q.

Cálculo de edades y errores

Según Hasebe *et al.* (2004), la ecuación general para calcular las edades (*t*) directamente a partir de la densidad de trazas espontáneas y contenido del ^{238}U es:

$$t = \frac{1}{\lambda_D} \ln\left(1 + \frac{p_S \lambda_D M}{\lambda_f N_A {}^{238}\mathrm{U}\, 10^{-6} d R_{SP}}\right) \quad (1)$$

en donde, p_S es la densidad de trazas espontáneas (en cm^{-2}); ^{238}U es la concentración del isótopo ^{238}U en ppm medida con LA-ICP-MS; λ_D es la constante de decaimiento total del ^{238}U (1.55125×10^{-10} a^{-1}; Jaffey

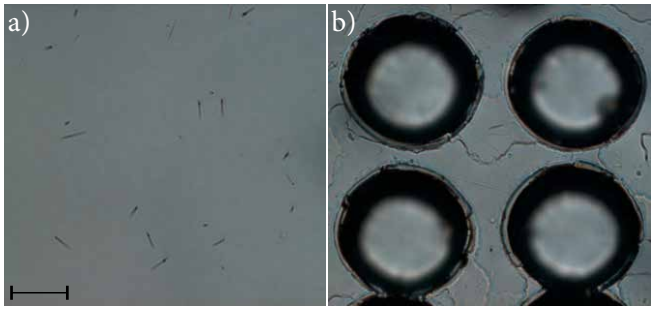

Figura 1. a) Fotografía de las trazas de fisión espontánea en el fluorapatito de Durango después del ataque químico (*etching*). b) Fotografía tomada después del análisis con ablación láser (LA-ICP-MS). La escala es de 20 μm. Los diámetros del *spot* corresponden a ~45 – 49 μm.

et al., 1971); *M* es la masa del ^{238}U (238.0508); λ_f es la constante de decaimiento por fisión espontánea del ^{238}U. La constante λ_f no está determinada exactamente hasta ahora y nosotros hemos escogido el valor de (8.45 ± 0.1)×10^{-17} a^{-1} recomendado por la IUPAC (*International Union of Pure and Applied Chemistry*; Holden y Hoffman, 2000). Este valor es el mismo que han aplicado muchos autores para las dataciones por TF tanto con el método convencional como con la técnica de LA-ICP-MS (*e.g*., Bernet *et al*., 2004; Hasebe *et al*., 2004, 2009; Hadler *et al*., 2009) y coincide perfectamente con los valores de λ_f obtenidos experimentalmente usando diferentes métodos (*e.g*., Spadavecchia y Hahn, 1967; Galliker *et al*., 1970; Guedes *et al*., 2003; Yoshioka *et al*., 2005). N_A es el número de Avogadro (6.022×10^{23} mol^{-1}); *d* es la densidad promedio de los apatitos (3.19 ± 0.04 g·cm^{-3}, Betekhtin, 1956; Hasebe *et al*., 2004, 2009); el factor R_{SP} representa la mitad de la longitud promedio de las trazas espontáneas en apatitos de rocas enfriadas rápidamente y sin consecuentes perturbaciones térmicas, *i.e*., de rocas volcánicas (típicamente es de 15 ± 0.5 μm; Gleadow *et al*., 1986; Chew y Donelick, 2012). Por lo tanto, se considera que R_{SP} es igual a (7.5 ± 0.25) × 10^{-4} cm (Hasebe *et al*., 2004, 2009).

Para calcular la incertidumbre total generada por el uso de la Ecuación 1 hemos propagado la desviación estándar de cada variable mediante derivación parcial, obteniendo las siguientes ecuaciones nuevas:

$$W = \frac{10^6 M p_S}{10^6 \lambda_D M p_S + d N_A R_{SP} {}^{238}\mathrm{U} \lambda_f} \quad (2)$$

$$\sigma^2(t) = W \left[\left(\frac{\sigma(\lambda_f)}{\lambda_f}\right)^2 + \left(\frac{\sigma(d)}{d}\right)^2 + \left(\frac{\sigma(R_{SP})}{R_{SP}}\right)^2 + \left(\frac{\sigma(^{238}\mathrm{U})}{^{238}\mathrm{U}}\right)^2 + \left(\frac{\sigma(p_S)}{p_S}\right)^2\right] \quad (3)$$

Se observa que la varianza $\sigma^2(t)$ de la edad es la suma de los cuadrados de las desviaciones estándar relativas multiplicada por un factor (*W*). La sesión con LA-ICP-MS mostró que los errores analíticos ± 1σ para el ^{238}U son menores al 1%. Es probable que haya una variación natural en el contenido de CaO de 54.5 ± 0.5% en peso (~1%) en el fluorapatito DUR, por lo tanto hemos tomado la incertidumbre total del ^{238}U como la suma entre de la precisión analítica y la incertidumbre generada por la variación del CaO, lo que al final da una incertidumbre total para el ^{238}U de ~2%.

Tabla 1. Concentraciones mínimas (Mín), promedio y máximas (Máx), con sus desviaciones estándares (Desv. Est.), de elementos traza y REE (en ppm) calculadas tomando en cuenta 104 análisis puntuales (*spot*) por medio de LA-ICP-MS. Los datos *[2] son los valores promedio tomados de Solé y Pi (2005).

	Mn	Sr	Y	La	Ce	Pr	Nd	Sm	Eu	Gd	Tb	Dy	Ho	Er	Tm	Yb	Lu	Th	^{238}U	Th/U
Mín	87.2	465	724	3321	4886	400	1371	192	17.1	182	20.7	115	23.0	58.6	8.5	39.4	4.6	208	11.4	16.1
Promedio:	91.0	499	800	3613	5287	446	1532	217	18.8	208	23.3	131	25.9	69.1	8.8	45.7	5.3	225	12.0	18.6
Máx	93.5	532	1000	4508	6317	498	1695	247	20.0	241	27.7	169	33.0	91.1	9.2	62.0	6.9	265	15.2	19.4
Desv. Est.	1.2	12	49	224	305	16	56	10	0.6	11	1.2	10	1.8	5.9	0.1	4.0	0.4	11	0.7	0.6
Datos *[2]		502	940	4070	6000	493	1700	244	22.1	187	28.0	152	29.2	83.3	10.8	52.9	6.2	256	13.5	18.8

RESULTADOS

Composición química

Las concentraciones mínimas, máximas y promedio, junto con las desviaciones estándar (SD), de los elementos traza y REE obtenidos en 104 *spots* se presentan en la Tabla 1. El contenido del ^{238}U es de 11.4 – 15.2 ppm y su promedio es de 12.0 ± 0.7 ppm (1 SD). La concentración del Th varía de 208 a 265 ppm con un promedio de 225 ± 11 ppm (1 SD). Las relaciones Th/U son de 16.1 – 19.4. Los errores analíticos ± 2σ para los elementos Mn, Y, Sr y los REE ligeros (LREE) están entre 0.5 y 1.5%, mientras que para Th, ^{238}U y los REE pesados son de 1 – 2%. Unas ligeras discordancias entre nuestros resultados y los datos de Solé y Pi (2005) medidos por ICP-MS en solución se pueden ver en la Tabla 1 y en los patrones de Y+(REE) (Figura 2) normalizados a los valores de la condrita C1 de McDonough y Sun (1995). La diferencia entre los resultados obtenidos por LA-ICP-MS y los obtenidos por ICP-MS en solución se debe a que Solé y Pi (2005) determinaron la composición en mineral total (200 mg), mientras que en este estudio los análisis químicos fueron puntuales en diferentes fragmentos escogidos al azar, y como se mencionó anteriormente, el fluorapatito DUR puede presentar zonación elemental. En este estudio los REE se analizaron con el fin de comparar las concentraciones obtenidas con los datos publicados y verificar la calidad de las mediciones por LA-ICP-MS. Como se puede ver en la Figura 2, los patrones de los REE normalizados muestran un enriquecimiento relativo de los LREE con anomalías negativas del Eu muy marcadas (el valor de Eu/Eu* es menor que 0.3, donde Eu* = (Sm+Gd)/2, todos los valores normalizados al condrito C1). Este tipo de comportamiento de las REE es muy común en apatitos de depósitos de hierro, como por ejemplo, en el apatito de DUR (*e.g.*, Belousova *et al.*, 2002; Lesnov, 2012).

Edades por trazas de fisión

En los fragmentos DUR, la densidad de trazas espontáneas varía de 0.1733×10^6 a 0.1956×10^6 cm^{-2}; sólo en el fragmento DUR8 se encontró una densidad de 0.2333×10^6 cm^{-2} (Tabla 2). Finalmente, se obtuvo una densidad promedio de $(0.1922 \pm 0.0124)\times10^6$ cm^{-2}. La densidad de trazas espontáneas puede variar en un cierto rango dependiendo del corte del cristal, del tiempo de ataque químico y de la experiencia del operador. Para el apatito DUR la variación común de p_S es de $(0.18 – 0.22)\times10^6$ cm^{-2}, aunque las p_S mínima y máxima pueden ser de 0.15×10^6 cm^{-2} y 0.25×10^6 cm^{-2}, respectivamente (Jonckheere *et al.*, 1993; Jonckheere y Van den Haute, 1996).

Las 104 edades con sus errores ±1σ (4 – 6%) obtenidas a partir de los análisis puntuales varían entre 28 y 33 Ma (Tabla 2, Figura 3a). La variación en las edades de diferentes fragmentos del fluorapatito DUR también fue observada por Solé y Pi (2005) usando el método (U-Th)/He. En el fragmento DUR8 las concentraciones son elevadas en comparación con el resto de los fragmentos(Figura 3b), para el ^{238}U es de 14.3 – 15.2 ppm, lo que se esperaba obtener antes de la sesión con LA-ICP-MS, a partir de su densidad de trazas elevada (0.2333×10^6 cm^{-2}) (Figura 3c). Las edades obtenidas en el DUR8 son prácticamente iguales a las edades de otros fragmentos (Tabla 2, Figura 3a). La edad promedio para el fluorapatito DUR se calculó con la ayuda de Isoplot (Ludwig, 2008) tomando en cuenta las 104 edades con sus errores. Se obtuvo una edad promedio de 31.2 ± 0.2 (1σ) Ma con un valor de la media cuadrática de las desviaciones ponderadas (MSWD, *Mean square of weighted deviates*) de 0.60 y una probabilidad de 1.000 (Figura 3a). El valor de MSWD menor a 1 indica que los errores de las edades individuales están ligeramente sobreestimados.

DISCUSIÓN

Los resultados químicos obtenidos para el fluorapatito DUR en este trabajo son concordantes con los datos publicados (*e.g.*, Young *et al.*, 1969; Belousova *et al.*, 2002; Hasebe *et al.*, 2004, 2009; Boyce y Hodges, 2005; Solé y Pi, 2005). La mayoría de las edades calculadas en diferentes puntos para el DUR se encuentran dentro del margen de error de la edad de referencia (31.4 ± 0.5 Ma), dando finalmente una edad promedio de 31.2 ± 0.2 Ma (Figuras 3a y 4). La reproducibilidad de los datos obtenidos a lo largo de este estudio es mejor que un 1%. En general, las edades TF para el fluorapatito de DUR determinadas anteriormente mediante LA-ICP-MS son 1-2 Ma más jóvenes que la edad de referencia (*e.g.*, Hasebe *et al.*, 2004; Hadler *et al.*, 2009). Nuestros resultados coinciden perfectamente con la edad aceptada (Figura 4) y probablemente eso tiene que ver con los siguientes factores: a) la cantidad de fragmentos utilizados y el número de análisis puntuales, lo cual juega un papel importante en la estadística; b) las mejoras analíticas instrumentales de los últimos años, especialmente para los equipos ICP-MS; c) las mejoras de los sistemas de ablación láser ocurridas en los últimos 10 años. Por ejemplo, Hasebe *et al.* (2004) utilizaron un láser de estado sólido de 266 nm de longitud de onda,

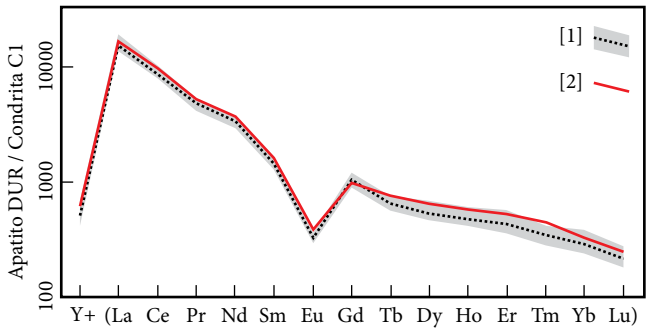

Figura 2. Patrones de Y+(REE) del fluorapatito de Durango normalizados a la condrita C1 (McDonough y Sun, 1995). El campo gris indica la dispersión de los patrones de los 104 *spots* y la línea punteada [1] es el patrón de los valores promedio. La línea roja sólida [2] representa los valores promedio obtenidos con ICP-MS (solución) por Solé y Pi (2005).

Tabla 2. Edades de trazas de fisión del fluorapatito de Cerro de Mercado (Durango, México). N_{frag} – número del fragmento estudiado, N_S – número de trazas espontáneas con probables errores registradas en el área S, N_{LA} – número del análisis puntual (*spot*) con LA-ICP-MS, p_S – densidad de trazas espontáneas, ^{238}U – concentración del isótopo en ppm, t_{TF} – edades de trazas de fisión con sus errores expresados como ±1σ.

N_{frag}	S (μm²)	N_S	N_{LA}	p_S (10^6·cm^{-2})	^{238}U (ppm)	t_{TF} (Ma)	±1σ (Ma)
DUR 1	30,000	52 ± 2	1	0.1733 ± 0.0067	11.82 ± 0.24	28.6	1.6
			2	0.1733 ± 0.0067	11.90 ± 0.24	28.4	1.6
			3	0.1733 ± 0.0067	11.95 ± 0.24	28.3	1.6
			4	0.1733 ± 0.0067	12.57 ± 0.25	26.9	1.5
			5	0.1733 ± 0.0067	12.33 ± 0.25	27.4	1.6
			6	0.1733 ± 0.0067	11.55 ± 0.23	29.3	1.7
DUR 2	30,000	57 ± 2	7	0.1900 ± 0.0067	11.85 ± 0.24	31.3	1.7
			8	0.1900 ± 0.0067	11.75 ± 0.24	31.5	1.7
			9	0.1900 ± 0.0067	11.96 ± 0.24	31.0	1.7
			10	0.1900 ± 0.0067	11.58 ± 0.23	32.0	1.8
			11	0.1900 ± 0.0067	12.04 ± 0.24	30.8	1.7
			12	0.1900 ± 0.0067	11.86 ± 0.24	31.2	1.7
DUR 3	30,000	54 ± 2	13	0.1800 ± 0.0067	11.75 ± 0.24	29.9	1.7
			14	0.1800 ± 0.0067	11.87 ± 0.24	29.6	1.7
			15	0.1800 ± 0.0067	11.82 ± 0.24	29.7	1.7
			16	0.1800 ± 0.0067	12.09 ± 0.24	29.0	1.6
			17	0.1800 ± 0.0067	11.78 ± 0.24	29.8	1.7
			18	0.1800 ± 0.0067	12.04 ± 0.24	29.2	1.6
DUR 4	30,000	57 ± 2	19	0.1900 ± 0.0067	11.85 ± 0.24	31.3	1.7
			20	0.1900 ± 0.0067	11.58 ± 0.23	32.0	1.8
			21	0.1900 ± 0.0067	11.43 ± 0.23	32.4	1.8
			22	0.1900 ± 0.0067	12.37 ± 0.25	30.0	1.7
			23	0.1900 ± 0.0067	11.68 ± 0.23	31.7	1.7
			24	0.1900 ± 0.0067	11.89 ± 0.24	31.2	1.7
DUR 5	30,000	58 ± 2	25	0.1933 ± 0.0067	11.84 ± 0.24	31.8	1.7
			26	0.1933 ± 0.0067	11.84 ± 0.24	31.8	1.7
			27	0.1933 ± 0.0067	11.79 ± 0.24	32.0	1.8
			28	0.1933 ± 0.0067	12.63 ± 0.25	29.9	1.6
			29	0.1933 ± 0.0067	12.41 ± 0.25	30.4	1.7
			30	0.1933 ± 0.0067	11.62 ± 0.23	32.5	1.8
DUR 6	30,000	55 ± 2	31	0.1833 ± 0.0067	11.38 ± 0.23	31.4	1.8
			32	0.1833 ± 0.0067	11.45 ± 0.23	31.2	1.7
			33	0.1833 ± 0.0067	11.52 ± 0.23	31.0	1.7
			34	0.1833 ± 0.0067	11.51 ± 0.23	31.1	1.7
			35	0.1833 ± 0.0067	11.63 ± 0.23	30.8	1.7
			36	0.1833 ± 0.0067	11.78 ± 0.24	30.4	1.7
DUR 7	30,000	53 ± 2	37	0.1767 ± 0.0067	11.67 ± 0.23	29.5	1.7
			38	0.1767 ± 0.0067	11.72 ± 0.23	29.4	1.7
			39	0.1767 ± 0.0067	11.84 ± 0.24	29.1	1.7
			40	0.1767 ± 0.0067	11.51 ± 0.23	29.9	1.7
			41	0.1767 ± 0.0067	11.44 ± 0.23	30.1	1.7
			42	0.1767 ± 0.0067	12.39 ± 0.25	27.8	1.6
DUR 8	30,000	70 ± 2	43	0.2333 ± 0.0067	14.52 ± 0.29	31.3	1.6
			44	0.2333 ± 0.0067	15.22 ± 0.30	29.9	1.5
			45	0.2333 ± 0.0067	14.76 ± 0.30	30.8	1.6
			46	0.2333 ± 0.0067	14.61 ± 0.29	31.2	1.6
			47	0.2333 ± 0.0067	14.32 ± 0.29	31.8	1.6
			48	0.2333 ± 0.0067	14.89 ± 0.30	30.6	1.6
DUR 9	30,000	56 ± 2	49	0.1867 ± 0.0067	11.88 ± 0.24	30.7	1.7
			50	0.1867 ± 0.0067	11.96 ± 0.24	30.4	1.7
			51	0.1867 ± 0.0067	11.82 ± 0.24	30.8	1.7

continúa

Tabla 2 (continuación). Edades de trazas de fisión del fluorapatito de Cerro de Mercado (Durango, México). N_{frag} – número del fragmento estudiado, N_S – número de trazas espontáneas con probables errores registradas en el área S, N_{LA} – número del análisis puntual (*spot*) con LA-ICP-MS, p_S – densidad de trazas espontáneas, ^{238}U – concentración del isótopo en ppm, t_{TF} – edades de trazas de fisión con sus errores expresados como ±1σ.

N_{frag}	S (μm²)	N_S	N_{LA}	p_S (10^6·cm^{-2})	^{238}U (ppm)	t_{TF} (Ma)	±1σ (Ma)
DUR 9 *continuación*	30,000	56 ± 2	52	0.1867 ± 0.0067	11.52 ± 0.23	31.6	1.8
			53	0.1867 ± 0.0067	11.40 ± 0.23	31.9	1.8
			54	0.1867 ± 0.0067	11.46 ± 0.23	31.8	1.8
DUR 10	47,040	92 ± 2	55	0.1956 ± 0.0043	11.95 ± 0.20	31.9	1.5
			56	0.1956 ± 0.0043	12.10 ± 0.22	31.5	1.5
			57	0.1956 ± 0.0043	11.88 ± 0.19	32.1	1.5
			58	0.1956 ± 0.0043	12.03 ± 0.21	31.7	1.5
			59	0.1956 ± 0.0043	11.98 ± 0.20	31.8	1.5
			60	0.1956 ± 0.0043	12.17 ± 0.20	31.3	1.4
			61	0.1956 ± 0.0043	11.84 ± 0.19	32.2	1.5
			62	0.1956 ± 0.0043	11.80 ± 0.19	32.3	1.5
			63	0.1956 ± 0.0043	12.10 ± 0.20	31.5	1.5
			64	0.1956 ± 0.0043	11.83 ± 0.18	32.2	1.5
DUR 11	89,340	174 ± 3	65	0.1948 ± 0.0034	11.89 ± 0.20	31.9	1.4
			66	0.1948 ± 0.0034	11.95 ± 0.19	31.8	1.4
			67	0.1948 ± 0.0034	11.07 ± 0.20	34.3	1.5
			68	0.1948 ± 0.0034	11.99 ± 0.20	31.7	1.4
			69	0.1948 ± 0.0034	12.08 ± 0.20	31.4	1.4
			70	0.1948 ± 0.0034	12.18 ± 0.19	31.2	1.4
			71	0.1948 ± 0.0034	12.11 ± 0.18	31.4	1.4
			72	0.1948 ± 0.0034	11.87 ± 0.18	32.0	1.4
			73	0.1948 ± 0.0034	12.07 ± 0.19	31.5	1.4
			74	0.1948 ± 0.0034	12.26 ± 0.19	31.0	1.4
			75	0.1948 ± 0.0034	12.09 ± 0.20	31.4	1.4
			76	0.1948 ± 0.0034	11.73 ± 0.19	32.4	1.4
			77	0.1948 ± 0.0034	11.87 ± 0.20	32.0	1.4
			78	0.1948 ± 0.0034	11.91 ± 0.19	31.9	1.4
			79	0.1948 ± 0.0034	12.11 ± 0.19	31.4	1.4
			80	0.1948 ± 0.0034	12.04 ± 0.19	31.6	1.4
			81	0.1948 ± 0.0034	12.13 ± 0.22	31.3	1.4
			82	0.1948 ± 0.0034	11.87 ± 0.18	32.0	1.4
			83	0.1948 ± 0.0034	12.00 ± 0.19	31.7	1.4
			84	0.1948 ± 0.0034	11.90 ± 0.20	31.9	1.4
DUR 12	87,750	171 ± 3	85	0.1949 ± 0.0034	12.42 ± 0.18	30.6	1.3
			86	0.1949 ± 0.0034	12.03 ± 0.18	31.6	1.4
			87	0.1949 ± 0.0034	11.80 ± 0.18	32.2	1.4
			88	0.1949 ± 0.0034	12.04 ± 0.19	31.6	1.4
			89	0.1949 ± 0.0034	12.20 ± 0.21	31.2	1.4
			90	0.1949 ± 0.0034	11.80 ± 0.20	32.2	1.4
			91	0.1949 ± 0.0034	11.86 ± 0.20	32.0	1.4
			92	0.1949 ± 0.0034	11.57 ± 0.19	32.8	1.5
			93	0.1949 ± 0.0034	11.71 ± 0.17	32.5	1.4
			94	0.1949 ± 0.0034	11.93 ± 0.19	31.9	1.4
			95	0.1949 ± 0.0034	12.14 ± 0.18	31.3	1.4
			96	0.1949 ± 0.0034	11.95 ± 0.19	31.8	1.4
			97	0.1949 ± 0.0034	12.07 ± 0.22	31.5	1.4
			98	0.1949 ± 0.0034	12.13 ± 0.21	31.3	1.4
			99	0.1949 ± 0.0034	11.52 ± 0.18	33.0	1.5
			100	0.1949 ± 0.0034	12.05 ± 0.20	31.5	1.4
			101	0.1949 ± 0.0034	11.86 ± 0.18	32.0	1.4
			102	0.1949 ± 0.0034	11.78 ± 0.20	32.3	1.4
			103	0.1949 ± 0.0034	11.88 ± 0.19	32.0	1.4
			104	0.1949 ± 0.0034	11.84 ± 0.20	32.1	1.4

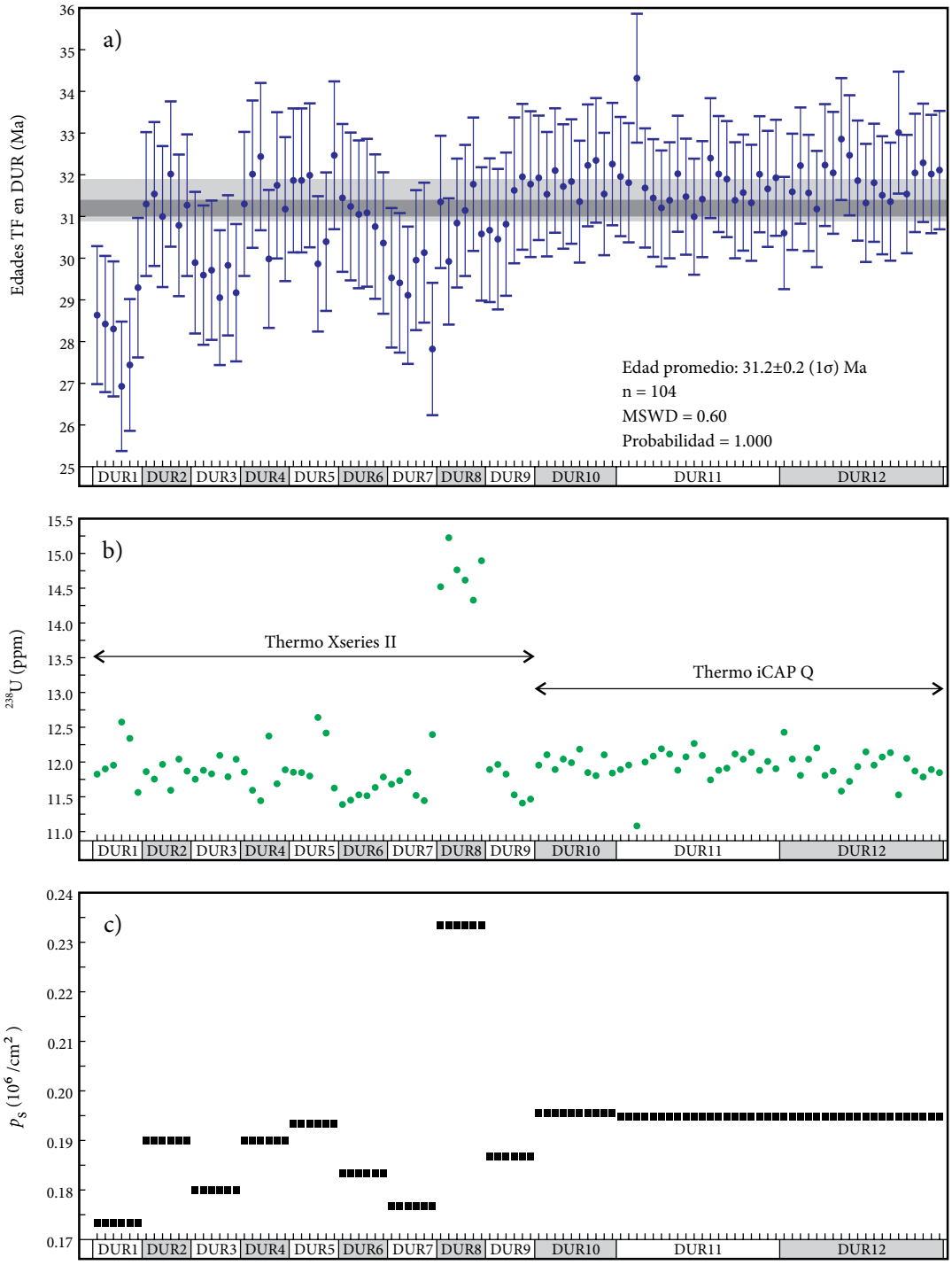

Figura 3. Resultados de la datación del fluorapatito de Durango por trazas de fisión. a: Edades de trazas de fisión (Ma) calculadas para cada punto analizado con sus incertidumbres expresadas como ±1σ en diferentes fragmentos (DUR1 – DUR12). El campo gris claro representa la edad de referencia (31.4 ± 0.5 Ma) y el campo gris oscuro representa la edad promedio obtenida en este estudio (31.2 ± 0.2 Ma). b: Concentraciones de ^{238}U en ppm medidas en 104 puntos usando dos diferentes instrumentos ICP-MS. c: Densidades de trazas espontáneas (p_S) obtenidas en 12 fragmentos del DUR.

con un error en la reproducibilidad de ± 10%, mientras que nosotros hemos usado un láser de excímeros de 193 nm longitud de onda, para el cual se ha reportado (*e.g.*, Günther *et al.*, 1997) que contribuye a un menor fraccionamiento analítico del U y Pb en comparación con otros tipos de láseres, con la excepción de los láseres de femtosegundo (Poitrasson *et al.*, 2003).

No es correcto resumir que el método nuevo es más preciso que el método convencional, porque la técnica EDM hasta la fecha sigue siendo el método más usado y mejor controlado en la mayoría de laboratorios del mundo. Sin embargo, la metodología LA-ICP-MS tiene algunas ventajas comparando con EDM. El método nuevo es obviamente más rápido, porque el EDM requiere un análisis más

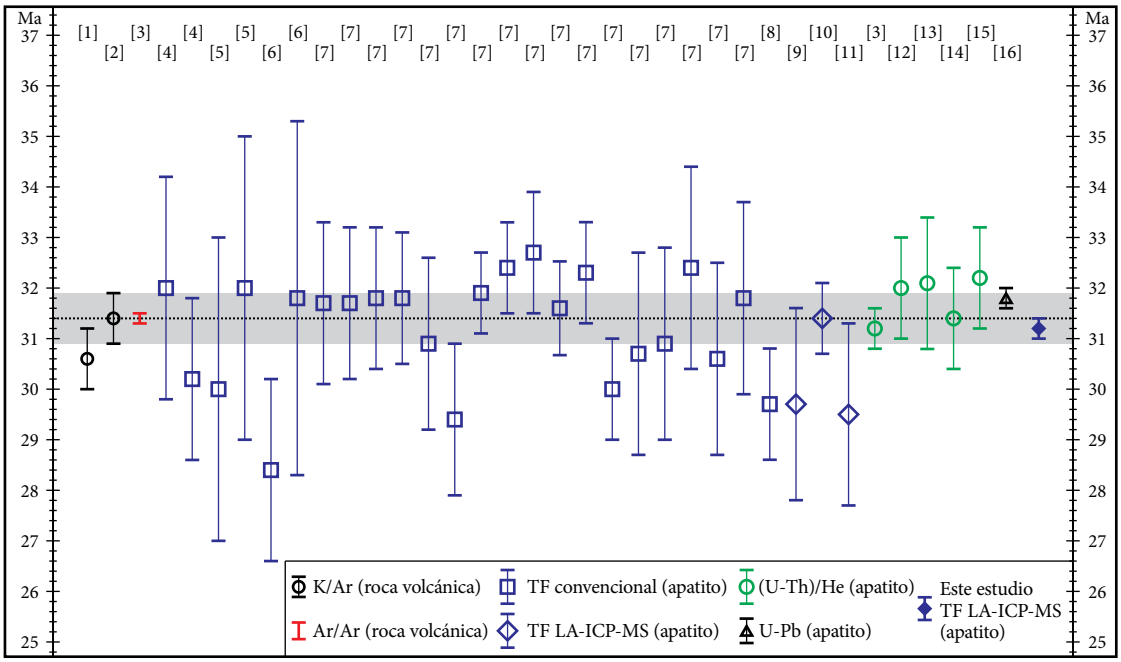

Figura 4. Comparación de la edad obtenida en este estudio con las edades reportadas por algunos autores. Las edades K/Ar y Ar/Ar representan edades de rocas volcánicas (*i.e.*, roca encajonante del fluorapatito de Durango). Referencias: [1] Naeser y Fleischer (1975), [2] Green (1985), [3] McDowell *et al.* (2005), [4] Hurford y Gleadow (1977), [5] Green (1978), [6] Märk *et al.* (1980), [7] Jonckheere *et al.* (1993), [8] Iunes *et al.* (2002), [9] Hasebe *et al.* (2004), [10] Chew y Donelick (2012), [11] Hadler *et al.* (2009), [12] Farley (2002), [13] House *et al.* (2000), [14] Solé y Pi (2005), [15] Johnstone *et al.* (2013), [16] Chew *et al.* (2014). Las edades se presentan en Ma con sus desviaciones estándares ±1σ. El campo gris es la edad aceptada para el fluorapatito de Durango y es igual a 31.4 ± 0.5 Ma.

complicado, con irradiación de las muestras, doble ataque químico (de minerales y detector) y doble conteo de trazas (p_S y p_i). Por otro lado, la técnica LA-ICP-MS permite medir las concentraciones del U y Th al mismo tiempo que las de otros elementos traza y REE, lo que puede tener aplicaciones para la triple datación de un solo cristal de apatito, es decir, TF, U-Pb y (U-Th)/He. Además, sabiendo el contenido de los elementos traza y REE en apatitos, es posible identificar el tipo de roca del cual provienen estos apatitos (Belousova *et al.*, 2002; Lesnov, 2012). La geoquímica de apatitos puede ser útil sobre todo para investigar la procedencia de sedimentos, lo que ha sido usado hasta la fecha en pocas ocasiones (Morton y Yaxley, 2007; Jafarzadeh *et al.*, 2014). Es importante mencionar también algunas desventajas del método alternativo. Por ejemplo, es destructivo y, a diferencia de EDM, es difícilmente aplicable a apatitos que presentan zonaciones fuertes de U o que contienen inclusiones de minerales. Las inclusiones de minerales enriquecidos en U (*e.g.*, monacita, circón) pueden mostrar alto contenido de U y consecuentemente generar edades TF anormalmente jóvenes, mientras que la zonación fuerte de U puede producir una sobreestimación de la edad del grano individual (Liu *et al.*, 2014).

Los usuarios de la técnica TF LA-ICP-MS en apatitos deberían tener en cuenta los siguientes requisitos importantes:

1) Para obtener la concentración de un isótopo *X* en apatitos con LA-ICP-MS se utiliza el calcio como estándar interno (en el estudio presente fue usado $X/^{43}Ca$). El contenido del CaO en los apatitos de diferente origen varía en un rango de 53 – 57 % en peso (Betekhtin, 1956; Belousova *et al.*, 2002; Lesnov, 2012) y se recomienda tomar la concentración de CaO para los apatitos desconocidos como 55 ± 2 % en peso, mientras que para el DUR se considera un valor de 54.5 ± 0.5 % en peso. En general este requisito se cumple suponiendo que el contenido de Ca en los apatitos es estequiométrico (Hasebe *et al.*, 2004, 2009; Donelick *et al.*, 2005; Chew y Donelick, 2012; Chew *et al.*, 2014).

2) El ataque químico (*etching*) necesario para poder observar las trazas espontáneas no cambia las concentraciones de elementos en apatitos (Hasebe *et al.*, 2009).

3) Es conveniente trabajar con granos mayores que 80 µm (anchura de prisma, diámetro), porque los apatitos no son tan resistentes a la ablación con láser como, por ejemplo, los circones (Belousova *et al.*, 2002).

4) Para un *spot* de ablación con diámetro de 44 µm, se tiene que escoger un área mínima para el conteo de trazas de 50×50 µm^2, lo que también depende de la homogeneidad de la distribución de trazas y del tamaño de cristal. Los muestreos con láser se tienen que realizar en los mismos campos para los cuales se determinó la densidad de trazas espontáneas. Por otro lado, en los apatitos en los que se usa un área grande de conteo de trazas (*i.e.*, más de 70×70 µm^2) es recomendable realizar la ablación con láser sobre todo el dominio de conteo, por ejemplo, usando el método de muestreo de barrido en zigzag (*zig-zag raster*) o muestreos puntuales múltiples (*e.g.*, De Grave *et al.*, 2012). En el caso del apatito de Durango es aceptable el uso de las mediciones simples (*i.e.*, sólo un *spot*) debido a que este apatito estándar normalmente presenta una distribución homogénea de trazas.

5) Es arriesgado analizar apatitos con muchas inclusiones o con zonación fuerte del U, lo que puede producir una sobreestimación de edad en algunos granos. Sin embargo, esto casi no afecta a la edad promedio (Liu *et al.*, 2014). Este requisito se puede ignorar en el caso de las dataciones de rocas ígneas y metamórficas. Sin embargo, es obligatorio tomar en cuenta lo mencionado anteriormente para las dataciones de rocas siliciclásticas, en donde las edades de grano individual pueden ser de interés capital.

6) Todos los errores analíticos se tienen que incluir en el cálculo de la incertidumbre final de las edades, por ejemplo, usando las Ecuaciones 2 y 3 propuestas en este trabajo.

7) El método LA-ICP-MS es destructivo y obviamente la medición de elementos con este instrumento es el último paso de la datación TF. Antes de iniciar la sesión con LA-ICP-MS es recomendable obtener fotografías digitales de los granos y campos con trazas ya contadas para comprobaciones posteriores.

8) Por último, se recomienda usar el apatito DUR como segundo estándar para controlar la calidad de los análisis químicos y dataciones por TF de apatitos desconocidos. Es decir, durante una misma sesión de análisis por LA-ICP-MS, por cada medición de 10 apatitos desconocidos realizar 1 a 2 *spots* en NIST612 y 1 a 2 *spots* en fragmentos del DUR con las densidades de trazas previamente determinadas.

CONCLUSIONES

Se reportan por primera vez en México análisis químicos del fluorapatito de Cerro de Mercado, Durango, realizados con LA-ICP-MS y su aplicación para la datación por trazas de fisión. Se muestra, tal como en algunos trabajos ya publicados (*e.g.*, Hasebe *et al*., 2004; Donelick *et al*., 2005; Chew y Donelick, 2012), que el método TF LA-ICP-MS es capaz de ser una alternativa al método convencional de detector externo (EDM). La composición de elementos trazas y REE y la edad obtenida (31.2 ± 0.2 Ma) para el apatito de Durango en este estudio presentan una buena precisión. Se concluye también que las metodologías utilizadas durante el conteo de trazas de fisión y el análisis de elementos traza por LA-ICP-MS están bien calibradas para la obtención de edades de trazas de fisión confiables.

AGRADECIMIENTOS

Este trabajo fue financiado por el proyecto de PAPIIT UNAM No. IN111414 y constituye una parte experimental de la tesis doctoral del primer autor bajo la tutoría de JS y el apoyo adicional de LS. El primer autor agradece al CONACyT por el otorgamiento de una beca para realizar los estudios de doctorado. Se agradece a las siguientes personas de la UNAM por ayudarnos en algunos pasos analíticos: Mtra. Consuelo Macías, Dra. Barbara Martiny y Dr. Rubén Alejandro Bernard Romero en la separación de minerales y preparación de muestras; Dr. Sergey Sedov, Mtro. Jaime Díaz y Mtra. Valentina Shchepetilnikova en los estudios microscópicos; Dr. Carlos Ortega-Obregón en las mediciones de elementos con LA-ICP-MS. Los autores agradecen atentamente al editor invitado de este volumen Dr. Peter Schaaf (responsable del Laboratorio Universitario de Geoquímica Isotópica, Instituto de Geofísica, UNAM) y a los expertos en termocronología de baja temperatura, Drs. Matthias Bernet (ISTerre, Université Joseph Fourier, Grenoble, Francia) y Mauricio A. Bermúdez (Laboratorio de Termocronología, Escuela de Geología, Minas y Geofísica, Universidad Central de Venezuela, Caracas, Venezuela) por sus comentarios y sugerencias que ayudaron a mejorar la presentación de este trabajo.

REFERENCIAS

Belousova, E.A., Griffin, W.L., O'Reilly, S.Y., Fisher, N.I., 2002, Apatite as an indicator mineral for mineral exploration: Trace-element compositions and their relationship to host rock type: Journal of Geochemical Exploration, 76, 45-69.

Bermúdez, M.A., Kohn, B.P., van der Beek, P.A., Bernet, M., O'Sullivan, P.B., Shagam, R., 2010, Spatial and temporal patterns of exhumation across the Venezuelan Andes: Implications for Cenozoic Caribbean geodynamics: Tectonics, 29(5), doi:10.1029/2009TC002635.

Bernet, M., Garver, J.I., 2005, Fission-track analysis of detrital zircon: Reviews in Mineralogy and Geochemistry, 58(1), 205-237.

Bernet, M., Brandon, M.T., Garver, J.I., Molitor, B.R., 2004, Fundamentals of detrital zircon fission-track analysis for provenance and exhumation studies with examples from the European Alps, *in* Bernet, M., Spiegel , C. (eds.) Detrital Thermochronology — Provenance Analysis, Exhumation, and Landscape Evolution of Mountain Belts: Geological Society of America, Special Paper 378, 25-36.

Betekhtin, A.G., 1956, Course of Mineralogy (en ruso): Moscow, Nedra, 558 pp.

Boyce, J.W., Hodges, K.V., 2005, U and Th zoning in Cerro de Mercado (Durango, Mexico) fluorapatite: Insights regarding the impact of recoil redistribution of radiogenic ^{4}He on (U-Th)/He thermochronology: Chemical Geology, 219, 261-274.

Brandon, M.T., Roden-Tice, M.K., Garver, J.I., 1998, Late Cenozoic exhumation of the Cascadian accretionary wedge in the Olympic Mountains, northwest Washington State: Geological Society of America Bulletin, 110, 985-1009.

Calmus, T., Poupeau, G., Bourgois, J., Michaud, F., Mercier de Lépinay, B., Labrin, E., Azdimousa, A., 1999, Late Mesozoic and Cenozoic thermotectonic history of the Mexican Pacific margin (18 to 25°N): new insight from apatite and zircon fission-track analysis of coastal and offshore plutonic rocks: Tectonophysics, 306, 163-182.

Calmus, T., Bernet, M., Hardwick, E., Lugo-Zazueta, R, 2012, Tertiary thermochronological evolution of the Sierra La Madera pluton and Hermosillo batholith, Sonora, Mexico: new results of apatite fission track ages (abstract), *en* Reunión Anual de la Unión Geofísica Mexicana, Puerto Vallarta, Jal.: GEOS, 32(1), p. 57.

Chew, D.M., Donelick, R.A., 2012, Combined apatite fission-track and U-Pb dating by LA-ICP-MS and its application in apatite provenance analysis, *in* Sylvester P. (ed.), Quantitative Mineralogy and Microanalysis of Sediments and Sedimentary Rocks: Mineralogical Association of Canada, Short Course 42, 219-247.

Chew, D.M., Petrus, J.A., Kamber, B.S., 2014, U–Pb LA–ICPMS dating using accessory mineral standards with variable common Pb: Chemical Geology, 363, 185-199.

Cox, R., Kosler, J., Sylvester, P., Hodych, P., 2000, Apatite fission-track (FT) dating by LAM-ICP-MS analysis, *in* Goldschmidt Conference, Oxford, UK: Journal of Conference Abstracts, 5(2), p. 322.

De Grave, J., Glorie, S., Ryabinin, A., Zhimulev, F., Buslov, M.M., Izmer, A., Elburg, M., Vanhaecke, F., Van den Haute, P., 2012, Late Palaeozoic and Meso-Cenozoic tectonic evolution of the southern Kyrgyz Tien Shan: Constraints from multi-method thermochronology in the Trans-Alai, Turkestan-Alai segment and the southeastern Ferghana Basin: Journal of Asian Earth Sciences, 44, 149-168.

Dodson, M.H., 1973, Closure temperature in cooling geochronological and petrological systems: Contributions to Mineralogy and Petrology, 40, 259-274.

Donelick, R.A., O'Sullivan, P.B., Ketcham, R.A., 2005, Apatite fission-track analysis: Reviews in Mineralogy and Geochemistry, 58, 49-94.

Ducea, M.N., Valencia, V.A., Shoemaker, S., Reiners, P.W., De Celles, P.G., Campa, M.F., Morán-Zenteno, D., 2004, Rates of sediment recycling beneath the Acapulco trench: Constraints from (U-Th)/He thermochronology: Journal of Geophysical Research, 109, B09404, doi:10.1029/2004JB003112.

Farley, K.A., 2002, (U-Th)/He dating: Techniques, calibrations, and applications, *in* Porcelli, D., Ballentine, C.J., Wieler, R. (eds.), Noble Gases in Geochemistry and Cosmochemistry: Washington, D.C., Geochemical Society and Mineralogical Society of America, Reviews in Mineralogy and Geochemistry, 47, 819-844.

Fleischer, R.L., Price, P.B., Walker, R.M., Leakey, L.S.B., 1965, Fission-track dating of Bed I, Olduvai Gorge: Science, 148, 72-74.

Flerov, G.N., Petrzhak, K.A., 1940, Spontaneous fission of uranium (en ruso): Journal Fisika, 3, 275-380.

Gallagher, K., 1995, Evolution temperature histories from apatite fission-track data: Earth and Planetary Science Letters, 136, 421-435.

Galliker, D., Hugentobler, E., Hahn, B., 1970, Spontane Kernspaltung von ^{238}U und ^{241}Am: Helvetica Physica Acta, 43, 593-606.

Gleadow, A.J.W., Duddy, I.R., Green, P.F., Lovering, J.F., 1986, Confined fission-track lengths in apatite: a diagnostic tool for thermal history analysis: Contributions to Mineralogy and Petrology, 94, 405-415.

Goldoff, B., Webster, J.D., Harlov, D.E., 2012, Characterization of fluor-chlorapatites by electron probe microanalysis with a focus on time-

dependent intensity variation of halogens: American Mineralogist, 97, 1103-1115.

Green, P.F., 1978, Registration and annealing of fission fragment and heavy ion tracks in crystals: applications to Earth and Space Sciences: Birmingham, University of Birmingham, Department of Physics, tesis doctoral 187 pp.

Green, P.F., 1985, Comparison of zeta calibration baselines for fission-track dating of apatite, zircon and sphene: Chemical Geology: Isotope Geoscience section, 58(1), 1-22.

Green P.F., Duddy I.R., 2006, Interpretation of apatite (U-Th)/He ages and fission-track ages from cratons: Earth and Planetary Science Letters, 244, 541-547.

Green, P.F., Duddy, I.R., Gleadow, A.J.W., Tingate, P.R., Laslett, G.M., 1986, Thermal annealing of fission tracks in apatite; 1, A qualitative description: Chemical Geology: Isotope Geoscience Section, 59, 237-253.

Guedes, S., Hadler, J.C., Sarkis, J.E.S., Oliveira, K.M.G., Kakazu, M.H., Iunes, P.J., Saiki, M., Tello, C.A., Paulo, S.R., 2003, Spontaneous-fission decay constant of ^{238}U measured by nuclear track techniques without neutron irradiation: Journal of Radioanalytical and Nuclear Chemistry, 258, 117-122.

Günther, D., Frischknecht, R., Heinrich, C.A., Kahlert, H.J., 1997, Capabilities of an argon fluoride 193 nm excimer laser for laser ablation inductively coupled plasma mass spectometry microanalysis of geological materials: Journal of Analytical Atomic Spectrometry, 12, 939-944.

Hadler, J.C., Iunes, P.J., Tello, C.A., Chemale Jr., F., Kawashita, K., Curvo, E.A.C., Santos, F.G.S., Gasparini, T.E., Moreira, P.A.F.P., Guedes, S., 2009, Experimental study of a methodology for fission-track dating without neutron irradiation: Radiation Measurements, 44, 955-957.

Hasebe, N., Barbarand, J., Jarvis, K., Carter, A., Hurford, A., 2004, Apatite fission-track chronometry using laser ablation ICP-MS: Chemical Geology, 207(3), 135-145.

Hasebe, N., Arai, S., Carter, A., Hurford, A.J., 2009, The effect of chemical etching on LA-ICP-MS analysis in determining uranium concentration for fission-track chronometry, *in* Lisker, F., Ventura, B., Glasmacher, U.A. (eds.), Thermochronological Methods: From Palaeotemperature Constraints to Landscape Evolution Models: Geological Society Special Publications, 324, 37-46.

Holden, N.E., Hoffman, D.C., 2000, Spontaneous fission half-lives for ground-state nuclides (Technical Report): International Journal of Pure and Applied Chemistry, 72(8), 1525-1562.

House, M.A., Farley, K.A., Stockli, D.F., 2000, Helium chronometry of apatite and titanite using Nd-YAG laser heating: Earth and Planetary Science Letters, 183, 365-368.

Hurford, A.J., Gleadow, A.J.W., 1977, Calibration of fission track dating parameters: Nuclear Track Detection, 1, 41-48.

Iunes, P. J., Hadler N, J. C., Bigazzi, G., Tello S, C. A., Guedes, O, S., Paulo, S. R., 2002, Durango apatite fission-track dating using length-based age corrections and neutron fluence measurements by natural thorium thin films and natural U-doped glasses calibrated through natural uranium thin films: Chemical Geology, 187(3), 201-211.

Jafarzadeh, M., Harami, R.M., Friis, H., Amini, A., Mahboudi, A., Lenaz, D., 2014, Provenance of the Oligocene–Miocene Zivah Formations, NW Iran, assessed using heavy mineral assemblage and detrital clinopyroxene and detrital apatite analyses: Journal of African Earth Sciences, 89, 56-71.

Jaffey, A.H., Flynn, K.F., Glendenin, L.E., Bentley, W.T., Essling, A.M., 1971, Precision measurement of half-lives and specific activities of ^{235}U and ^{238}U: Physical Review, 4(5), 1889-1906.

Johnstone, S., Hourigan, J., Gallagher, C., 2013, LA-ICP-MS depth profile analysis of apatite: Protocol and implications for (U-Th)/He thermochronometry: Geochimica et Cosmochimica Acta, 109, 143-161.

Jonckheere, R., Van den Haute, P., 1996, Observations on the geometry of etched fission tracks in apatite: Implications for models of track revelation: American Mineralogist, 81, 1476-1493.

Jonckheere, R., Mars, M., Van den Haute, P., Rebetez, M., Chambaudet, A., 1993, L'apatite de Durango (Mexique): Analyse d'un minéral standard pour la datation par traces de fission: Chemical Geology, 103, 141-154.

Ketcham, R.A., Donelick, R.A., Carlson, W.D., 1999, Variability of apatite fission-track annealing kinetics. III. Extrapolation to geological time scales: American Mineralogist, 84, 1235-1255.

Kowallis, B.J., Swisher, C.C., Carranza-Castañeda, O., Miller, W.D., Tingey, D.G., 1998, Fission-track and single-crystal ^{40}Ar/^{39}Ar laser-fusion ages from volcanic ash layers in fossil-bearing Pliocene sediments in Central Mexico: Revista Mexicana de Ciencias Geológicas, 15(2), 157-160.

Lesnov, F.P., 2012, Rare Earth Elements in Ultramafic and Mafic Rocks and their Minerals, Minor and accessory minerals: London, UK, Taylor and Francis Group, 314 pp.

Liu, W., Zhang, J., Sun, T., Wang, J., 2014, Application of apatite U–Pb and fission-track double dating to determine the preservation potential of magnetite–apatite deposits in the Luzong and Ningwu volcanic basins, eastern China: Journal of Geochemical Exploration, 138, 22-32.

Ludwig, K.R., 2008, Manual for Isoplot 3.7: Berkeley Geochronology Center, Special Publication No. 4., rev. August 26, 2008, 77 pp.

Märk, T.D., Pahl, M., Vartanian, R., 1980, Fission track annealing and fission track age – temperature relationship in sphene: Nuclear Technology, 52, 295-305.

McDonough W.F., Sun S.S., 1995, The composition of the Earth: Chemical Geology, 120, 223-253.

McDowell, F.W., McIntosh, W.C., Farley, K.A., 2005, A precise ^{40}Ar/^{39}Ar reference age for the Durango apatite (U-Th)/He and fission-track dating standard: Chemical Geology, 214, 249-263.

Morton, A., Yaxley, G., 2007, Detrital apatite geochemistry and its application in provenance studies, *in* Arribas, J., Johnsson, M.J., Critelli, S. (eds.), Sedimentary Provenance and Petrogenesis: Perspectives from Petrography and Geochemistry: Geological Society of America, Special Paper 420, 319-344.

Naeser, C.W., Fleischer, R.L., 1975, Age of the apatite at Cerro de Mercado, Mexico: A problem for fission-track annealing corrections: Geophysical Research Letters, 2(2), 67-70.

Pi, T., Solé, J., Taran, Y., 2005, (U-Th)/He dating of fluorite: application to the La Azul fluorspar deposit in the Taxco mining district, Mexico: Mineralium Deposita, 39, 976-982.

Poitrasson, F., Mao, X., Mao, S.S., Freydier, R., Russo, R.E., 2003, Comparison of ultraviolet femtosecond and nanosecond laser ablation inductively coupled plasma mass spectrometry analysis in glass, monazite, and zircon: Analytical Chemistry, 75, 6184-6190.

Price, P.B., Walker, R.M., 1962, Observation of fossil particle tracks in natural micas: Nature, 196, 732-734.

Price, P.B., Walker, R.M., 1963, Fossil tracks of charged particles in mica and the age of minerals: Journal of Geophysical Research, 68(16), 4847-4862.

Qiu, N., Chang, J., Zuo, Y., Wang, J., Li, H., 2012, Thermal evolution and maturation of lower Paleozoic source rocks in the Tarim Basin, Northwest China: American Association of Petroleum Geologists Bulletin, 96(5), 789-821.

Ratschbacher, L., Franz, L., Min, M., Bachmann, R., Martens, U., Stanek, K., Stübner, K., Nelson, B.K., Herrmann, U., Weber, B., López-Martínez, M., Jonckheere, R., Sperner, B., Tichomirowa, M., McWilliams, M.O., Gordon, M., Meschede, M., Bock, P., 2009, The North American–Caribbean plate boundary in Mexico–Guatemala–Honduras, *in* James, K., Lorente, M., Pindell, J. (eds.), The Origin and Evolution of the Caribbean Plate: Geological Society of London Special Publications, 328, 219-239.

Shen, C., Mei, L., Xu, S., 2009, Fission track dating of Mesozoic sandstones and its tectonic significance in the Eastern Sichuan Basin, China: Radiation Measurements, 44(9-10), 945-949.

Solari, L.A., Gómez-Tuena, A., Bernal, J.P., Pérez-Arvizu, O., Tanner, M., 2010, U-Pb zircon geochronology with an integrated LA-ICP-MS microanalytical workstation: Achievements in precision and accuracy: Geostandards and Geoanalytical Research, 34, 5-18.

Solé, J., Pi, T., 2005, An empirical calibration for ^{4}He quantification in minerals and rocks by laser fusion and noble gas mass spectrometry using Cerro de Mercado (Durango, Mexico) fluorapatite as a standard: Analytica Chimica Acta, 535, 325-330.

Solov'ev, A.V., Rogov, M.A., 2010, First fission-track dating of zircons from Mesozoic complexes of the Crimea: Stratigraphy and Geological Correlation, 18(3), 298-306.

Spadavecchia, A., Hahn, B., 1967, Die Rotationskammer und einige Anwendungen: Helvetica Physica Acta, 40, 1063-1079.

Steiger, R.H., Jäger, E., 1977, Subcommission on Geochronology: Convention on the use of decay constants in geo- and cosmochronology: Earth and Planetary Science Letters, 36(3), 359-362.

Svojtka, M., Košler, M., 2002, Fission-track dating of zircon by LA-ICP-MS,

in 12th Annual V. M. Goldschmidt Conference, Davos, Switzerland: Journal of Conference Abstracts, Special Supplement of Geochimica et Cosmochimica Acta, 66, A756.

Wagner, G., Van den Haute, P., 1992, Fission Track Dating: Dordrecht, Holland, Kluwer, Earth Sciences Library, 285 pp.

Witt, C., Brichau, S., Carter, A., 2012, New constraints on the origin of the Sierra Madre de Chiapas (south Mexico) from sediment provenance and apatite thermochronometry: Tectonics, 31(6), doi:10.1029/2012TC003141.

Yan, Y., Lin, G., Wang, Y., Guo, F., Li, Z., Li, X., Zhao, C., 2003, Apatite fission track age of Mesozoic sandstones from Beipiao basin, eastern China: implications for basin provenance and tectonic evolution: Geochemical Journal, 37, 377-389.

Yoshioka, T., Tsuruta, T., Iwano, H., Danhara, T., 2005, Spontaneous fission decay constant of ^{238}U determined by SSNTD method using CR-39 and DAP plates: Nuclear Instruments and Methods in Physics Research A, 555, 386-395.

Young, E.J., Myers, A.T., Munson, E.L., Conklin, N.M., 1969, Mineralogy and geochemistry of fluorapatite from Cerro de Mercado, Durango, Mexico: United States Geological Survey, Professional Paper 650, D84-D93.

Zhang, Z., Zhu, W., Shu, L., Wan, J., Yang, W., Su, J., Zheng, B., 2009, Apatite fission track thermochronology of the Precambrian Aksu blueschist, NW China: Implications for thermo-tectonic evolution of the north Tarim basement: Gondwana Research, 16, 182-188.

Manuscrito recibido: Enero 23, 2014
Manuscrito corregido recibido: Mayo 6, 2014
Manuscrito aceptado: Mayo 12, 2014

5. EVENTOS TERMO-TECTÓNICOS Y MAGMÁTICOS

Los apatitos de las areniscas de la Formación Todos Santos se dataron con el método de trazas de fisión mediante LA-ICP-MS. Los resultados obtenidos permiten detectar los rangos de algunos eventos geológicos que ocurrieron en la Sierra de Chiapas: (1) un periodo de levantamiento (con tasas de enfriamiento menores de 3°C/Ma) durante el Cretácico superior–Eoceno inferior (~83–51 Ma), lo cual puede ser relacionado con la Orogenia Laramide; (2) un periodo de quiescencia tectónica relativa para el periodo comprendido entre el Eoceno inferior y el Mioceno inferior; y (3) un evento termo-tectónico en el Mioceno medio–superior (el evento Chiapaneco).

Los detalles de este estudio se presentan en el siguiente artículo:

Abdullin, F., Solé, J., Meneses-Rocha, J.D.J., Solari, L., Shchepetilnikova, V., and Ortega-Obregón, C., (2016a).

LA-ICP-MS-based apatite fission-track dating of the Todos Santos Formation sandstones from the Sierra de Chiapas (SE Mexico) and its tectonic significance: *International Geology Review*, v. 58 (1), p. 32–48.

INTERNATIONAL GEOLOGY REVIEW, 2016
VOL. 58, NO. 1, 32–48
http://dx.doi.org/10.1080/00206814.2015.1055596

Taylor & Francis
Taylor & Francis Group

LA-ICP-MS-based apatite fission track dating of the Todos Santos Formation sandstones from the Sierra de Chiapas (SE Mexico) and its tectonic significance

Fanis Abdullin[a], Jesús Solé[b], Javier de Jesús Meneses-Rocha[c], Luigi Solari[d], Valentina Shchepetilnikova[a] and Carlos Ortega-Obregón[d]

[a]Posgrado en Ciencias de la Tierra, Instituto de Geología, Universidad Nacional Autónoma de México, México D.F, México; [b]Departamento de Geoquímica, Instituto de Geología, Universidad Nacional Autónoma de México, México D.F, México; [c]Consulting Geologist, Villahermosa, Tabasco, México; [d]Centro de Geociencias, Campus Juriquilla, Universidad Nacional Autónoma de México, Querétaro, Qro., México

ABSTRACT

This study reports the first LA-ICP-MS-based apatite fission track age data from the Toarcian–Oxfordian Todos Santos Formation sandstones exposed in the Sierra de Chiapas (SCH), SE Mexico. Single-grain fission track ages obtained from four rock samples vary between 232 ± 31 (1σ) and 40 ± 3 (1σ) Ma, indicating partial resetting of detrital apatite populations by post-depositional heating during diagenesis. Decomposed data were interpreted as follows: (a) cooling of the sediment source area at 203 ± 7 (1σ) and 163 ± 3 (1σ) Ma, which are respectively coincident with the late Permian–Triassic thermo-tectonic event and Early–Middle Jurassic arc volcanism that affected the Chiapas Massif Complex; and (b) a post-burial cooling period (with variable cooling rates of <3°C Ma^{-1}) in the range of ~83–51 Ma controlled by a Late Cretaceous–early Eocene tectonic activity, which can be correlated with the Laramide orogeny that occurred along central and northern Mexico during the same period of time (i.e. from 85–80 to 50–40 Ma). The results obtained in the present study, as well as previously published data, indicate that the SCH has experienced a multi-episodic thermo-tectonic evolution with at least four main stages.

ARTICLE HISTORY
Received 9 February 2015
Accepted 23 May 2015

KEYWORDS
laser ablation; apatite fission track dating; Todos Santos Formation; Sierra de Chiapas; Laramide orogeny; thermo-tectonic evolution

1. Introduction and objectives

Fission tracks form at known rates (Holden and Hoffman 2000) and with constant initial lengths (16.3 ± 0.9 µm) in apatite crystals by the spontaneous fission of natural uranium (e.g. Donelick *et al*. 2005). The spontaneous fission track density and ^{238}U content measured *in situ* in apatites by the laser ablation–inductively coupled plasma–mass spectrometry technique (LA-ICP-MS) allow the determination of apatite fission track (AFT) ages, thus avoiding the thermal neutron irradiation of samples (e.g. Cox *et al*. 2000; Hasebe *et al*. 2004, 2009; Donelick *et al*. 2005; Chew and Donelick 2012; Liu *et al*. 2014; Abdullin *et al*. 2014b, 2014c). The effective closure temperature for AFT dating in common apatites (i.e. fluoroapatites) normally varies from 90°C to 120°C depending on the cooling rates (e.g. Donelick *et al*. 2005; Reiners 2005), whereas in chlorine-rich apatites (≥3 wt.% Cl) this value may be increased above 150°C (Ketcham *et al*. 1999; Donelick *et al*. 2005). Barbarand *et al*. (2003) observed that AFT annealing properties and closure temperatures are also controlled by rare earth element (REE) concentrations in apatites. The temperature range between ~60°C and ~110°C (Gleadow *et al*. 1986; Green *et al*. 1989) is often referred to as the partial annealing zone (PAZ) of AFT in the case of F-apatites; but for typical Cl-apatites, PAZ corresponds to a higher temperature interval (i.e. around 90–160°C or above; Ketcham *et al*. 1999; Donelick *et al*. 2005; Abdullin *et al*. 2014c). Partial annealing will reduce the apparent AFT age and shorten the length of tracks, while total annealing (i.e. at temperatures higher than effective closure temperatures) will reset the AFT age to ~0 Ma, removing all ^{238}U spontaneous fission tracks (e.g. Gleadow *et al*. 1986; Green *et al*. 1989; Ketcham *et al*. 1999; Donelick *et al*. 2005). AFT is a very sensitive low-temperature thermochronometric method that can be used to resolve many geological problems in numerous geological settings (e.g. Green *et al*. 1989; Calmus *et al*. 1999; Yan *et al*. 2003; Donelick *et al*. 2005; Vermeesch *et al*. 2006; Lisker *et al*. 2009; Vamvaka *et al*. 2010; Zhu *et al*. 2010; Chew and Donelick 2012; Witt *et al*. 2012; Liu *et al*. 2014; Abdullin *et al*. 2014c). For example, AFT thermochronology is one of the few radioisotope techniques used to reconstruct a detailed thermo-tectonic history of sedimentary basins

CONTACT Fanis Abdullin fanisius@yandex.ru

(e.g. Lisker *et al*. 2009; Witt *et al*. 2012). This method also has applications in sedimentary provenance studies (e.g. Yan *et al*. 2003; Vermeesch *et al*. 2006; Vamvaka *et al*. 2010; Chew and Donelick 2012), as well as in the exploration of hydrocarbon fields (e.g. Donelick *et al*. 2005) and ore deposits (e.g. Liu *et al*. 2014).

In this study, four sandstones from the Jurassic Todos Santos Formation, which is exposed in the western portion of the Sierra de Chiapas (SCH) (SE Mexico; Figure 1a and c), were analysed by the LA-ICP-MS-based AFT dating method. Most previous geochronological studies have focused on the dating of granitoids and metamorphic rocks from the Chiapas Massif Complex (CMC) using high- to medium-temperature geochronometers such as U–Pb, Rb–Sr, and K–Ar (e.g. Damon *et al*. 1981; Schaaf *et al*. 2002; Weber *et al*. 2005, 2007, 2008; Estrada-Carmona *et al*. 2009, 2012; Pompa-Mera 2009). The first AFT data were reported for seven rocks of the CMC by Ratschbacher *et al*. (2009), indicating cooling of this crystalline basement during the Oligocene that can probably be related to the arrival of the Chortís block to the Gulf of Tehuantepec area (Figure 1b). Witt *et al*. (2012) analysed three granitoids from the CMC and seven sandstones from Tertiary sedimentary sequences using AFT analysis and apatite (U-Th)/He dating. These integrated AFT and apatite He data suggest that almost the entire territory of the SCH was rapidly cooled (i.e. uplifted) during the middle–late Miocene, due to the landward migration of the transpressional deformation from the Tonalá shear zone to the Tuxtla–Malpaso Fault System (Witt *et al*. 2012) (Figure 1a and c). This Miocene tectonic event is known as the Chiapanecan orogeny (e.g. Sánchez-Montes de Oca 1969, 1979, 2006; Carfantan 1981, 1985; Meneses-Rocha 1985, 1991, 2001; Guzmán-Speziale and Meneses-Rocha 2000; Padilla y Sánchez 2007; Guzmán-Speziale 2010).

Previously, on the basis of abrupt changes observed in the stratigraphy, many geologists recognized an important tectonic event that occurred in the SCH from the Late Cretaceous to Eocene (e.g. Gutiérrez-Gil 1956; Sánchez-Montes de Oca 1979, 2006; Carfantan 1981, 1985; Meneses-Rocha 1985, 1991, 2001; Burkart *et al*. 1987). Nevertheless, these authors were unable to propose an exact time range for this event by means of detailed structural analyses, since the middle–late Miocene tectonic pulse (i.e. the Chiapanecan orogeny) removed (i.e. reactivated) practically all the deformation signals of earlier tectonic events. Because the SCH represents an extremely complex geological province (e.g. Sánchez-Montes de Oca 1979, 2006; Meneses-Rocha 1985, 1991, 2001; Padilla y Sánchez 2007; Guzmán-Speziale 2010; Witt *et al*. 2012; Molina-Garza *et al*. 2015), a complete understanding of its tectonic evolution requires additional low-temperature thermochronological data. The main objective of the present AFT study is the timing of those earlier tectonic events that affected the SCH before the Miocene, studying the Todos Santos Formation, a Jurassic siliciclastic unit widespread in both southern Mexico and the northern part of Guatemala. This formation was chosen to resolve the main goal of this study because of its convenient temporal and spatial distribution (see details in Section 3.1). The secondary aim is to divide the thermo-tectonic evolution of the SCH into stages based on existing published data and the results obtained in this work.

2. Regional geology and tectonics

2.1. Tectonic setting

The SCH is part of the Maya block (Figure 1a) and tectonically represents a complex region controlled by the interaction of the North American, Caribbean, and Cocos plates (Guzmán-Speziale *et al*. 1989; Guzmán-Speziale and Meneses-Rocha 2000; Guzmán-Speziale 2010; Witt *et al*. 2012; Molina-Garza *et al*. 2015). According to many authors (e.g. Sánchez-Montes de Oca 1979, 2006; Meneses-Rocha 1985, 1991, 2001; Guzmán-Speziale 2010), the SCH can be subdivided, from SW to NE, into five principal subprovinces (Figure 1c) showing different lithostratigraphic units and distinct topographic or tectonic architectures: (1) the CMC as the crystalline basement of the SCH; (2) the Sierra Monocline (or the Central Depression) that represents a large homocline parallel to the CMC, mostly composed of Mesozoic sedimentary lithologies; (3) the Chicomuselo Anticlinorium that is represented by folded Palaeozoic metasediments and Mesozoic sedimentary rocks; (4) the Strike-Slip Faults Province (SSFP) mainly constructed by anticlines and left–lateral strike-slip faults, which trend in a general NW–SE direction; and (5) the Reverse Faults Province (RFP) formed by series of reverse faults and long, narrow anticlines, where the intervening synclines are generally absent.

Witt *et al*. (2012) demonstrated that almost the entire SCH area was affected by the middle–late Miocene Chiapanecan thermo-tectonic event. However, some of its subprovinces show temporally heterogeneous tectonic histories prior to the Chiapanecan orogeny. For example, the ~35–25 Ma cooling period, which was previously determined using AFT data (Ratschbacher *et al*. 2009; Witt *et al*. 2012), can be observed only for the CMC area. This exhumation period is closely

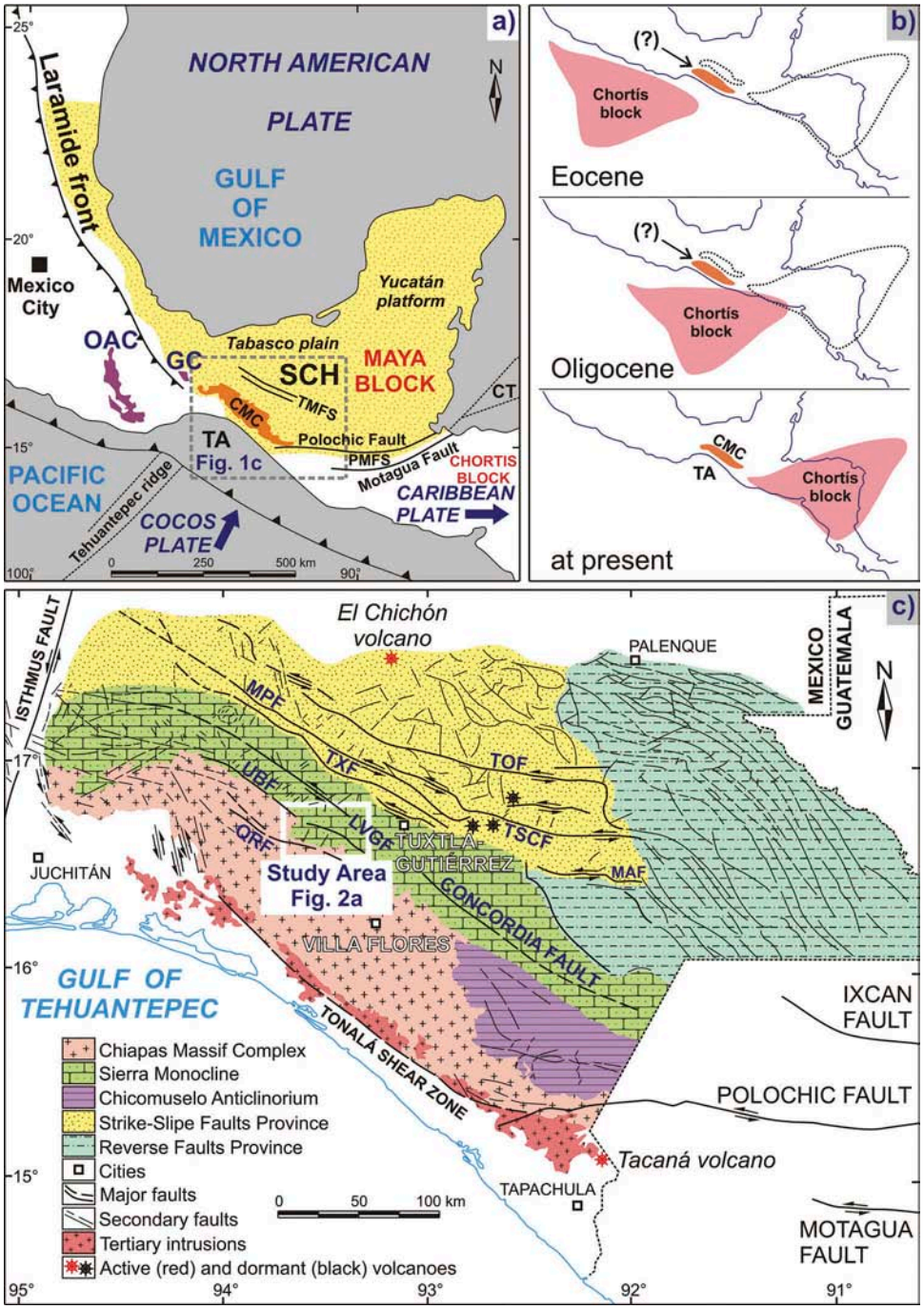

Figure 1. (a) Geodynamic setting of southern Mexico modified from Guzmán-Speziale (2010) and Witt *et al*. (2012). The yellow area on the map approximately corresponds to the continental part of the Maya block (Weber *et al*. 2005; Estrada-Carmona *et al*. 2009, 2012). The Laramide front for the central and northern portions of Mexico was redrawn from English *et al*. (2003) and Gray and Lawton (2011). OAC, Grenville-age Oaxacan Complex; GC, Grenville-age Guichicovi Complex; TA, Tehuantepec area; CMC, Chiapas Massif Complex; SCH, Sierra de Chiapas; TMFS, Tuxtla–Malpaso Fault System; PMFS, Polochic–Motagua Fault System; CT, Cayman trough. The inset shows the SCH and the Gulf of Tehuantepec area. (b) Simplified map showing the migration of the Chortís block from the Oligocene to the present according to the prevalent model (e.g. Ratschbacher *et al*. 2009; Ferrari *et al*. 2014). The CMC, as well as the major part of the SCH area, was probably located closer to the current Tehuantepec area during the Oligocene, as was previously suggested by Witt *et al*. (2012). (c) Tectonic map of the SCH (modified after Meneses-Rocha 1985) showing the five main subprovinces with major and secondary faults. MPF, Malpaso fault; TOF, Tecpatán–Ocosingo fault; TXF, Tuxtla fault; TSCF, Telestaquin–San Cristóbal fault; MAF, Malpaso–Aztlán fault; UBF, Uzpanapa–El Brillante fault; LVGF, La Venta–Grijalva fault; QRF, Quintana Roo fault. The inset corresponds to the study area.

contemporaneous with the hypothetical arrival of the Chortís block to the Gulf of Tehuantepec area (e.g. Ratschbacher *et al*. 2009; Witt *et al*. 2012; Ferrari *et al*. 2014; Figure 1b).

Almost all the major tectonic elements of the SCH (Figure 1a and c), including the Tuxtla–Malpaso Fault System (TMFS) and Polochic–Motagua Fault System (PMFS), are seismically active (Guzmán-Speziale *et al*. 1989; Guzmán-Speziale and Meneses-Rocha 2000; Guzmán-Speziale 2010). Both the PMFS and TMFS apparently show, to the present day, overland boundaries between the North American and Caribbean plates (e.g. Guzmán-Speziale 2010; Witt *et al*. 2012; Molina-Garza *et al*. 2015; Figure 1a).

2.2. Crystalline basement

The CMC was formed from an active continental margin during the Permian–Triassic and represents the crystalline basement of the southern Maya block (e.g. Torres *et al*. 1999; Weber *et al*. 2005; Estrada-Carmona *et al*. 2009, 2012; Pompa-Mera 2009). This basement extends to the north into the Tabasco plain and probably into most parts of the Yucatán platform, and the western limit of its outcropping portion is coincident with the Tonalá shear zone (e.g. Meneses-Rocha 2001; Estrada-Carmona *et al*. 2009, 2012; Witt *et al*. 2012; Molina-Garza *et al*. 2015; Figure 1a and c). The CMC mainly consists of calc-alkaline granitoids, most of which are deformed and metamorphosed (e.g. Damon *et al*. 1981; Torres *et al*. 1999; Schaaf *et al*. 2002; Weber *et al*. 2005, 2007, 2008). The first reliable geochronological data for the CMC were reported by Damon *et al*. (1981), who built a Rb–Sr whole-rock isochron for 10 granites with an age of 256 ± 10 (2σ) Ma. Torres *et al*. (1999) compiled older K–Ar biotite ages (with closure temperatures of 300–350°C; e.g. Faure and Mensing 2005) ranging from 261 ± 10 (2σ) to 239 ± 5 (2σ) Ma. Rb–Sr ages for mica–whole-rock pairs (with closure temperatures around 350–400°C; Faure and Mensing 2005) vary from 244 ± 12 (2σ) to 214 ± 11 (2σ) Ma (Schaaf *et al*. 2002), indicating cooling during the Triassic. Weber *et al*. (2007, 2008) interpreted zircon U–Pb lower intercepts of 258 ± 2 and 251 ± 2 Ma as either igneous crystallization or metamorphic ages, and they also identified sedimentary protoliths mainly correlated with the Palaeozoic metasediments from the Jocote, Custepec, and Sepultura units. This means that the CMC was formed as a widespread granitoid intrusion into these Palaeozoic metasedimentary sequences. The CMC also includes some Ordovician granitoids, which were affected by medium- to high-grade metamorphism at 253 ± 1 Ma (Weber *et al*. 2005, 2007, 2008; Pompa-Mera 2009; Estrada-Carmona *et al*. 2012). A Grenville-aged component was also reported for the CMC basement by means of Sm–Nd model ages (Schaaf *et al*. 2002) and U–Pb zircon core ages (Weber *et al*. 2007, 2008). Godinez-Urban *et al*. (2011) recognized a significant pulse of the Early–Middle Jurassic arc volcanism (i.e. the Nazas magmatic arc) in rocks that overlie the CMC. During the late Eocene–early Oligocene and Miocene, igneous activities took place in the CMC, generating granitic intrusions along the Tonalá shear zone (García-Palomo *et al*. 2006; Witt *et al*. 2012; Collard *et al*. 2014; Molina-Garza *et al*. 2015) (Figure 1c).

2.3. Sedimentary cover

The base of the SCH sedimentary cover is represented by Lower Jurassic volcanoclastic deposits of the La Silla Formation that is exposed in the southern Sierra Monocline subprovince (Godinez-Urban *et al*. 2011). This formation can be stratigraphically correlated with the informally named unit Pueblo Viejo andesites, which crops out in the northern parts of the Sierra Monocline (e.g. Meneses-Rocha 1985, 1991; Sánchez-Montes de Oca 2006; Godinez-Urban *et al*. 2011). Continental red beds and salt of the Todos Santos Formation were deposited in the SCH during the Jurassic (e.g. Meneses-Rocha 1985, 1990; Herrera and Estavillo 1991; Godinez-Urban *et al*. 2011). According to Blair (1987), Godinez-Urban *et al*. (2011), and Abdullin *et al*. (2014a), the Todos Santos sediments were mainly derived from the CMC rocks. The base of this formation is composed of conglomerates, volcanoclastic materials, and fine-grained lacustrine sediments, while its upper part mostly contains red fluvial medium- to coarse-grained arkosic sandstones and conglomerates (e.g. Blair 1987; Herrera and Estavillo 1991; Godinez-Urban *et al*. 2011). The Todos Santos Formation unconformably overlies the Early Jurassic volcanoclastic deposits and/or CMC rocks (Figure 2a and b). Its variation in thickness from 250 to 1350 m is related to a graben-type geometry derived from the extensional processes associated with continental rifting at the beginning of the opening of the Gulf of Mexico (Meneses-Rocha 1985, 2001; Blair 1987; Sánchez-Montes de Oca 2006; Padilla y Sánchez 2007; Godinez-Urban *et al*. 2011; Witt *et al*. 2012). Because the Todos Santos Formation is continental, it is difficult to determine its exact stratigraphic age. Nevertheless, many previous studies (e.g. Quezada-Muñetón 1983; Meneses-Rocha 1985, 1990; Herrera and Estavillo 1991; Mandujano Velásquez 1996; Sánchez *et al*. 2004; Godinez-Urban *et al*. 2011) suggest that the Todos Santos Formation was most likely

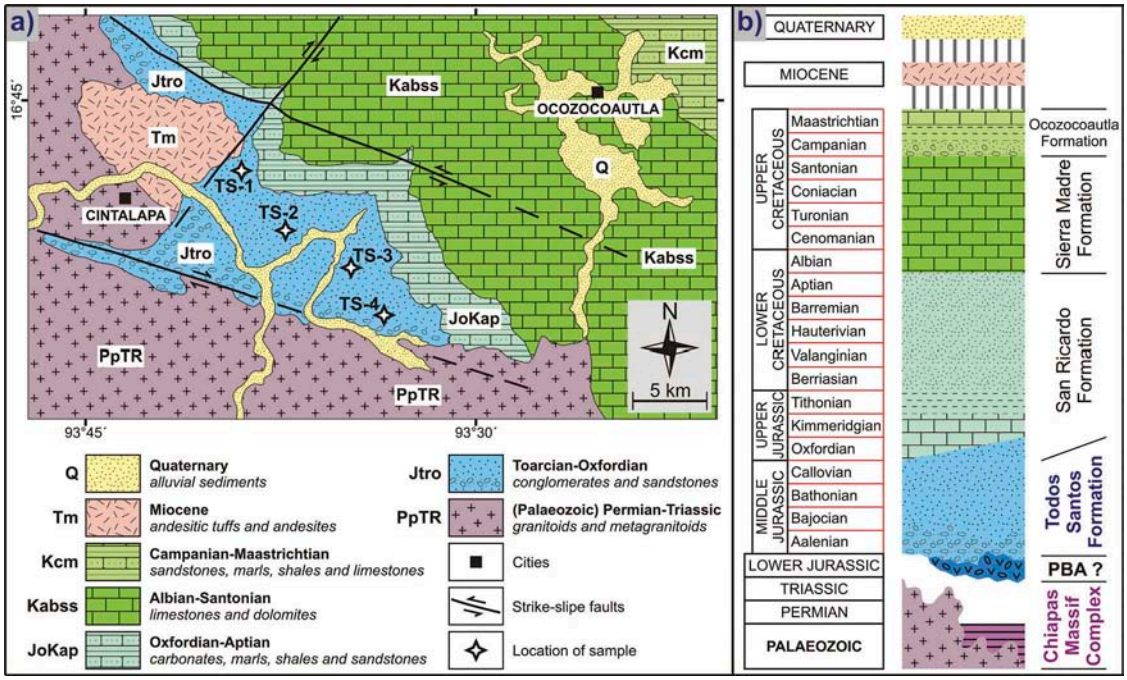

Figure 2. (a) Simplified geological map (modified from Sánchez-Montes de Oca 2006) showing the location of collected rock samples and (b) lithostratigraphic column of the study area. PBA corresponds to the Pueblo Viejo andesites unit (e.g. Sánchez-Montes de Oca 2006; Godinez-Urban *et al*. 2011).

deposited during the Toarcian–Oxfordian period. The San Ricardo Formation (Oxfordian–Aptian), which crops out in the northern portion of the Sierra Monocline, conformably overlays the Todos Santos Formation. It contains three members which are, from bottom to top (Figure 2a and b), the Oxfordian–Kimmeridgian carbonates, Tithonian marls and shales, and the Berriasian to Aptian fine-grained sandstones (Quezada-Muñetón 1983; Mandujano Velásquez 1996; Sánchez *et al*. 2004). This formation has a variable total thickness of 510–1420 m and it was interpreted as a transgressive sequence above the Todos Santos Formation (Quezada-Muñetón 1983; Meneses-Rocha 1985, 2001). Its lithostratigraphic analogue is the Jericó Formation cropping out at the south of the Sierra Monocline subprovince (e.g. Quezada-Muñetón 1983; Mandujano Velásquez 1996). In the NW sector of the SCH, the Kimmeridgian–Aptian sediments are mainly thin-bedded biomicrites intercalated with biocalcarenites and shales of the Chinameca Formation, which was deposited in an offshore basinal environment (Burckhardt 1930; Meneses-Rocha 1985, 1991). The Albian–Santonian times (Figure 2a and b) are represented by the Sierra Madre Formation (1000–2400 m thick) composed of limestones and dolomites deposited on a marine platform during the post-rift stage (i.e. a period of tectonic stability) in the Gulf of Mexico tectonic evolution (e.g. Rosales-Domínguez *et al*. 1997; Rosales-Domínguez 1998; Meneses-Rocha 2001; Sánchez *et al*. 2004; Padilla y Sánchez 2007; Witt *et al*. 2012). The Campanian–Maastrichtian sequences (the Ocozocoautla, Xochitlán, Méndez, and Angostura Formations) are characterized by a mixture of high- to low-energy siliciclastic sediments and carbonates (Sánchez-Montes de Oca 1969, 2006; Quezada-Muñetón 1987; Mandujano Velásquez 1996). For example, the 300–820 m-thick Ocozocoautla Formation (Figure 2a and b) consists, from base to top, of gravel, coarse-grained and marly sandstones, alternate thin layers of marls and shales, and limestones (Gutiérrez-Gil 1956; Rosales-Domínguez 1998; Omaña 2006). In the northern and central parts of the SCH, the lateral equivalent of the Angostura Formation (470–1100 m thick) is the Turonian–Maastrichtian Jolpabuchil Formation, which is composed of ~200 m of thin- to medium-bedded wackestones with bands and nodules of black chert (Sánchez-Montes de Oca 1969, 2006; Meneses-Rocha 1985, 1991; Mandujano Velásquez 1996; Sánchez *et al*. 2004).

The Cenozoic stratigraphy of the SCH is predominantly siliciclastic in composition (e.g. Meneses-Rocha 1985, 1991, 2001; Quezada-Muñetón 1987; Mandujano Velásquez 1996; Sánchez-Montes de Oca 2006; Padilla y Sánchez 2007; Witt *et al*. 2012). The Palaeocene marks the final transition to regional terrigenous sedimentation with deposition of shallow water platform sediments, slope turbidites (Palaeocene–Eocene Lutitas

Nanchital Formation, 300–1100 m thick), and deep basin deposits (Palaeocene Soyaló Formation, about 900 m thick) that mainly crop out in the SSFP (Meneses-Rocha 1985; Quezada-Muñetón 1987; Mandujano Velásquez 1996; Witt *et al*. 2012). Eocene–Oligocene units contain continental clastic (early Eocene El Bosque Formation, 200–2000 m thick) and minor shallow water deposits locally associated with carbonate platforms (Eocene Lomut and Oligocene Mompuyil Formations, 500–900 and 500–1400 m thick, respectively), all of which are exposed in both the SSFP and RFP (e.g. Quezada-Muñetón 1987; Mandujano Velásquez 1996; Perrilliat *et al*. 2006). Sediment provenance studies of Witt *et al*. (2012), using detrital zircon U–Pb geochronology, show that Palaeocene–Eocene siliciclastic materials were derived from the CMC rocks and Grenville-age basement sources (i.e. very likely from the Oaxacan and/or Guichicovi granulitic complexes; Figure 1a). Oligocene and Miocene sedimentary sequences (e.g. the Simojovel, La Laja, Depósito, Encanto, and Ixtapa Formations) record a marked increase in continental sedimentation, which has been linked to uplift and erosion of the CMC (Quezada-Muñetón 1987; Meneses-Rocha 2001). The uppermost part of the SCH stratigraphic column mostly includes Quaternary alluvial sediments and volcanoclastic deposits derived from the Pleistocene to present volcanic activity (e.g. Meneses-Rocha 1985; Collard *et al*. 2014). The total sedimentary cover in the SCH is about 3500–10,000 m thick (Peterson 1983); however, the western portion of the SSFP (i.e. the Ixtapa Graben) has a total sediment thickness greater than 15,000 m (Meneses-Rocha 1991, 2001).

3. Samples and analytical methods

3.1. Sampling

Our study is focused on a small area located in the western part of the SCH (northern Sierra Monocline; Figure 1c), between the cities of Ocozocoautla and Cintalapa (Figure 2a). The study area has exposures of CMC granitoids, Mesozoic sedimentary rocks, and Miocene volcaniclastic deposits, as well as of Quaternary lacustrine and fluvial sediments. The Todos Santos Formation was chosen to resolve the central goal of this AFT study proposing that, due to its convenient depositional age (i.e. the Toarcian–Oxfordian), sandstones should contain some thermochronological information about the Late Cretaceous–Eocene tectonic event that affected the SCH, which was previously suggested by several authors (e.g. Gutiérrez-Gil 1956; Sánchez-Montes de Oca 1979; Carfantan 1981; Burkart *et al*. 1987; Meneses-Rocha 2001). Four samples of coarse-grained arkose (TS-1, TS-2, TS-3, and TS-4) were collected from the Todos Santos Formation (Figure 2a; Table 1).

3.2. Sample preparation and fission track counting

Heavy minerals were concentrated from the three narrow grain-size fractions of 60–125, 125–180, and 180–250 μm using conventional techniques/instruments such as crushing, sieving, the Wilfley™ table, Frantz™ isodynamic magnetic separator, and heavy liquids. Approximately 400 apatite grains, extracted from each rock sample under a binocular microscope, were mounted with epoxy resin in a 2.5 cm-diameter plastic ring, and then were sequentially polished with sandpaper P2500 (8.3 μm) and alumina suspensions (5, 3, 1, 0.25, and 0.05 μm). Polished apatites were etched in 5.5M HNO_3 at 21°C for 20 s (Donelick *et al*. 2005) to reveal ^{238}U spontaneous fission tracks. Apatite grains were randomly selected for AFT dating. Spontaneous fission track counting was performed using an Olympus™ BX51 microscope with 60× and 100× dry objectives at total magnifications of 900× and 1500×, respectively. Only those few grains (i.e. ~10% from each selected group per rock sample) showing many visible U-enriched mineral inclusions (magnetite, zircon, monazite, etc.) and with a strong track density zoning (i.e. with a strong zonation of U) were excluded from AFT dating, because these can give abnormally young or old AFT ages using the LA-ICP-MS technique (e.g. Liu *et al*. 2014; Abdullin *et al*. 2014c). Sample preparation, chemical etching,

Table 1. Results of LA-ICP-MS-based AFT dating for detrital apatites from the Todos Santos Formations sandstones.

			p_S ($\times 10^5$ cm^{-2})			^{238}U (ppm)			AFT age ± 1σ (Ma)			
Rock sample	N_{gr}	N_s tot	Min	Mean	Max	Min	Mean	Max	Min	Central	Max	$P(\chi^2)$
TS-1 16°42′30″ N, 93°38′47″ W, 564 m.a.s.l.	54	2260	0.255	9.265	38.46	1.2	24.4	133.6	40.3 ± 3.0	73 ± 4	221.5 ± 27.5	0%
TS-2 16°41′04″ N, 93°37′06″ W, 550 m.a.s.l.	93	3616	0.855	11.04	58.91	1.7	23.9	139.8	47.4 ± 4.0	85 ± 4	232.0 ± 30.6	<1%
TS-3 16°39′03″ N, 93°34′20″ W, 538 m.a.s.l.	62	2003	1.314	7.579	41.30	2.0	13.0	75.7	48.5 ± 5.9	106 ± 6	230.3 ± 26.6	0%
TS-4 16°37′13″ N, 93°32′13″ W, 590 m.a.s.l.	53	1243	0.952	4.459	13.87	1.0	9.6	24.8	41.1 ± 3.8	90 ± 5	192.1 ± 15.1	<1%

Note: N_{gr} is the number of dated apatite crystals; N_s tot is the sum of the ^{238}U spontaneous fission tracks registered for all apatites; p_S is the spontaneous track density; ^{238}U represents the uranium-238 concentration in ppm measured by LA-ICP-MS; AFT age corresponds to apatite fission track age in Ma with its absolute ±1σ error; $P(\chi^2)$ is the chi-squared probability.

and fission track counting were performed at the Instituto de Geología (UNAM, Mexico City).

3.3. LA-ICP-MS measurements

Uranium-238 measurements on apatites were carried out at the Laboratorio de Estudios Isotópicos, Centro de Geociencias (UNAM, Campus Juriquilla) using a Resonetics™ M050 193 nm ArF excimer laser ablation system coupled to a Thermo™ iCAP-Qc quadrupole ICP-MS. In this study, the double standard method chosen for LA-ICP-MS is based on the following scheme: two spots in a NIST-612 glass, one spot in standard Durango fluorapatite (DFA; Cerro de Mercado, Durango, Mexico), and 10 spots in unknown apatites. Laser ablation was performed in a He atmosphere (700 ml min^{-1}) using a laser pulse energy of 6 J cm^{-2}, spot diameter of 50 µm, and 5 Hz laser repetition rate. The ablated material was carried to the plasma in a mixed gas stream of He and Ar. For each analysis, the gas blank was acquired over 20 s, laser triggered, and the signal acquired for a further 30 s. The ^{238}U content of each studied grain, including the DFA fragments, was carefully measured within the areas (Figure 3a and b) used previously to determine spontaneous track densities (p_S). Single-spot sampling was performed on the DFA and unknown apatites with track-counted areas smaller than ~5000 $µm^2$. In some apatite grains in which the p_S values were obtained from larger zones (~5000–10,000 $µm^2$), the ^{238}U concentration was measured by two to four spots covering the entire track-counted area. The results for ^{238}U obtained using the NIST-612 glass were normalized using ^{43}Ca as an internal standard and taking an average CaO concentration for all analysed apatites of 55% (e.g. Hasebe *et al*. 2004, 2009; Jafarzadeh *et al*. 2014; Abdullin *et al*. 2014c).

3.4. Fission track age calculation

AFT grain ages (t) were calculated following Hasebe *et al*. (2004, 2009):

$$t = \frac{1}{\lambda_D}\ln\left(1 + \frac{p_s\lambda_D M}{\lambda_f N_A U 10^{-6} d R_{SP}}\right), \quad (1)$$

where λ_D is the total decay constant for ^{238}U (1.55125×10^{-10} a^{-1}; Jaffey *et al*. 1971); p_S is the spontaneous track density (i.e. $\times 10^5$ tracks cm^{-2}); M is the atomic mass of ^{238}U (238.0508 u); λ_f is the ^{238}U spontaneous fission decay constant, for which we selected the value of $(8.45 \pm 0.1) \times 10^{-17}$ $year^{-1}$ as recommended by the International Union of Pure and Applied Chemistry (Holden and Hoffman 2000); N_A is Avogadro's number (6.022×10^{23} mol^{-1}); U is the ^{238}U content (in µg· g^{-1}) measured by LA-ICP-MS; d is the apatite density (3.19 ± 0.04 g· cm^{-3}); R_{SP} represents half of the mean etchable spontaneous fission track length in apatites from geologically rapidly cooled rocks (i.e. undisturbed volcanic-type cooling) without subsequent thermal disturbance (~15 ± 0.5 µm; Gleadow *et al*. 1986; Chew and Donelick 2012), and is equal to $(7.5 \pm 0.25) \times 10^{-4}$ cm (Hasebe *et al*. 2004, 2009; Abdullin *et al*. 2014c).

The absolute ± 1σ errors of AFT grain ages are obtained taking into account all possible analytical uncertainties (Abdullin *et al*. 2014c):

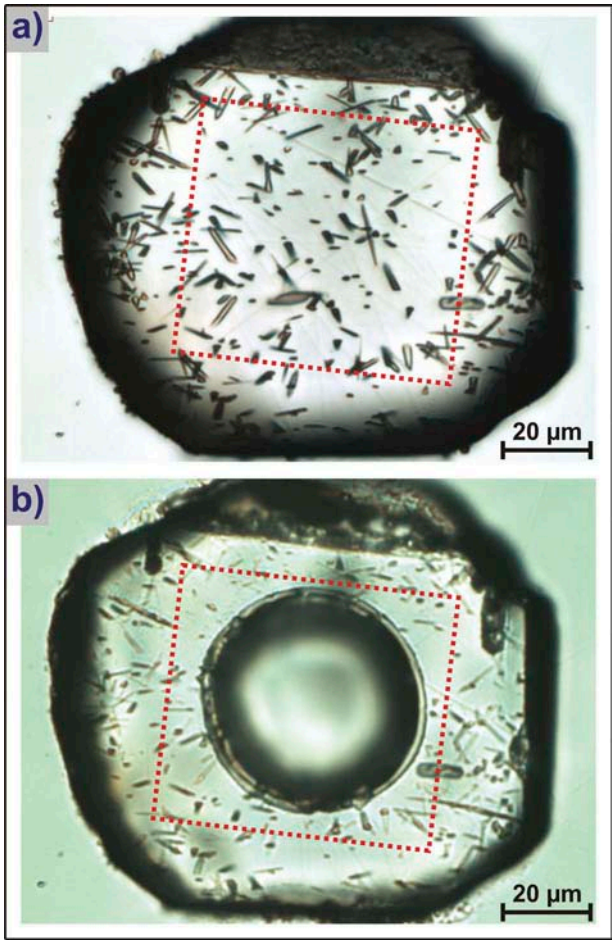

Figure 3. An example of apatite crystal from the Todos Santos Formation sandstone sample dated by the LA-ICP-MS-based AFT method. (a) Microphotograph showing the polished and etched surface of the apatite crystal. The linear damage in apatite, with random directions, represents the fission track generated by the spontaneous fission of natural ^{238}U. The area bounded by red dashed lines corresponds to the ^{238}U spontaneous fission track-counting area. (b) The same microphotograph showing the ablation crater formed by ^{238}U measurement using LA-ICP-MS technique. Note that micro-sampling was performed by laser ablation within the track-counted area. The scale bars in both microphotographs correspond to 20 µm.

$$\sigma^2(t) = W\left[\left(\frac{\sigma(\lambda_f)}{\lambda_f}\right)^2 + \left(\frac{\sigma(d)}{d}\right)^2 + \left(\frac{\sigma(R_{SP})}{R_{SP}}\right)^2 + \left(\frac{\sigma(U)}{U}\right)^2 + \left(\frac{\sigma(p_s)}{p_s}\right)^2\right], \quad (2)$$

where

$$W = \frac{10^6 Mp_s}{10^6 \lambda_D Mp_s + dN_A R_{SP} U\lambda_f}, \quad (3)$$

where $\sigma(U)$ represents the total uncertainty for ^{238}U content, including the analytical $\pm 1\sigma$ error of LA-ICP-MS measurements (~1.5–2.5%) and an error (~3.6%) generated by the common CaO variation (55 ± 2%) in F- and Cl-apatites of different origin (Belousova *et al*. 2002; Barbarand *et al*. 2003; Lesnov 2012). The value of $\sigma(p_S)$ is subjective for AFT dating, because it depends on the sample preparation (including polishing) and etching qualities, number of counted tracks, and the operator experience. Based on our own experiences, we obtained $\sigma(p_S)$ for each analysed apatite during track counting, and for the present AFT study this is normally less than 10–12% of the p_S value.

4. Results and interpretation

For the DFA, used as a reference material, a mean age of 31.8 ± 0.3 (1σ) Ma was obtained from 34 spot analyses based on the Excel™ macro Isoplot of Ludwig (2008), which is in line with its accepted standard age of 31.4 ± 0.5 (1σ) Ma (e.g. Green 1985; Solé and Pi 2005; Abdullin *et al*. 2014c). Detailed information on our AFT and LA-ICP-MS experiments (number of spontaneous fission tracks counted to determine p_S, ^{238}U concentrations, analytical errors, ages of the DFA and unknown apatites, etc.) is given in Supplementary Table A (see http://dx.doi.org/10.1080/00206814.2015.1055596).

Individual grain AFT ages obtained for the Todos Santos Formation sandstones vary over a wide range, from 232 ± 31 (1σ) to 40 ± 3 (1σ) Ma (Table 1), indicating partial resetting of detrital apatite populations by burial-related heating during diagenesis. For each studied rock sample, the chi-squared (χ^2) test was used to detect the probability that all analysed apatites belong to a single population of ages (Galbraith 1981). A probability of <5% is evidence of an asymmetric spread of single-grain ages. In this case, the rock sample AFT age is commonly represented as the 'central age', which is essentially a weighted-mean age (Galbraith 1981; Galbraith and Green 1990; Galbraith and Laslett 1993; Vermeesch 2009).

The central AFT ages of sandstones were calculated using the RadialPlotter™ software of Vermeesch (2009) and displayed as radial plots (Figure 4). All four rock samples (TS-1, TS-2, TS-3, and TS-4) show very high single-grain age dispersion (40–45%) and undoubtedly failed the chi-squared probability test, yielding $P(\chi^2)$ values less than 1% (Table 1). The central values of AFT ages from the Todos Santos Formation samples range between 106 ± 6 (1σ) and 73 ± 4 (1σ) Ma (Table 1; Figure 4). It is well known that the annealing characteristics of fission tracks in apatites are strongly controlled by its chemical composition, particularly by the chlorine concentration, and Cl-apatites are more resistant to thermal annealing than F-apatites (Ketcham *et al*. 1999; Barbarand *et al*. 2003; Donelick *et al*. 2005). Partial annealing (or partial resetting) of detrital apatites during diagenesis is very common, since these can be derived from diverse types of igneous and metamorphic source lithologies, which petrogenetically control their chemical composition, including chlorine content (Belousova *et al*. 2002; Barbarand *et al*. 2003; Lesnov 2012; Jafarzadeh *et al*. 2014; Abdullin *et al*. 2014a). For partially reset samples, the central age obviously has no real geological sense, because it indicates only an average AFT age. The interpretation of mixed ages is generally complex, and it is necessary to decompose the sample AFT grain age distribution into groups of component distributions (Galbraith and Green 1990; Galbraith and Laslett 1993; Vermeesch 2009), which can provide very useful information about the cooling of sediment source area, depositional age, and post-burial cooling history (e.g. Yan *et al*. 2003; Donelick *et al*. 2005; Vermeesch *et al*. 2006; Lisker *et al*. 2009; Vamvaka *et al*. 2010; Chew and Donelick 2012).

In this study, we grouped all single-grain ages obtained for 262 detrital apatites and decomposed them using the RadialPlotter™ software in automatic mode (Vermeesch 2009) based on the statistical method of Galbraith and Green (1990). The first two peaks that were obtained from no or slightly annealed apatites give ages of 203 ± 7 (1σ) and 163 ± 3 (1σ) Ma (Figure 5a), which mainly correspond to the cooling of sediment source rocks, inasmuch as these age peaks are greater than or equal to the depositional age of the Todos Santos Formation. Nonetheless, most of the apatites (~74%), as shown in Figure 5a and b, were completely reset owing to sufficient heating during diagenesis (i.e. especially due to the deposition of very thick carbonate sequences during the Albian–Santonian platform) and contain information about the post-burial cooling history of the Todos Santos Formation sandstones, showing three dominant peaks at 83 ± 1 (1σ), 66 ± 2 (1σ), and 51 ± 1 (1σ) Ma, all of which are significantly younger than their

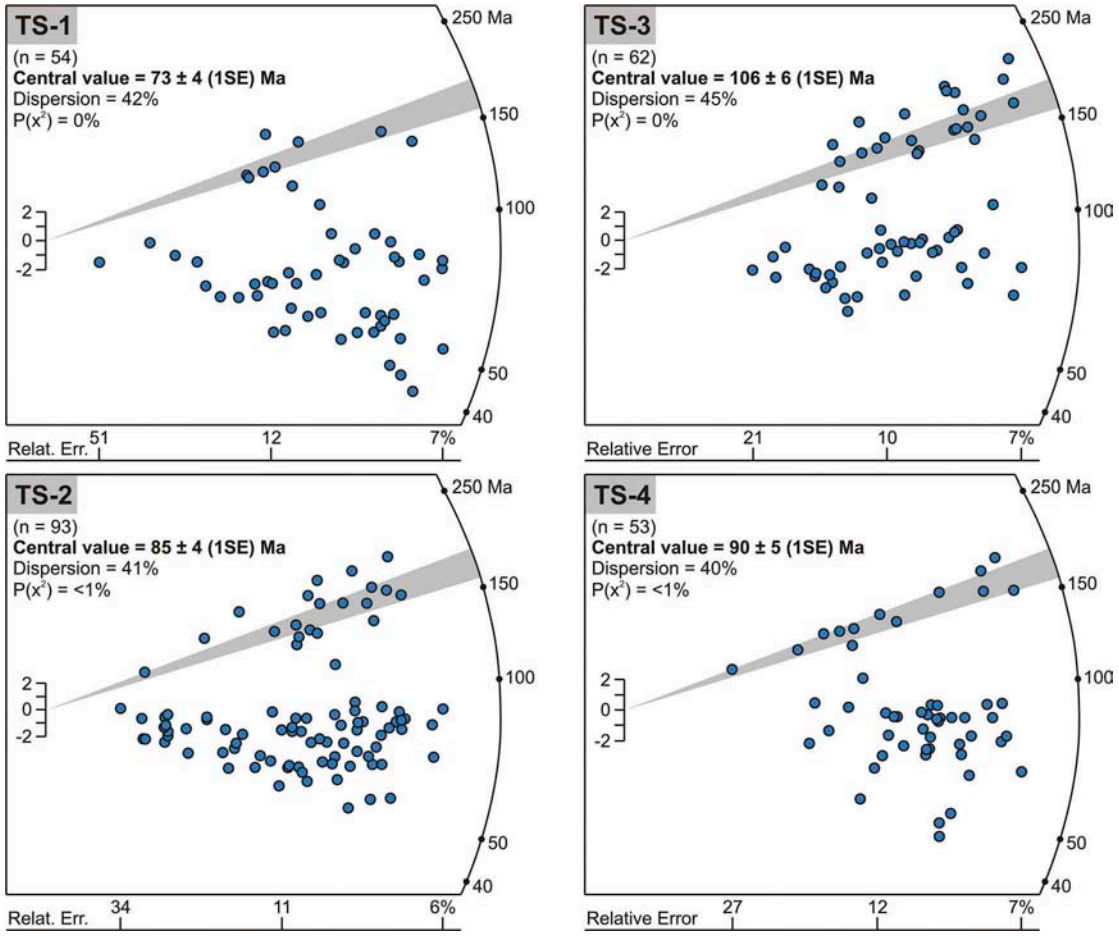

Figure 4. Radial plots of AFT ages for the Todos Santos Formation arkoses (samples TS-1, TS-2, TS-3, and TS-4) constructed using the RadialPlotter™ of Vermeesch (2009). The central ages (with 1σ errors) and single-grain age dispersions were also obtained by means of the RadialPlotter™ software. The grey field in each radial plot represents the depositional age of the Toarcian–Oxfordian Todos Santos Formation. n, number of dated apatite grains.

stratigraphic ages. In addition, on the basis of variations in thickness of the Todos Santos, San Ricardo, and Sierra Madre Formations from the study area (e.g. Quezada-Muñetón 1983; Blair 1987; Rosales-Domínguez *et al*. 1997; Rosales-Domínguez 1998; Sánchez *et al*. 2004), we calculated roughly that the Todos Santos Formation samples were buried to a minimum depth of 3 km before the Campanian. Therefore, taking into account the global average geothermal gradient of 25–30°C km^{-1}, it was established that burial-related heating of the studied sandstones was sufficient to reset the majority of detrital apatites (i.e. in particular, F-apatites; Abdullin *et al*. 2014b). Reset apatites also have mixed ages (Table 1; Figure 5a and b), due to differences in thermal annealing properties and relatively slow cooling of samples through the PAZ.

5. Discussion

The first AFT age peak of 203 ± 7 (1σ) Ma obtained from ~8% of dated detrital apatites is approximately coincident with the late Permian–Triassic cooling of the CMC (Figure 5a), which was identified as a main source terrane for the Todos Santos Formation sediments (Damon *et al*. 1981; Blair 1987; Godinez-Urban *et al*. 2011; Abdullin *et al*. 2014a). The late Permian–Triassic tectonothermal event that occurred along the CMC can be related to high- and medium-grade metamorphism with associated anatexis, and to the major intrusion of Permian plutons into Palaeozoic metasediments (Weber *et al*. 2005, 2007, 2008; Estrada-Carmona *et al*. 2009, 2012; Pompa-Mera 2009). The peak of this event took place at ~260–250 Ma (e.g. Weber *et al*. 2007, 2008), and the subsequent cooling of the CMC occurred

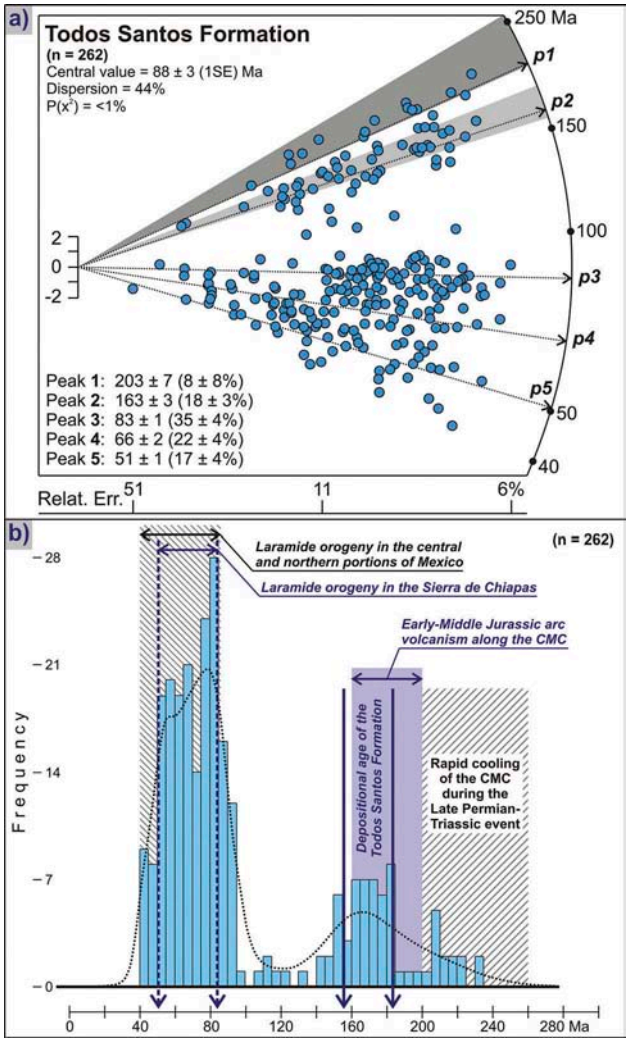

Figure 5. (a) Results of decomposition of the AFT single-grain ages obtained for 262 detrital apatites from four Todos Santos Formation sandstones. The decomposition was performed using the RadialPlotter™ software in automatic mode (Vermeesch 2009) based on the statistical method of Galbraith and Green (1990). The light grey field in the radial plot represents the depositional age of the Todos Santos Formation. The dark grey field corresponds to rapid cooling of the CMC during the late Permian–Triassic thermo-tectonic event (e.g. Damon *et al*. 1981; Torres *et al*. 1999; Schaaf *et al*. 2002; Weber *et al*. 2005; Estrada-Carmona *et al*. 2009, 2012; Pompa-Mera 2009). (b) AFT age spectra for 262 detrital apatites. The depositional age of the Todos Santos Formation, as well as the periods of certain tectonic and magmatic events, which occurred in the SCH, are also represented in the age spectra. Early–Middle Jurassic arc volcanism occurred along the CMC according to Godinez-Urban *et al*. (2011). The Laramide orogeny affected the central and northern parts of Mexico during the Late Cretaceous–Eocene (i.e. from 85–80 to 50–40 Ma; e.g. Damon *et al*. 1981; Calmus *et al*. 1999; English *et al*. 2003; Ramos-Velázquez *et al*. 2008; Gray and Lawton 2011). The time span of ~83–51 Ma, which is denoted by thick dashed lines, corresponds to the Laramide orogeny that affected the SCH (according to the results obtained in the present study).

up to the late Triassic (Damon *et al*. 1981; Torres *et al*. 1999; Schaaf *et al*. 2002; Weber *et al*. 2005). The second peak of 163 ± 3 (1σ) Ma (~18% of apatites) is within the stratigraphic age of the Todos Santos Formation (Figure 5a), and several non- or slightly annealed apatites (i.e. ~14% of grains) are located in the time range of ~200–160 Ma (Figure 5b). This population of detrital apatite crystals was apparently derived from igneous lithologies that were formed along the CMC during the Early–Middle Jurassic arc volcanism (Godinez-Urban *et al*. 2011). Abdullin *et al*. (2014a), based on single-grain apatite geochemistry (REE and trace elements) and using petrogenetic diagrams of Belousova *et al*. (2002), also demonstrated that several apatite grains (~5–10%) from the Todos Santos Formation sandstones have geochemical signatures typical of those belonging to volcanic and subvolcanic rocks. A Jurassic magmatic event was previously proposed for the CMC by Damon *et al*. (1981) and Schaaf *et al*. (2002). Hence, both the AFT age peaks of 203 ± 7 (1σ) and 163 ± 3 (1σ) Ma obtained for the studied sandstones evidently indicate the cooling of the sediment source lithologies (i.e. from the CMC).

According to Quezada-Muñetón (1987) and Witt *et al*. (2012), the inward portions of the SCH (i.e. the SSFP and RFP; Figure 1c) did not experience any significant uplift during the middle Eocene–Oligocene period. AFT dating results obtained from the Todos Santos Formation sandstones in the present study suggest that this period of tectonic quiescence also has sense for the Sierra Monocline subprovince, because only ~9% of fully reset apatites give ages of less than ~50 Ma (Figure 5a and b). A tectonically stable period for the middle Eocene–Oligocene can also be observed in the time–temperature histories preliminarily simulated by Abdullin *et al*. (2014b) for the samples TS-2 and TS-4 based on complete AFT analysis (see details in Figure 6). As can be seen from Figure 6, the models TS-2 and TS-4 show two similar periods of slow cooling (i.e. with variable cooling rates of <3°C Ma^{-1}), controlled by a Late Cretaceous–Eocene tectonic event, of ~87–55 Ma (from 95–90 to 65–60°C) and ~82–50 Ma (from 90–85 to 65–60°C), respectively. The thermal history curves of the samples TS-2 and TS-4 only apparently detect the Chiapanecan event (Figure 6), because the middle–late Miocene cooling pathways are mostly located outside the PAZ (i.e. <60°C), where thermal modelling is generally ambiguous. These time–temperature paths, which correspond to a complex thermal history, clearly show that the Todos Santos Formation sandstones passed through the PAZ during many tens of million years

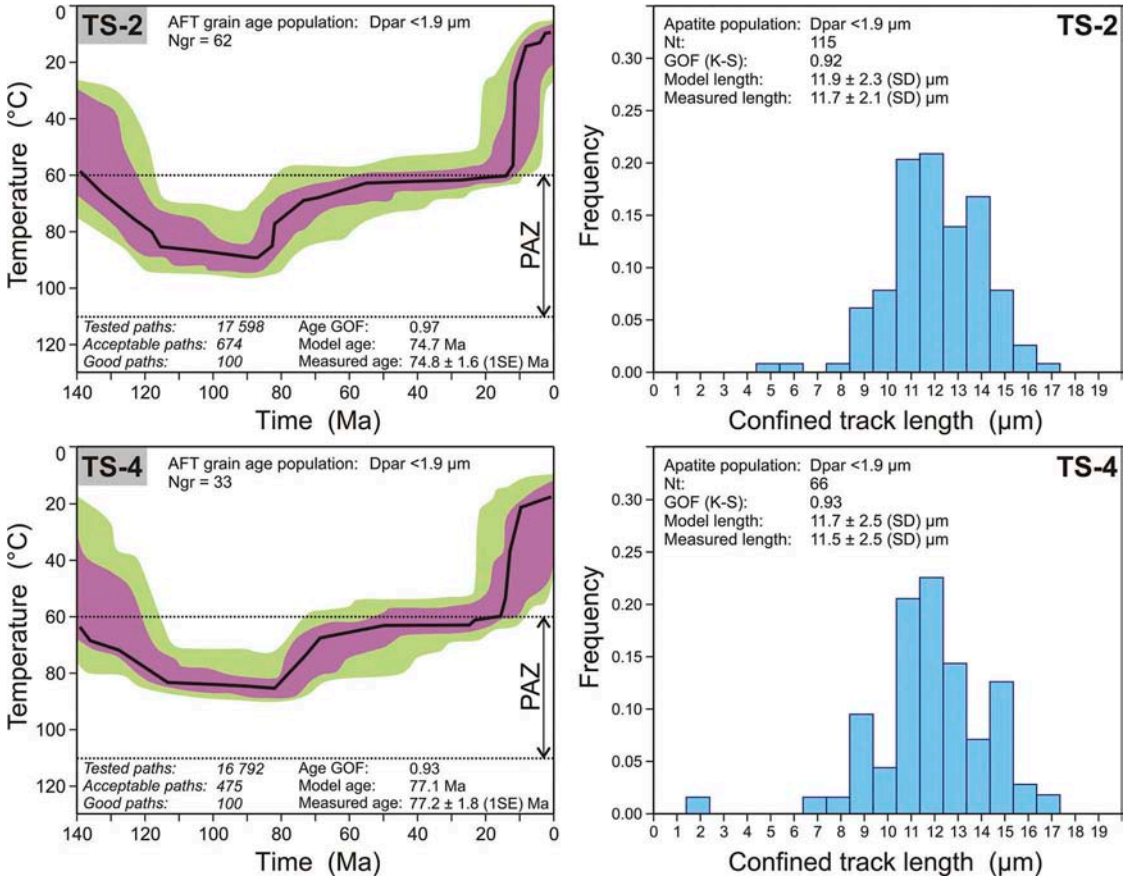

Figure 6. Time–temperature modelling results for Todos Santos Formation samples TS-2 and TS-4 based on complete AFT analysis (presented by Abdullin *et al*. 2014b). The simulation of thermal histories was carried out using HeFTy™ software (Ketcham 2005) based on the annealing model of Ketcham *et al*. (2007). The value of D_{par} (Donelick 1995; Donelick *et al*. 2005), which represents a mean etch pit length obtained from four to eight etch pits measured on a polished and etched surface of apatite parallel to the crystallographic C-axis (i.e. using reflected light), was used as a kinetic parameter of AFT calibration for both dated apatite grains and measured confined (horizontal) fission tracks. The modelling was performed for a defined population of apatites and confined tracks with D_{par} values of less than 1.9 µm, which mainly correspond to F-apatites. N_{gr} is the number of dated apatite crystals showing D_{par} values of <1.9 µm. N_t is the number of confined fission tracks measured in apatites with D_{par} values of <1.9 µm. The thick black lines denote the 'best-fit' curves, and the light green and purple areas represent 'acceptable' and 'good' thermal history ranges, respectively. 'K-S' is the Kolmogorov–Smirnov test. 'Age GOF' is the goodness-of-fit between the model and measured ages, whereas 'GOF K-S' represents the goodness-of-fit between the model and measured confined track lengths. In this case, the measured AFT ages are represented as the 'pooled ages', which were calculated from the sums of ^{238}U concentrations and spontaneous fission track densities obtained from apatites with D_{par} values of <1.9 µm. The modelled thermal history can be acceptable when N_t used for the simulation is more than 50 and both 'Age GOF' and 'GOF K-S' give values higher than 0.6. PAZ is the partial annealing zone for F-apatites, which is taken from ~60 to ~110°C (Gleadow *et al*. 1986; Green *et al*. 1989).

(Figure 6), with the consequence of a partial resetting of detrital apatite groups. Partial annealing of apatites by diagenesis is also recorded on the horizontally confined track-length distributions from the samples TS-2 and TS-4 yielding the measured mean track lengths of 11.7 ± 2.1 (SD) and 11.5 ± 2.5 (SD) µm, respectively (Figure 6), which are of a mixed-type population (e.g. Gleadow *et al*. 1986; Yan *et al*. 2003; Vermeesch *et al*. 2006).

The AFT data presented in this work, as well as the thermal history curves (Figure 6) constructed by Abdullin *et al*. (2014b), strongly indicate that an important thermo-tectonic event occurred along the SCH between the Late Cretaceous (83 ± 1 Ma) and early Eocene (51 ± 1 Ma) (Figure 5a and b). Furthermore, it was observed that the base of the Campanian–Maastrichtian Ocozocoautla Formation (Figure 2a and b) displays many high-energy deposits like gravel and coarse-grained sandstones (Gutiérrez-Gil 1956; Sánchez-Montes de Oca 1969, 2006; Rosales-Domínguez 1998), indicating the beginning of this tectonic event that subsequently destroyed some

parts of the Albian–Santonian carbonate platform in the SCH. Incidentally, Sánchez-Montes de Oca (2006) interpreted the Ocozocoautla Formation siliciclastic materials as recycled sediments derived from the Todos Santos Formation. Moreover, flysch-like deposits of the Soyaló and Lutitas Nanchital Formations mark the first intensive input of terrigenous clastics into the SSFP and RFP (Figure 1c) during the Palaeocene–Eocene period (e.g. Meneses-Rocha 1985, 1991; Quezada-Muñetón 1987; Sánchez *et al*. 2004). On the basis of single-grain U–Pb geochronology, Witt *et al*. (2012) demonstrated that Palaeocene–Eocene sequences from the internal portion of the SCH (i.e. southern SSFP; Figure 1c) include many detrital zircons with ages from ~260 to ~220 Ma, a typical zircon U–Pb age range for the CMC basement (Weber *et al*. 2007, 2008) and Todos Santos Formation sandstones (Godinez-Urban *et al*. 2011). This implies that these Palaeocene–Eocene terrigenous materials were predominantly derived from the CMC lithologies and recycled Todos Santos Formation sediments, which in turn suggests a period of uplift and erosion of the CMC area and Sierra Monocline subprovince during the Palaeocene–Eocene. It is also important to mention that the influence of Grenville-aged basement sources for Palaeocene–Eocene siliciclastic sequences is strongly marked along the northern section of the SSFP (Witt *et al*. 2012), which suggests sedimentary provenance from the Oaxacan and/or Guichicovi metamorphic complexes (Figure 1a).

The time span of ~83–51 Ma obtained for fully annealed apatites from the Todos Santos samples (Figure 5a) is in close agreement with the Laramide orogeny (Figure 5b) that occurred in the central and northern parts of Mexico (Figure 1a) during the Late Cretaceous–Eocene (from 85–80 to 50–40 Ma; e.g. Damon *et al*. 1981; Calmus *et al*. 1999; English *et al*. 2003; Ramos-Velázquez *et al*. 2008; Gray and Lawton 2011). Based upon sedimentological and stratigraphic observations, several authors (e.g. Carfantan 1981, 1985; Burkart *et al*. 1987; Meneses-Rocha 1991, 2001; Sánchez-Montes de Oca 2006) proposed that the Laramide orogeny also affected the SCH, a hypothesis that seems to be confirmed by the AFT data obtained in the present work. For example, in accordance with Meneses-Rocha (1985, 1991), the well-marked change between the flysch-like deposits of the Palaeocene Soyaló Formation and the molasse sediments of the early Eocene El Bosque Formation indicates an episode of uplift of the hinterland contemporaneous with the Laramide orogeny. Besides, Moravec (1983) suggested that the monocline flexure along the boundary between the Sierra Monocline and CMC in the area La Concordia (i.e. in the southern part of the Sierra Monocline; Figure 1c) also represents a tectonic event coeval with the Laramide orogeny.

Based on the results of decomposition of grain age distributions (Figure 5a) and taking into account two time–temperature histories (Figure 6) presented in Abdullin *et al*. (2014b), we reconstructed the detailed thermal history of the studied Todos Santos Formation sandstones from the cooling of its sediment source area through burial-related heating to post-burial cooling (see diagram in Figure 7). The ~35–25 Ma uplift-related cooling period proposed for the CMC by Ratschbacher *et al*. (2009) and Witt *et al*. (2012) was not identified for the Todos Santos Formation rock samples (Figures 6 and 7) collected from the northern part of the Sierra Monocline. This is in agreement with the interpretations of Witt *et al*. (2012), who suggested that the Oligocene tectonic event is only observed for the CMC. The ~35–25 Ma exhumation period of the CMC area is contemporaneous with the proposed arrival of the Chortís block to the Gulf of Tehuantepec area (e.g. Ratschbacher *et al*. 2009; Witt *et al*. 2012; Ferrari *et al*. 2014). In this scenario, the CMC area has probably been located closer to the current Gulf of Tehuantepec area during the Oligocene (Figure 1b), as was also suggested by Witt *et al*. (2012). This period of cooling may be strongly related to the influence of the Chortís block on the exhumation of the CMC (e.g. Ratschbacher *et al*. 2009; Witt *et al*. 2012). However, this exhumation period was observed neither for the SSFP (Witt *et al*. 2012) nor for the Sierra Monocline subprovince (this study). As opposed to low-temperature thermochronological data obtained from the internal SCH (Witt *et al*. 2012), the northern Sierra Monocline has no records concerning burial-related heating for the Palaeocene–Oligocene period (Figures 6 and 7). Sedimentation during the Palaeocene–Oligocene probably took place mainly in the SSFP and RFP (e.g. Meneses-Rocha 1985, 1991, 2001; Quezada-Muñetón 1987; Mandujano Velásquez 1996; Padilla y Sánchez 2007; Figure 1c), where post-Eocene burying was sufficient to reset detrital apatites from Palaeocene–Eocene sequences and thus giving apatite He and AFT cooling ages and curves which correspond to middle–late Miocene Chiapanecan orogeny (Witt *et al*. 2012). These differences in thermotectonic evolution across the SCH (i.e. between the data of Witt *et al*. (2012) and of this study) strongly indicate that this complex region should be considered as a juxtaposition of distinct palaeogeographic domains. According to the results obtained in this work (Figure 7), the Sierra Monocline subprovince, like the CMC area, emerged during the Late Cretaceous–early Eocene

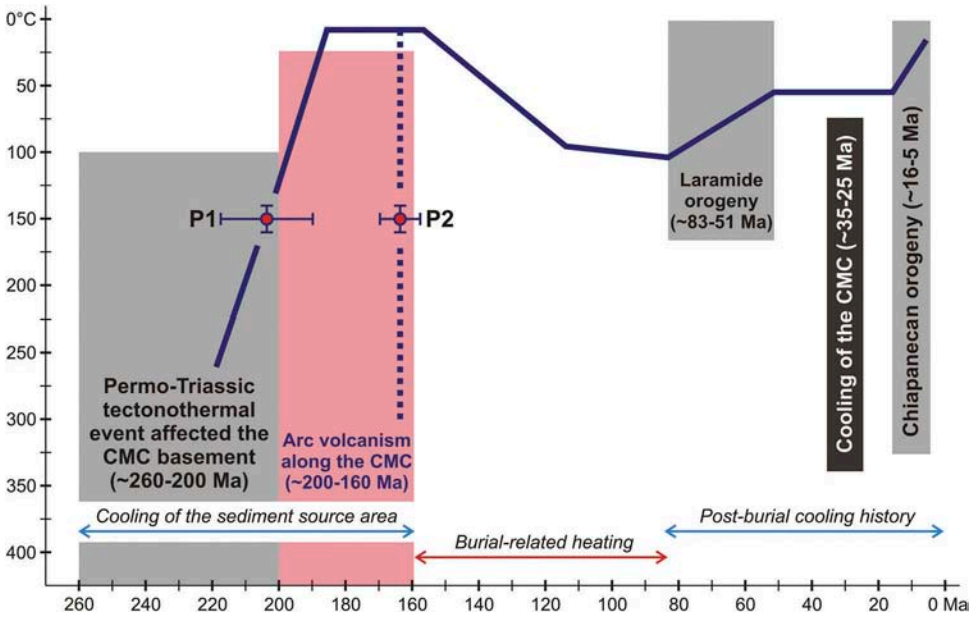

Figure 7. Detailed thermal history of the Todos Santos Formation sediments (shown in the scheme as thick solid and dashed lines) from cooling of its sediment source area to post-depositional cooling. P1 and P2 correspond to the AFT age peaks of 203 ± 14 (2σ) and 163 ± 6 (2σ) Ma, respectively. The periods of the most important tectonic and magmatic events which occurred in the SCH are also represented in the diagram. Rapid cooling of the CMC occured during the late Permian–Triassic (~260–200 Ma) thermo-tectonic event (e.g. Damon *et al*. 1981; Schaaf *et al*. 2002; Weber *et al*. 2005). Early–Middle Jurassic arc volcanism (~200–160 Ma) occurred along the CMC (Godinez-Urban *et al*. 2011). The Laramide orogeny affected the SCH during the Late Cretaceous–early Eocene (~83–51 Ma; this study). The ~35–25 Ma exhumation of the CMC is related to the arrival of the Chortís block to the Gulf of Tehuantepec area (Ratschbacher *et al*. 2009; Witt *et al*. 2012). The time interval for the Chiapanecan orogeny was chosen as the middle–late Miocene (~16–5 Ma) according to data of Witt *et al*. (2012).

period due to the Laramide orogeny, which is in close agreement with the generally accepted palaeogeographic models proposed for the SCH by several authors (e.g. Meneses-Rocha 1985, 2001; Sánchez-Montes de Oca 2006; Padilla y Sánchez 2007; Witt *et al*. 2012).

6. Conclusions

The low-temperature thermochronological data obtained in the present study could be useful towards a better reconstruction of the thermo-tectonic history of southern Mexico. Combining the AFT ages of this study with previous geological data, we can conclude that the SCH experienced a multi-episodic thermo-tectonic evolution with at least four main stages (Figures 5b and 7):

(1) Rapid cooling of the crystalline basement (CMC) of the SCH due to the late Permian–Triassic thermo-tectonic event (e.g. Damon *et al*. 1981; Torres *et al*. 1999; Schaaf *et al*. 2002; Weber *et al*. 2005; Estrada-Carmona *et al*. 2009, 2012.

(2) The Laramide orogeny (Carfantan 1981; Moravec 1983; Burkart *et al*. 1987; Meneses-Rocha 1991, 2001; Sánchez-Montes de Oca 2006), which affected the SCH during the Late Cretaceous–early Eocene period (i.e. ~83–51 Ma), as shown by the present fission track study.

(3) Cooling of the CMC during the Oligocene, presumably related to the arrival of the Chortís block in front of the Gulf of Tehuantepec area (Ratschbacher *et al*. 2009; Witt *et al*. 2012).

(4) Fast exhumation of the SCH during the Chiapanecan orogeny (middle–late Miocene), which was controlled by the transpressional deformation related to the triple junction of the North American, Caribbean, and Cocos plates, as it is currently organized (e.g. Witt *et al*. 2012). This recent tectonic event caused extensive erosion and abundant terrigenous sediment supply from the SCH to the north into the Tabasco plain (e.g. Sánchez-Montes de Oca 1979, 2006; Carfantan 1981; Meneses-Rocha 1985, 2001; Guzmán-Speziale 2010).

Acknowledgements

This study forms part of a PhD thesis of the first author, who thanks the Consejo Nacional de Ciencia y Tecnología (CONACyT) for a scholarship. The authors are very grateful to Barbara Martiny, Consuelo Macías, Alejandro Rodríguez-Trejo, and Jaime Díaz (all from UNAM) for their help with

sample preparation for AFT dating. Cesar Witt (Lille 1 University, France), one anonymous reviewer, and the Editor-in-Chief, Robert J. Stern are acknowledged for their constructive suggestions that substantially improved this manuscript.

Disclosure statement

No potential conflict of interest was reported by the authors.

Funding

This research was financially supported by the UNAM PAPIIT (Programa de Apoyo a Proyectos de Investigación e Innovación Tecnológica) grant no [IN111414] to Jesús Solé. The authors also acknowledge the UNAM PAPIIT grant no [IN102414] to Luigi Solari, for funding parts of the analytical developments.

Supplemental data

Supplemental data for this paper can be accessed at http://dx.doi.org/10.1080/00206814.2015.1055596.

References

Abdullin, F., Sole, J., Shchepetilnikova, V., and Ortega Obregon, C., 2014a, Análisis químico (elementos traza y REE) de apatitos detríticos usando LA-ICP-MS: Aplicaciones para procedencia de sedimentos siliciclásticos del Mesozoico de Chiapas (SE México): Reunión Anual de la Unión Geofísica Mexicana, Puerto Vallarta 2014, Abstracts with Programs. [in Spanish.]

Abdullin, F., Sole, J., Shchepetilnikova, V., Solari, L., and Ortega Obregon, C., 2014b, LA-ICP-MS apatite fission track thermochronology of Mesozoic sandstones and its tectonic significance in the Sierra Madre de Chiapas, SE Mexico: Reunión Anual de la Unión Geofísica Mexicana, Puerto Vallarta 2014, Abstracts with Programs.

Abdullin, F., Solé, J., and Solari, L., 2014c, Datación mediante trazas de fisión y análisis multielemental con LA-ICP-MS del fluorapatito de Cerro de Mercado (Durango, México): Revista Mexicana de Ciencias Geológicas, v. 31, p. 395–406. [in Spanish with English abstract.]

Barbarand, J., Carter, A., Wood, I., and Hurford, T., 2003, Compositional and structural control of fission-track annealing in apatite: Chemical Geology, v. 198, p. 107–137. doi:10.1016/S0009-2541(02)00424-2

Belousova, E.A., Griffin, W.L., O'Reilly, S.Y., and Fisher, N.I., 2002, Apatite as an indicator mineral for mineral exploration: Trace-element compositions and their relationship to host rock type: Journal of Geochemical Exploration, v. 76, p. 45–69. doi:10.1016/S0375-6742(02)00204-2

Blair, T.C., 1987, Tectonic and hydrologic controls on cyclic alluvial fan, fluvial, and lacustrine rift-basin sedimentation, Jurassic-lowermost Cretaceous Todos Santos Formation, Chiapas, Mexico: Journal of Sedimentary Research, v. 57, p. 845–862.

Burckhardt, 1930, Étude synthétique sur le Mésozoïque Mexicain: Société Paléontologique Suisse, Mémoire, v. 49–50, p. 280. [in French.]

Burkart, B., Deaton, B.C., Dengo, C., and Moreno, G., 1987, Tectonic wedges and offset Laramide structures along the Polochic fault of Guatemala and Chiapas, Mexico: Reaffirmation of large Neogene displacement: Tectonics, v. 6, p. 411–422. doi:10.1029/TC006i004p00411

Calmus, T., Poupeau, G., Bourgois, J., Michaud, F., Mercier De Lépinay, B., Labrin, E., and Azdimousa, A., 1999, Late Mesozoic and Cenozoic thermotectonic history of the Mexican Pacific margin (18 to 25°N): New insight from apatite and zircon fission-track analysis of coastal and offshore plutonic rocks: Tectonophysics, v. 306, p. 163–182. doi:10.1016/S0040-1951(99)00049-9

Carfantan, J.C., 1981, Evolución estructural del sureste de México, Paleogeografía e historia tectónica de las zonas internas mesozoicas: Revista Mexicana de Ciencias Geológicas, v. 5, p. 207–216. [in Spanish with English abstract.]

Carfantan, J.C., 1985, Du système cordillerain Nord-Américain au domaine Caraïbe. Étude géologique du Mexique méridional [Ph.D. thesis]: Université de Savoie, France, 558 p. [in French.]

Chew, D.M., and Donelick, R.A., 2012, Combined apatite fission-track and U-Pb dating by LA-ICP-MS and its application in apatite provenance analysis, *in* Sylvester, P., ed., Quantitative mineralogy and microanalysis of sediments and sedimentary rocks: St John's, NL, Mineralogical Association of Canada, Short Course, v. 42, p. 219–247.

Collard, N., Taran, Y., Peiffer, L., Campion, R., and Paz, M.P.J., 2014, Solute fluxes and geothermal potential of Tacaná volcano-hydrothermal system, Mexico–Guatemala: Journal of Volcanology and Geothermal Research, v. 288, p. 123–131. doi:10.1016/j.jvolgeores.2014.10.012

Cox, R., Košler, J., Sylvester, P., and Hodych, P., 2000, Apatite fission-track (FT) dating by LAM-ICP-MS analysis. Goldschmidt Conference, UK, Oxford: Journal of Conference Abstracts, v. 5, 322 p.

Damon, P.E., Shafiqullah, M., and Clark, K., 1981, Age trends of igneous activity in relation to metallogenesis in the southern Cordillera, *in* Dickinson, W., and Payne, W.D., eds., Relations of tectonics to ore deposits in the southern Cordillera: Arizona Geological Society Digest, v. 14, p. 137–153.

Donelick, R.A., 1995, A method of fission track analysis utilizing bulk chemical etching of apatite: Australia, Patent No. 658,800.

Donelick, R.A., O'Sullivan, P.B., and Ketcham, R.A., 2005, Apatite fission-track analysis: Reviews in Mineralogy and Geochemistry, v. 58, p. 49–94. doi:10.2138/rmg.2005.58.3

English, J.M., Johnston, S.T., and Wang, K., 2003, Thermal modelling of the Laramide orogeny: Testing the flat-slab subduction hypothesis Earth and Planetary Science Letters, v. 214, p. 619–632. doi:10.1016/S0012-821X(03)00399-6

Estrada-Carmona, J., Weber, B., Hecht, L., and Martens, U., 2009, PTt trajectory of metamorphic rocks from the central Chiapas Massif Complex: The Custepec Unit, Chiapas, México: Revista Mexicana de Ciencias Geológicas, v. 26, p. 243–259.

Estrada-Carmona, J., Weber, B., Martens, U., and López-Martínez, M., 2012, Petrogenesis of Ordovician magmatic

rocks in the southern Chiapas Massif Complex: Relations with the early Palaeozoic magmatic belts of northwestern Gondwana: International Geology Review, v. 54, p. 1918–1943. doi:10.1080/00206814.2012.685553

Faure, G., and Mensing, T.M., 2005, Isotopes: Principles and applications: New York, John Wiley & Sons, 897 p.

Ferrari, L., Bergomi, M., Martini, M., Tunesi, A., Orozco-Esquivel, T., and López-Martínez, M., 2014, Late cretaceous-Oligocene magmatic record in southern Mexico: The case for a temporal slab window along the evolving Caribbean-North America-Farallon triple boundary: Tectonics, v. 33, p. 1738–1765. doi:10.1002/tect.v33.9

Galbraith, R.F., 1981, On statistical models for fission track counts: Journal of the International Association for Mathematical Geology, v. 13, p. 471–478. doi:10.1007/BF01034498

Galbraith, R.F., and Green, P.F., 1990, Estimating the component ages in a finite mixture: International Journal of Radiation Applications and Instrumentation. Part D. Nuclear Tracks and Radiation Measurements, v. 17, p. 197–206. doi:10.1016/1359-0189(90)90035-V

Galbraith, R.F., and Laslett, G.M., 1993, Statistical models for mixed fission track ages: Nuclear Tracks and Radiation Measurements, v. 21, p. 459–470. doi:10.1016/1359-0189(93)90185-C

García-Palomo, A., Macías, J.L., Arce, J.L., Mora, J.C., Hughes, S., Saucedo, R., Espíndola, J.M., Escobar, R., and Layer, P., 2006, Geological evolution of the Tacaná Volcanic Complex, Mexico–Guatemala: Geological Society of America, Special Paper, v. 412, p. 39–57.

Gleadow, A.J.W., Duddy, I.R., Green, P.F., and Lovering, J.F., 1986, Confined fission track lengths in apatite: A diagnostic tool for thermal history analysis: Contributions to Mineralogy and Petrology, v. 94, p. 405–415. doi:10.1007/BF00376334

Godinez-Urban, A., Lawton, T.F., Molina Garza, R.S., Iriondo, A., Weber, B., and Lopez-Martinez, M., 2011, Jurassic volcanic and sedimentary rocks of the La Silla and Todos Santos Formations, Chiapas: Record of Nazas arc magmatism and rift-basin formation prior to opening of the Gulf of Mexico: Geosphere, v. 7, p. 121–144. doi:10.1130/GES00599.1

Gray, G.G., and Lawton, T.F., 2011, New constraints on timing of Hidalgoan (Laramide) deformation in the Parras and La Popa basins, NE Mexico: Boletín de la Sociedad Geológica Mexicana, v. 63, p. 333–343.

Green, P.F., 1985, Comparison of zeta calibration baselines for fission-track dating of apatite, zircon and sphene: Chemical Geology: Isotope Geoscience Section, v. 58, p. 1–22. doi:10.1016/0168-9622(85)90023-5

Green, P.F., Duddy, I.R., Laslett, G.M., Hegarty, K.A., Gleadow, A. J.W., and Lovering, J.F., 1989, Thermal annealing of fission tracks in apatite 4. Quantitative modelling techniques and extension to geological timescales: Chemical Geology: Isotope Geoscience Section, v. 79, p. 155–182. doi:10.1016/0168-9622(89)90018-3

Gutiérrez-Gil, R., 1956, Bosquejo geológico del estado de Chiapas. *in* Geología del Mesozoico y estratigrafía Pérmica del Estado de Chiapas: México, Libreto-guía Excursión C-15, Congreso Geológico Internacional 20, p. 9–32. [in Spanish.].

Guzmán-Speziale, M., 2010, Beyond the Motagua and Polochic faults: Active strike-slip faulting along the Western North America–Caribbean plate boundary zone: Tectonophysics, v. 496, p. 17–27. doi:10.1016/j.tecto.2010.10.002

Guzmán-Speziale, M., and Meneses-Rocha, J.J., 2000, The North America–Caribbean plate boundary west of the Motagua–Polochic fault system: A fault jog in Southeastern Mexico: Journal of South American Earth Sciences, v. 13, p. 459–468. doi:10.1016/S0895-9811(00)00036-5

Guzmán-Speziale, M., Pennington, W.D., and Matumoto, T., 1989, The triple junction of the North America, Cocos, and Caribbean plates: Seismicity and tectonics: Tectonics, v. 8, p. 981–997. doi:10.1029/TC008i005p00981

Hasebe, N., Barbarand, J., Jarvis, K., Carter, A., and Hurford, A.J., 2004, Apatite fission-track chronometry using laser ablation ICP-MS: Chemical Geology, v. 207, p. 135–145. doi:10.1016/j.chemgeo.2004.01.007

Hasebe, N., Carter, A., Hurford, A.J., and Arai, S., 2009, The effect of chemical etching on LA-ICP-MS analysis in determining uranium concentration for fission-track chronometry, *in* Lisker, F., Ventura, B., and Glasmacher, U.A., eds., Thermochronological methods: From palaeotemperature constraints to landscape evolution models: Geological Society of London, Special Publications, v. 324, p. 37–46. doi:10.1144/SP324.3

Herrera, S.M., and Estavillo, G.C., 1991, Análisis estratigráfico y modelo de sedimentación de la Formación Todos Santos en el área del Alto Uzpanapa–Matías Romero, Oaxaca: Revista del Instituto Mexicano del Petróleo, v. 23, p. 5–42. [in Spanish.]

Holden, N.E., and Hoffman, D.C., 2000, Spontaneous fission half-lives for ground-state nuclide (Technical report) Pure and Applied Chemistry, v. 72, p. 1525–1562. doi:10.1351/pac200072081525

Jafarzadeh, M., Harami, R.M., Friis, H., Amini, A., Mahboubi, A., and Lenaz, D., 2014, Provenance of the Oligocene–Miocene Zivah Formation, NW Iran, assessed using heavy mineral assemblage and detrital clinopyroxene and detrital apatite analyses: Journal of African Earth Sciences, v. 89, p. 56–71. doi:10.1016/j.jafrearsci.2013.10.005

Jaffey, A.H., Flynn, K.F., Glendenin, L.E., Bentley, W.C., and Essling, A.M., 1971, Precision measurement of the half-lives and specific activities of ^{235}U and ^{238}U: Physical Review C, v. 4, p. 1889–1906. doi:10.1103/PhysRevC.4.1889

Ketcham, R.A., 2005, Forward and inverse modeling of low-temperature thermochronometry data: Reviews in Mineralogy and Geochemistry, v. 58, p. 275–314. doi:10.2138/rmg.2005.58.11

Ketcham, R.A., Carter, A., Donelick, R.A., Barbarand, J., and Hurford, A.J., 2007, Improved modeling of fission-track annealing in apatite: American Mineralogist, v. 92, p. 799–810. doi:10.2138/am.2007.2281

Ketcham, R.A., Donelick, R.A., and Carlson, W.D., 1999, Variability of apatite fission-track annealing kinetics. III. Extrapolation to geological time scales: American Mineralogist, v. 84, p. 1235–1255.

Lesnov, F.P., 2012, Rare earth elements in ultramafic and mafic rocks and their minerals: Minor and accessory minerals: London, Taylor and Francis Group, p. 314 p.

Lisker, F., Ventura, B., and Glasmacher, U.A., 2009, Apatite thermochronology in modern geology: Geological Society

of London, Special Publications, v. 324, p. 1–23. doi:10.1144/SP324.1

Liu, W., Zhang, J., Sun, T., and Wang, J., 2014, Application of apatite U–Pb and fission-track double dating to determine the preservation potential of magnetite–apatite deposits in the Luzong and Ningwu volcanic basins, eastern China: Journal of Geochemical Exploration, v. 138, p. 22–32. doi:10.1016/j.gexplo.2013.12.006

Ludwig, K.R., 2008, Manual for Isoplot 3.7: Berkeley Geochronology Center, Special Publication 4, 77 p.

Mandujano Velásquez, J., 1996, Cuatro megasecuencias de evolución litoestratigráfica en la Sierra de Chiapas: Boletín de la Asociación Mexicana de Geólogos Petroleros, v. 45, p. 46–60. [in Spanish with English abstract.]

Meneses-Rocha, J.J., 1985, Tectonic evolution of the Strike-slip Fault province of Chiapas, Mexico [M.S. thesis]: Austin, University of Texas at Austin, 315 p.

Meneses-Rocha, J.J., 1990, Marco Tectónico y Paleogeografía del Triásico Tardío-Jurásico en el Sureste de México: Boletín de la Asociación Mexicana de Geólogos Petroleros, v. 39, p. 3–68. [in Spanish with English abstract.]

Meneses-Rocha, J.J., 1991, Tectonic development of the Ixtapa graben, Chiapas, Mexico [Ph.D. thesis]: Austin, University of Texas at Austin, 308 p.

Meneses-Rocha, J.J., 2001, Tectonic evolution of the Ixtapa Graben, an example of a strike-slip basin of southeastern Mexico: Implications for regional petroleum systems, *in* Bartolini, C., Buffler, R.T., and Cantú-Chapa, A., eds., The western gulf of Mexico basin: Tectonics, sedimentary basins and petroleum systems: American Association of Petroleum Geologists Memoir, v. 75, p. 183–216.

Molina-Garza, R.S., Geissman, J.W., Wawrzyniec, T.F., Peña Alonso, T.A., Iriondo, A., Weber, B., and Aranda-Gómez, J., 2015, Geology of the coastal Chiapas (Mexico) Miocene plutons and the Tonalá shear zone: Syntectonic emplacement and rapid exhumation during sinistral transpression: Lithosphere, v. 7, p. 257–274.

Moravec, D., 1983, Study of the Concordia Fault System near Jericó, Chiapas, Mexico [M.S. thesis]: Austin, University of Texas at Austin, 155 p.

Omaña, L., 2006, Late Cretaceous (Maastrichtian) foraminiferal assemblage from the inoceramid beds, Ocozocoautla Formation, central Chiapas, SE Mexico: Revista Mexicana de Ciencias Geológicas, v. 23, p. 125–132.

Padilla y Sánchez, R.J., 2007, Evolución geológica del sureste mexicano desde le Mesozoico al presente en el contexto regional del Golfo de México: Boletín de la Sociedad Geológica Mexicana, v. 59, p. 19–42. [in Spanish with English abstract.]

Perrilliat, M.C., Avendaño, J., Vega, F.J., and Solé, J., 2006, Lower Eocene gastropods from the El Bosque Formation, central Chiapas, Mexico: The Veliger, v. 48, p. 151–169.

Peterson, J.A., 1983, Petroleum geology and resources of southeastern Mexico, northern Guatemala, and Belize: U.S. Geological Survey Circular, v. 760, 44 p.

Pompa-Mera, V., 2009, Geoquímica y Geocronología de los Complejos Intrusivos en el sureste de Chiapas, México [M. S. thesis]: México, UNAM, 160 p. [in Spanish.]

Quezada-Muñetón, J.M., 1983, Las Formaciones San Ricardo y Jericó del Jurásico Medio– Cretácico Inferior en el SE de México: Boletín de la Asociación Mexicana de Geólogos Petroleros, v. 35, p. 37–64. [in Spanish with English abstract.]

Quezada-Muñetón, J.M., 1987, El Cretácico medio–Superior y el límite Cretácico Superior– Terciario inferior en la Sierra de Chiapas: Boletín de la Asociación Mexicana de Geólogos Petroleros, v. 39, p. 3–98. [in Spanish with English abstract.]

Ramos-Velázquez, E., Calmus, T., Valencia, V., Iriondo, A., Valencia-Moreno, M., and Bellon, H., 2008, U-Pb and 40Ar/39Ar geochronology of the coastal Sonora batholith: New insights on Laramide continental arc magmatism: Revista Mexicana de Ciencias Geológicas, v. 25, p. 314–333.

Ratschbacher, L., Franz, L., Min, M., Bachmann, R., Martens, U., Stanek, K., Stübner, K., Nelson, B.K., Herrmann, U., Weber, B., López-Martínez, M., Jonckheere, R., Sperner, B., Tichomirowa, M., McWilliams, M.O., Gordon, M., Meschede, M., and Bock, P., 2009, The North American–Caribbean plate boundary in Mexico–Guatemala–Honduras, *in* James, K., Lorente, M., and Pindell, J., eds., The origin and evolution of the Caribbean plate: Geological Society of London, Special Publications, v. 328, p. 219–293. doi:10.1144/SP328.11

Reiners, P., 2005, Zircon (U-Th)/He Thermochronometry Reviews in Mineralogy and Geochemistry, v. 58, p. 151–179. doi:10.2138/rmg.2005.58.6

Rosales-Domínguez, M.D.C., 1998, Biohorizontes cronoestratigráficos en las facies carbonatadas de plataforma del Cretácico medio–superior de Chiapas, México: Revista Mexicana de Ciencias Geológicas, v. 15, p. 73–77. [in Spanish with English abstract.]

Rosales-Domínguez, M.D.C., Bermúdez-Santana, J.C., and Aguilar-Piña, M., 1997, Mid and Upper Cretaceous foraminiferal assemblages from the Sierra de Chiapas, southeastern Mexico: Cretaceous Research, v. 18, p. 697–712. doi:10.1006/cres.1997.0081

Sánchez, M.O., Franco, N.A., Navarrete, S.F., and Martínez, M.G., 2004, Estratigrafía y evolución de facies del Cretácico Superior en el Sureste de México: Boletín de la Asociación Mexicana de Geólogos Petroleros, Special Paper No. 697, p. 39–61. [in Spanish.]

Sánchez-Montes de Oca, R., 1969, Estratigrafía y paleogeografía del Mesozoico de Chiapas: México, D.F., Instituto Mexicano del Petróleo, Seminario sobre exploración petrolera, Mesa redonda 4, Capítulo 5, 31 p. [in Spanish.]

Sánchez-Montes de Oca, R., 1979, Geología petrolera de la Sierra de Chiapas: Boletín de la Asociación Mexicana de Geólogos Petroleros, v. 31, p. 67–97. [in Spanish with English abstract.]

Sánchez-Montes de Oca, R., 2006, Curso Cuenca del Sureste: México, Petróleos Mexicanos, 296 p. [in Spanish.]

Schaaf, P., Weber, B., Weis, P., Groβ, A., Ortega-Gutiérrez, F., and Kohler, H., 2002, The Chiapas Massif (Mexico) revised: New geologic and isotopic data and basement characteristics, *in* Miller, H.E., ed., Contributions to Latin-American Geology: Neues Jahrbuch für Geologie und Paläontologie, Abhandlungen, v. 225, p. 1–23.

Solé, J., and Pi, T., 2005, An empirical calibration for 4He quantification in minerals and rocks by laser fusion and noble gas mass spectrometry using Cerro de Mercado (Durango, Mexico) fluorapatite as a standard: Analytica Chimica Acta, v. 535, p. 325–330. doi:10.1016/j.aca.2004.12.020

Torres, R., Ruiz, J., Patchett, P.J., and Grajales, J.M., 1999, Permo-Triassic continental arc in eastern Mexico: Tectonic implications for reconstructions of southern North America: Geological Society of America, Special Paper, v. 340, p. 191–196.

Vamvaka, A., Spiegel, C., Frisch, W., Danišik, M., and Kilias, A., 2010, Fission track data from the Mesohellenic Trough and the Pelagonian zone in NW Greece: Cenozoic tectonics and exhumation of source areas: International Geology Review, v. 52, p. 223–248. doi:10.1080/00206810802674402

Vermeesch, P., 2009, RadialPlotter: A Java application for fission track, luminescence and other radial plots: Radiation Measurements, v. 44, p. 409–410. doi:10.1016/j.radmeas.2009.05.003

Vermeesch, P., Miller, D.D., Graham, S.A., De Grave, J., and McWilliams, M.O., 2006, Multimethod detrital thermochronology of the Great Valley Group near New Idria, California: Geological Society of America Bulletin, v. 118, p. 210–218. doi:10.1130/B25797.1

Weber, B., Cameron, K.L., Osorio, M., and Schaaf, P., 2005, A late Permian tectonothermal event in Grenville crust of the southern Maya terrane: U-Pb zircon ages from the Chiapas Massif, southeastern Mexico: International Geology Review, v. 47, p. 509–529. doi:10.2747/0020-6814.47.5.509

Weber, B., Iriondo, A., Premo, W.R., Hecht, L., and Schaaf, P., 2007, New insights into the history and origin of the southern Maya block, SE México: U–Pb–SHRIMP zircon geochronology from metamorphic rocks of the Chiapas massif: International Journal of Earth Sciences, v. 96, p. 253–269. doi:10.1007/s00531-006-0093-7

Weber, B., Valencia, V.A., Schaaf, P., Pompa-Mera, V., and Ruiz, J., 2008, Significance of provenance ages from the Chiapas massif complex (Southeastern Mexico): Redefining the Paleozoic basement of the Maya block and its evolution in a Peri-Gondwanan Realm: The Journal of Geology, v. 116, p. 619–639. doi:10.1086/596575

Witt, C., Brichau, S., and Carter, A., 2012, New constraints on the origin of the Sierra Madre de Chiapas (south Mexico) from sediment provenance and apatite thermochronometry: Tectonics, v. 31, p. TC6001. doi:10.1029/2012TC003141

Yan, Y., Lin, G., Wang, Y.J., Guo, F., Li, Z.A., Li, X.M., and Zhao, C., 2003, Apatite fission track ages of Mesozoic sandstones from Beipiao basin, eastern China: Implications for basin provenance and tectonic evolution: Geochemical Journal, v. 37, p. 377–390. doi:10.2343/geochemj.37.377

Zhu, W., Zhang, Z., Shu, L., Wan, J., Lu, H., Wang, S., Yang, W., and Su, J., 2010, Thermotectonic evolution of Precambrian basement rocks of the Kuruktag uplift, NE Tarim craton, China: Evidence from apatite fission-track data: International Geology Review, v. 52, p. 941–954. doi:10.1080/00206810903211062

5.1. Datos adicionales de trazas de fisión en apatitos

En este estudio se fecharon también cinco rocas del Macizo de Chiapas por el método de trazas de fisión en apatitos (Tabla 5.1), las cuales se colectaron en su parte norte (Figura 5.1). Las edades centrales (*i.e.*, promedio) en estas rocas varían de 44 ± 1 Ma a 15 ± 1 Ma (Tabla 5.1; Figura 5.2). Todos los grupos de apatitos del Macizo de Chiapas producen unas dispersiones de edades menores de 10% (Tabla 5.1) indicando que estos cristales, fechados por muestra, pertenecen a una sola población de edades (*e.g.*, Galbraith y Laslett, 1993). Los apatitos de estas muestras se identificaron como F-apatitos (Tabla 5.1) debido a sus bajos valores de D-par (Donelick *et al.*, 2005). Por lo tanto, se interpreta que los resultados obtenidos indican las edades de enfriamiento de estas rocas a través de paleoisotermas de ~110–100 °C.

Tabla 5.1. Resultados de trazas de fisión en apatitos de muestras del Macizo de Chiapas (los datos de este estudio así como los resultados reportados por Ratschbacher *et al.*, 2009 y Witt *et al.*, 2012).

Sample	Cr/Mt age	Sample location	Elevation (m.a.s.l.)	Ngr	$T \pm 1\sigma$ (Ma)	D (%)	MTL ± SD (μm)	Ntr	D-par ± SD (μm)	Data source/method
CM-5	P_3-Tr_1	16°48′52″N; 93°49′24″W	630	18	26 ± 1	7.1	12.3 ± 1.4	13	1.61 ± 0.11	this study/LA-ICP-MS
CM-1	P_3-Tr_1	16°34′11″N; 93°38′31″W	570	23	44 ± 1	8.3	12.4 ± 1.6	11	1.45 ± 0.05	this study/LA-ICP-MS
CM-2	P_3-Tr_1	16°28′47″N; 93°42′08″W	580	15	32 ± 1	9.2	12.5 ± 2.1	8	1.57 ± 0.08	this study/LA-ICP-MS
CM-3	P_3-Tr_1	16°24′46″N; 93°47′42″W	660	15	24 ± 1	7.2	12.1 ± 1.9	9	1.42 ± 0.06	this study/LA-ICP-MS
CM-4	P_3-Tr_1	16°22′22″N; 93°51′31″W	690	14	15 ± 1	6.1	14.3 ± 0.8	5	1.64 ± 0.09	this study/LA-ICP-MS
Wt-1	P_3-Tr_1	16°24′04″N; 93°24′55″W	680	14	32 ± 3	–	–	–	–	Witt et al. (2012)/EDM
Wt-2	P_3-Tr_1	16°20′41″N; 93°52′26″W	700	22	10 ± 1	–	–	–	–	Witt et al. (2012)/EDM
Rs-1	P_3-Tr_1	16°20′21″N; 93°32′40″W	690	14	39 ± 2	–	–	–	–	Ratschbacher et al. (2009)/EDM
Rs-2	Pz	16°16′53″N; 93°36′53″W	750	12	36 ± 1	–	–	–	–	Ratschbacher et al. (2009)/EDM
Rs-3	P_3-Tr_1	16°07′09″N; 93°41′34″W	220	62	16 ± 1	–	–	–	–	Ratschbacher et al. (2009)/EDM
Rs-4	P_3-Tr_1	16°06′36″N; 93°26′20″W	670	11	33 ± 1	–	–	–	–	Ratschbacher et al. (2009)/EDM
Rs-5	P_3-Tr_1	16°05′31″N; 93°11′01″W	590	45	31 ± 1	–	–	–	–	Ratschbacher et al. (2009)/EDM
Rs-6	P_3-Tr_1	16°04′23″N; 93°12′21″W	590	51	28 ± 1	–	–	–	–	Ratschbacher et al. (2009)/EDM
Rs-7	P_3-Tr_1	16°02′28″N; 93°13′37″W	630	11	25 ± 1	–	–	–	–	Ratschbacher et al. (2009)/EDM

Nota: (1) Cr/Mt – edad de cristalización o de metamorfismo; P_3-Tr_1 – Pérmico superior a Triásico; Pz – rocas pre-batolíticas; (2) Ngr – número de apatitos datados; (3) $T \pm 1\sigma$ – la edad central (promedio) por trazas de fisión; (4) D – dispersión de edades en granos individuales; (5) MTL – longitud promedio de trazas confinadas; (6) Ntr – número de trazas que se midieron; (7) D-par – parámetro para calibrar las temperaturas de cierre en apatitos y las propiedades del borrado térmico de sus trazas (longitud promedio de *etch pits*, ver detalles en Donelick *et al.*, 2005); (8) EDM – método de detector externo.

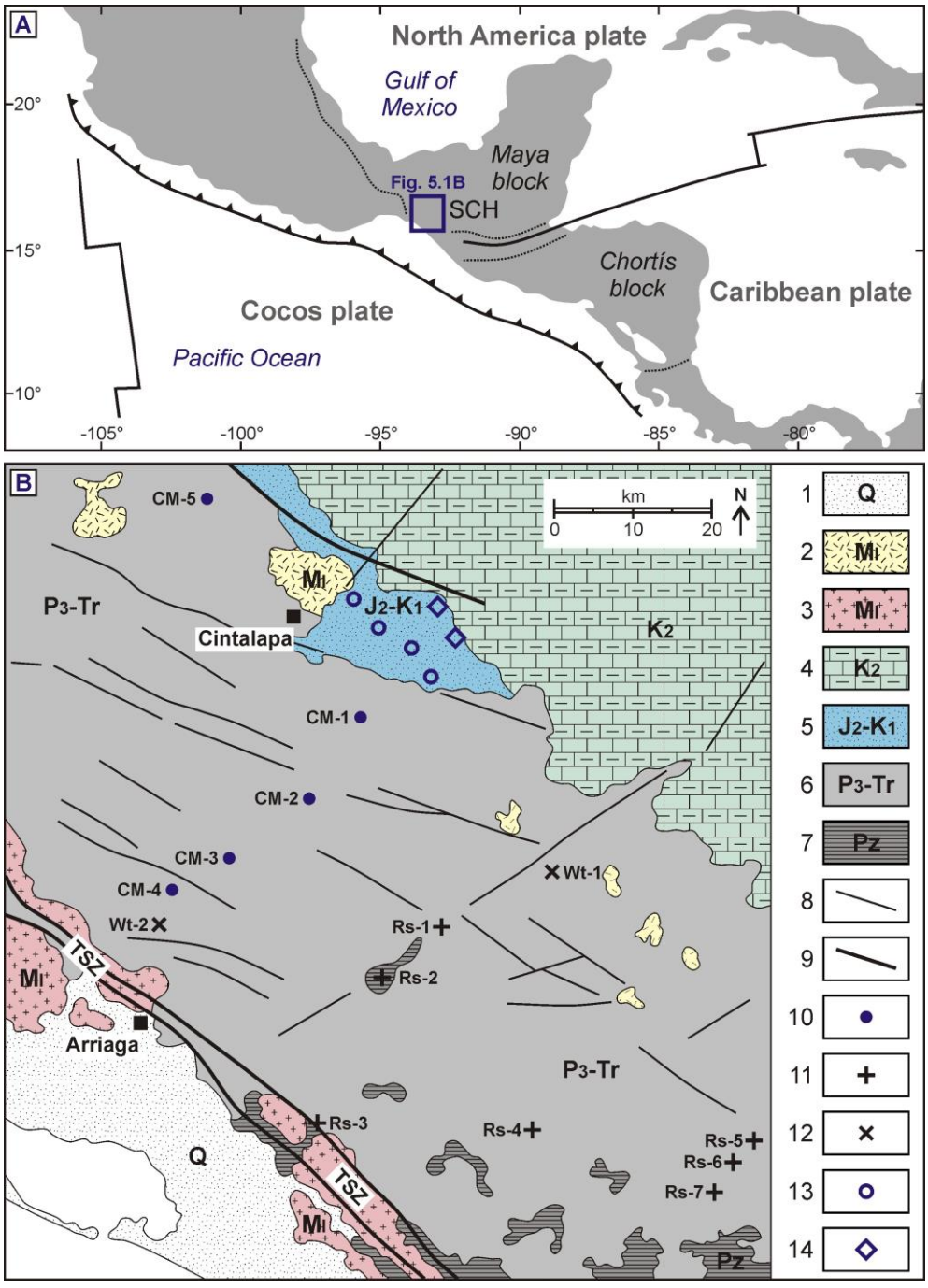

Figura 5.1. (A) Situación geodinámica de Mesoamérica, SCH–Sierra de Chiapas. (B) Mapa geológico simplificado (modificado de Weber *et al*., 2008 y Molina-Garza *et al*., 2015) que muestra la ubicación de las muestras analizadas con el método de trazas de fisión en apatitos. (1) – sedimentos Cuaternarios;

(2) – rocas volcánicas y volcanoclásticas del Mioceno; (3) – granitos del Mioceno; (4) carbonatos y rocas clásticas del Cretácico superior; (5) – rocas siliciclásticas del Jurásico medio al Cretácico inferior; (6) – rocas ígneas y metaígneas del Pérmico superior–Triásico; (7) – rocas pre-batolíticas del Paleozoico; (8) – fallas secundarias; (9) – fallas mayores; (10) – datos de trazas de fisión (este estudio); (11) – resultados publicados por Ratschbacher *et al.* (2009); (12) – rocas datadas por Witt *et al.* (2012); (13) – datos obtenidos por Abdullin *et al.* (2016a); se pueden ver también en el capítulo 5 de esta tesis; (14) – dataciones por trazas de fisión de la Formación San Ricardo (detalles en los capítulos 5 y 6).

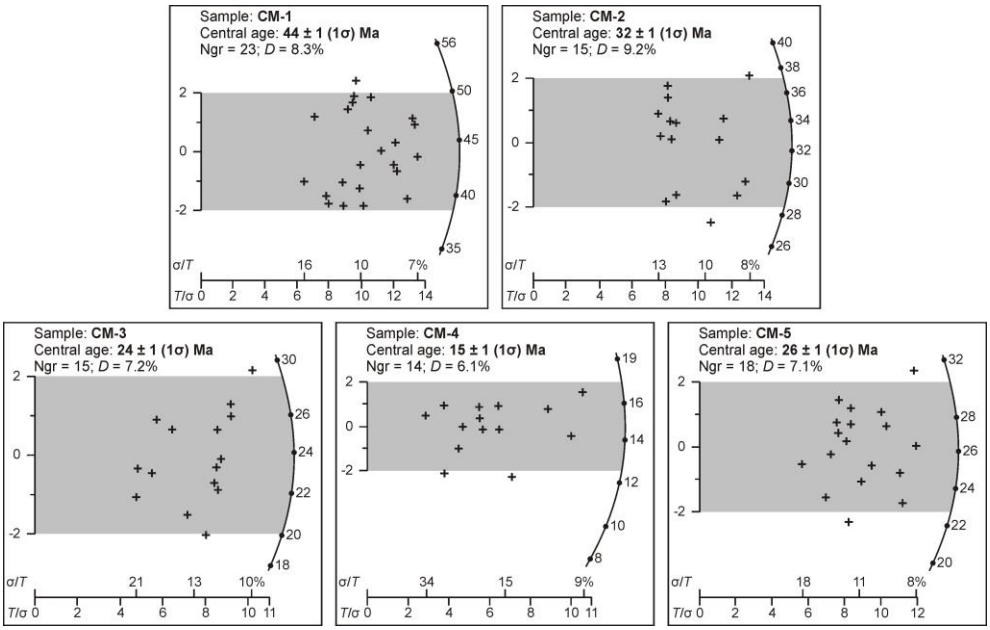

Figura 5.2. Diagramas radiales que muestran los resultados de dataciones de apatitos de las rocas del Macizo de Chiapas mediante trazas de fisión. Ngr – número de cristales, *D* – dispersión de edades (%).

La mayoría de rocas del Macizo de Chiapas analizadas por la técnica de trazas de fisión (Ratschbacher *et al.*, 2009; Witt *et al.*, 2012; este trabajo) varían en un rango bastante amplio, de ~45 Ma a 23 Ma y sin una correlación clara entre la elevación de

las muestras y sus edades (ver Figura 5.3). Por lo tanto, esto puede indicar que el Macizo de Chiapas no sufrió ningún tipo de levantamiento significativo en el Eoceno medio y en el Oligoceno, lo que ha sido sugerido también en otros trabajos (Quezada-Muñetón, 1987; Meneses-Rocha, 2001; Witt *et al*., 2012; Molina-Garza *et al*., 2015). La mayoría de muestras del Macizo de Chiapas analizadas en este estudio muestran unas longitudes promedio de trazas confinadas de 12.1 µm a 12.5 µm con unas desviaciones estándares grandes (Tabla 5.1), lo cual significa también que estas rocas se enfriaron lentamente a través de la zona del borrado térmico parcial (*Partial Annealing Zone*, de 110 °C a 60 °C para F-apatitos, Gleadow *et al*., 1986; Donelick *et al*., 2005). Además, los datos de la modelación térmica basada en el análisis completo de trazas de fisión (ver los detalles en la Fig. 6 de Abdullin *et al*., 2016a) señalan que en el área del Macizo de Chiapas y de la Sierra Monoclinal tuvo lugar un periodo de quiescencia tectónica durante el Eoceno inferior–Mioceno inferior (Figura 5.3).

Es importante señalar que tres rocas muestreadas (Ratschbacher *et al*., 2009; Witt *et al*., 2012; este estudio) a lo largo de la Zona de Cizalla de Tonalá (Figura 5.1) tienen unas edades de enfriamiento muy similares (~17–9 Ma; ver Tabla 5.1), a pesar de sus diferencias en la elevación (Figura 5.3). Esto podría indicar que el territorio del Macizo de Chiapas fue afectado por un levantamiento significativo durante el evento tectónico del Mioceno. Además, este evento también se detectó en la porción norte de la Sierra Monoclinal analizando unas areniscas de la Formación Todos Santos (ver la Figura 6 en Abdullin *et al*., 2016a). De acuerdo con Molina-Garza *et al*. (2015), este evento tectónico reciente podría relacionarse con el movimiento del Bloque Chortís.

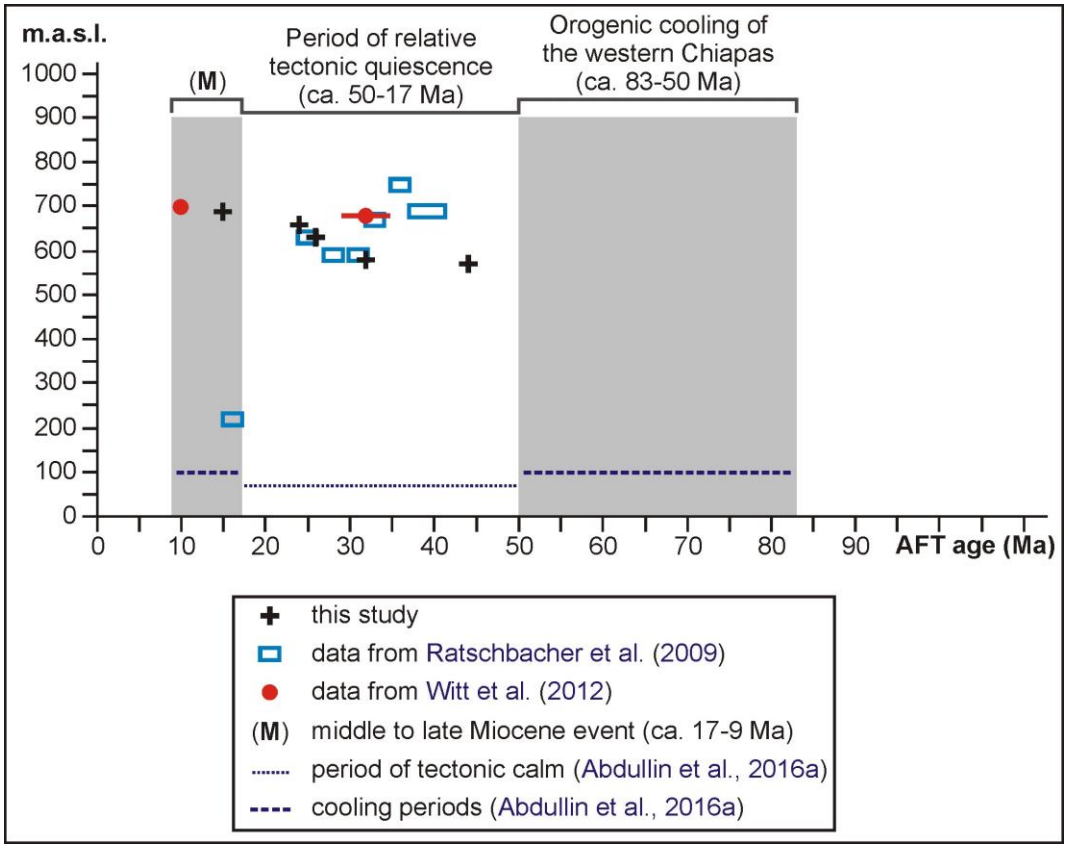

Figura 5.3. Edades de trazas de fisión contra las elevaciones de las muestras. Los periodos de algunos eventos termo-tectónicos también se muestran en el diagrama presente.

Dos muestras de la Formación San Ricardo (miembro arenoso del Berriasiano al Aptiano) también se analizaron mediante trazas de fisión en apatitos detríticos. Los resultados se grafican en la Figura 5.4. Todos los apatitos de estas dos muestras (SR-1 y SR-2) tienen unas edades de enfriamiento que son mayores a la edad estratigráfica del miembro arenoso (Figura 5.4). Esto evidentemente significa que estos apatitos no se resetearon para el sistema de trazas de fisión durante la diagénesis. Por lo tanto, las

edades obtenidas corresponden a las edades de enfriamiento de sus rocas fuente (ver detalles en Abdullin *et al*., 2016b que se encuentra en el capítulo 6). Las coordenadas y lugares del muestreo se pueden ver también en Abdullin *et al*. (2016b).

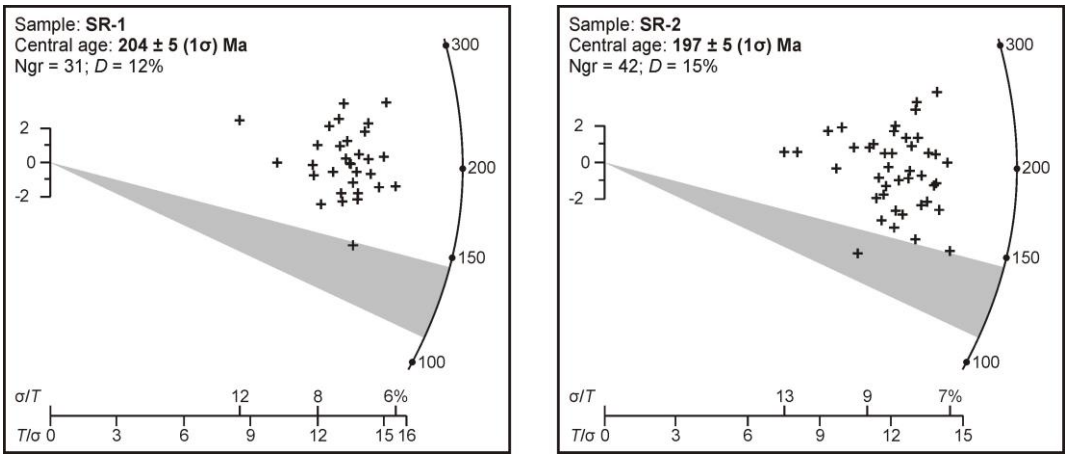

Figura 5.4. Diagramas radiales que muestran los resultados de dataciones de apatitos detríticos del miembro arenoso de la Formación San Ricardo. Ngr – número de cristales fechados, *D* – dispersión de edades (%). El campo gris es la edad de depósito del miembro arenoso (*i.e*., Berriasiano–Aptiano).

Con el objetivo de identificar los eventos tectónicos del Mioceno o los eventos más recientes, se fecharon cuatro areniscas micáceas de la Formación El Bosque (del Ypresiano–Luteciano). Las coordenadas y lugares de muestreo se pueden consultar en Abdullin *et al*. (2016b). Los apatitos detríticos analizados en la Formación El Bosque tampoco se resetearon completamente para el termocronómetro de trazas de fisión, ya que la mayoría de estos cristales tienen unas edades iguales o mayores de la

edad de depósito (Figura 5.5). Por lo tanto, estas edades obtenidas durante este estudio deben corresponder a las edades de enfriamiento de sus rocas fuente.

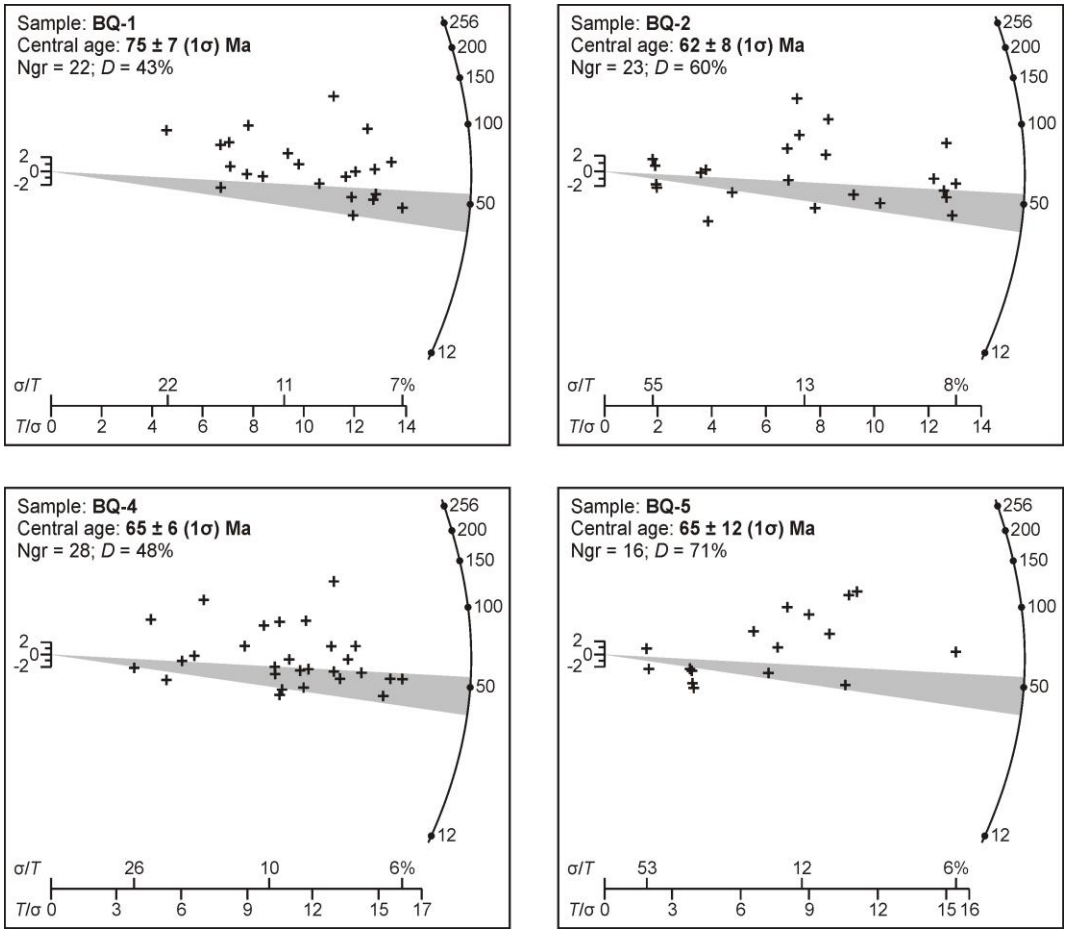

Figura 5.5. Diagramas radiales que muestran los resultados de dataciones de apatitos detríticos de la Formación El Bosque. Ngr – número de cristales fechados, *D* – dispersión de edades en %. El campo gris corresponde a la edad estratigráfica de la Formación El Bosque (*i.e.*, Ypresiano–Luteciano).

Es muy difícil identificar las áreas fuente para los sedimentos siliciclásticos de la Formación El Bosque únicamente basándose en las edades de apatitos, ya que la

mayoría de éstos tienen edades parecidas a las de los apatitos en la Formación Todos Santos (Figura 5.6). Esto aparentemente señala que los sedimentos de la Formación El Bosque proceden del Macizo de Chiapas y de la Sierra Monoclinal. Sin embargo, Witt *et al*. (2012), utilizando las edades U–Pb en zircones detríticos, demostraron claramente que la mayor porción de los sedimentos clásticos del Eoceno (incluyendo la Formación El Bosque) en la Sierra de Chiapas no proviene de estas área fuente. Los estudios de procedencia de sedimentos realizados recientemente indican que los sedimentos clásticos de la Formación El Bosque provienen principalmente del Centro de Guatemala (ver detalles en Abdullin *et al*., 2016b que se encuentra en el capítulo 6 de esta tesis). Este estudio de procedencia se basa en las composiciones geoquímicas de apatitos individuales (elementos trazas y REE) obtenidas en las muestras de varias unidades muestreadas. El método basado en la geoquímica de apatitos aparentemente demuestra como éste puede superar, en algunos casos, a los métodos geocronológicos tales como U–Pb en zircones o trazas de fisión y producir mejores resultados sobre la procedencia de sedimentos (ver el capítulo 6).

Las edades de trazas de fisión obtenidas en todos los apatitos detríticos en este estudio se resumen en la Figura 5.6. La información detallada sobre los resultados de trazas de fisión (*i.e*., número de trazas contadas, concentraciones del isótopo "padre", densidades de trazas de fisión espontanea, errores analíticos, *etc*.) así como sobre las composiciones geoquímicas (Sr, Y, Th, U y los REE) en todos los apatitos analizados se puede consultar en los apéndices de esta tesis (ver la parte final del documento).

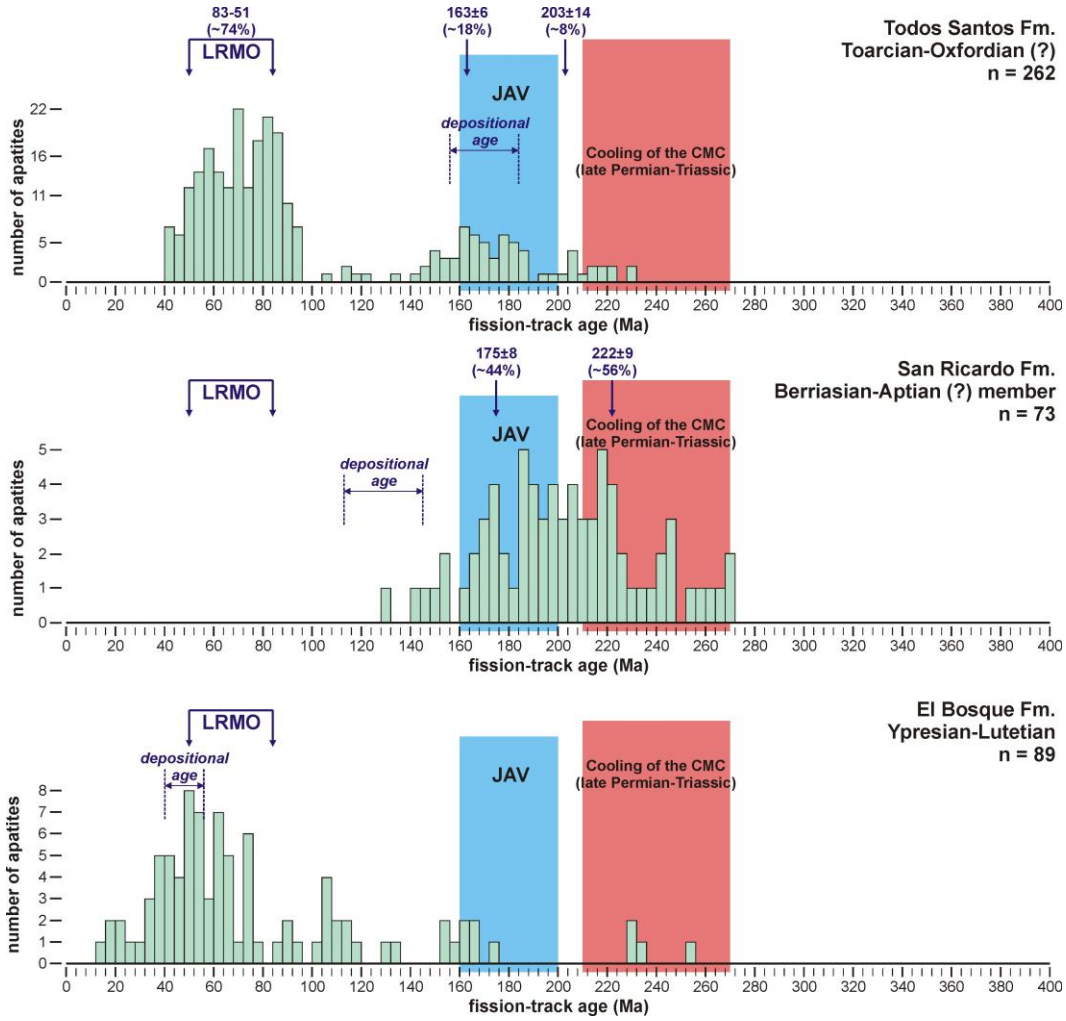

Figura 5.6. Edades por trazas de fisión de todos los apatitos detríticos analizados en tres diferentes Formaciones en el presente estudio. LRMO – intervalo de tiempo que corresponde a la Orogenia Laramide que afectó la Sierra de Chiapas (*i.e.*, de acuerdo con los resultados de Abdullin *et al.*, 2016a). JAV – volcanismo de arco del Jurásico inferior–medio que tuvo lugar en el área del Macizo de Chiapas (*e.g.*, Sánchez-Montes de Oca, 2006; Ham-Wong, 2007; Godinez-Urban *et al.*, 2012). En esta gráfica se presenta también el evento Permo–Triásico, el cual formó el Macizo de Chiapas (*e.g.*, Schaaf *et al.*, 2002; Weber *et al.*, 2005, 2007, 2008; Estrada-Carmona *et al.*, 2009); n – número de apatitos datados.

Los resultados termocronológicos del estudio presente y algunos datos geológicos ya reportados previamente permiten dividir la evolución termo-tectónica y magmática de la Sierra de Chiapas en las siguientes etapas principales:

(1) El evento tectono-magmático del Permo–Triásico que tuvo lugar en el Macizo de Chiapas. Este evento se relaciona a un metamorfismo con anatexis asociada así como con la intrusión de voluminosos plutones del Permo–Triásico (*e.g.*, Schaaf *et al*., 2002; Weber *et al*., 2005, 2008; Estrada-Carmona *et al*., 2009).

(2) Un volcanismo de arco del Jurásico inferior–medio, el cual afectó al territorio del Macizo de Chiapas. Este evento probablemente fue controlado por el volcanismo Nazas (según la hipótesis de Godinez-Urban *et al*., 2011).

(3) La Orogenia Laramide que afectó al área de Chiapas en el Cretácico superior–Eoceno inferior (~83–51 Ma; datos termocronológicos de este estudio), como se había sugerido previamente (*e.g.*, Carfantan, 1981; Moravec, 1983; Burkart *et al*., 1987; Meneses-Rocha, 2001; Sánchez-Montes de Oca, 2006).

(4) Un evento termo-tectónico del Mioceno medio–superior (evento Chiapaneco), el cual fue el más significativo en el desarrollo de las estructuras geológicas y de la topografía irregular en la Sierra de Chiapas (*e.g.*, Meneses-Rocha, 1985, 2001; Guzmán-Speziale, 2010; Witt *et al*., 2012; Molina-Garza *et al*., 2015; este estudio). Este evento reciente fue acompañado por un magmatismo a lo largo de la Zona de Cizalla de Tonalá y fue la causa de una erosión extensa en Chiapas y de un gran aporte de sedimentos hacía la Planicie de Tabasco.

(5) Un nuevo volcanismo del Plioceno a reciente en Chiapas (Mora *et al*., 2012).

6. PROCEDENCIA DE LOS SEDIMENTOS SILICICLÁSTICOS

Las concentraciones de elementos trazas (Sr, Y, Th, U; REE) que se midieron en los apatitos durante los análisis por trazas de fisión permiten identificar el área fuente para los sedimentos clásticos de las unidades estudiadas. Los resultados indican que los sedimentos del Jurásico–Cretácico inferior (las Formaciones Todos Santos y San Ricardo) proceden principalmente de las rocas del Macizo de Chiapas. Un cambio significativo en el área fuente se detectó entre las rocas sedimentarias del Mesozoico y las del Paleoceno–Eoceno. Los sedimentos del Eoceno (Formación El Bosque), que se estudiaron detalladamente, definitivamente no proceden del Macizo de Chiapas. Estos sedimentos provienen principalmente de las rocas fuente ubicada en el norte y centro de Guatemala.

Este estudio se detalla en el siguiente artículo:

Abdullin, F., Solé, J., Solari, L., Shchepetilnikova, V., Meneses-Rocha, J.J., Pavlinova, N., and Rodríguez-Trejo, A., (2016b).

Single-grain apatite geochemistry of Permian–Triassic granitoids and Mesozoic and Eocene sandstones from Chiapas, SE Mexico: implications for sediment provenance:

International Geology Review, doi:10.1080/00206814.2016.1150212

INTERNATIONAL GEOLOGY REVIEW, 2016
http://dx.doi.org/10.1080/00206814.2016.1150212

Taylor & Francis
Taylor & Francis Group

Single-grain apatite geochemistry of Permian–Triassic granitoids and Mesozoic and Eocene sandstones from Chiapas, SE Mexico: implications for sediment provenance

Fanis Abdullin[a], Jesús Solé[b], Luigi Solari[c], Valentina Shchepetilnikova[a], Javier J. Meneses-Rocha[d], Natalia Pavlinova[e] and Alejandro Rodríguez-Trejo[f]

[a]Posgrado en Ciencias de la Tierra, Instituto de Geología, Universidad Nacional Autónoma de México, México D.F., México; [b]Departamento de Geoquímica, Instituto de Geología, Universidad Nacional Autónoma de México, México D.F., México; [c]Centro de Geociencias, Campus Juriquilla, Universidad Nacional Autónoma de México, Querétaro, México; [d]Consulting Geologist, Villahermosa, Tabasco, México; [e]Department of Geology and Mineral Resources, Faculty of Engineering, Peoples' Friendship University of Russia (RUDN), Moscow, Russia; [f]Posgrado en Ciencias de la Tierra, Instituto de Geofísica, Universidad Nacional Autónoma de México, México D.F., México

AQ1

ABSTRACT

This article reports single-grain multi-elemental results (Sr, Y, Th, U, and rare earth elements) obtained in 966 apatites from 18 rocks (sandstones and granitoids) that were sampled from the Mesozoic (Todos Santos and San Ricardo Formations) and Eocene (the El Bosque Formation) successions as well as from the Permian–Triassic Chiapas Massif Complex (CMC), all of which are exposed within the Sierra de Chiapas (SCH), SE Mexico. The objectives of the present study are (1) to establish changes in provenance between the Mesozoic and Eocene sedimentary sequences using single-grain apatite geochemistry, and (2) to identify source areas for siliciclastic materials from the Todos Santos, San Ricardo, and the El Bosque Formations. The results of the present work strongly suggest that apatites from the Todos Santos and San Ricardo Formations were mainly derived from intermediate to felsic I-type granitoids as well as from arc-related volcanic rocks, indicating that the CMC basement was the most important source area for the Mesozoic sandstones in the SCH. An abrupt change in provenance from Mesozoic to Eocene units was identified based on single-grain apatite geochemistry. Detrital apatites of the Ypresian–Lutetian El Bosque Formation were derived from diverse source rocks such as mafic–ultramafic rocks, intermediate to felsic I-type plutons, strongly fractionated S-type granites and pegmatites, as well as from different metamorphic source lithologies (including high-pressure rocks) such as gneisses, migmatites, metapelites, and/or eclogites. It was proposed, therefore, that most Eocene sediments of the SCH were derived from the Guatemala Suture Complex, which involves all the rock types mentioned above. A minor portion of the El Bosque Formation sediments was derived from the CMC area and/or from recycled sandstones from the Mesozoic Todos Santos and San Ricardo Formations. Some advantages and disadvantages of provenance studies based on detrital apatite chemistry were also observed and briefly discussed.

ARTICLE HISTORY
Received 9 September 2015
Accepted 31 January 2016

KEYWORDS
single-grain apatite geochemistry; sedimentary provenance; Mesozoic; Eocene; Chiapas Massif Complex; Guatemala Suture Complex; southern Mexico; Chortís block

1. Introduction and objectives

Provenance studies of both ancient and recent siliciclastic sediments often aim to reveal the lithological composition and tectonic evolution of their source areas (e.g. Morton and Yaxley 2007; Godinez-Urban *et al.* 2011; Jafarzadeh *et al.* 2014). The mineralogical and geochemical characteristics of sediments are controlled by a complex interplay of several variables, including the composition of their source rocks, intensity of weathering, mode of transportation mechanism of clastic materials from source region to depocenter, as well as by post-depositional processes such as diagenesis and/or metamorphism. It is also very important to take into account that most clastic rocks and modern sediments frequently represent a mixture derived from various types of igneous, metamorphic, and older (i.e. recycled) sedimentary rocks. Therefore, the identification of provenance of siltstones and sandstones by means of conventional geochemical methods, like bulk composition of sample, is sometimes problematic (e.g. Morton 1991; Morton and Yaxley 2007; Jafarzadeh *et al.* 2014). In some cases, detrital mineral geochemistry (e.g. apatites, garnets, rutiles, pyroxenes, and zircons) provides much better constraints on source rocks, since particular mineral compositions can be specific to

CONTACT Fanis Abdullin fanisius@yandex.ru Posgrado en Ciencias de la Tierra, Instituto de Geología, Universidad Nacional Autónoma de México, México D.F., México

certain parageneses (e.g. Morton 1991; Belousova *et al*. 2002; Morton and Yaxley 2007; Jafarzadeh *et al*. 2014; Philander and Rozendaal 2015).

Laser ablation–inductively coupled plasma–mass spectrometry (LA-ICP-MS) allows an accurate determination of REE (rare earth elements: from La to Lu) and trace element (e.g. Mn, Y, Sr, U, and Th) contents of individual apatite crystals using a rapid (~60 s per crystal) single-spot micro-sampling (e.g. Belousova *et al*. 2002; Morton and Yaxley 2007; Chu *et al*. 2009; Cao *et al*. 2012; Gawęda *et al*. 2014). Detrital apatite geochemistry is a powerful tool for sedimentary provenance studies owing to the following reasons: (1) apatite is a common accessory mineral in virtually all igneous lithologies, and it is also a common component of many metamorphic and sedimentary rocks (e.g. Piccoli and Candela 2002; Spear and Pyle 2002); (2) because apatite can contain a large range of trace and minor elements substituting on both cation and anion sites, it may exert a dominant control on the geochemical behaviour of trace components like the REEs, Mn, Sr, Y, U, and Th in melts and magmatic fluids (Belousova *et al*. 2002; Webster and Piccoli 2015); (3) accordingly, the geochemical composition of this phosphate, which is a very sensitive petrogenetic indicator, can yield reliable information about its host rock (e.g. Sha and Chappell 1999; Belousova *et al*. 2002; Piccoli and Candela 2002; Morton and Yaxley 2007; Chu *et al*. 2009; Cao *et al*. 2012; Webster and Piccoli 2015); and (4) apatite is sufficiently stable during sediment transport and burial diagenesis while preserving its original geochemical composition (Dill 1994; Morton and Hallsworth 2007; Morton and Yaxley 2007; Jafarzadeh *et al*. 2014).

This article reports the first LA-ICP-MS-based single-grain geochemical data (Y, Sr, U, Th, and REE) of apatite populations from Mesozoic (Todos Santos and San Ricardo Formations) and Eocene (El Bosque Formation) sandstones as well as from Permo–Triassic plutons (Chiapas Massif Complex), which are exposed in the Sierra de Chiapas (SCH), SE Mexico (Figure 1a and b). Several previous studies performed on SCH have focused on the understanding of its tectonic evolution (e.g. Meneses-Rocha 2001; Weber *et al*. 2005; Witt *et al*. 2012; Abdullin *et al*. 2016) as well as on the characterization of its stratigraphic column (e.g. Quezada-Muñetón 1983, 1987; Mandujano Velásquez 1996; Rosales-Domínguez 1998; Sánchez *et al*. 2004; Weber *et al*. 2009). Numerous petrogenetic and geochronological studies were carried out along the Chiapas Massif Complex (CMC; e.g. Damon *et al*. 1981; Schaaf *et al*. 2002; Weber *et al*. 2005, 2007, 2008; Estrada-Carmona *et al*. 2012; Molina-Garza *et al*. 2015). However, detailed provenance studies of siliciclastic rocks (Godinez-Urban *et al*. 2011; Witt *et al*. 2012) and metasediments (Weber *et al*. 2009) in the SCH have received relatively less attention. It is well established that Mesozoic sediments of the SCH are mainly derived from the CMC basement (Meneses-Rocha 1985, 2001; Blair 1987; Sánchez-Montes de Oca 2006), which was verified using detrital zircon U–Pb results from the Todos Santos Formation sandstones (Godinez-Urban *et al*. 2011). Interesting zircon U–Pb data were obtained from Tertiary clastic sequences of the SCH (particularly, in the El Bosque Formation) by Witt *et al*. (2012), who first noted that most Cenozoic sediments of the SCH were not derived from the CMC source area. Sedimentary provenance studies of Cenozoic units of the SCH are of particular interest, siliciclastic sediments that may contain useful information about the Cenozoic geodynamic evolution of southern Mexico (i.e. the Maya block as part of the North American plate) and Central Guatemala (the Chortís block within the Caribbean plate).

The main objectives of this study are (1) the detection of changes in provenance between the Mesozoic and Eocene sedimentary successions using single-grain apatite chemistry; and (2) the identification of source regions for clastic materials from the Todos Santos, San Ricardo, and El Bosque Formations on the basis of reported data and the results obtained in the present work.

2. Plate tectonics and regional geology

2.1. Tectonic setting

The SCH forms part of the Maya block, which is within the North American plate (Figure 1a), and geodynamically represents a complex region controlled by the interaction of the North American, Caribbean, and Cocos plates (e.g. Ratschbacher *et al*. 2009; Guzmán-Speziale 2010; Witt *et al*. 2012; Molina-Garza *et al*. 2015). According to Meneses-Rocha (1985) and Sánchez-Montes de Oca (2006), the SCH can be divided into five (Figure 1b) tectonic subprovinces: (1) the CMC as the crystalline basement of the southern Maya block; (2) the Sierra Monocline (or the Sierra Homocline), which represents a large homocline parallel to the CMC subprovince, mostly composed of Mesozoic sedimentary lithologies; (3) the Chicomuselo Anticlinorium represented by folded Palaeozoic to Mesozoic metasedimentary and sedimentary rocks; (4) the Strike–Slip Faults Province (SSFP), which is mainly composed of anticlines and left-lateral strike–slip faults, which trend in a general NW–SE direction; and (5) the Reverse Faults Province (RFP), which is formed by series of reverse

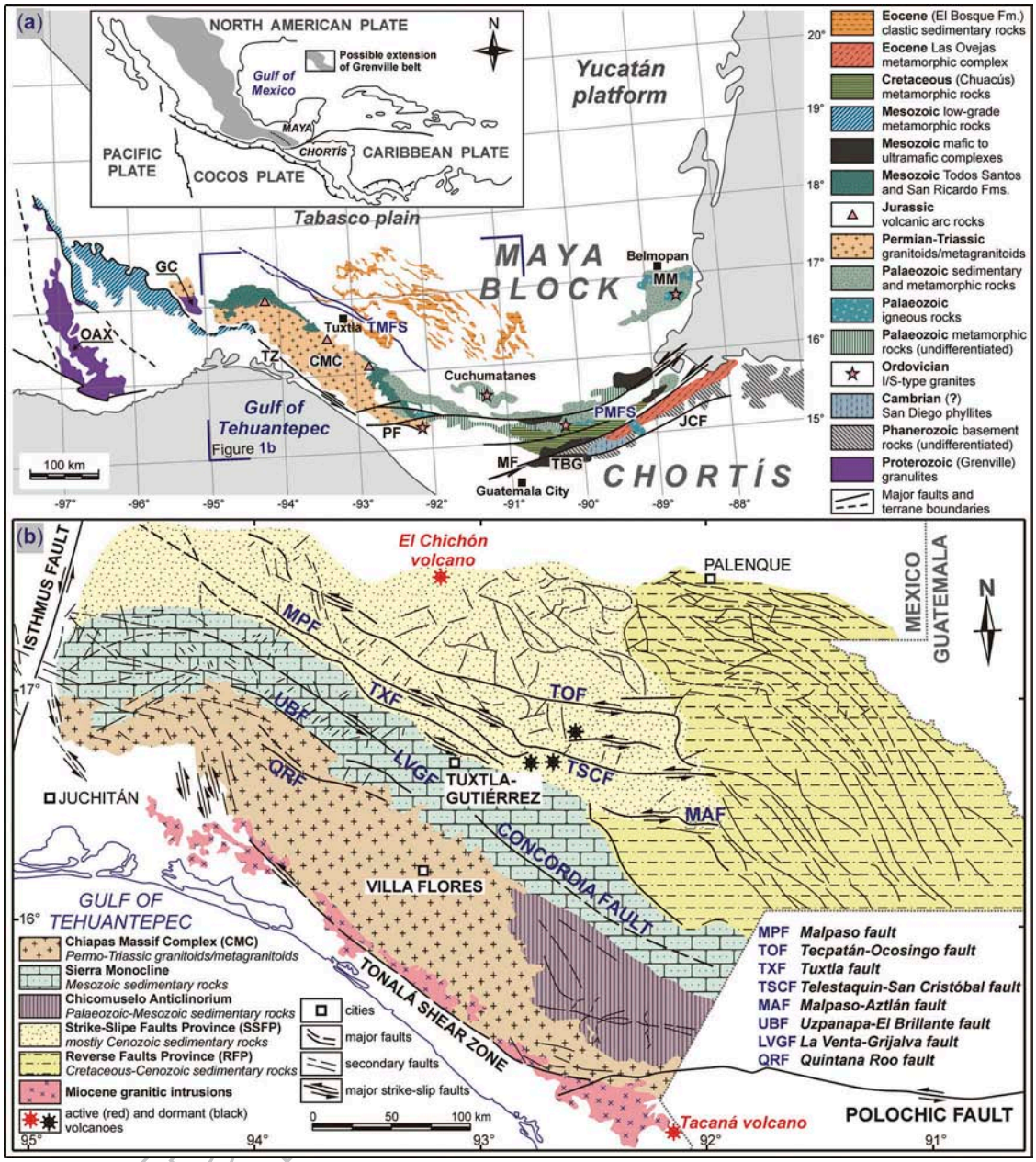

Figure 1. (a) Regional geological setting of southern Mexico and Central Guatemala (modified after Martínez-Amador *et al*. 2005; Weber *et al*. 2008; Godinez-Urban *et al*. 2011; Estrada-Carmona *et al*. 2012; Torres-de León *et al*. 2012; Solari *et al*. 2013). The inset shows the Sierra de Chiapas (SCH) and the Gulf of Tehuantepec. OAX, Oaxacan Complex; GC, Guichicovi Complex; CMC, Chiapas Massif Complex; MM, Maya Mountains; TZ, Tonalá shear zone; PF, Polochic fault; MF, Motagua fault; TBG, El Tambor group; JCF, Jocotán–Chamelecón fault; TMFS, Tuxtla–Malpaso Fault System; PMFS, Polochic–Motagua Fault System.

faults and long, narrow anticlines where the intervening synclines are mostly buried.

The SCH has experienced several magmatic and tectonic events (Meneses-Rocha 2001; Schaaf *et al*. 2002; Weber *et al*. 2005, 2007, 2008, 2015; Godinez-Urban *et al*. 2011; Witt *et al*. 2012; Molina-Garza *et al*. 2015; Abdullin *et al*. 2016). Despite this, the Miocene Chiapanecan orogeny and the Pliocene to present volcanism were the most significant for the development of geological structures (particularly in the SSFP and RFP) and of the steep present-day topography (from ~20 to ~4100 m.a.s.l.) along the SCH (Witt *et al*. 2012). Most major tectonic elements of the SCH, including the Tuxtla–Malpaso Fault System (TMFS) and the Polochic–Motagua Fault System (PMFS), are seismically active (Guzmán-Speziale 2010). Both the PMFS and the TMFS (Figure 1a) apparently correspond to the current overland boundaries between the North America and Caribbean plates (e.g. Guzmán-Speziale 2010; Witt *et al*. 2012).

2.2. Crystalline basement

The CMC is the root of an active continental margin formed during the Permian–Triassic and represents the crystalline basement of the southern Maya block (Figure 1a; e.g. Damon *et al*. 1981; Schaaf *et al*. 2002; Weber *et al*. 2005). This unit predominantly consists of calc-alkaline plutonic lithologies, varying in composition from gabbro to granite, most of which are deformed while some are metamorphosed (Schaaf *et al*. 2002; Weber *et al*. 2005; Estrada-Carmona *et al*. 2012). The CMC basement extends to the north into the Tabasco plain and probably into most parts of the Yucatán platform (e.g. Meneses-Rocha 2001; Sánchez-Montes de Oca 2006; Witt *et al*. 2012). The first reliable geochronological data for the CMC was reported by Damon *et al*. (1981), who built an Rb–Sr whole-rock isochron from ten rock samples giving an apparent age of 256 ± 10 Ma. Rb–Sr ages for mica–whole-rock pairs vary from 244 ± 12 to 214 ± 11 Ma (Schaaf *et al*. 2002), indicating rapid cooling of the CMC during the Triassic. Weber *et al*. (2005), (2008)) interpreted zircon U–Pb lower intercepts of 258 ± 2 Ma and 251 ± 2 Ma as either igneous crystallization or metamorphic ages, and they also identified sedimentary protoliths that can be correlated with the Palaeozoic Jocote, Custepec, and Sepultura units (prebatholitic). The CMC includes some Ordovician granitoids (e.g. Weber *et al*. 2008; Estrada-Carmona *et al*. 2012). A Grenville-aged component was also reported for the CMC by means of Sm–Nd model ages (0.9–1.2 Ga; Schaaf *et al*. 2002) and zircon U–Pb-derived upper intercept ages (1.0–1.2 Ga; Weber *et al*. 2005, 2008). Godinez-Urban *et al*. (2011) recognized an extensive pulse of early to Middle Jurassic volcanism in rocks that overlie the CMC area. During the middle to late Miocene, igneous activity took place in the CMC and generated ubiquitous granitic intrusions along the Tonalá shear zone (Figure 1b; e.g. Witt *et al*. 2012; Molina-Garza *et al*. 2015).

2.3. Sedimentary cover

The base of the SCH sedimentary cover is represented by Lower Jurassic volcanoclastic materials (La Silla Formation) deposited prior to opening of the Gulf of Mexico (pre-rift setting), which are exposed in the southern Sierra Monocline (Godinez-Urban *et al*. 2011). Continental red beds of the Todos Santos Formation and salt were deposited in the SCH during the Jurassic (Blair 1987; Meneses-Rocha 2001). The base of this Formation is composed of conglomerates, volcanoclastic deposits, and fine-grained lacustrine sediments, while its upper portion contains fluvial medium- to coarse-grained arkoses and conglomerates (e.g. Blair 1987; Godinez-Urban *et al*. 2011). The Todos Santos Formation unconformably overlays the CMC (Figures 2 and 3). Its thickness variation from 250 to 1350 m has been related to a graben-type geometry derived from the extensional processes associated with continental rifting at the beginning of the opening of the Gulf of Mexico (e.g. Meneses-Rocha 2001; Godinez-Urban *et al*. 2011; Witt *et al*. 2012). Some previous studies (e.g. Quezada-Muñetón 1983; Mandujano Velásquez 1996; Sánchez *et al*. 2004; Sánchez-Montes de Oca 2006; Godinez-Urban *et al*. 2011) suggest that this Formation was probably deposited during the Toarcian–Oxfordian (?). The San Ricardo Formation (Oxfordian–Aptian?), cropping out in the northern Sierra Monocline, conformably overlays the Todos Santos Formation (Figure 2). It includes three members which are, from bottom to top, the Oxfordian–Kimmeridgian carbonates, the Tithonian marls with shales, and the Berriasian to Aptian (?) fine-grained sandstones (Quezada-Muñetón 1983; Mandujano Velásquez 1996; Sánchez *et al*. 2004). This unit displays a variable total thickness from 500 to 1400 m and its lowermost part can be interpreted as a transgressive sequence above the Todos Santos Formation (Quezada-Muñetón 1983; Meneses-Rocha 1985, 2001; Sánchez-Montes de Oca 2006). Its stratigraphic analogue is the Jericó Formation cropping out along the southern Sierra Monocline, which is predominantly composed of continental clastic rocks such as medium- to coarse-grained sandstones with gravels and conglomerates (e.g. Quezada-Muñetón 1983; Sánchez-Montes de Oca 2006). The Albian to Santonian period (Figure 2) is represented by the Sierra Madre Formation (1000–2400 m thick), which is composed of limestones and dolomites deposited on a marine platform during a period of tectonic stability (e.g. Mandujano Velásquez 1996; Rosales-Domínguez 1998; Sánchez *et al*. 2004). The Campanian–Maastrichtian successions (the Ocozocoautla, Xochitlán, Méndez, and Angostura Formations; Figure 2) are mainly characterized by a mixture of high- to low-energy sediments and carbonates (Quezada-Muñetón 1987; Mandujano Velásquez 1996). For example, the 300- to 800-m-thick Ocozocoautla Formation, which was deposited in a shoreline environment, consists, from base to top, of gravel, coarse-grained to marly sandstones, alternate thin layers of shales and marls, and limestones (Rosales-Domínguez 1998). Menses-Rocha (1985, 2001) and Sánchez-Montes de Oca (2006) proposed, based on field observations, that clastic sediments of this unit were mostly derived from recycled sandstones from the Todos Santos Formation.

AQ3

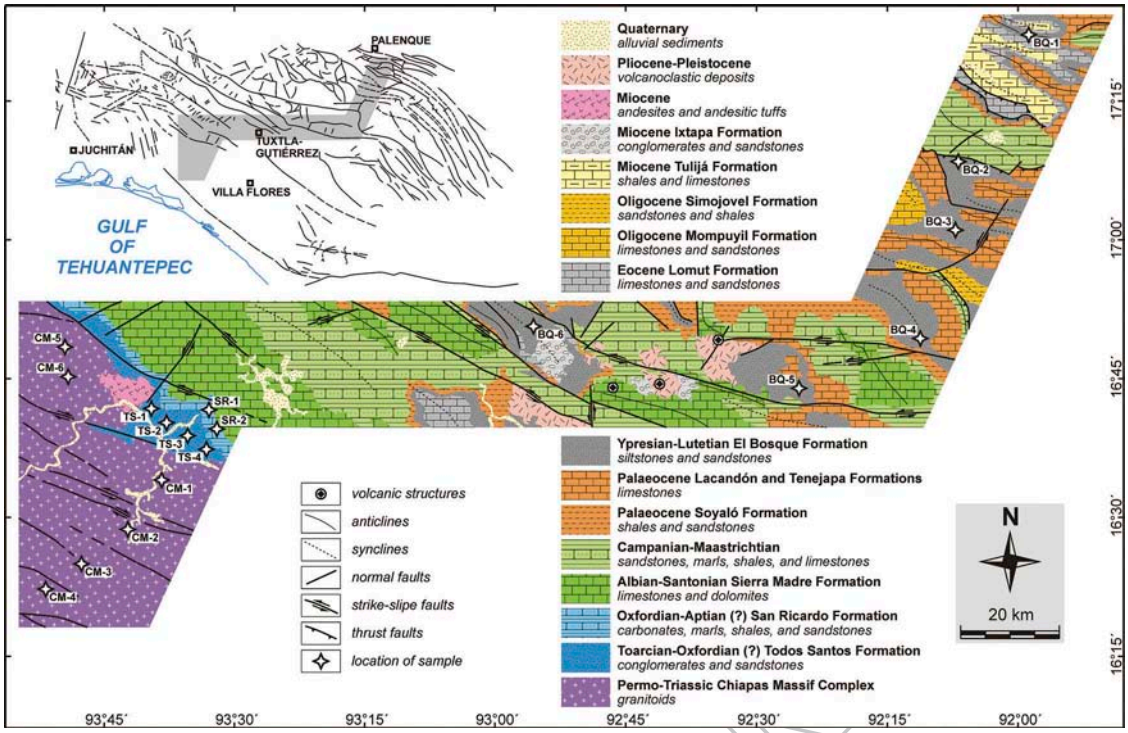

Figure 2. Geological map of the study area (modified after Meneses-Rocha 1985; Martínez-Amador *et al*. 2005; Sánchez-Montes de Oca 2006) showing the location of collected rocks: CM-(from 1 to 6), CMC granitoids; TS-(1 to 4), Todos Santos Formation sandstones; SR-(1 and 2), San Ricardo Formation sandstones from its Berriasian to Aptian (?) sandy member; BQ-(1 to 6), El Bosque Formation micaceous sandstones. Geographic coordinates (latitudes, longitudes, and altitudes) of the sampled rocks are detailed in Supplementary Table 2 (see //xxxxxx//).

The Cenozoic stratigraphy of the SCH (Figures 2 and 3) is predominantly siliciclastic (Quezada-Muñetón 1987; Sánchez *et al*. 2004; Sánchez-Montes de Oca 2006). The Palaeocene marks the final transition to regional terrigenous sedimentation with deposition of shallow water platform sediments, slope turbidites (e.g. Palaeocene–Eocene Lutitas Nanchital Formation, 300–1100 m thick), and deep basin deposits (Palaeocene Soyaló Formation, about 900 m thick) that mostly crop out along the SSFP (Meneses-Rocha 1985, 2001; Quezada-Muñetón 1987; Sánchez-Montes de Oca 2006). Eocene–Oligocene units (Figures 2 and 3) include continental clastic (e.g. early Eocene El Bosque Formation) and some shallow water deposits locally associated with carbonate platforms (Eocene Lomut and Oligocene Mompuyil Formations, 500–900 and 500–1400 m, respectively), all of which are exposed in both the SSFP and the RFP (Sánchez-Montes de Oca 2006; Witt *et al*. 2012). Several authors (e.g. Meneses-Rocha 1985, 2001; Quezada-Muñetón 1987; Perrilliat *et al*. 2006; Sánchez-Montes de Oca 2006) suggest that the El Bosque Formation was deposited during the Ypresian–Lutetian. This unit consists of mica-rich (mainly muscovite crystals; see Figure 4) reddish sandstones and siltstones, varying from 200 to 1000 (?) m in thickness (Quezada-Muñetón 1987; Perrilliat *et al*. 2006). It is very important to mention that in the northern SCH and in the Tabasco plain the El Bosque Formation is represented by transitional (platform–basin) sediments and deep-basin deposits, respectively (Meneses-Rocha 1985; Quezada-Muñetón 1987; Sánchez-Montes de Oca 2006). Oligocene–Miocene successions (the Simojovel, La Laja, Depósito, Encanto, Ixtapa, Filisola, and Concepción Formations) record a marked increase in terrigenous sedimentation (Figures 2 and 3). The uppermost portion of the stratigraphic column mostly includes Quaternary sediments and volcanoclastic deposits derived from the Pliocene to present volcanic activity (Figures 2 and 3).

3. Samples and methods

A total of 18 rocks were sampled (Figures 2 and 3): six micaceous sandstones from the Ypresian to Lutetian El Bosque Formation (BQ-1, BQ-2, BQ-3, BQ-4, BQ-5, and BQ-6); four coarse-grained arkoses from the Toarcian–Oxfordian (?) Todos Santos Formation (samples TS-1, TS-2, TS-3, and TS-4); two fine-grained sandstones from the Berriasian to Aptian (?) sandy member of the San Ricardo

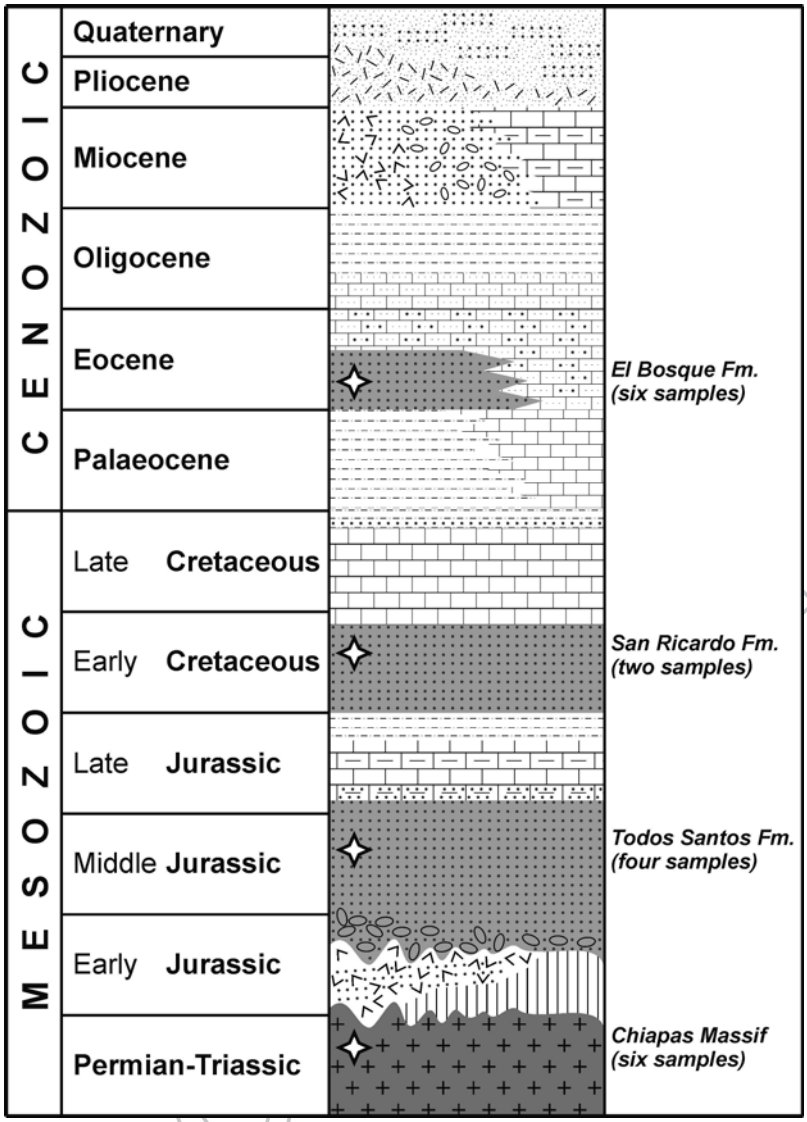

Figure 3. Simplified stratigraphic column of the SCH (modified from Meneses-Rocha 1985) displaying the sampled units.

Formation (SR-1 and SR-2); and six Permian–Triassic granitoids from the northern CMC (CM-1, CM-2, CM-3, CM-4, CM-5, and CM-6). The CMC igneous samples were collected with the purpose of comparing the chemical compositions of their apatites with those of detrital apatite groups, to test whether or not this crystalline basement was a dominant source region for both the Mesozoic and the Eocene siliciclastic sequences in the SCH. Geographic coordinates (latitude, longitude, and altitude in m.a.s.l.) of samples are given in Supplementary Table 2 (see http://dx.doi.org/10.1080/00206814.2016.1150212 for supplementary tables).

Heavy minerals were concentrated from the three narrow grain-size fractions of 60–125, 125–180, and 180–250 μm using conventional techniques. Approximately 300 apatites, extracted from each rock sample under a binocular microscope, were mounted with epoxy resin in a 2.5-cm diameter plastic ring, and then were polished. Most apatite crystals from the CMC rocks and Todos Santos sandstones are euhedral and subhedral (Figure 5a and b), whereas the San Ricardo Formation sediments contain euhedral and sub-rounded apatites (Figure 5c). In contrast, the El Bosque Formation samples mostly include rounded to sub-rounded detrital apatite grains (Figure 5d). Sample preparation was carried out at the Laboratorio de Separación de Minerales, Instituto de Geología (UNAM, Mexico City). The measurements of trace elements (Sr, Y, Th, and U) and REE (from La to Lu, except Pm and Tm) were performed on randomly selected apatites at the Laboratorio de Estudios Isotópicos, Centro de Geociencias (Campus Juriquilla, UNAM) using a Resonetics™ M050 193 nm ArF excimer laser ablation

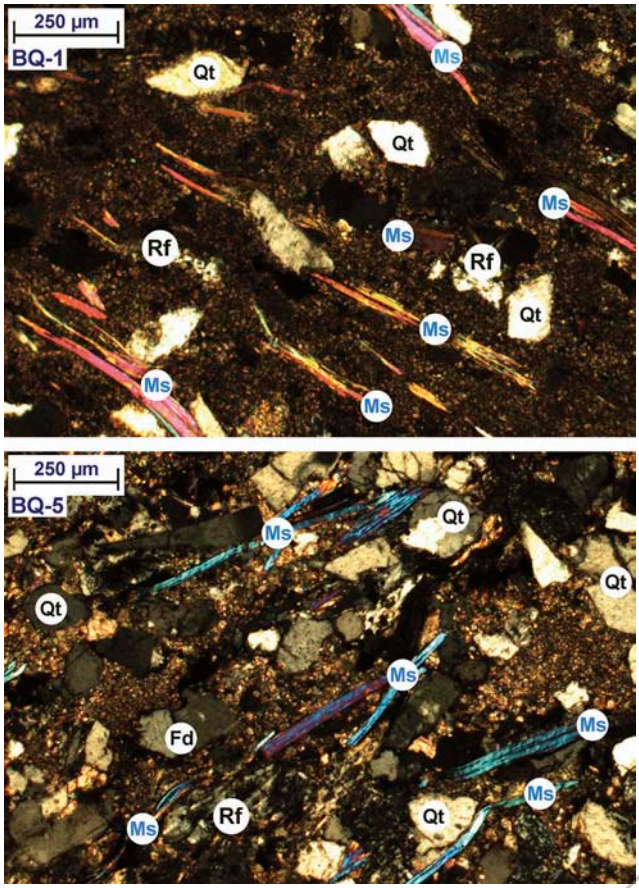

COLOUR ONLINE BLACK & WHITE IN PRINT

Figure 4. Transmitted-light (with crossed nicols) photomicrographs of thin-sections from the El Bosque Formation sandstone samples BQ-1 and BQ-5. Qt, quartz; Fd, feldspars; Rf, rock fragments; Ms, muscovites. Note the abundance of detrital muscovite flakes.

system coupled to a Thermo™ iCAP-Qc quadrupole ICP-MS. Laser ablation was conducted in a He atmosphere (700 ml min^{-1}) using a laser pulse energy of 6 J cm^{-2}, spot diameter of 50 µm, and 5 Hz laser repetition rate. The ablated material was carried to the plasma in a mixed gas stream of He and Ar. For each analysis, the gas blank was acquired over 20 s, laser triggered, and the signal acquired for a further 35 s. In this study, the double standard method was used, which comprises two spot analyses in a NIST-612 glass, one spot in standard Durango F-apatite, and ten spot analyses in unknown apatite grains. The results obtained using the NIST-612 were normalized using ^{43}Ca as an internal standard and taking an average CaO content for all analysed apatites of 55 wt.% (e.g. Abdullin *et al.* 2016). The total uncertainties for the measured elements are about 5–6%, including the analytical ± 2σ errors (~1.5–2.5%) and an error of ~3.6% generated by the typical CaO variation in apatites of different origin (55 ± 2 wt.%; e.g. Belousova *et al.* 2002; Chu *et al.* 2009; Lesnov 2012).

4. Results and interpretation

A total of 966 single-grain multi-elemental compositions were obtained in apatites from the 18 rocks sampled. The minimum, average, and maximum contents of measured elements (Sr, Y, Th, U, and ΣREE; in ppm) as well as the minimum, average, and maximum values of Th/U, La/Nd, (La + Ce + Pr)/ΣREE (%), $(Eu/Eu^*)_{cn}$ (i.e. the Europium anomaly), $(Ce/Yb)_{cn}$ (cn denotes chondrite-normalized), and LREE/HREE for apatite populations from twelve sandstones and six granitoids are listed in Supplementary Table 1 (see //xxxxxx//). LREE and HREE correspond to the light REE (from La to Sm) and heavy REE (Eu to Lu), respectively. The full data set of apatite compositions is detailed in Supplementary Table 2 (see //xxxxxx//).

4.1. Apatite REE patterns

The shape of normalized REE patterns of apatite is mostly controlled by the host rock composition, particularly by the degree of magmatic differentiation (Belousova *et al.* 2002). In the case of plutonic lithologies, the slope of apatite REE patterns, which can be expressed using $(Ce/Yb)_{cn}$, decreases from ultramafic–mafic (including mantle-derived rocks and carbonatites) through intermediate to strongly fractionated (granites and felsic pegmatites) rocks (Belousova *et al.* 2002; Chu *et al.* 2009; Lesnov 2012). Most apatites from migmatites and metamorphic rocks display nearly flat to LREE-depleted (i.e. with $Ce_{cn}/Yb_{cn} \leq 1$) REE profiles (e.g. Fleischer and Altschuler 1986; Bea *et al.* 1994; Tribuzio *et al.* 1996; Ayres and Harris 1997; Bea and Montero 1999; Sassi *et al.* 2000; Spear and Pyle 2002; Morton and Yaxley 2007; Nutman 2007; Guo *et al.* 2013; Hammerli *et al.* 2014), though LREE-enriched REE spectra were also observed in apatites from some augen gneisses and granulites (e.g. Bingen *et al.* 1996; Bea and Montero 1999).

The behaviour of REE as well as other trace elements in apatite seems to be interpreted as a result of its competition with other REE-carrier minerals. For example, a strong depletion in the LREE in apatites from highly fractionated igneous and metamorphic rocks is related to the crystallization of monazite and/or allanite, which preferentially incorporate the LREE (Budzinski and Tischendorf 1989; Bea *et al.* 1994; Bea and Montero 1999; Spear and Pyle 2002; Spandler *et al.* 2003), eventually forming roughly flat to LREE-depleted REE spectra in apatites (Tribuzio *et al.* 1996; Sha and Chappell 1999; Spear and Pyle 2002; Nutman 2007; Chu *et al.* 2009; Gawęda *et al.* 2014; Hammerli *et al.* 2014). The crystallization of xenotime, garnet, and zircon, which are

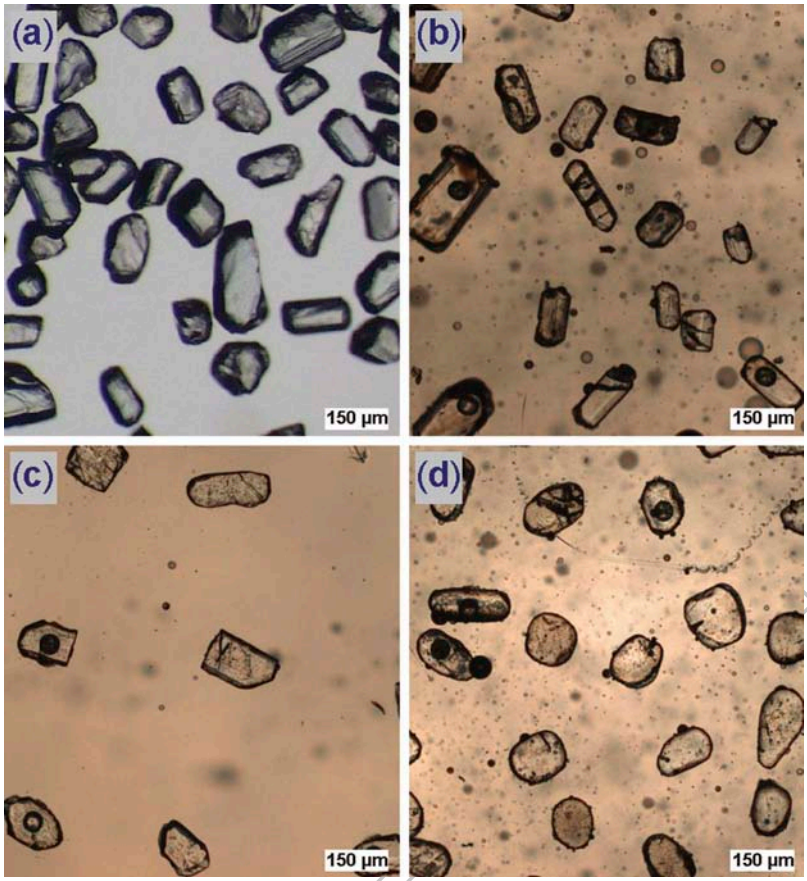

Figure 5. Transmitted-light photomicrographs showing examples of apatite grains analysed from the CMC plutons (a) as well as from the Todos Santos (b), San Ricardo (c), and El Bosque Formation (d) sandstone samples.

common HREE-enriched phases (Bea *et al*. 1994; Hermann 2002; Spear and Pyle 2002; Lesnov 2012; Solari *et al*. 2014; Shchepetilnikova *et al*. 2015), may cause a significant depletion of the HREE in apatites (Bingen *et al*. 1996; Bea and Montero 1999; Belousova *et al*. 2001; Hermann 2002; Chu *et al*. 2009; Cao *et al*. 2012; Gawęda *et al*. 2014). According to several authors (e.g. Gromet and Silver 1983; Budzinski and Tischendorf 1989; Bea *et al*. 1994; Bea and Montero 1999; Belousova *et al*. 2002; Morton and Yaxley 2007; Lesnov 2012), negative Eu anomalies in apatite REE patterns are most probably caused by feldspar crystallization (both K-feldspars and plagioclases), which removes the major amounts of the Eu^{2+} from the melt. Most apatites display negative Eu anomalies (with $Eu_{cn}/Eu^*_{cn} < 1$), which are highly expressed in those from strongly evolved granites and granite pegmatites (i.e. $Eu_{cn}/Eu^*_{cn} < 0.3$; Sha and Chappell 1999; Belousova *et al*. 2002). The redox state of silicic host magma can also control the Eu behaviour in apatite (Belousova *et al*. 2001, 2002; Lesnov 2012) as well as the behaviour of other trace elements such as Mn (e.g. Miles *et al*. 2014), and apatites from moderately and highly oxidized granitoids may show null to strong positive Eu anomalies (with $Eu_{cn}/Eu^*_{cn} \geq 1$; e.g. see Cao *et al*. 2012).

Chondrite-normalized REE plots were made for apatites from six plutonic samples of the CMC (Figure 6) using the CI composition proposed by McDonough and Sun (1995). In the case of sandstone samples from the Todos Santos (Figure 7a), San Ricardo (Figure 7b), and the El Bosque Formations (Figure 8), the CI-normalized REE patterns were constructed for the first ten detrital apatites per each rock sample listed in Supplementary Table 2 (see //xxxxxx//).

4.1.1. CMC granitoids

Apatites from sample CM-1 display slight LREE enrichments relative to the HREE with $(Ce/Yb)_{cn}$ and LREE/HREE values of 5.9–9.4 and of 6.6–9.1, respectively (Supplementary Table 1; Figure 6). These grains are characterized by $(Eu/Eu^*)_{cn}$ of 0.62–0.74 (Supplementary Table 1). The granitoid sample CM-3 includes apatites with $(Ce/Yb)_{cn}$ and LREE/HREE of 11.8–14.9 and of 10.2–11.8, respectively; whereas those from sample CM-5 yield $(Ce/Yb)_{cn}$ and LREE/HREE that respectively vary in the ranges of 16.8–32.3 and 11.2–16.2 (Supplementary

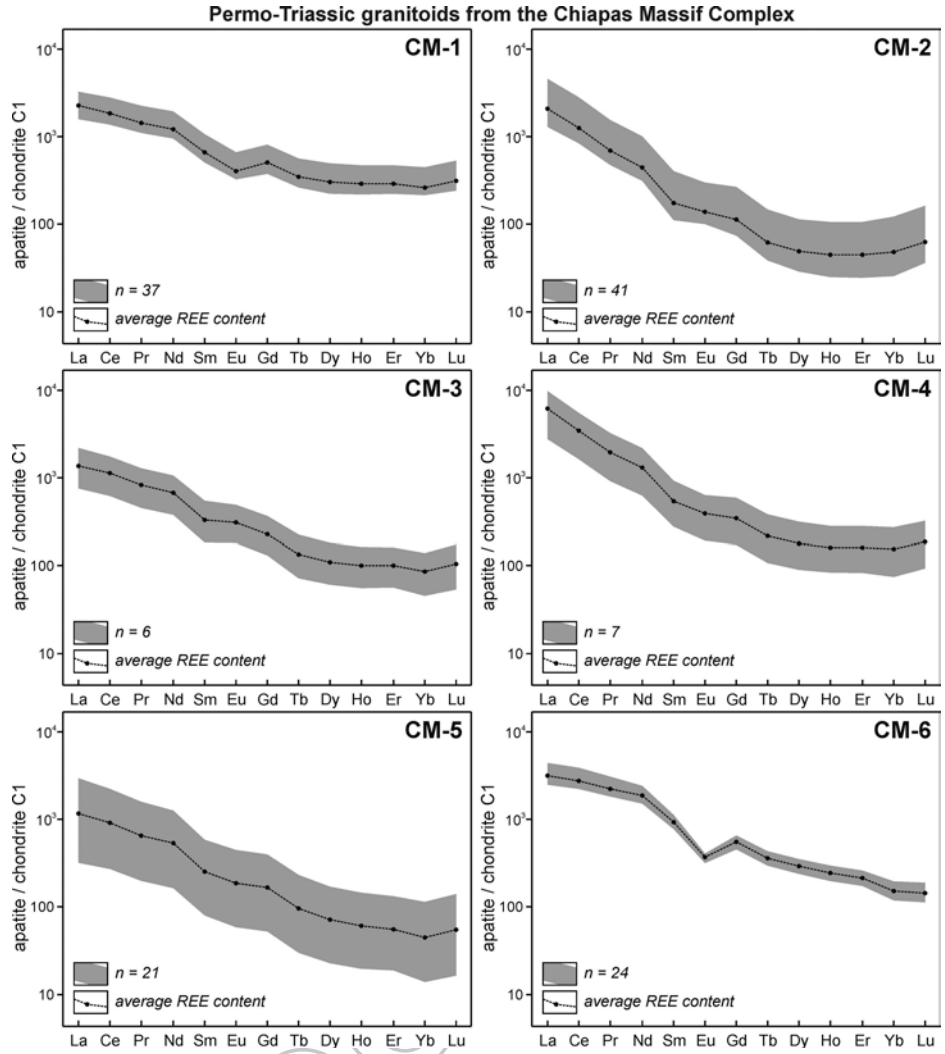

Figure 6. Chondrite (CI)-normalized rare earth element (REE) patterns of apatites from CMC rock samples (CM-1, –2, –3, –4, –5, and –6). CI-normalizing values are from McDonough and Sun (1995). The grey field in each plot represents the CI-normalized REE profiles from all apatites analysed per sample (e.g. n = 21 from CM-5). Mean CI-normalized REE concentrations of apatite populations are shown as black dashed lines. Single-grain apatite REE data are given in Supplementary Table 2 (see //xxxxxx//).

Table 1). Both the samples CM-3 and CM-5 contain apatites with no apparent Eu anomalies (see Figure 6). The sample CM-6 includes apatite grains with $(Ce/Yb)_{cn}$ and LREE/HREE from 16.4 to 21.5 and from 11.4 to 15, respectively (Supplementary Table 1). These crystals, like those from sample CM-1, show moderate negative Eu anomalies (Figure 6); but yield lower $(Eu/Eu^*)_{cn}$, between 0.44 and 0.53 (Supplementary Table 1). Apatite crystals from samples CM-3, CM-5, and CM-6 display REE signatures typical for apatites from intermediate to felsic I-type granitoids (Gromet and Silver 1983; Sha and Chappell 1999; Belousova *et al*. 2001, 2002; Chu *et al*. 2009; Cao *et al*. 2012; Lesnov 2012; Gawęda *et al*. 2014). Apatites from samples CM-2 and CM-4 are chemically very similar and, compared to the remaining four CMC samples analysed, show steeper normalized REE plots (Figure 6) with $(Ce/Yb)_{cn}$ and LREE/HREE (i.e. taking from both these samples) from 17.2 to 40.2 and from 18.8 to 32.5, respectively (Supplementary Table 1). These grains show a marked LREE enrichment relative to the HREE with insignificant Eu anomalies (Figure 6). This type of the normalized REE plot (i.e. apparently U-shaped patterns with depleted HREE) was observed in some apatites associated with intermediate–felsic plutons (e.g. Chu *et al*. 2009). Overall, the CMC igneous samples CM-2, CM-3, CM-4, CM-5, and CM-6 can be interpreted as intermediate to felsic granitoids, whereas sample CM-1 is apparently more evolved as suggested by its apatites with flatter REE patterns and with negative Eu anomalies (Figure 6).

4.1.2. Mesozoic sandstones

The Todos Santos Formation mostly includes apatites that show LREE enrichments with extremely dispersed

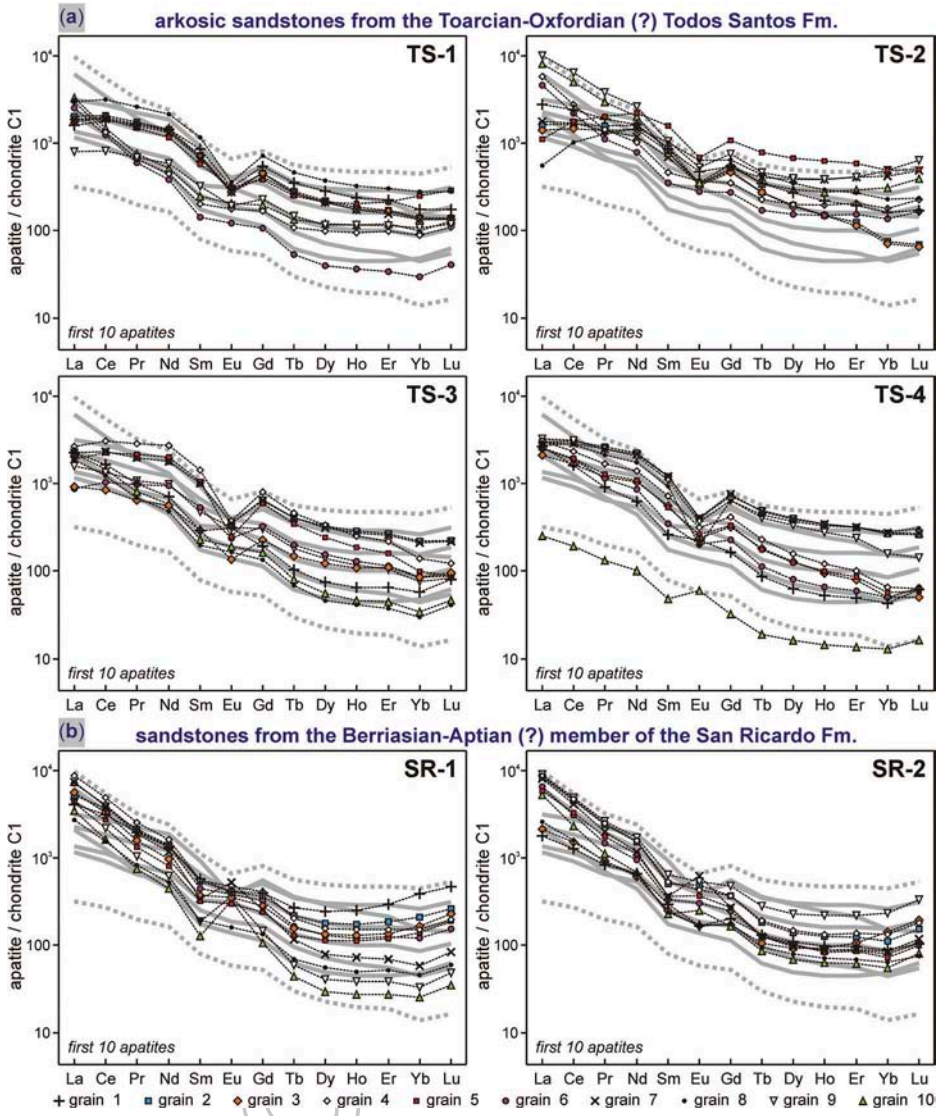

Figure 7. (a) CI-normalized rare earth element (REE) patterns for the first ten detrital apatite grains (shown by black dashed lines) from the Todos Santos Formation sandstones (TS-1, −2, −3, and −4). CI-normalizing values are taken from McDonough and Sun (1995). (b) CI-normalized REE profiles for the first ten apatites from the San Ricardo Formation sandstones (SR-1 and SR-2). The grey thick solid lines in each plot correspond to the mean CI-normalized REE patterns from the CMC apatite groups (see also in Figure 6). The grey dotted lines represent the maximum and minimum normalized REE contents from all the CMC apatite crystals analysed (i.e. from n = 136). The full data of apatite compositions is detailed in Supplementary Table 2 (see //xxxxxx//).

515 $(Ce/Yb)_{cn}$ and LREE/HREE ratios, which vary from 2.8 to 61.2 (mean = 19.3) and from 3.3 to 42.4 (mean = 14.3), respectively (Supplementary Table 1; Figure 7a). These crystals also display a broad variation of the Eu anomaly, yielding $(Eu/Eu^*)_{cn}$ that range between 0.2 and 1.77 520 with an average of 0.67 (Supplementary Table 1). Detrital apatites from the San Ricardo Formation sandstones are characterized by moderate to marked LREE enrichments with LREE/HREE from 4.6 to 40.1, with a mean ratio of 20.8 (Supplementary Table 1). These 525 grains, compared with those of the Todos Santos and CMC samples, show steeper normalized REE plots (Figure 7a and b) and yield higher $(Ce/Yb)_{cn}$, from 4.2 to 66.5, with a mean of 23.6 (Supplementary Table 1). The San Ricardo Formation sandstones include apatites with higher $(Eu/Eu^*)_{cn}$ ratios, between 0.28 and 2.79, 530 with an average of 0.98 (Supplementary Table 1). Some of these crystals (e.g. SR-1: grains 9 and 10; SR-2: grain 7) display positive Eu anomalies (Figure 7b). Most apatites from both these Mesozoic Formations, like those of the CMC-derived igneous samples (see 535 Figures 6, 7a and b), display REE characteristics typical for apatite crystals from intermediate to felsic I-type granitoids (e.g. Sha and Chappell 1999; Belousova *et al*. 2001; Chu *et al*. 2009; Cao *et al*. 2012; Gawęda *et al*. 2014). A marked depletion in the LREE was also 540

observed in some grains from the Todos Santos Formation sandstones (e.g. TS-2: grains 5 and 8; Figure 7a). This type of depletion in the LREE, pronounced from La to Nd, is common in apatite crystals from highly fractionated granites, and this is most probably caused by the crystallization of monazite that favours the LREE (Bea and Montero 1999; Spear and Pyle 2002; Chu *et al*. 2009; Lesnov 2012; Gawęda *et al*. 2014).

There are no strong differences in the normalized REE diagrams of apatites between the Mesozoic sedimentary and CMC basement rocks (Figures 6, 7a and b). However, several apatites from the San Ricardo Formation are strongly enriched in the LREE compared to the HREE (e.g. TS-2: grains 2, 4–7, and 10 in Figure 7b; see also Supplementary Table 1 to compare the ratios of Ce_{cn}/Yb_{cn} and LREE/HREE), which can be observed for those from mafic–intermediate and intermediate–felsic volcanic rocks (Chu *et al*. 2009; Tang *et al*. 2012; Jafarzadeh *et al*. 2014).

4.1.3. Eocene sandstones

Detrital apatites from the El Bosque Formation sandstones show normalized REE patterns that are significantly different compared with those in apatites from the Mesozoic sandstones and CMC granitoids (Figure 8). Most apatites are characterized by slight relative LREE depletions or relative HREE enrichments with $(Ce/Yb)_{cn}$ and LREE/HREE of 0.03–46.3 (mean = 4.6) and 0.1–24.3 (mean = 3.8), respectively (Supplementary Table 1).

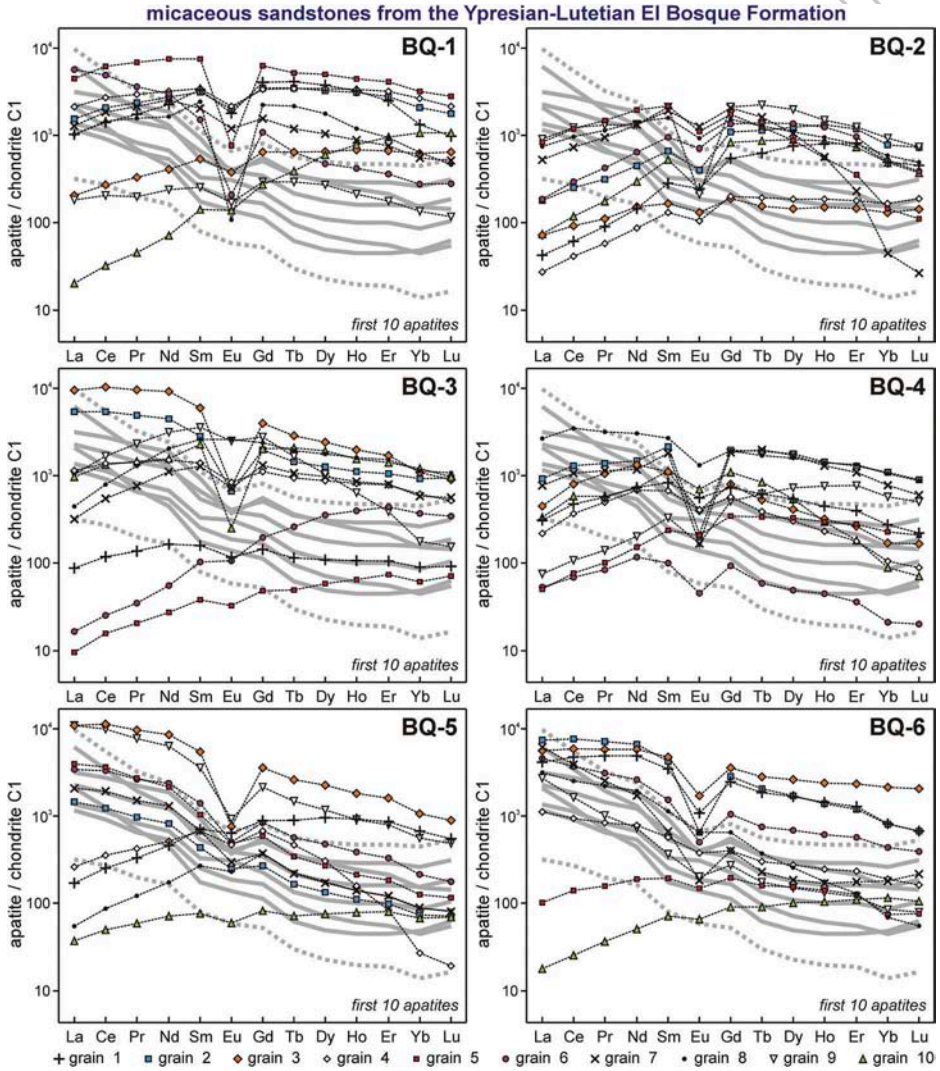

Figure 8. Cl-normalized REE patterns for the first ten detrital apatite grains (shown as black dashed lines) from the El Bosque Formation sandstone samples (BQ-1, –2, –3, –4, –5, and –6). Cl-normalizing values are from McDonough and Sun (1995). The grey thick solid lines in each plot correspond to the average Cl-normalized REE contents from the CMC apatite samples (see also in Figures 6, 7a and b), whereas the grey dotted lines represent the maximum and minimum normalized REE concentrations from all the CMC crystals analysed. Single-grain apatite REE compositions are listed in Supplementary Table 2 (see //xxxxxx//).

These samples, compared to those from the CMC and Mesozoic sequences, include apatites with relatively lower $(Eu/Eu^*)_{cn}$, ranging from 0.05 to 1.33 with a mean of 0.58 (Supplementary Table 1). There are some apatite grains with flat REE patterns and strongest negative Eu anomalies (e.g. BQ-1: grain 8; BQ-2: grain 9; BQ-3: grain 10; BQ-4: grains 2 and 7; Figure 8) that may have been derived from highly evolved S-type granites (e.g. Sha and Chappell 1999; Chu *et al*. 2009) or from granitic pegmatites (Belousova *et al*. 2002; Lesnov 2012). Most detrital apatite grains from the El Bosque Formation sandstones display nearly flat REE patterns with slight negative Eu anomalies (Figure 8), which correspond to apatites from migmatites (e.g. Bea *et al*. 1994; Nutman 2007) and/or from other metamorphic rocks like metapelites and high-pressure rocks (Tribuzio *et al*. 1996; Ayres and Harris 1997; Bea and Montero 1999; Spear and Pyle 2002; Spandler *et al*. 2003; Nutman 2007; Zhang *et al*. 2008; Guo *et al*. 2013; Hammerli *et al*. 2014). Such flat normalized REE patterns in apatites from metamorphic rocks are the result of the REE redistribution among newly formed and recrystallized minerals like lawsonite, garnet, monazite, zircon, apatite, and allanite, most likely due to the geochemical re-equilibration under metamorphic (i.e. temperature and pressure) conditions (e.g. Tribuzio *et al*. 1996; Spear and Pyle 2002; Spandler *et al*. 2003; Nutman 2007; Hammerli *et al*. 2014).

Some apatites (BQ-2: grain 7; BQ-3: grain 9; BQ-4: grain 10; BQ-5: grain 4; Figure 8) were very likely derived from eclogites, because of their convex-upward REE plots with strongly depleted HREE, which were sequestered by garnet and zircon (e.g. Hermann 2002; Zhang *et al*. 2008). Unlike the CMC granitoids and Mesozoic sandstones, the El Bosque Formation sediments include many apatites rich in REE (e.g. BQ-3: grains 2 and 3; BQ-5: grains 3 and 9; BQ-6: grains 1–3; Figure 8). There are also several crystals with strongly depleted LREE relative to the HREE (BQ-1: grain 10; BQ-2: grain 1; BQ-3: grains 5 and 6; BQ-4: grain 9; BQ-6: grain 10; Figure 8), which is not typical for igneous apatites, except for some apatites from strongly evolved granites with abundant LREE-enriched minerals like allanite and monazite (Chu *et al*. 2009). This type of REE plot can mostly be observed in apatites from low/medium-temperature–high-pressure rocks (Hammerli *et al*. 2014) such as mafic greenschists–blueschists and metasediments (e.g. Spandler *et al*. 2003; Morton and Yaxley 2007). There are a few detrital apatites that display REE spectra closely similar to those from the CMC and Mesozoic apatite crystals (Figures 6, 7a and b), which were mainly identified in samples BQ-5 (grains 2, 5–7) and BQ-6 (grains 6, 7, and 9; Figure 8).

REE concentrations of detrital apatites indicate that the El Bosque Formation sediments were derived from different types of source rocks such as intermediate to felsic I-type plutons, S-type granites and/or granite pegmatites, as well as from medium–high-grade metamorphic source lithologies like gneisses/migmatites, metasediments, and high-pressure mafic rocks.

4.2. Discrimination diagrams

4.2.1. La/Nd versus (La + Ce + Pr)/ΣREE (%)

Fleischer and Altschuler (1986) first observed that the gradient shown by the LREE is an important discriminator of apatites from acidic, intermediate–mafic, and alkaline igneous rocks, and proposed the diagram of La/Nd vs. (La + Ce + Pr)/ΣREE (%). All the apatite compositions, according to their stratigraphic units, were plotted on the La/Nd vs. (La–Pr)/ΣREE graph (Figure 9). The CMC igneous samples contain apatites with La/Nd and (La + Ce + Pr)/ΣREE from 0.8 to 3.1 (mean = 1.5) and from 62% to 85% (mean = 72%; Supplementary Table 1), respectively. As shown in Figure 9 and Supplementary Table 1, detrital apatites from the Todos Santos Formation sandstones yielded more scattered ratios of La/Nd and (La–Pr)/ΣREE, from 0.2 to 5.4 (mean = 1.4) and from 42% to 89% (mean = 69%), respectively. These grains display averages of La/Nd and (La–Pr)/ΣREE closely similar to those from the CMC crystals (Supplementary Table 1). The San Ricardo Formation includes apatites with higher La/Nd (0.5–4.9; mean = 2.1) and (La–Pr)/ΣREE (52–89%; mean = 79; see in Supplementary Table 1). The method of Fleischer and Altschuler (1986) only apparently indicates that most Mesozoic detrital grains were derived from the CMC plutons. Our data suggest that this discrimination plot yields questionable results. For instance, apatites of the CMC igneous samples (i.e. calc-alkaline intermediate–felsic granitoids), as well as detrital apatites from both the Todos Santos and the San Ricardo Formation samples, are identified as apatites derived from intermediate–mafic and alkaline igneous rocks (Figure 9). However, the normalized REE plots in apatites (Figure 7a and b) indicated that these Mesozoic sediments are mainly derived from intermediate to felsic plutons of the CMC. Moreover, whole-rock compositions reported by some authors (e.g. Schaaf *et al*. 2002; Weber *et al*. 2005; Estrada-Carmona *et al*. 2012) clearly show that the CMC basement is mostly composed of intermediate to felsic granitoids with calc-alkaline rather than alkaline affinities.

Apatite grains of the El Bosque Formation siliciclastic sediments are noticeably different from those of the Mesozoic and CMC rock samples (Figure 9). These

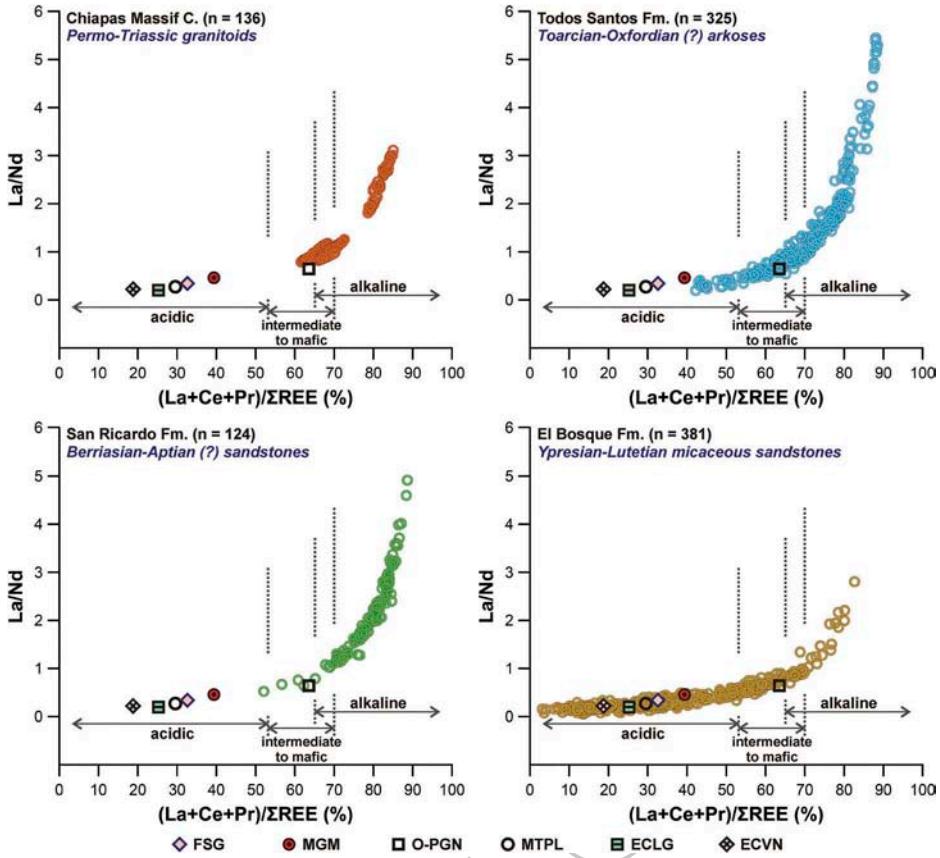

Figure 9. Apatite compositions from all the studied rock samples plotted on the La/Nd *versus* (La + Ce + Pr)/ΣREE (%) classification diagram of Fleischer and Altschuler (1986). *n* is the number of all apatites analysed per each lithostratigraphic unit (e.g. *n* = 381 from six El Bosque Formation sandstones). Average values of (La–Pr)/ΣREE and La/Nd for apatites from some rock types are also plotted using previously reported data. FSG: S-type granites with SiO_2 greater than 70 wt.% (n_{ap} = 74; Sha and Chappell 1999; Chu *et al.* 2009). MGM: felsic migmatites (n_{ap} = 9; Bea *et al.* 1994; Nutman 2007). O-PGN: granulite-facies orthogneisses and paragneisses (n_{ap} = 37; Bingen *et al.* 1996; Bea and Montero 1999; Nutman 2007). MTPL: medium–high-grade metasediments (n_{ap} = 33; Ayres and Harris 1997; Bea and Montero 1999; Nutman 2007). ECLG: eclogites (n_{ap} = 18; Sassi *et al.* 2000; Hermann 2002; Spandler *et al.* 2003; Guo *et al.* 2013). ECVN: high-pressure metamorphic veins (n_{ap} = 3; Zhang *et al.* 2008). n_{ap} is the number of chemical analyses from published data performed by solution-ICP-MS as well as by LA-ICP-MS.

apatites are characterized by low La/Nd (0.05–2.8; mean = 0.4) as well as by depleted (La–Pr)/ΣREE (3–83%; mean = 37%; Supplementary Table 1), which mostly fall in the field of acidic lithologies such as strongly fractionated granites, granitic pegmatites, and gneisses/migmatites (Figure 9). It is important to note, however, that apatites from metapelites and/or high-pressure mafic rocks are also located within the field of felsic rocks (some examples were plotted on Figure 9), because of their nearly flat to LREE-depleted REE profiles (e.g. Tribuzio *et al.* 1996; Ayres and Harris 1997; Sassi *et al.* 2000; Spandler *et al.* 2003; Nutman 2007; Zhang *et al.* 2008; Hammerli *et al.* 2014). Therefore, the El Bosque Formation siliciclastic materials were derived from various types of igneous and/or metamorphic source rocks. A minor part of the El Bosque Formation apatites, like those from the Mesozoic sandstones, was probably derived from intermediate to felsic calc-alkaline granitoids (i.e. from the CMC), as suggested by the La/Nd vs. (La–Pr)/ΣREE method (Figure 9). The geochemical results of this study, like some reported data set (e.g. apatites from eclogites; Tribuzio *et al.* 1996; Sassi *et al.* 2000; Hermann 2002; Spandler *et al.* 2003; Guo *et al.* 2013), suggest that the La/Nd vs. (La–Pr)/ΣREE diagram cannot be used to determine the type of source rock. Nonetheless, this method may be used to check the differences in apatite composition between distinct stratigraphic units, which is especially useful for siliciclastic samples like sandstones (Morton and Yaxley 2007; this study).

4.2.2 *U (ppm)* versus *Th (ppm)*

The U (ppm) vs. Th (ppm) plot of Dill (1994) can also be applied in provenance analyses (e.g. Morton and Yaxley 2007; Jafarzadeh *et al.* 2014), and this may be partially explained by the different behaviour of the two

elements during magmatic and metamorphic processes. Generally, the Th contents are lower (Th < U) in apatites derived from highly fractionated igneous rocks and metamorphic rocks (especially from metapelites), possibly due to the crystallization of monazite that preferentially concentrates Th (e.g. Belousova *et al*. 2001, 2002; Morton and Yaxley 2007; Nutman 2007; Cao *et al*. 2012).

Virtually all the apatites from the Todos Santos and San Ricardo Formations, like those of the CMC plutons, fall along the field of Th > U and display Th/U ratios with averages greater than 2.3 (Figure 10; Supplementary Table 1), suggesting that these grains were mainly derived from intermediate to felsic igneous sources (Dill 1994; Morton and Yaxley 2007; Jafarzadeh *et al*. 2014). There are no differences in Th/U between the Mesozoic detrital and CMC igneous apatites, though these from the San Ricardo Formation samples yielded higher concentrations of U and Th (Supplementary Table 1).

Unlike the Mesozoic and CMC rocks, most apatite grains from the El Bosque Formation sandstones are located within the area of Th < U (Figure 10) showing highly dispersed Th/U values (0.01–13) with a mean of 1.7 (Supplementary Table 1). According to some published data (Ayres and Harris 1997; Sha and Chappell 1999; Morton and Yaxley 2007; Nutman 2007), such low Th/U in these grains strongly indicate that the El Bosque sediments were partly derived from evolved granites, felsic pegmatites, migmatites, and metasediments (see details in Figure 10). There are also several apatite grains that are strongly depleted in both these elements (Figure 10), which can be observed for those from high-pressure rocks like metapelites, metamorphic veins, blueschists, or eclogites (Spandler *et al*. 2003; Zhang *et al*. 2008; Guo *et al*. 2013). Finally, the U vs. Th diagram suggests that the Ypresian–Lutetian siliciclastic sediments of the El Bosque Formation were derived from

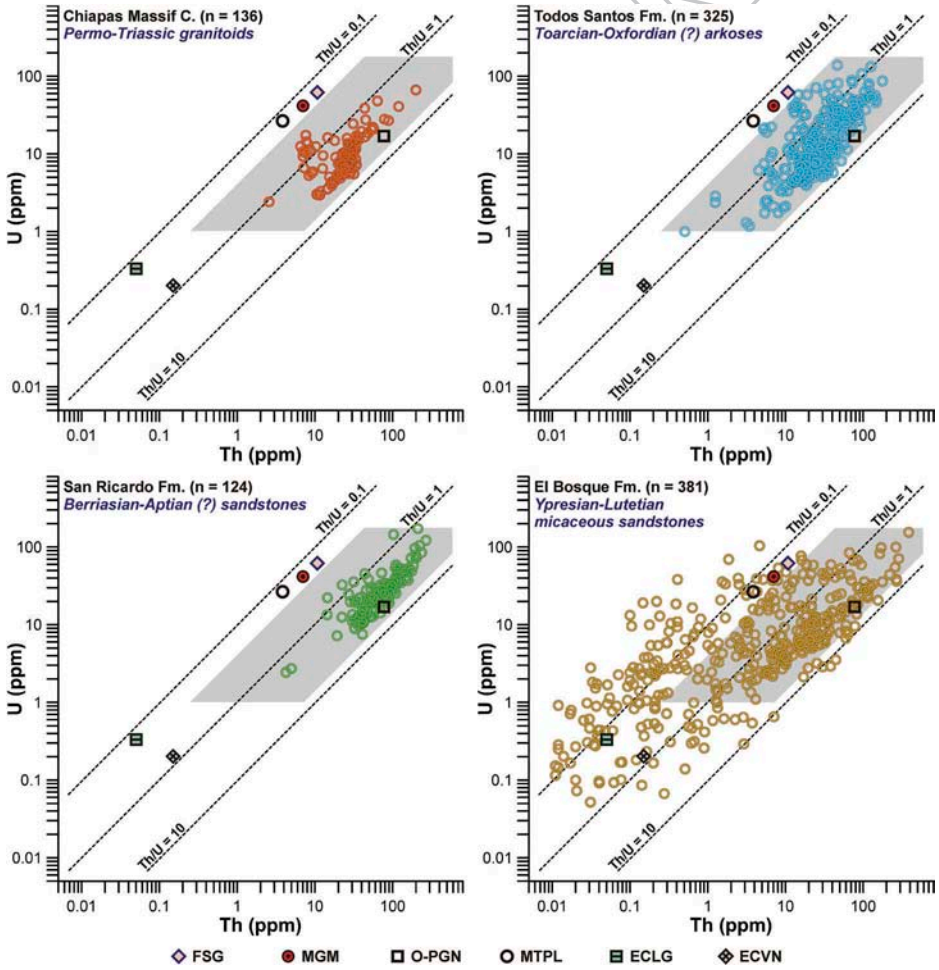

Figure 10. Apatite compositions from all the studied rocks plotted on the U (ppm) *versus* Th (ppm) binary plot after Dill (1994). n is the number of all analysed apatites per each sampled unit (e.g. *n* = 124 from two San Ricardo Formation sandstones). The grey field in each graph nearly corresponds to U and Th variations in apatites from the CMC plutons and Mesozoic sandstones. The meanings of FSG, MGM, O-PGN, MTPL, ECLG, and ECVN are detailed in the description for Figure 9.

a large range of igneous and metamorphic source lithologies.

4.2.3. Sr (ppm) versus Y (ppm)

Based on experimental geochemical analyses of apatite crystals from a range of intrusive rock types, Belousova *et al*. (2002) proposed some petrogenetic diagrams such as Sr (ppm) vs. Y (ppm) and $(Ce/Yb)_{cn}$ vs. ΣREE (wt.%) which have potential applications in provenance studies (Morton and Yaxley 2007; Jafarzadeh *et al*. 2014). In this study, a field apparently belonging to mafic–intermediate to intermediate–felsic volcanic lithologies (including arc-derived rocks) was added into both these discriminators using some reported data set (Chu *et al*. 2009; Tang *et al*. 2012; Jafarzadeh *et al*. 2014). It seems very likely that apatites from intermediate–felsic volcanic and plutonic products of a same magmatic system should contain closely similar amounts of Sr and Y (e.g. Piccoli and Candela 2002; Chu *et al*. 2009). Nonetheless, higher concentrations of Sr (i.e. more than 1000–1500 ppm) were obtained in some apatites derived from mafic–intermediate and intermediate volcanic rocks (e.g. Tang *et al*. 2012; Jafarzadeh *et al*. 2014). Therefore, some systematic comparative studies are required on this topic.

As expected, apatites from the CMC samples fall in the field of granitoids in the Sr vs. Y plot (Figure 11) and yield Sr and Y that vary in the ranges of 155–598 (mean = 347) and 34–823 ppm (mean = 266), respectively (Supplementary Table 1). Almost all apatites from the Mesozoic sandstones are also located within the area of granitoids (Figure 11). The San Ricardo Formation apatites yield Sr and Y concentrations closely similar to those in the CMC crystals, from 122 to 464 (mean = 324) and from 48 to 937 ppm (mean = 281), respectively (Supplementary Table 1). Detrital apatites from the Todos Santos Formation samples are characterized by more scattered Sr and Y (Supplementary

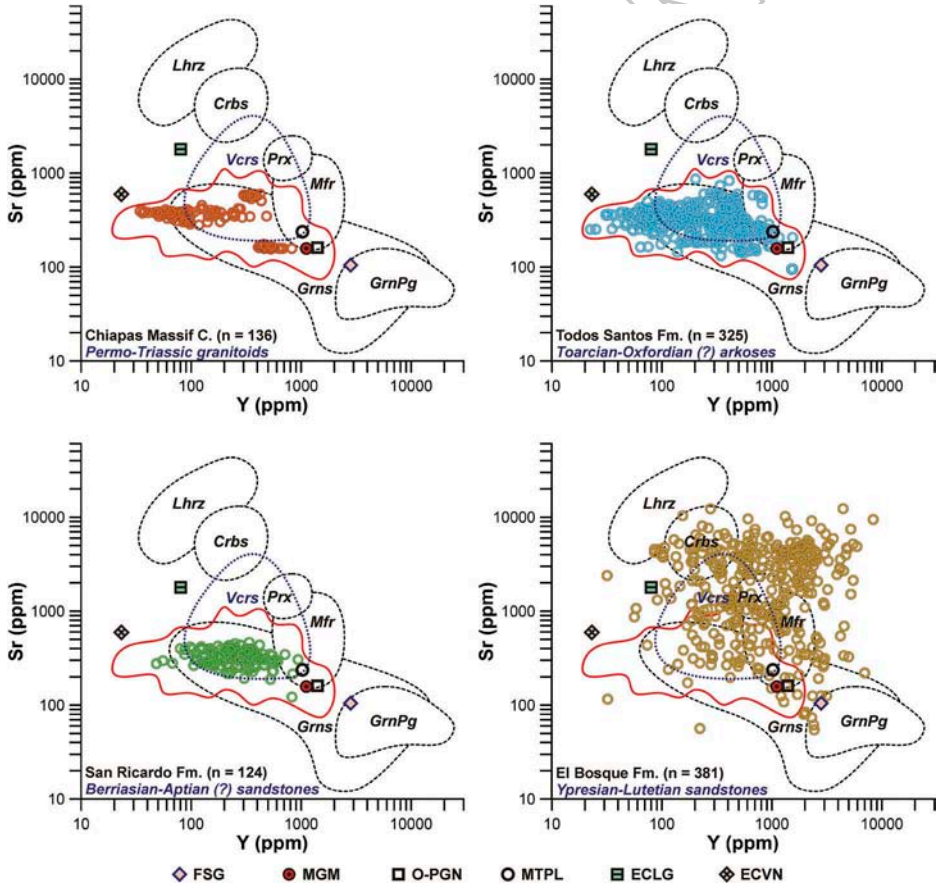

Figure 11. The Sr (ppm) *versus* Y (ppm) genetic diagram (modified from Belousova *et al*. 2002) showing apatite compositions from all the rocks studied. n is the number of all analysed apatites per each unit (e.g. n = 325 from four Todos Santos rock samples). Rock types: *Lhrz*, lherzolites; *Crbs*, carbonatites; *Prx*, pyroxenites; *Mfr*, mafic rocks; *Grns*, granitoids; *GrnPg*, granitic pegmatites. A field apparently belonging to volcanic rocks (*Vcrs*, mafic–intermediate and intermediate–felsic; except strongly fractionated rhyolites) was added using some reported data set (from Chu *et al*. 2009; Tang *et al*. 2012; Jafarzadeh *et al*. 2014). The field outlined by red solid lines in each plot roughly corresponds to Sr and Y variations in apatites of the CMC and Mesozoic samples. The meanings of FSG, MGM, O-PGN, MTPL, ECLG, and ECVN are given in Figure 9.

Table 1), which range between 95 and 865 (mean = 331) and between 22 and 1548 ppm (mean = 319), respectively.

It appears that the Sr concentration decreases and Y increases in apatite during magmatic fractionation (Belousova *et al*. 2002; Chu *et al*. 2009; Cao *et al*. 2012; Jafarzadeh *et al*. 2014). Apatite crystals from the Mesozoic sandstones and CMC plutons show no significant positive or negative correlation between Sr and Y (Figure 11). This can imply that these crystals are from intermediate to felsic igneous rocks. However, sample CM-1 is probably more evolved than the remaining five granitoids of the CMC, as shown by its apatites with relatively depleted Sr (mean = 164) and enriched Y (mean = 509 ppm; see Supplementary Table 1); this is also supported by the normalized apatite REE patterns (Figure 6). The Sr vs. Y method suggests that a few detrital apatites of the Todos Santos Formation sandstones are from mafic source rocks (Figure 11). In general, apatites of both the Todos Santos and the San Ricardo Formations, like those from the CMC rocks, fall in the same compositional area (Figure 11). It is very possible that both these Mesozoic units include some detrital apatites derived from intermediate to felsic volcanic arc rocks (according to data of Chu *et al*. 2009), apatites from which yield Sr and Y contents that are roughly similar to those in apatites from their plutonic analogues (see details in Figure 11).

Detrital apatites of the El Bosque Formation sandstones are significantly different from those of the Mesozoic and CMC samples. These apatite grains show extremely variable Sr and Y that are in the ranges of 54–12,320 (mean = 2520) and 32–8344 ppm (mean = 1260), respectively (Supplementary Table 1); thus reflecting a strong heterogeneity in their source region. Many of the El Bosque Formation apatites fall outside the genetic fields corresponding to different igneous rocks (Figure 11), which could suggest that these are of metamorphic origin. Most apatites fall near and within the areas of lherzolites, carbonatites, pyroxenites, as well as of volcanic and mafic rocks (Figure 11). Higher Sr contents are very common in apatites from mafic–ultramafic and carbonatitic rocks (Belousova *et al*. 2002; Chakhmouradian *et al*. 2002; Tang *et al*. 2012; Jafarzadeh *et al*. 2014). The incorporation of additional Sr into apatite may also be related to the breakdown of other Ca-minerals like plagioclase, lawsonite, and titanite during high-pressure metamorphism (Spandler *et al*. 2003; Krenn and Finger 2004; Zhang *et al*. 2008; Guo *et al*. 2013), all of which contain appreciable levels of Sr. There are also some apatites significantly enriched in both Sr (more than 2000 ppm) and Y (more than 2500–3000 ppm; Figure 11), which is not common for igneous apatites (e.g. Belousova *et al*. 2002; Lesnov 2012). These apatite grains were probably crystallized in strongly fractionated felsic protoliths such as granites and pegmatites that typically include Y-rich apatites (Sha and Chappell 1999; Belousova *et al*. 2002; Chu *et al*. 2009; Cao *et al*. 2012), which were then also enriched in Sr due to high-pressure metamorphism as explained above. Some grains are located around the points of S-type granites, metapelites, gneisses, and migmatites (see in Figure 11). The Sr vs. Y plot shows that the El Bosque Formation sediments were derived from different source rocks such as mafic to ultramafic (including mantle-derived) rocks and various metamorphic lithologies, as well as from I-type granitoids (or from their volcanic analogues), S-type granites and/or felsic pegmatites.

4.2.4. $(Ce/Yb)_{cn}$ versus ΣREE (wt.%)

In the $(Ce/Yb)_{cn}$ vs. ΣREE (wt.%) plot of Belousova *et al*. (2002), apatites from the CMC and Mesozoic siliciclastic samples (the Todos Santos and San Ricardo Formations) mainly fall within the field of granitoids (Figure 12). No strong difference in apatite compositions between the Todos Santos and San Ricardo sandstones and the CMC plutons is observed by means of the $(Ce/Yb)_{cn}$ vs. ΣREE diagram. Nevertheless, the San Ricardo Formation samples, compared to those from the CMC and Todos Santos Formation, include a larger population of apatite crystals with higher $(Ce/Yb)_{cn}$ ratios and relatively enriched ΣREE (Supplementary Table 1; Figure 12). This can imply that many apatites of the San Ricardo Formation samples were also derived from intermediate (e.g. andesites) to felsic volcanic source rocks, as shown in Figure 12 (according to data set from Chu *et al*. 2009; Tang *et al*. 2012; and Jafarzadeh *et al*. 2014) and also suggested by a variety of methods tested above.

In contrast, the El Bosque Formation apatite grains yield lower $(Ce/Yb)_{cn}$ (Supplementary Table 1) and mostly fall in the fields of granitoids and granitic pegmatites (Figure 12). Some of these apatites show geochemical signatures identical to those in apatites from the Mesozoic and CMC rock samples (Figure 12). It is logical that apatites from migmatites and medium- to high-grade metamorphic rocks (including metasediments and high-pressure ultramafic/mafic rocks) have also to lie in the compositional areas belonging to granitoids and/or felsic pegmatites of the $(Ce/Yb)_{cn}$ vs. ΣREE plot (see details in Figure 12), due to their very low $(Ce/Yb)_{cn}$ (e.g. Bea *et al*. 1994; Tribuzio *et al*. 1996; Ayres and Harris 1997; Bea and Montero 1999; Sassi *et al*. 2000; Spear and Pyle 2002; Spandler *et al*. 2003; Morton and Yaxley 2007; Nutman 2007; Zhang *et al*. 2008; Guo *et al*. 2013; Hammerli *et al*. 2014). It is

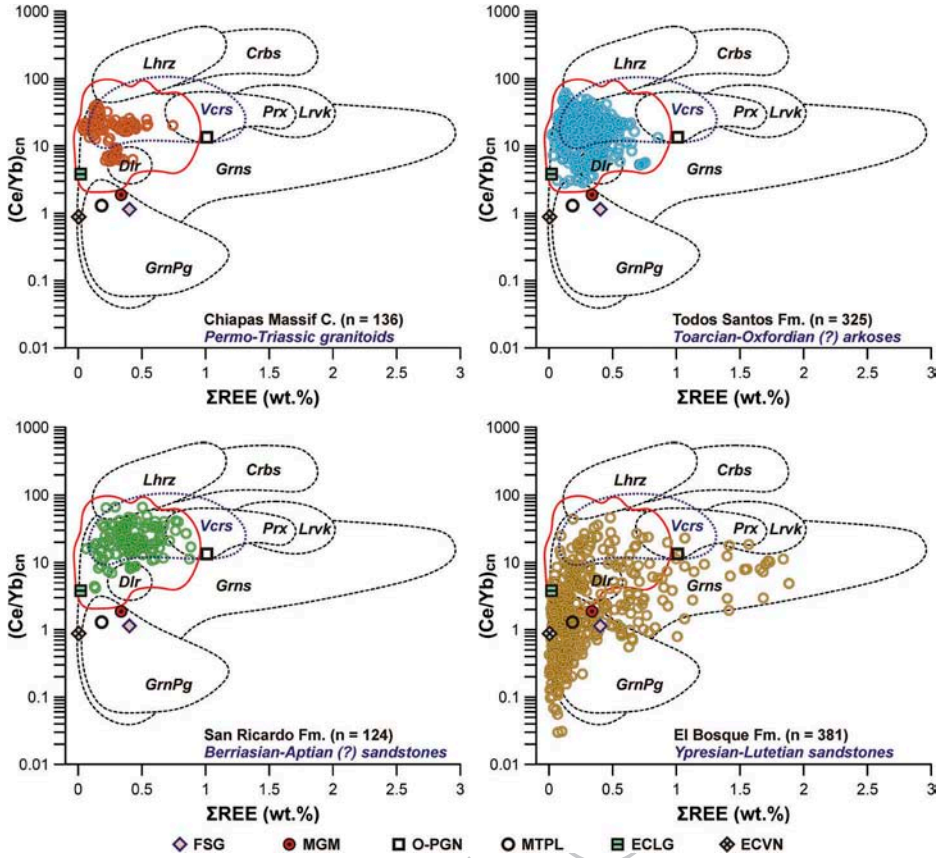

Figure 12. The $(Ce/Yb)_{cn}$ *versus* ΣREE (wt.%) diagram (modified from Belousova *et al*. 2002) displaying apatite compositions from the sampled rocks, together with the range of apatite compositions in a variety of igneous rock types. n is the number of all analysed apatites per each lithostratigraphic unit (e.g. n = 325 from four Todos Santos rock samples). Rock types: *Lhrz*, lherzolites; *Crbs*, carbonatites; *Prx*, pyroxenites; *Lrvk*, larvikite; *Dlr*, dolerites; *Grns*, granitoids; *GrnPg*, felsic pegmatites. A field belonging to volcanic rocks (*Vcrs*, mafic–intermediate to intermediate–felsic; except rhyolites) was added based on some published data (Chu *et al*. 2009; Tang *et al*. 2012; Jafarzadeh *et al*. 2014). The field shown by red solid lines in each graph closely corresponds to $(Ce/Yb)_{cn}$ and ΣREE variations in apatites from the CMC plutons and Mesozoic sandstones. The meanings of FSG, MGM, O-PGN, MTPL, ECLG, and ECVN are detailed in Figure 9.

important to note that, unlike the Mesozoic and CMC rocks, the El Bosque Formation samples include some apatites with ΣREE greater than 0.9 wt.% (Figure 12), supporting the hypothesis that the Ypresian–Lutetian clastic sediments of the SCH were partly derived from relatively unfractionated, mafic to ultramafic rocks (including mantle-derived rocks; Belousova *et al*. 2002; Piccoli and Candela 2002; Lesnov 2012). Detrital apatites derived from S-type granites and pegmatites are also identified (Figure 12). Some apatite grains of the El Bosque and Todos Santos Formation sediments were apparently derived from dolerites or from other mafic source rocks like gabbros or basalts, as suggested by the $(Ce/Yb)_{cn}$ vs. ΣREE method (Figure 12); this is partially supported by the Sr vs. Y diagram (Figure 11).

Therefore, siliciclastic sediments of the Ypresian to Lutetian El Bosque Formation were derived from diverse rock types, from mafic–ultramafic to highly fractionated rocks (i.e. I/S-type granites and granitic pegmatites) as well as from different metamorphic source rocks, as was also supported by the other methods used above.

5. Discussion

5.1. Provenance of Mesozoic sandstones

The geochemical results obtained for apatite groups indicate that the Mesozoic sediments of the Todos Santos and San Ricardo Formations were mostly derived from intermediate to felsic igneous rocks of the CMC basement. This is suggested by the normalized apatite REE plots from the Mesozoic sandstones that are closely identical to those in the CMC plutons (Figures 6, 7a and b). The petrogenetic diagrams tested in this study also show that apatites from both the CMC and the Mesozoic rock samples display similar chemical signatures (Figures 9–12; Supplementary Table 1). Several apatites from the Todos Santos Formation fall within

the fields of mafic rocks in the Sr vs. Y and $(Ce/Yb)_{cn}$ vs. ΣREE plots (Figures 11 and 12), which is in agreement with the variety of basement rocks in the CMC (i.e. from gabbros to highly evolved granites; Schaaf *et al*. 2002; Weber *et al*. 2005; Estrada-Carmona *et al*. 2012). Both the Mesozoic sequences and the CMC include many apatite grains with $(Eu/Eu^*)_{cn}$ of ~1 or above (Supplementary Table 1; see also REE spectra in Figures 6, 7a and b). According to Cao *et al*. (2012), null to strong positive Eu anomalies can be found in apatites crystallized from oxidized magmas. Thereby, the presence of apatites with positive Eu anomalies in the composition of the Mesozoic clastic sediments once again supports the hypothesis of their provenance from the CMC source area, inasmuch as the CMC is a product of subduction-related magmatism (Schaaf *et al*. 2002; Weber *et al*. 2005) which commonly generates oxidized plutons (e.g. Blevin 2004; Cao *et al*. 2012).

Based on zircon U–Pb geochronology, Godinez-Urban *et al*. (2011) demonstrated that the CMC was the most important source area for the Todos Santos sediments studied in the southern Sierra Monocline (Figure 1b) that include many detrital zircons with ages from ~270 to ~230 and from ~480 to ~440 Ma (Figure 13a), typical zircon U–Pb age ranges for the CMC rocks (Weber *et al*. 2005, 2007, 2008). As can be seen from Figure 13a, the Todos Santos Formation includes some zircons with U–Pb ages of 0.9–1.2 Ga (Godinez-Urban *et al*. 2011), which are common for the Grenville-aged Guichicovi and Oaxacan granulitic complexes (Weber and Hecht 2003; Solari *et al*. 2014; Shchepetilnikova *et al*. 2015) located to the west from the SCH (Figure 1a). These detrital zircons, however, could have also been derived from the CMC, for which Grenville-aged components (including inherited zircon crystals) were reported (Schaaf *et al*. 2002; Weber *et al*. 2005, 2007, 2008). Jurassic-aged zircon grains were also reported in the Todos Santos Formation (Figure 13a), which were derived from igneous rocks formed along the CMC during the Early to Middle Jurassic volcanism (Godinez-Urban *et al*. 2011). In addition, provenance of the Mesozoic sandstones from the CMC area was also verified using fission-track thermochronology in detrital apatites from the Todos Santos Formation samples (TS-1, TS-2, TS-3, and TS-4), some of which (slightly annealed and unreset Cl-apatites) yielded two peaks at 203 ± 14 and 163 ± 6 Ma (Figure 13c; Abdullin *et al*. 2016). These apparent age peaks indicate cooling periods of the source rocks through ~150°C to ~120°C palaeo-isotherms, which are respectively coeval with the late Permian–Triassic tectono-thermal event (e.g. Schaaf *et al*. 2002; Weber *et al*. 2005, 2007) and Jurassic arc magmatism (~200–160 Ma; e.g. Sánchez-Montes de Oca 2006; Godinez-Urban *et al*. 2011) that affected the CMC basement.

It was also suggested that both the Mesozoic siliciclastic successions include some apatite grains derived from volcanic rocks, which were particularly observed in the composition of the San Ricardo Formation (Figures 7b, 11 and 12). The presence of apatites of volcanic origin could indicate that these Mesozoic clastic sediments were partly derived from Jurassic arc-related rocks formed along the CMC, as proposed by Godinez-Urban *et al*. (2011). This hypothesis is strongly supported by the presence of volcanic ashes in some layers of the Jericó Formation (see Sánchez-Montes de Oca 2006), which can be stratigraphically correlated with the San Ricardo Formation. Besides, Abdullin *et al*. (2014) obtained two equally important peaks of fission-track ages of 222 ± 9 (~44%) and of 175 ± 8 (~56%) Ma for unreset apatites from the Berriasian–Aptian (?) sandy member (SR-1 and SR-2) of the San Ricardo Formation (Figure 13d; single-grain apatite fission-track ages are detailed in Supplementary Table 3; see //xxxxx//). These age peaks, nearly similar to those from the Todos Santos detrital samples (Figure 13c and d), also indicate cooling periods of the source rocks from the CMC area during the late Permian to Triassic and Jurassic (~200–160 Ma) times.

5.2. Provenance of Eocene sandstones

Provenance analyses performed by Witt *et al*. (2012) show that the El Bosque Formation sandstones mostly include Grenville-age (~0.9–1.2 Ga) detrital zircon grains (Figure 13b). These authors proposed, therefore, that Eocene sediments of the SCH were predominantly derived from the Grenville Oaxacan and Guichicovi metamorphic complexes, both of which are exposed to the west from the SCH (Figure 1a). Alternatively, other possible source regions for these Eocene sediments have also been suggested by Witt *et al*. (2012), including some units from Belize (i.e. from the Maya Mountains) and Central Guatemala (Figure 1a). In our view, it is highly difficult to identify their provenance using single-grain zircon U–Pb chronology, particularly in southern Mexico and in Guatemala where Grenville-aged zircons have been extensively documented for a large range of igneous, metamorphic, and siliciclastic rocks (i.e. inherited/detrital zircon cores in other younger units). For instance, metasedimentary rocks from the late Palaeozoic Sepultura and Ordovician–Devonian Custepec units, which are exposed in the southern SCH and in Guatemala (i.e. in the Sierra de los Cuchumatanes; Figure 1a), include many Grenville zircons (Weber *et al*. 2008). Almost all detrital zircons in

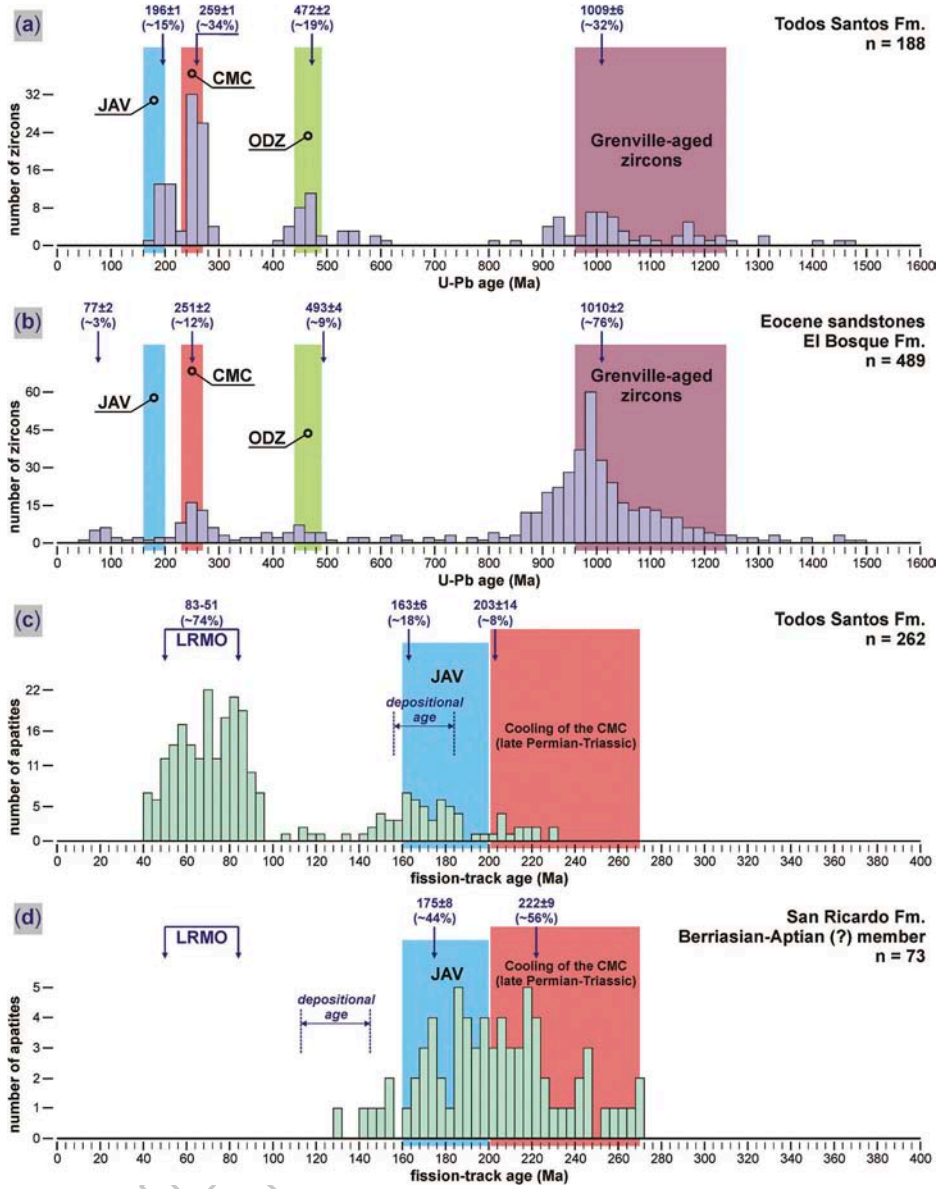

Figure 13. (a) Single-grain U–Pb ages of detrital zircons from the Todos Santos Formation studied in the southern Sierra Monocline subprovince (data from Godinez-Urban *et al*. 2011). (b) Single-grain U–Pb ages of detrital zircons from Eocene sandstones sampled in the SCH (data set from Witt *et al*. 2012). CMC and ODZ represent the typical zircon U–Pb age ranges of ~270–230 Ma and of ~480–440 for the Chiapas Massif Complex (Weber *et al*. 2005, 2007, 2008). JAV corresponds to Jurassic-aged zircons (~200–160 Ma) derived from igneous lithologies formed along the Chiapas Massif Complex during the Jurassic volcanism (Godinez-Urban *et al*. 2011). (c) Detrital apatite fission-track ages from the Todos Santos Formation sandstones (data from Abdullin *et al*. 2016). (d) Fission-track ages for unreset apatites from the San Ricardo Formation (data from Abdullin *et al*. 2014). LRMO shows the time span belonging to the Laramide orogeny (e.g. Meneses-Rocha 2001; Abdullin *et al*. 2016). Rapid cooling of the Chiapas Massif Complex occurred during the late Permian to Triassic (~270 to ~200 Ma) event (Schaaf *et al*. 2002; Weber *et al*. 2005, 2007) is also presented in the diagram. The decomposition of zircon/apatite ages was performed using RadialPlotter of Vermeesch (2009). *n* is the number of analysed crystals.

metasediments from the Palaeozoic Baldy unit (i.e. the Maya Mountains, Belize; Martens *et al*. 2010) as well as in those from the San Diego unit (Guatemala; see in Torres-de León *et al*. 2012) yielded Grenville ages. The Chuacús metamorphic complex, cropping out along the PMFS region (Figure 1a), also contains a large group of Grenville zircons (e.g. Ratschbacher *et al*. 2009). Within the SCH, the CMC plutons/metagranitoids and the Todos Santos Formation sandstones contain Grenville-aged components (Schaaf *et al*. 2002), including inherited/detrital zircon crystals (e.g. Weber *et al*. 2005, 2007, 2008; Godinez-Urban *et al*. 2011). Furthermore, Weber *et al*. (2015) recently discovered outcrops of Grenville basement rocks in the southernmost portion of the CMC region, opening new perspectives to the geological history of Mesoamerica. These are only a few

examples of stratigraphic units from the Maya and Chortís blocks that include many Grenville-aged zircons.

In this study, some important provenance signals of the source rocks were detected in the El Bosque Formation sandstones based on single-grain detrital apatite chemistry. First of all, it is very obvious that the CMC was not the dominant source area for Eocene sediments in the SCH, as also discussed in Witt *et al*. (2012). It was shown that detrital apatite grains of the Ypresian–Lutetian El Bosque Formation were derived from diverse source rocks such as ultramafic–mafic rocks, intermediate to felsic I-type granitoids, strongly fractionated I/S-type granites and granitic pegmatites, as well as from various medium- and high-grade metamorphic source lithologies like gneisses, migmatites, high-pressure metasediments, and eclogites (Figures 8–12). Consequently, we can suggest that Eocene sediments of the SCH were mainly derived from a lithologically very heterogeneous source area that may be perfectly correlated with the Guatemala Suture Complex (GSC; renamed by Martens *et al*. 2012), a region that covers the PMFS (see Figure 1a). The GSC includes all the rock types mentioned above (e.g. Ortega-Gutiérrez *et al*. 2004, 2007; Chiari *et al*. 2006; Ratschbacher *et al*. 2009; Solari *et al*. 2009; Estrada-Carmona *et al*. 2012; Martens *et al*. 2012; Torres-de León *et al*. 2012; Flores *et al*. 2013), from which most clastic sediments of the El Bosque Formation could be derived.

There are several facts that support our hypothesis, some of which are detailed below:

(1) Some apatites of the El Bosque Formation are from relatively unfractionated, mafic and ultramafic rocks, which were likely derived from Mesozoic mafic–ultramafic complexes such as the El Tambor ophiolitic succession (see Figure 1a). These complexes are mostly composed of serpentinized mantle-derived peridotites (including harzburgites), gabbros, and pillow basalts (Ortega-Gutiérrez *et al*. 2004, 2007; Chiari *et al*. 2006).

(2) Several detrital apatites in the El Bosque Formation rocks display geochemical signatures that correspond to apatites from medium- and high-grade metamorphic lithologies, as was suggested by apatite REE profiles (Figure 8) as well as by some discrimination diagrams (Figures 10–12). These detrital apatites were probably derived from migmatites, gneisses, metasediments, and eclogites, which were reported in some units within the GSC (Figure 1a) like the Chuacús metamorphic complex (Ortega-Gutiérrez *et al*. 2007; Ratschbacher *et al*. 2009; Martens *et al*. 2012).

(3) The presence of apatites derived from highly evolved S-type granites and pegmatites was also identified based on apatite geochemistry (Figures 8–12). These apatite crystals could also have been derived from the GSC region, within which ubiquitous granitic pegmatites (mostly Cretaceous) and some Ordovician S-type granites were reported by many authors (e.g. Ortega-Gutiérrez *et al*. 2007; Ratschbacher *et al*. 2009; Solari *et al*. 2010; Martens *et al*. 2012; Torres-de León *et al*. 2012).

(4) The Ypresian to Lutetian el Bosque Formation is exceptionally characterized by abundant flakes of aligned muscovites (Meneses-Rocha 1985; Sánchez-Montes de Oca 2006; see also photomicrographs in Figure 4), which indicates that Eocene clastic sediments of the SCH were derived from a source area that should include many gneisses and metapelites like white mica-schists and phyllites, rock types that are widely exposed in the Chuacús complex and in the San Diego unit (e.g. Ortega-Gutiérrez *et al*. 2004, 2007; Ratschbacher *et al*. 2009; Martens *et al*. 2012; Torres-de León *et al*. 2012). It is important to note that most deformed pegmatitic bodies in the GSC are also composed by abundant muscovite crystals (e.g. Martens *et al*. 2012). Hence, the Eocene sediments of the SCH were derived from the GSC region, rather than from the Guichicovi and Oaxacan granulitic complexes which typically display outcrops of biotite- and garnet-rich gneisses (Weber and Hecht 2003; Solari *et al*. 2014; Shchepetilnikova *et al*. 2015).

(5) Marked facies changes from south (i.e. continental siliciclastic and transitional sediments in the SCH) to north (deep-basin sediments in the Tabasco plain; Meneses-Rocha 1985; Quezada-Muñetón 1987; Sánchez-Montes de Oca 2006) also indicate that the El Bosque Formation sediments were derived from the GSC (Central Guatemala), rather than from western source areas such as the Guichicovi and/or Oaxacan complexes.

(6) The presence of conglomeratic lenses containing clasts of mafic to ultramafic igneous and metamorphic rocks in the El Bosque Formation (Sánchez-Montes de Oca 2006) supports the hypothesis of provenance of Eocene sediments from the GSC, which were very likely derived

from one of the Mesozoic ophiolite sequences of Guatemala (see in Figure 1a).

(7) Burkart *et al*. (1987) observed deformation signals of a late Cretaceous–Eocene orogenic event along the PMFS (i.e. along the GSC region), which is contemporaneous with the deposition of the El Bosque Formation sampled in the SCH.

(8) By the way, a peak of 77 ± 2 Ma (~3% of Eocene zircons; Figure 13b) observed in U–Pb data set proposed by Witt *et al*. (2012) could be correlated with the age of eclogite-facies metamorphism of the Chuacús complex (~76 ± 2 Ma), which was determined by Martens *et al*. (2012) using U–Pb dating of metamorphic rims in zircon grains. On the other hand, these ages can indicate the crystallization ages of Cretaceous pegmatites from the GSC.

The results obtained from the Ypresian to Lutetian El Bosque Formation could be useful towards a better understanding of the Cenozoic geodynamic evolution of southern Mexico (i.e. the Maya block within the North America plate) and Guatemala (the Chortís block as the western portion of the Caribbean plate). The Palaeogene location of the Chortís block relative to southern Mexico is a hotly debated topic (e.g. see Morán-Zenteno *et al*. 2009). There are two predominant hypothetical models proposed: (1) the *traditional* model that places the Chortís block adjacent to southwestern Mexico (roughly between 95°W and 105°W), with migration to its current position occurring throughout the Cenozoic (e.g. Schaaf *et al*. 1995; Pindell *et al*. 2006; Ratschbacher *et al*. 2009); and (2) the *in situ* model which infers little or no relative motion (James 2006, 2009). Unfortunately, we have no possibility to propose a new updated palaeogeographic reconstruction for the Cenozoic Era based of one of these hypothetical models, because additional detailed provenance studies are needed from other Tertiary sequences of the SCH, clastic sediments from which should contain useful information about the Cenozoic interaction between the Maya block and the Chortís block. Nonetheless, the most interesting finding of this study that can be used for further geodynamic reconstructions may be emphasized as follows. Several stratigraphic units of the GSC like the Chuacús complex as well as some of the Mesozoic mafic–ultramafic complexes have already been located near or not too far from the SCH, at least since the Eocene (Figure 14a and b).

A minor portion of Eocene sediments of the SCH was derived from the CMC and Sierra Monocline source areas (Figure 1a and b). This is suggested by some detrital apatites from the El Bosque Formation samples that display geochemical properties identical to those in apatites from the CMC plutons and the Todos Santos and San Ricardo Formation sandstones (this study). Witt *et al*. (2012) came to the same conclusion on the basis of detrital zircon crystals, some of which yielded Permo–Triassic (~12%) and Ordovician (~9%) U–Pb ages (Figure 13b) belonging to the common zircon age ranges from the CMC lithologies (Weber *et al*. 2005, 2007, 2008) as well as from the Todos Santos Formation sandstones (Godinez-Urban *et al*. 2011). Therefore, the CMC was definitely not the main source region for the El Bosque Formation sediments. Additionally, apatite fission-track analyses performed by Abdullin *et al*. (2016) indicate that the western SCH (i.e. the CMC and the Sierra Monocline province; Figure 1b) has not experienced any significant tectonic uplift during the Ypresian–early Miocene period.

Although it was demonstrated in the present work that Eocene sediments in the SCH were predominantly derived from the GSC source region, we consider that some of these siliciclastic materials could have also been derived from the Guichicovi complex that is situated relatively near the SCH (Figure 1a), partially supporting the hypothesis proposed by Witt *et al*. (2012).

6. Concluding remarks

(1) The geochemical compositions (REE, Y, Sr, U, and Th) of apatite populations obtained in this study indicate that the Mesozoic terrigenous sediments of the Todos Santos and San Ricardo Formations were derived from the CMC source rocks, including Permo–Triassic intermediate to felsic I-type granitoids and Jurassic arc volcanic rocks. The San Ricardo Formation may partially include second-cycle sediments derived from the Todos Santos Formation. A significant change in provenance between the Mesozoic and the Eocene sedimentary sequences was identified based on single-grain apatite geochemistry. The CMC was definitely not the dominant source region for Eocene clastic sediments. Detrital apatites of the Ypresian–Lutetian El Bosque Formation were derived from diverse source rocks like mafic to ultramafic rocks, intermediate to felsic I-type granitoids, highly evolved I/S-type granites and pegmatites, as well as from various medium- to high-grade metamorphic sources such as gneisses, migmatites, metapelites, and eclogites. It was proposed, therefore, that most Eocene sediments of the SCH were derived from the GSC area that includes all the rock types mentioned above. A small portion of the El Bosque

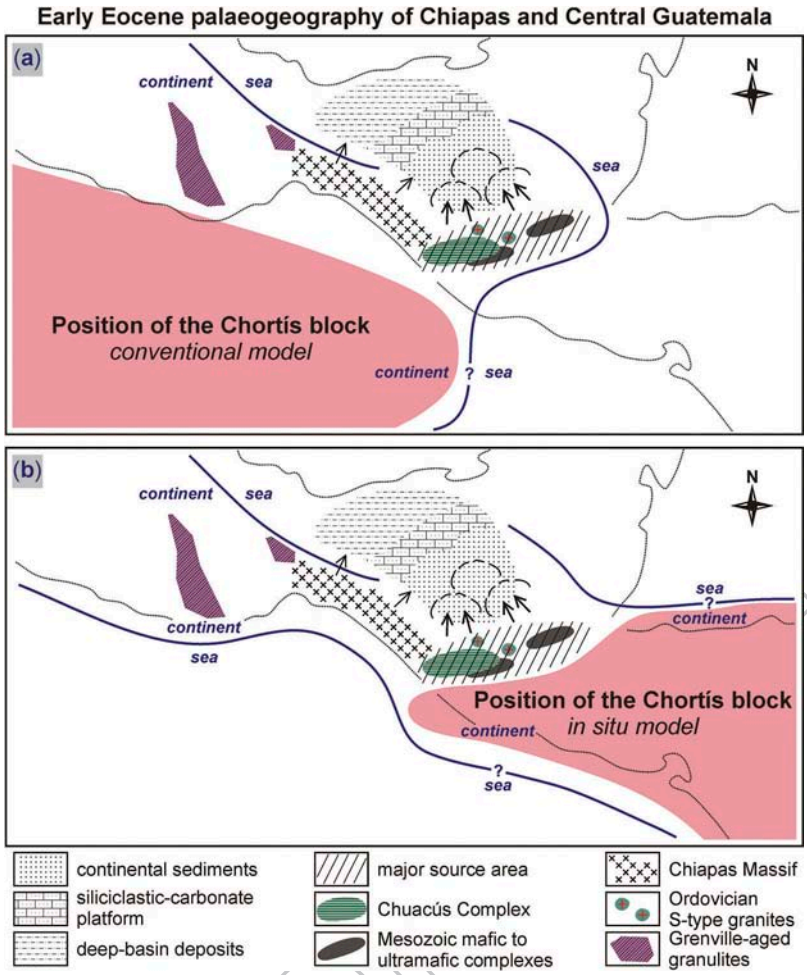

COLOUR ONLINE BLACK & WHITE IN PRINT

Figure 14. Schematic palaeogeographic reconstruction for the early Eocene (modified from Meneses-Rocha 2001). (a) Early Eocene position of the Chortís block according to the *conventional* model (e.g. Schaaf *et al*. 1995; Pindell *et al*. 2006; Ratschbacher *et al*. 2009). (b) Early Eocene position of the Chortís block according to the *in situ* model (James 2006, 2009).

AQ6
AQ7

Formation clastic materials was apparently derived from the CMC basement rocks and/or from recycled sandstones from the Mesozoic Formations, as also suggested by detrital apatite geochemistry.

(2) This study, like the studies pioneered by Morton and Yaxley (2007) and Jafarzadeh *et al*. (2014), once again demonstrates that LA-ICP-MS-based single-grain apatite chemistry has many potential applications in sediment provenance analyses. Some advantages and disadvantages of the methodology used were observed and outlined below. For example, the comparison of apatite compositions between the sediments and their potential source rocks is extremely useful. The U vs. Th (Dill 1994) and the La/Nd vs. (La–Pr)/ΣREE (Fleischer and Altschuler 1986) discriminators can hardly be used to determine the type of host rock. The petrogenetic plots of Belousova *et al*. (2002) have higher potential in provenance studies when apatites are derived from igneous rocks (Morton and Yaxley 2007; Jafarzadeh *et al*. 2014; this study). However, in the case of sediments derived from metamorphic lithologies, the methods of Belousova *et al*. (2002) may yield questionable results (e.g. Morton and Yaxley 2007; this study), since their diagrams were primarily proposed for apatites of igneous origin. Acquisition of geochemical data on a more large range of apatite-bearing rocks (including volcanic igneous rocks, and more importantly, metamorphic rocks) are urgently required and will help to improve these discrimination diagrams. In our opinion, despite of some limitations of the methodology (see also in Morton and Yaxley 2007), all the petrogenetic discrimination plots tested in different apatite populations can easily be used to check the source homogeneity and to detect the changes in provenance between temporally and spatially distinct stratigraphic units, which is particularly useful for siliciclastic sequences.

Acknowledgements

This study is part of a PhD thesis of F.A, who thanks CONACyT for his scholarship. The authors are very grateful to the Editor-in-Chief, Prof. Robert Stern for his very important suggestions that helped to interpret the geochemical results. Barbara Martiny, Jaime Díaz, Consuelo Macías, and Carlos Ortega are acknowledged for their help with data acquisition. Professor Cesar Witt (Lille 1 University, France) and two anonymous reviewers are also acknowledged for their strong but constructive criticism that helped us to improve our manuscript significantly.

Disclosure statement

No potential conflict of interest was reported by the authors.

Funding

This study was supported by PAPIIT [grant number IN111414] to J.S. and [grant number IN102414] to L.S.

References

Abdullin, F., Solé, J., Meneses-Rocha, J.D.J., Solari, L., Shchepetilnikova, V., and Ortega-Obregón, C., 2016, LA-ICP-MS-based apatite fission track dating of the Todos Santos Formation sandstones from the Sierra de Chiapas (SE Mexico) and its tectonic significance: International Geology Review, v. 58, no. 1, p. 32–48. doi:10.1080/00206814.2015.1055596

Abdullin, F., Solé-Viñas, J., Shchepetilnikova, V., Solari, L., and Ortega Obregon, C., 2014, LA-ICP-MS apatite fission track thermochronology of Mesozoic sandstones and its tectonic significance in the Sierra Madre de Chiapas: SE Mexico, Puerto Vallarta 2014, México, Reunión Anual de la Unión Geofísica Mexicana, Libro de Resúmenes, p. 105–106.

Ayres, M., and Harris, N., 1997, REE fractionation and Nd-isotope disequilibrium during crustal anatexis: Constraints from Himalayan leucogranites: Chemical Geology. v. 139, p. 249–269. doi:10.1016/S0009-2541(97)00038-7

Bea, F., and Montero, P., 1999, Behaviour of accessory phases and redistribution of Zr, REE, Y, Th, and U during metamorphism and partial melting of metapelites in the lower crust: An example from the Kinzigite Formation of Ivrea-Verbano, NW Italy: Geochimica Et Cosmochimica Acta, v. 63, no. 7–8, p. 1133–1153. doi:10.1016/S0016-7037(98)00292-0

Bea, F., Pereira, M.D., and Stroh, A., 1994, Mineral/leucosome trace-element partitioning in a peraluminous migmatite (a laser ablation-ICP-MS study): Chemical Geology, v. 117, no. 1–4, p. 291–312. doi:10.1016/0009-2541(94)90133-3

Belousova, E.A., Griffin, W.L., O'Reilly, S.Y., and Fisher, N.I., 2002, Apatite as an indicator mineral for mineral exploration: Trace-element compositions and their relationship to host rock type: Journal of Geochemical Exploration. v. 76, p. 45–69. doi:10.1016/S0375-6742(02)00204-2

Belousova, E.A., Walters, S., Griffin, W.L., and O'Reilly, S.Y., 2001, Trace-element signatures of apatites in granitoids from the Mt Isa Inlier, northwestern Queensland: Australian Journal of Earth Sciences. v. 48, p. 603–619. doi:10.1046/j.1440-0952.2001.00879.x

Bingen, B., Demaiffe, D., and Hertogen, J., 1996, Redistribution of rare earth elements, thorium, and uranium over accessory minerals in the course of amphibolite to granulite facies metamorphism: The role of apatite and monazite in orthogneisses from southwestern Norway: Geochimica Et Cosmochimica Acta, v. 60, no. 8, p. 1341–1354. doi:10.1016/0016-7037(96)00006-3

Blair, T.C., 1987, Tectonic and hydrologic controls on cyclic alluvial fan, fluvial, and lacustrine rift-basin sedimentation, Jurassic–lowermost Cretaceous Todos Santos Formation, Chiapas, Mexico: Journal of Sedimentary Research, v. 57, p. 845–862.

Blevin, P.L., 2004, Redox and Compositional Parameters for Interpreting the Granitoid Metallogeny of Eastern Australia: Implications for Gold-rich Ore Systems: Resource Geology. v. 54, p. 241–252. doi:10.1111/rge.2004.54.issue-3

Budzinski, H., and Tischendorf, G., 1989, Distribution of REE among minerals in the Hercynian postkinematic granites of Westerzgebirge–Vogland, GDR: Zeitschrift Fur Geologische Wissenschaften, v. 17, p. 1019–1031.

Burkart, B., Deaton, B.C., Dengo, C., and Moreno, G., 1987, Tectonic wedges and offset Laramide structures along the Polochic fault of Guatemala and Chiapas, Mexico: Reaffirmation of Large Neogene Displacement: Tectonics, v. 6, p. 411–422.

Cao, M., Li, G., Qin, K., Seitmuratova, E.Y., and Liu, Y., 2012, Major and trace element characteristics of apatites in granitoids from Central Kazakhstan: Implications for petrogenesis and mineralization: Resource Geology. v. 62, p. 63–83. doi:10.1111/rge.2012.62.issue-1

Chakhmouradian, A.R., Reguir, E.P., and Mitchell, R.H., 2002, Strontium-apatite: New occurrences, and the extent of Sr-for-Ca substitution in apatite-group minerals: The Canadian Mineralogist, v. 40, no. 1, p. 121–136. doi:10.2113/gscanmin.40.1.121

Chiari, M., Dumitrica, P., Marroni, M., Pandolfi, L., and Principi, G., 2006, Radiolarian biostratigraphic evidence for a Late Jurassic age of the El Tambor Group ophiolites (Guatemala): Ofioliti, v. 31, no. 2, p. 141–150.

Chu, M.-F., Wang, K.-L., Griffin, W.L., Chung, S.-L., O'Reilly, S.Y., Pearson, N.J., and Iizuka, Y., 2009, Apatite composition: Tracing petrogenetic processes in Transhimalayan granitoids: Journal of Petrology. v. 50, p. 1829–1855. doi:10.1093/petrology/egp054

Damon, P.E., Shafiqullah, M., and Clark, K.F., 1981, Evolución de los arcos magmáticos en México y su relación con la metalogénesis: Revista Mexicana de Ciencias Geológicas, v. 5, p. 223–238. in Spanish with English abstract.

Dill, H.G., 1994, Can REE patterns and U-Th variations be used as a tool to determine the origin of apatite in clastic rocks?: Sedimentary Geology. v. 92, p. 175–196. doi:10.1016/0037-0738(94)90105-8

Estrada-Carmona, J., Weber, B., Martens, U., and López-Martínez, M., 2012, Petrogenesis of Ordovician magmatic rocks in the southern Chiapas Massif Complex: Relations with the early Palaeozoic magmatic belts of northwestern Gondwana: International Geology Review. v. 54, p. 1918–1943. doi:10.1080/00206814.2012.685553

Fleischer, M., and Altschuler, Z.S., 1986, The lanthanides and yttrium in minerals of the apatite group–an analysis of the

available data: Neues Jahrbuch für Mineralogie Monatshefte, v. 10, p. 467–480.
Flores, K.E., Martens, U.C., Harlow, G.E., Brueckner, H.K., and Pearson, N.J., 2013, Jadeitite formed during subduction: In situ zircon geochronology constraints from two different tectonic events within the Guatemala Suture Zone: Earth and Planetary Science Letters. v. 371-372, p. 67–81. doi:10.1016/j.epsl.2013.04.015
Gawęda, A., Szopa, K., and Chew, D., 2014, LA-ICP-MS U-Pb dating and REE patterns of apatite from the Tatra Mountains, Poland as a monitor of the regional tectono-magmatic activity: Geochronometria. v. 41, p. 306–314. doi:10.2478/s13386-013-0171-0
Godinez-Urban, A., Lawton, T.F., Molina Garza, R.S., Iriondo, A., Weber, B., and Lopez-Martinez, M., 2011, Jurassic volcanic and sedimentary rocks of the La Silla and Todos Santos Formations, Chiapas: Record of Nazas arc magmatism and rift-basin formation prior to opening of the Gulf of Mexico: Geosphere. v. 7, p. 121–144. doi:10.1130/GES00599.1
Gromet, L.P., and Silver, L.T., 1983, Rare earth element distributions among minerals in a granodiorite and their petrogenetic implications: Geochimica Et Cosmochimica Acta. v. 47, p. 925–939. doi:10.1016/0016-7037(83)90158-8
Guo, S., Ye, K., Wu, T.F., Chen, Y., Yang, Y.H., Zhang, L.M., Liu, J. B., Mao, Q., and Ma, Y.G., 2013, A potential method to confirm the previous existence of lawsonite in eclogite: The mass imbalance of Sr and LREEs in multistage epidote (Ganghe, Dabie UHP terrane): Journal of Metamorphic Geology, v. 31, no. 4, p. 415–435. doi:10.1111/jmg.2013.31.issue-4
Guzmán-Speziale, M., 2010, Beyond the Motagua and Polochic faults: Active strike-slip faulting along the Western North America–Caribbean plate boundary zone: Tectonophysics. v. 496, p. 17–27. doi:10.1016/j.tecto.2010.10.002
Hammerli, J., Kemp, A.I.S., and Spandler, C., 2014, Neodymium isotope equilibration during crustal metamorphism revealed by in situ microanalysis of REE-rich accessory minerals: Earth and Planetary Science Letters. v. 392, p. 133–142. doi:10.1016/j.epsl.2014.02.018
Hermann, J., 2002, Allanite: Thorium and light rare earth element carrier in subducted crust: Chemical Geology, v. 192, no. 3–4, p. 289–306. doi:10.1016/S0009-2541(02)00222-X
Jafarzadeh, M., Harami, R.M., Friis, H., Amini, A., Mahboubi, A., and Lenaz, D., 2014, Provenance of the Oligocene–Miocene Zivah Formation, NW Iran, assessed using heavy mineral assemblage and detrital clinopyroxene and detrital apatite analyses: Journal of African Earth Sciences. v. 89, p. 56–71. doi:10.1016/j.jafrearsci.2013.10.005
James, K.H., 2006, Arguments for and against the Pacific origin of the Caribbean Plate: Discussion, finding for an inter-American origin: Geologica Acta, v. 4, p. 279–302.
James, K.H., 2009, In situ origin of the Caribbean: Discussion of data: Geological Society, Volume 328: London, Special Publications, p. 77–125
Krenn, E., and Finger, F., 2004, Metamorphic formation of Sr-apatite and Sr-bearing monazite in a high-pressure rock from the Bohemian Massif: American Mineralogist. v. 89, p. 1323–1329. doi:10.2138/am-2004-8-921
Lesnov, F.P., 2012, Rare earth elements in ultramafic and mafic rocks and their minerals: Minor and accessory minerals: London, Taylor and Francis Group, 314 p.
Mandujano Velásquez, J., 1996, Cuatro megasecuencias de evolución litoestratigráfica en la Sierra de Chiapas: Boletín De La Asociación Mexicana De Geólogos Petroleros, v. 45, p. 46–60. in Spanish with English abstract.
Martens, U., Weber, B., and Valencia, V.A., 2010, U/Pb geochronology of Devonian and older Paleozoic beds in the southeastern Maya block, Central America: Its affinity with peri-Gondwanan terranes: Geological Society of America Bulletin. v. 122, p. 815–829. doi:10.1130/B26405.1
Martens, U.C., Brueckner, H.K., Mattinson, C.G., Liou, J.G., and Wooden, J.L., 2012, Timing of eclogite-facies metamorphism of the Chuacús complex, Central Guatemala: Record of Late Cretaceous continental subduction of North America's sialic basement: Lithos. v. 146-147, p. 1–10. doi:10.1016/j.lithos.2012.04.021
Martínez-Amador, H., Rosendo-Brito, B., Fitz-Bravo, C., Tinajera-Fuentes, E., and Beltrán-Castillo, H.D., 2005, Carta Geológica: Tuxtla Gutiérrez, Chiapas E5-11: Servicio Geológico Mexicano, Scale, v. 1. 250000. AQ5
McDonough, W.F., and Sun, -S.-S., 1995, The composition of the Earth: Chemical Geology. v. 120, p. 223–253. doi:10.1016/0009-2541(94)00140-4
Meneses-Rocha, J.J., 1985, Tectonic evolution of the Strike-slip Fault province of Chiapas, Mexico [M.S. thesis]: Austin, University of Texas at Austin, 315 p.
Meneses-Rocha, J.J., 2001, Tectonic evolution of the Ixtapa Graben, an example of a strike-slip basin of southeastern Mexico: Implications for regional petroleum systems, *in* Bartolini, C., Buffler, R.T., and Cantú-Chapa, A., eds., The western gulf of Mexico basin: Tectonics, sedimentary basins and petroleum systems, Volume 75: American Association of Petroleum Geologists Memoir, p. 183–216.
Miles, A.J., Graham, C.M., Hawkesworth, C.J., Gillespie, M.R., Hinton, R.W., and Bromiley, G.D., 2014, Apatite: A new redox proxy for silicic magmas?: Geochimica Et Cosmochimica Acta. v. 132, p. 101–119. doi:10.1016/j.gca.2014.01.040
Molina-Garza, R.S., Geissman, J.W., Wawrzyniec, T.F., Peña Alonso, T.A., Iriondo, A., Weber, B., and Aranda-Gómez, J., 2015, Geology of the coastal Chiapas (Mexico) Miocene plutons and the Tonalá shear zone: Syntectonic emplacement and rapid exhumation during sinistral transpression: Lithosphere. v. 7, p. 257–274. doi:10.1130/L409.1
Morán-Zenteno, D.J., Keppie, D.J., Martiny, B., and González-Torres, E., 2009, Reassessment of the Paleogene position of the Chortís block relative to southern Mexico: Hierarchical ranking of data and features: Revista Mexicana de Ciencias Geológicas, v. 26, p. 177–188.
Morton, A.C., 1991, Geochemical studies of detrital heavy minerals and their applications to provenance research, in Morton, A.C., Todd, S.P., and Haughton, P.D.W., eds., Developments in Sedimentary Provenance Studies, Volume 57: Geological Society of London, Special Publication, p. 31–45.
Morton, A.C., and Hallsworth, C., 2007, Stability of detrital heavy minerals during burial diagenesis: Developments in Sedimentology, v. 58, p. 215–245.
Morton, A.C., and Yaxley, G., 2007, Detrital apatite geochemistry and its application in provenance studies, *in* Arribas, J., Critelli, S., and Johnsson, M.J., eds., Sediment Provenance and Petrogenesis: Perspectives from Petrography and

Geochemistry: Geological Society of America, p. 319–344. [Special Paper 420].

Nutman, A.P., 2007, Apatite recrystallisation during prograde metamorphism, Cooma, southeast Australia: Implications for using an apatite–graphite association as a biotracer in ancient metasedimentary rocks: Australian Journal of Earth Sciences. v. 54, p. 1023–1032. doi:10.1080/08120090701488321

Ortega-Gutiérrez, F., Solari, L.A., Ortega-Obregón, C., Elías-Herrera, M., Martens, U., Morán-Icál, S., Chiquín, M., Keppie, J.D., De León, R., and Schaaf, P., 2007, The Maya-Chortís Boundary: A Tectonostratigraphic Approach:: International Geology Review. v. 49, p. 996–1024. doi:10.2747/0020-6814.49.11.996

Ortega-Gutiérrez, F., Solari, L.A., Solé-Viñas, J., Martens, U., Gómez-Tuena, A., Morán-Ical, S., Reyes-Salas, M., and Ortega-Obregón, C., 2004, Polyphase, high-temperature eclogite-facies metamorphism in the Chuacús Complex, Central Guatemala: International Geology Review. v. 46, p. 445–470. doi:10.2747/0020-6814.46.5.445

Perrilliat, M.C., Avendaño, J., Vega, F.J., and Solé, J., 2006, Lower Eocene gastropods from the El Bosque Formation, central Chiapas, Mexico: The Veliger, v. 48, p. 151–169.

Philander, C., and Rozendaal, A., 2015, Detrital zircon geochemistry and U–Pb geochronology as an indicator of provenance of the Namakwa Sands heavy mineral deposit, west coast of South Africa: Sedimentary Geology. v. 328, p. 1–16. doi:10.1016/j.sedgeo.2015.08.001

Piccoli, P.M., and Candela, P.A., 2002, Apatite in igneous systems: Reviews in Mineralogy and Geochemistry. v. 48, p. 255–292. doi:10.2138/rmg.2002.48.6

Pindell, J., Kennan, L., Draper, G., Maresch, W.V., and Stanek, K. P., 2006, Foundations of Gulf of Mexico and Caribbean evolution: Eight controversies resolved: Geologica Acta, v. 4, p. 303–341.

Quezada-Muñetón, J.M., 1983, Las Formaciones San Ricardo y Jericó del Jurásico Medio–Cretácico Inferior en el SE de México: Boletín De La Asociación Mexicana De Geólogos Petroleros, v. 35, p. 37–64. [in Spanish with English abstract].

Quezada-Muñetón, J.M., 1987, El Cretácico medio–Superior y el límite Cretácico Superior– Terciario inferior en la Sierra de Chiapas: Boletín De La Asociación Mexicana De Geólogos Petroleros, v. 39, p. 3–98. [in Spanish with English abstract].

Ratschbacher, L., Franz, L., Min, M., Bachmann, R., Martens, U., Stanek, K., Stübner, K., Nelson, B.K., Herrmann, U., Weber, B., López-Martínez, M., Jonckheere, R., Sperner, B., Tichomirowa, M., McWilliams, M.O., Gordon, M., Meschede, M., and Bock, P., 2009, The North American–Caribbean plate boundary in Mexico–Guatemala–Honduras, *in* James, K., Lorente, M., and Pindell, J., eds., The origin and evolution of the Caribbean plate, Volume 328: Geological Society of London, Special Publication, p. 219–293.

Rosales-Domínguez, M.D.C., 1998, Biohorizontes cronoestratigráficos en las facies carbonatadas de plataforma del Cretácico medio–superior de Chiapas, México: Revista Mexicana de Ciencias Geológicas, v. 15, p. 73–77. [in Spanish with English abstract].

Sánchez, M.O., Franco, N.A., Navarrete, S.F., and Martínez, M.G., 2004, Estratigrafía y evolución de facies del Cretácico Superior en el Sureste de México: Boletín de la Asociación Mexicana de Geólogos Petroleros, Special Paper No. 697, p. 39–61. [in Spanish.]

Sánchez-Montes de Oca, R., 2006, Curso Cuenca del Sureste: México, Petróleos Mexicanos, 296 p. [in Spanish].

Sassi, R., Harte, B., Carswell, D.A., and Yujing, H., 2000, Trace element distribution in Central Dabie eclogites: Contributions to Mineralogy and Petrology, v. 139, no. 3, p. 298–315. doi:10.1007/s004100000133

Schaaf, P., Morán-Zenteno, D., Del Sol Hernández-Bernal, M., Solís-Pichardo, G., Tolson, G., and Köhler, H., 1995, Paleogene continental margin truncation in southwestern Mexico: Geochronological evidence: Tectonics. v. 14, p. 1339–1350. doi:10.1029/95TC01928

Schaaf, P., Weber, B., Weis, P., Groβ, A., Ortega-Gutiérrez, F., and Kohler, H., 2002, The Chiapas Massif (Mexico) revised: New geologic and isotopic data and basement characteristics, *in* Miller, H.E., ed., Contributions to Latin-American Geology, Volume 225: Neues Jahrbuch für Geologie und Paläontologie, p. 1–23.

Sha, L.K., and Chappell, B.W., 1999, Apatite chemical composition, determined by electron microprobe and laser-ablation inductively coupled plasma mass spectrometry, as a probe into granite petrogenesis: Geochimica Et Cosmochimica Acta. v. 63, p. 3861–3881. doi:10.1016/S0016-7037(99)00210-0

Shchepetilnikova, V., Solé, J., Solari, L., and Abdullin, F., 2015, A chronological and chemical zircon study of some pegmatite dikes and lenses from the central part (Ayoquezco-Ejutla) of the Oaxacan Complex, southern Mexico: Revista Mexicana de Ciencias Geológicas, v. 32, p. 123–143.

Solari, L.A., Garcia-Casco, A., Martens, U., Lee, J.K., and Ortega-Rivera, A., 2013, Late Cretaceous subduction of the continental basement of the Maya block (Rabinal Granite, central Guatemala): Tectonic implications for the geodynamic evolution of Central America: Geological Society of America Bulletin. v. 125, p. 625–639. doi:10.1130/B30743.1

Solari, L.A., Ortega-Gutiérrez, F., Elías-Herrera, M., Gómez-Tuena, A., and Schaaf, P., 2010, Refining the age of magmatism in the Altos Cuchumatanes, western Guatemala, by LA-ICPMS, and tectonic implications: International Geology Review. v. 52, p. 977–998. doi:10.1080/00206810903216962

Solari, L.A., Ortega-Gutiérrez, F., Elías-Herrera, M., Ortega-Obregón, C., Macías-Romo, C., and Reyes-Salas, M., 2014, Detrital provenance of the Grenvillian Oaxacan Complex, Southern Mexico: A zircon perspective: International Journal of Earth Sciences. v. 103, p. 1301–1315. doi:10.1007/s00531-013-0938-9

Solari, L.A., Ortega-Gutierrez, F., Elias-Herrera, M., Schaaf, P., Norman, M., de Leon, R.T., Ortega-Obregon, C., Chiquin, M., and Morán-Ical, S., 2009, U–Pb zircon geochronology of Paleozoic units in western and central Guatemala: Insights into the tectonic evolution of Middle America, Volume 328: Geological Society London Special Publications, p. 295–313

Spandler, C., Hermann, J., Arculus, R., and Mavrogenes, J., 2003, Redistribution of trace elements during prograde metamorphism from lawsonite blueschist to eclogite facies; implications for deep subduction-zone processes: Contributions to Mineralogy and Petrology. v. 146, p. 205–222. doi:10.1007/s00410-003-0495-5

Spear, F.S., and Pyle, J.M., 2002, Apatite, monazite, and xenotime in metamorphic rocks: Reviews in Mineralogy and Geochemistry. v. 48, p. 293–335. doi:10.2138/rmg.2002.48.7

Tang, M., Wang, X.L., Xu, X.S., Zhu, C., Cheng, T., and Yu, Y., 2012, Neoproterozoic subducted materials in the generation of Mesozoic Luzong volcanic rocks: Evidence from apatite geochemistry and Hf–Nd isotopic decoupling: Gondwana Research, v. 21, no. 1, p. 266–280. doi:10.1016/j.gr.2011.05.009

Torres-de León, R., Solari, L.A., Ortega-Gutiérrez, F., and Martens, U., 2012, The Chortís Block—Southwestern México connections: U-Pb zircon geochronology constraints: American Journal of Science, v. 312, no. 3, p. 288–313. doi:10.2475/03.2012.02

Tribuzio, R., Messiga, B., Vannucci, R., and Bottazzi, P., 1996, Rare earth element redistribution during high-pressure–low-temperature metamorphism in ophiolitic Fe-gabbros (Liguria, northwestern Italy): Implications for light REE mobility in subduction zones: Geology. v. 24, p. 711–714. doi:10.1130/0091-7613(1996)024<0711:REERDH>2.3.CO;2

Vermeesch, P., 2009, RadialPlotter: A Java application for fission track, luminescence and other radial plots: Radiation Measurements. v. 44, p. 409–410. doi:10.1016/j.radmeas.2009.05.003

Weber, B., Cameron, K.L., Osorio, M., and Schaaf, P., 2005, A late Permian tectonothermal event in Grenville crust of the southern Maya terrane: U-Pb zircon ages from the Chiapas Massif, southeastern Mexico: International Geology Review. v. 47, p. 509–529. doi:10.2747/0020-6814.47.5.509

Weber, B., González Guzmean, R., Cisneros De León, A., Manjarrez Juárez, R., Martens, U., Estrada Carmona, J., and Hecht, L., 2015, El Macizo de Chiapas – registro geológico de una evolución tectónica de 1000 Ma: Puerto Vallarta 2015: México, Reunión Anual de la Unión Geofísica Mexicana, SE05-2.

Weber, B., and Hecht, L., 2003, Petrology and geochemistry of metaigneous rocks from a Grenvillian basement fragment in the Maya block: The Guichicovi complex, Oaxaca, southern Mexico: Precambrian Research. v. 124, p. 41–67. doi:10.1016/S0301-9268(03)00078-0

Weber, B., Iriondo, A., Premo, W.R., Hecht, L., and Schaaf, P., 2007, New insights into the history and origin of the southern Maya block, SE México: U–Pb–SHRIMP zircon geochronology from metamorphic rocks of the Chiapas massif: International Journal of Earth Sciences. v. 96, p. 253–269. doi:10.1007/s00531-006-0093-7

Weber, B., Valencia, V.A., Schaaf, P., and Ortega-Gutiérrez, F., 2009, Detrital zircon ages from the Lower Santa Rosa Formation, Chiapas: Implications on regional Palaeozoic stratigraphy: Revista Mexicana de Ciencias Geológicas, v. 26, p. 260–276.

Weber, B., Valencia, V.A., Schaaf, P., Pompa-Mera, V., and Ruiz, J., 2008, Significance of Provenance Ages from the Chiapas Massif Complex (Southeastern Mexico): Redefining the Paleozoic Basement of the Maya Block and Its Evolution in a Peri-Gondwanan Realm: The Journal of Geology. v. 116, p. 619–639. doi:10.1086/591994

Webster, J.D., and Piccoli, P.M., 2015, Magmatic apatite: A powerful, yet deceptive, mineral: Elements. v. 11, p. 177–182. doi:10.2113/gselements.11.3.177

Witt, C., Brichau, S., and Carter, A., 2012, New constraints on the origin of the Sierra Madre de Chiapas (south Mexico) from sediment provenance and apatite thermochronometry: Tectonics, v. 31, p. TC6001. doi:10.1029/2012TC003141

Zhang, Z.-M., Shen, K., Sun, W.-D., Liu, Y.-S., Liou, J.G., Shi, C., and Wang, J.-L., 2008, Fluids in deeply subducted continental crust: Petrology, mineral chemistry and fluid inclusion of UHP metamorphic veins from the Sulu orogen, eastern China: Geochimica Et Cosmochimica Acta, v. 72, no. 13, p. 3200–3228. doi:10.1016/j.gca.2008.04.014

7. RECONSTRUCCIONES PALEOGEOGRÁFICAS

Los resultados de las dataciones termocronológicas y los datos de procedencia de sedimentos obtenidos en esta tesis pueden ser útiles para un mejor entendimiento de la evolución paleogeográfica de la Sierra de Chiapas y el norte de Guatemala. En este trabajo, se propone, a grandes rasgos, una reconstrucción paleogeográfica para el territorio de estudio, desde el Cretácico hasta el Plioceno, tomando en cuenta las reconstrucciones realizadas previamente (*e.g.*, Meneses-Rocha, 1991, 2001).

Paleogeografía del Albiano–Santoniano (Figura 7.1):

Durante el Albiano al Santoniano, prácticamente todo el territorio de Chiapas y de la Plataforma Yucatán estaba cubierto por una extensa plataforma carbonatada del Grupo Sierra Madre (Rosales-Domínguez, 1998; Meneses-Rocha, 2001; Sánchez *et al*., 2004). Los resultados termocronológicos obtenidos para la subprovincia Sierra Monoclinal (ver las modelaciones térmicas en la Figura 6 de Abdullin *et al*., 2016a) confirman también que la parte occidental de la Sierra de Chiapas estaba cubierta por esta plataforma, ya que los apatitos detríticos de la Formación Todos Santos sufrieron un reseteo significativo debido a su sepultamiento durante el Cretácico. La ausencia de actividades magmáticas así como la ausencia de aporte de sedimentos terrígenos

reflejan un periodo importante de quiescencia tectónica para el periodo Albiano–Santoniano (*e.g.*, Meneses-Rocha, 2001; Sánchez-Montes de Oca, 2006).

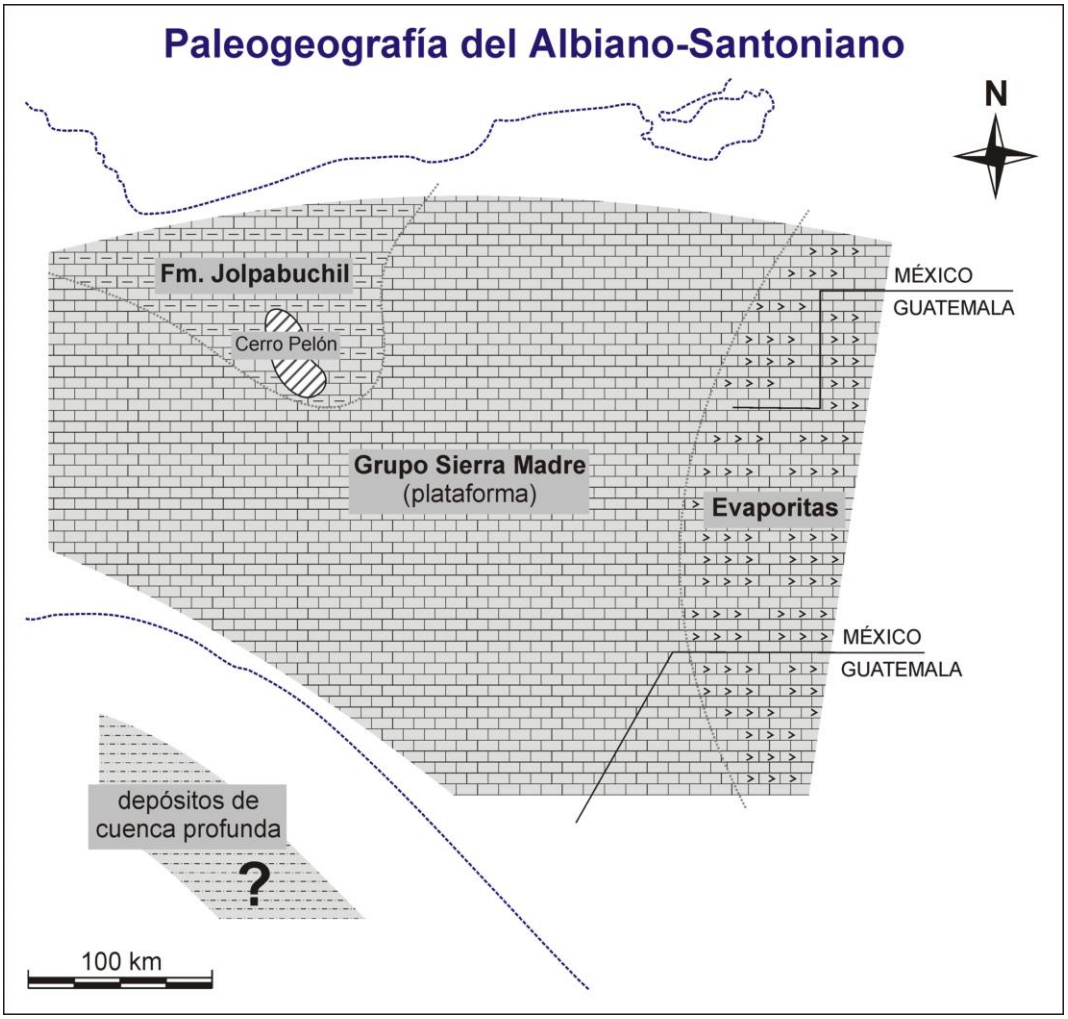

Figura 7.1. Modelo paleogeográfico para el periodo Albiano–Santoniano.

Modificado de Meneses-Rocha (1991, 2001).

El único lugar de Chiapas en donde ha sido registrada una actividad tectónica es el área del Cerro Pelón (ver Figura 7.1), la cual aparentemente fue causada por un movimiento de la Sal Jurásica (Meneses-Rocha, 1991).

Paleogeografía del Campaniano–Maastrichtiano (Figura 7.2):

Durante el Campaniano al Maastrichtiano tuvo lugar un cambio drástico en la sedimentación. Un evento tectónico destruyó, en parte, la plataforma carbonatada del Cretácico. Este evento fue la causa principal de la exhumación de algunas partes del Macizo de Chiapas (Figura 7.2), del cual provinieron los sedimentos clásticos de alta energía que se depositaron en un ambiente costero (la Formación Ocozocoautla). En varias secuencias del Campaniano–Maastrichtiano se pueden observar también las brechas carbonatadas (Meneses-Rocha, 2001), las cuales seguramente representan un reciclaje de carbonatos del Grupo Sierra Madre (Figura 7.2). Para el área de Chiapas, han sido reportadas también evidencias de un evento volcánico de edad Campaniana (Meneses-Rocha, 1991). De acuerdo con muchos autores, el Campaniano de Chiapas refleja el inicio de la Orogenia Laramide (Carfantan, 1981; Moravec, 1983; Meneses-Rocha, 1985, 1991, 2001; Burkart *et al*., 1987; Sánchez-Montes de Oca, 2006; Ham-Wong, 2007). Esta hipótesis se confirmó también en este estudio usando la técnica de trazas de fisión en apatitos (ver en Abdullin *et al*., 2016a).

Es importante decir que este evento, al parecer, también afectó al área que ocupa actualmente el Golfo de Tehuantepec, ya que Sánchez-Barreda (1981) observó una discordancia en esta región entre el Santoniano y el Paleoceno (Figura 7.2).

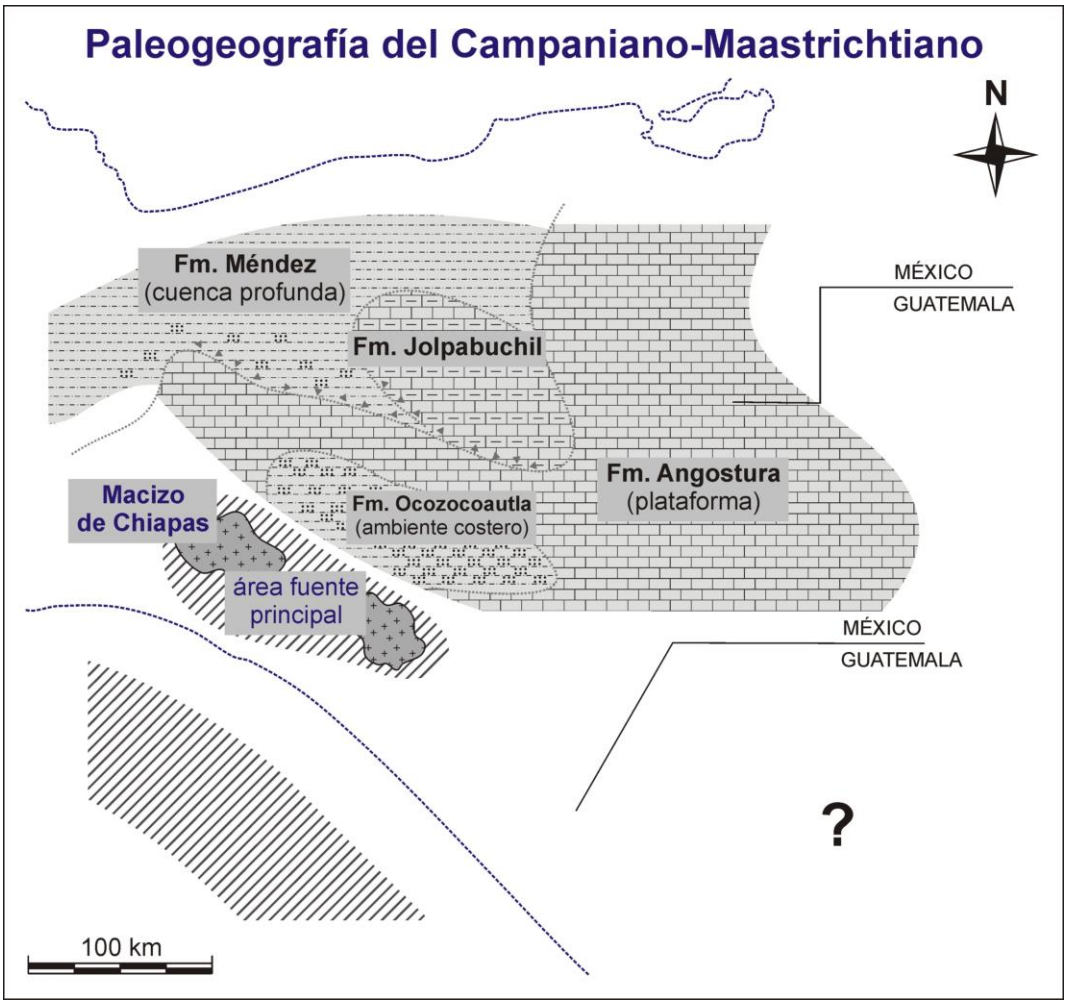

Figura 7.2. Modelo paleogeográfico para el periodo Campaniano–Maastrichtiano. Modificado de Meneses-Rocha (1991, 2001).

Paleogeografía del Paleoceno (Figura 7.3):

El carácter de la sedimentación en la Sierra de Chiapas cambió mucho en el Paleoceno. Durante esta etapa se depositaron los sedimentos turbidíticos que forman las Formaciones Soyaló y Lutitas Nanchital (Figura 7.3). La mayor proporción de los sedimentos de estas unidades litoestratigráficas no provienen del Macizo de Chiapas (Witt *et al*., 2012). De acuerdo con Meneses-Rocha (1991, 2001), estos sedimentos siliciclásticos proceden principalmente del Grupo Santa Rosa así como del complejo metamórfico Chuacús (Figura 7.3). Los datos termocronológicos obtenidos en las rocas de la Formación Todos Santos (Abdullin *et al*., 2016a) indican que el área del Macizo de Chiapas y de la Sierra Monoclinal sufrió un levantamiento relativamente lento (con unas tasas de enfriamiento menores de 3 °C/Ma) durante el Paleoceno (el evento Laramídico), lo cual podría implicar también que el Macizo de Chiapas no fue el área fuente principal para las secuencias sedimentarias del Paleoceno en Chiapas. Por lo tanto, los sedimentos del Paleoceno, igual que los del Eoceno, deben provenir principalmente de áreas fuente de Guatemala (Meneses-Rocha, 1991, 2001; Abdullin *et al*., 2016a). Sin embargo, se requiere realizar urgentemente estudios de procedencia detallados de los sedimentos de las Formaciones del Paleoceno.

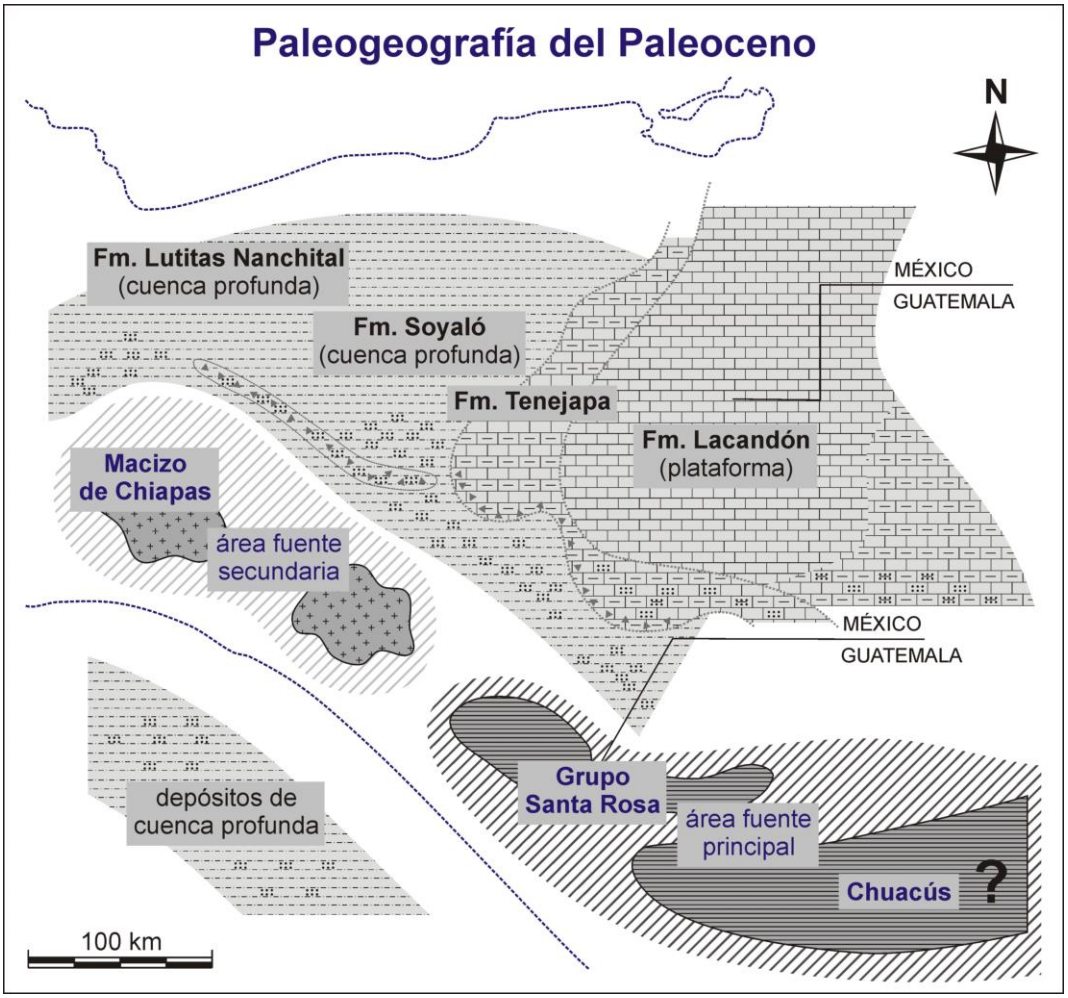

Figura 7.3. Modelo paleogeográfico para el Paleoceno. Modificado de Meneses-Rocha (1991, 2001).

Paleogeografía del Eoceno (Figura 7.4):

El inicio del Eoceno marca el fin de la Orogenia Laramide en Chiapas (*e.g.*, Meneses-Rocha, 2001; Abdullin *et al*., 2016a). Los primeros estudios de procedencia de sedimentos realizados por Witt *et al*. (2012) demuestran que los sedimentos del

Eoceno no provienen del Macizo de Chiapas. Estos materiales clásticos proceden principalmente de rocas fuente del sur de Chiapas y de Guatemala (Meneses-Rocha, 1991, 2001; Abdullin *et al*., 2016b). Además, los datos de trazas de fisión de este estudio indican que el área del Macizo de Chiapas y de la Sierra Monoclinal no sufrió ningún tipo de levantamiento notable durante el Eoceno inferior y el Oligoceno.

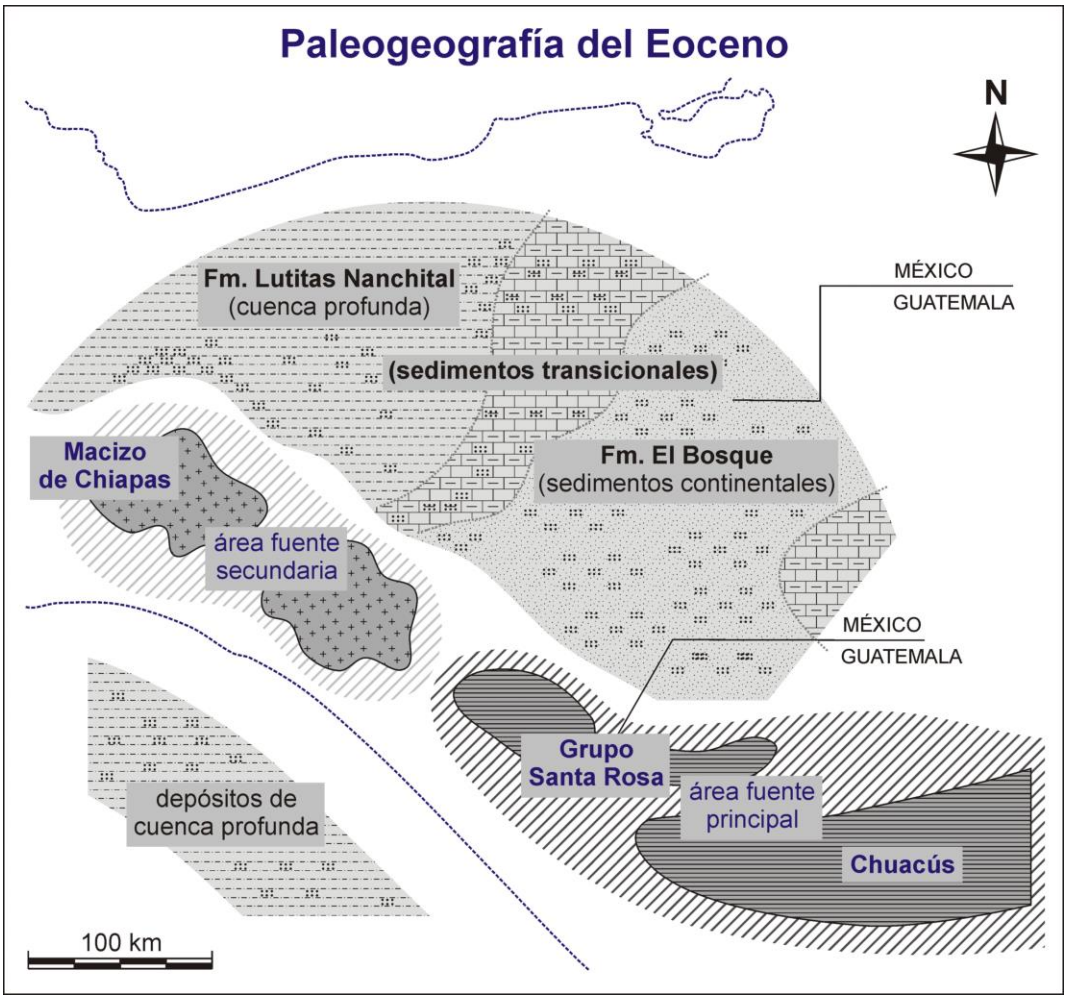

Figura 7.4. Modelo paleogeográfico para el Eoceno. Modificado de Meneses-Rocha (1991, 2001).

Paleogeografía del Oligoceno (Figura 7.5):

En el Oligoceno (Figura 7.5), la mayor parte del territorio de la Sierra de Chiapas empieza a erosionarse (*e.g.*, ver Quezada-Muñetón, 1987) y se depositan los sedimentos mixtos así como los de cuenca profunda (son de baja energía).

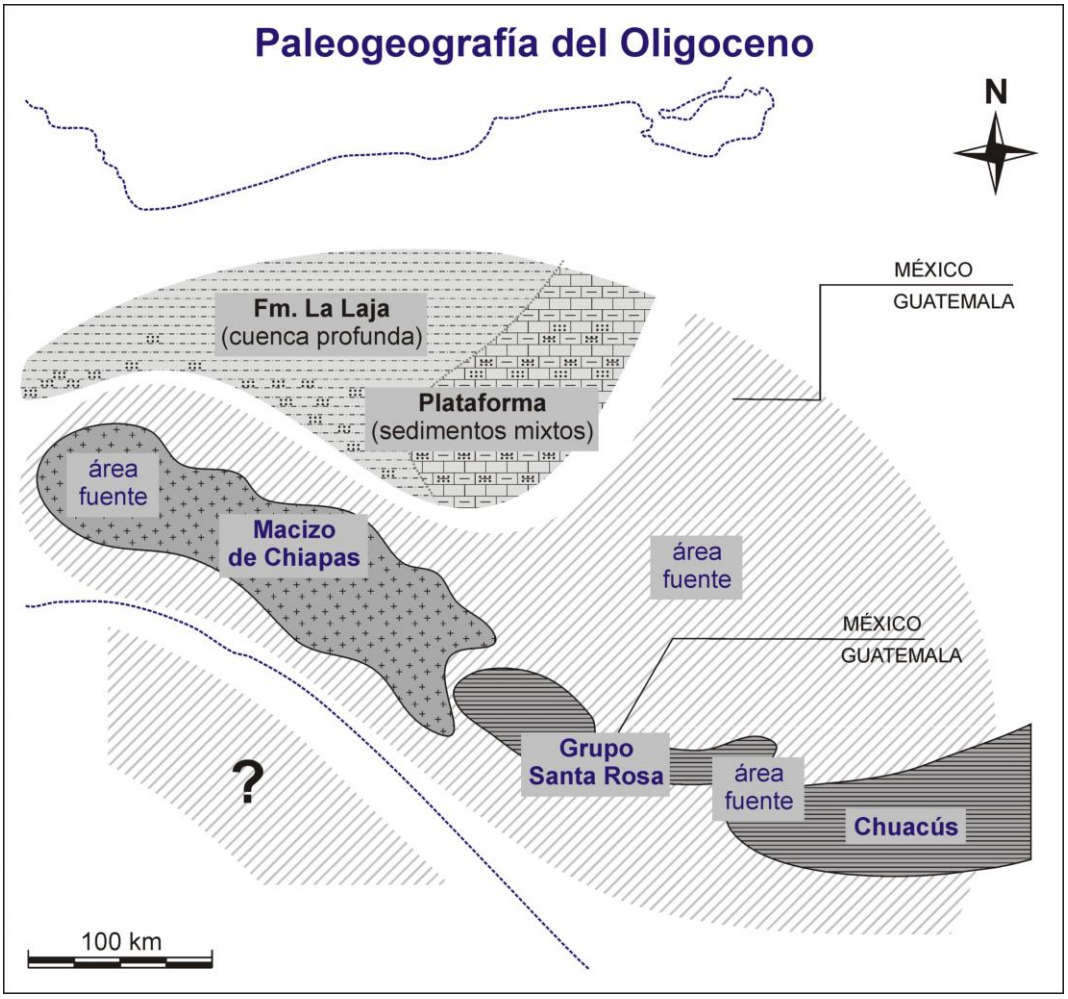

Figura 7.5. Modelo paleogeográfico para el Oligoceno. Modificado de Meneses-Rocha (1991, 2001).

Paleogeografía del Mioceno–Plioceno (Figura 7.6):

El evento termo-tectónico Chiapaneco tuvo lugar durante el Mioceno medio y superior y fue el más importante en el desarrollo de las estructuras geológicas actuales (Figura 7.6). Este evento fue detectado en todo el territorio de la Sierra de Chiapas usando métodos termocronológicos (Ratschbacher *et al*., 2009; Witt *et al*., 2012; este estudio). El evento del Mioceno fue acompañado por un magmatismo a lo largo de la Zona de Cizalla de Tonalá (Witt *et al*., 2012; Molina-Garza *et al*., 2015) y fue la causa de una erosión extensa en Chiapas (Figura 7.6) y de un aporte importante de sedimentos clásticos hacía la Planicie de Tabasco (*e.g*., Sánchez-Montes de Oca, 1979, 2007; Carfantan, 1981; Meneses-Rocha, 1985, 1991, 2001; Quezada-Muñetón, 1987; Guzmán-Speziale, 2010). De acuerdo con algunos autores (*e.g*., Molina-Garza *et al*., 2015), este evento podría relacionarse hipotéticamente con el movimiento del Bloque Chortís, aunque no se conoce hasta ahora, con certeza, su interacción con el Bloque Maya. Durante el Plioceno, se generan muchas rocas volcánicas a lo largo del área de Chiapas (Figura 7.6), las cuales forman parte del Arco Volcánico Chiapaneco (del Plioceno hasta reciente; *e.g*., ver Mora *et al*., 2012).

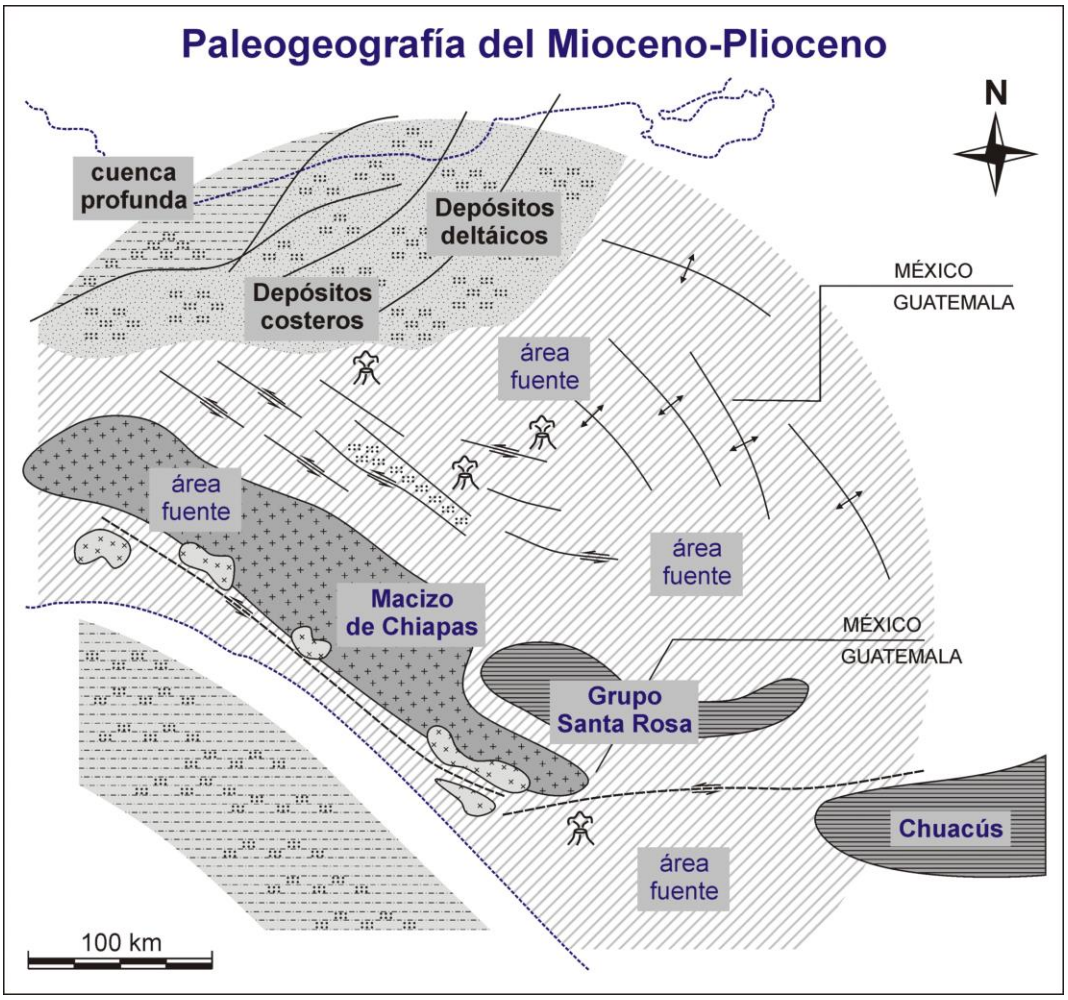

Figura 7.6. Modelo paleogeográfico para el periodo Mioceno–Plioceno.

Modificado de Meneses-Rocha (1991, 2001).

8. CONCLUSIONES GENERALES

1. Este estudio demostró que la técnica de trazas de fisión por medio de LA-ICP-MS es capaz de ser una alternativa al método clásico de detector externo. El método con LA-ICP-MS tiene más ventajas que desventajas si se compara con el método de detector externo. Por ejemplo, es más rápido y económico ya que no requiere la irradiación de las muestras en un reactor nuclear. Además, el método basado en las mediciones directas de U permite al mismo tiempo medir las concentraciones de otros elementos traza y REE, lo que es muy útil para los estudios petrogenéticos y, sobre todo, para identificar la procedencia de sedimentos siliciclásticos.

2. Los resultados termocronológicos y geoquímicos obtenidos en este estudio, así como datos geológicos previamente reportados, indican que la Sierra de Chiapas experimentó una evolución geodinámica bastante compleja y con múltiples episodios. Un total de cinco eventos termo-tectónicos y tectono-magmáticos importantes se pueden proponer para el territorio de Chiapas, desde el Pérmico hasta el reciente: (a) El evento tectono-magmático del Pérmico–Triásico que formó el Macizo de Chiapas; (b) Un volcanismo de arco del Jurásico inferior–medio, el cual afectó al Macizo de Chiapas; (c) La Orogenia Laramide que tuvo lugar en la Sierra de Chiapas durante el Cretácico superior–Eoceno inferior; (d) El evento Chiapaneco que tuvo lugar en el Mioceno medio y superior; y (e) Un nuevo arco volcánico del Plioceno al Holoceno.

3. El estudio de la procedencia de sedimentos que se ha realizado a partir de los datos geoquímicos de apatitos obtenidos durante los análisis por trazas de fisión indican: (a) los sedimentos clásticos del Jurásico–Cretácico inferior (las Formaciones Todos Santos y San Ricardo) provienen principalmente de la erosión del Macizo de Chiapas; (b) los sedimentos del Cenozoico, particularmente del Eoceno (Formación El Bosque), provienen de la erosión de una cadena montañosa al norte de Guatemala.

REFERENCIAS BIBLIOGRÁFICAS

Abdullin, F., Solé, J., y Solari, L., 2014, Datación mediante trazas de fisión y análisis multielemental con LA-ICP-MS del fluorapatito de Cerro de Mercado (Durango, México): Revista Mexicana de Ciencias Geológicas, v. 31 (3), p. 395–406.

Abdullin, F., Solé, J., Meneses-Rocha, J.D.J., Solari, L., Shchepetilnikova, V., and Ortega-Obregón, C., 2016a, LA-ICP-MS-based apatite fission-track dating of the Todos Santos Formation sandstones from the Sierra de Chiapas (SE Mexico) and its tectonic significance: International Geology Review, v. 58 (1), p. 32–48.

Abdullin, F., Solé, J., Solari, L., Shchepetilnikova, V., Meneses-Rocha, J.J., Pavlinova, N., and Rodríguez-Trejo, A., 2016b, Single-grain apatite geochemistry of Permian–Triassic granitoids and Mesozoic and Eocene sandstones from Chiapas, SE Mexico: implications for sediment provenance: International Geology Review, doi:10.1080/00206814.2016.1150212.

Andreani, L., and Gloaguen, R., 2016, Geomorphic analysis of transient landscapes in the Sierra Madre de Chiapas and Maya Mountains (northern Central America): implications for the North American-Caribbean-Cocos plate boundary: Earth Surface Dynamics, v. 4 (1), p. 71.

Barbarand, J., Carter, A., Wood, I., and Hurford, T., 2003, Compositional and structural control of fission-track annealing in apatite: Chemical Geology, v. 198, p. 107–137.

Bernet, M., Brandon, M.T., Garver, J.I., and Molitor, B.R., 2004, Fundamentals of detrital zircon fission-track analysis for provenance and exhumation studies with examples from the European Alps, in Bernet, M., Spiegel , C. (eds.) Detrital Thermochronology – Provenance Analysis, Exhumation, and Landscape Evolution of Mountain Belts: Geological Society of America, Special Paper 378, p. 25–36.

Bernet, M., and Garver, J.I., 2005, Fission-track analysis of detrital zircon. Reviews in Mineralogy and Geochemistry, v. 58 (1), p. 205–237.

Bernet, M., 2009, A field-based estimate of the zircon fission-track closure temperature: Chemical Geology, v. 259 (3), p. 181–189.

Blair, T.C., 1987, Tectonic and hydrologic controls on cyclic alluvial fan, fluvial, and lacustrine rift-basin sedimentation, Jurassic–lowermost Cretaceous Todos Santos Formation, Chiapas, Mexico: Journal of Sedimentary Research, v. 57, p. 845–862.

Burkart, B., Deaton, B.C., Dengo, C., and Moreno, G., 1987, Tectonic wedges and offset Laramide structures along the Polochic fault of Guatemala and Chiapas, Mexico: Reaffirmation of large Neogene displacement: Tectonics, v. 6, p. 411–422.

Calmus, T., Poupeau, G., Bourgois, J., Michaud, F., Mercier de Lépinay, B., Labrin, E., and Azdimousa, A., 1999, Late Mesozoic and Cenozoic thermotectonic history of the Mexican Pacific margin (18 to 25°N): new insight from apatite and zircon fission-track analysis of coastal and offshore plutonic rocks: Tectonophysics, v. 306, p. 163–182.

Calmus, T., Bernet, M., Lugo-Zazueta, R., Hardwick, E., and Mendivil-Quijada, H., 2015, Apatite fission-track thermochronology of Laramide plutonic rocks in northwestern Mexico: Distinguishing Basin and Range extension versus Gulf of California rifting. Revista Mexicana de Ciencias Geológicas, v. 32 (3), p. 529–541.

Carfantan, J.C., 1981, Evolución estructural del sureste de México, Paleogeografía e historia tectónica de las zonas internas mesozoicas: Revista Mexicana de Ciencias Geológicas, v. 5, p. 207–216.

Chew, D.M., and Donelick, R.A., 2012, Combined apatite fission-track and U-Pb dating by LA-ICP-MS and its application in apatite provenance analysis, *in* Sylvester, P., ed., Quantitative Mineralogy and Microanalysis of Sediments and Sedimentary Rocks: Mineralogical Association of Canada, Short Course 42, p. 219–247.

Cochrane, R., Spikings, R.A., Chew, D., Wotzlaw, J.F., Chiaradia, M., Tyrrell, S., ... and Van der Lelij, R., 2014, High temperature (> 350 C) thermochronology and mechanisms of Pb loss in apatite: Geochimica et Cosmochimica Acta, v. 127, p. 39–56.

Coyle, D.A., and Wagner, G.A., 1998, Positioning the titanite fission-track partial annealing zone: Chemical Geology, v. 149 (1), p. 117–125.

Curvo, E.A.C., Carter, A., Dias, A.N.C., Soares, C.J., Nakasuga, W.M., Resende, R.S., ... and Hadler, J.C., 2013, Zircon fission track and U–Pb dating methods applied to São Paulo and Taubaté Basins located in the southeast Brazil: Radiation Measurements, v. 50, p. 172–180.

Damon, P.E., Shafiqullah, M., and Clark, K.F., 1981, Evolución de los arcos magmáticos en México y su relación con la metalogénesis: Revista Mexicana de Ciencias Geológicas, v. 5, p. 223–238.

Dodson, M.H., 1973, Closure temperature in cooling geochronological and petrological systems: Contributions to Mineralogy and Petrology, v. 40, p. 259–274.

Donelick, R.A., O'Sullivan, P.B., and Ketcham, R.A., 2005, Apatite fission-track analysis: Reviews in Mineralogy and Geochemistry, v. 58, p. 49–94.

Ducea, M.N., Valencia, V.A., Shoemaker, S., Reiners, P.W., De Celles, P.G., Campa, M.F., and Morán-Zenteno, D., 2004, Rates of sediment recycling beneath the Acapulco trench: Constraints from (U-Th)/He thermochronology: Journal of Geophysical Research, v. 109, B09404, doi:10.1029/2004JB003112.

Estrada-Carmona, J., Weber, B., Hecht, L., and Martens, U., 2009, PTt trajectory of metamorphic rocks from the central Chiapas Massif Complex: the Custepec Unit, Chiapas, México: Revista Mexicana de Ciencias Geológicas, v. 26, p. 243–259.

Estrada-Carmona, J., Weber, B., Martens, U., and López-Martínez, M., 2012, Petrogenesis of Ordovician magmatic rocks in the southern Chiapas Massif Complex: Relations with the early Palaeozoic magmatic belts of northwestern Gondwana: International Geology Review, v. 54, p. 1918–1943.

Farley, K.A., 2002, (U-Th)/He dating: techniques, calibrations, and applications: Reviews in Mineralogy and Geochemistry, v. 47 (1), p. 819–844.

Fleischer, R.L., Price, P.B., Walker, R.M., Leakey, L.S.B., 1965, Fission-track dating of Bed I, Olduvai Gorge: Science, v. 148, p. 72–74.

Fleischer, R.L., Price, P.B., and Walker, R.M., 1975, Nuclear tracks in solids: principles and applications. University of California Press.

Flerov, G.N., and Petrzhak, K.A., 1940, Spontaneous fission of uranium (in Russian): Journal Fisika, v. 3, p. 275–380.

Galbraith, R.F., and Laslett, G.M., 1993, Statistical models for mixed fission track ages: Nuclear Tracks and Radiation Measurements, v. 21, p. 459–470.

Gallagher, K., 1995, Evolution temperature histories from apatite fission-track data: Earth and Planetary Science Letters, v. 136, p. 421–435.

Gleadow, A.J.W., Duddy, I.R., Green, P.F., and Lovering, J.F., 1986, Confined fission track lengths in apatite: a diagnostic tool for thermal history analysis: Contributions to Mineralogy and Petrology, v. 94, p. 405–415.

Gleadow, A., Harrison, M., Kohn, B., Lugo-Zazueta, R., and Phillips, D., 2015, The Fish Canyon Tuff: a new look at an old low-temperature thermochronology standard: Earth and Planetary Science Letters, v. 424, p. 95–108.

Godinez-Urban, A., Lawton, T.F., Molina Garza, R.S., Iriondo, A., Weber, B., and Lopez-Martinez, M., 2011, Jurassic volcanic and sedimentary rocks of the La Silla and Todos Santos Formations, Chiapas: Record of Nazas arc magmatism and rift-basin formation prior to opening of the Gulf of Mexico: Geosphere, v. 7, p. 121–144.

Guedes, S., Hadler, J.C., Sarkis, J.E.S., Oliveira, K.M.G., Kakazu, M.H., Iunes, P.J., Saiki, M., Tello, C.A., and Paulo, S.R., 2003, Spontaneous-fission decay constant of ^{238}U measured by nuclear track techniques without neutron irradiation: Journal of Radioanalytical and Nuclear Chemistry, v. 258, p. 117–122.

Guo, S., Ye, K., Wu, T.F., Chen, Y., Yang, Y.H., Zhang, L.M., Liu, J.B., Mao, Q., and Ma, Y.G., 2013, A potential method to confirm the previous existence of lawsonite in eclogite: the mass imbalance of Sr and LREEs in multistage epidote (Ganghe, Dabie UHP terrane): Journal of Metamorphic Geology, v. 31(4), p. 415–435.

Guzmán-Speziale, M., 2010, Beyond the Motagua and Polochic faults: Active strike-slip faulting along the Western North America–Caribbean plate boundary zone: Tectonophysics, v. 496, p. 17–27.

Hadler, J.C., Iunes, P.J., Tello, C.A., Chemale, Jr.F., Kawashita, K., Curvo, E.A.C., Santos, F.G.S., Gasparini, T.E., Moreira, P.A.F.P., and Guedes, S., 2009, Experimental study of a methodology for fission-track dating without neutron irradiation: Radiation Measurements, v. 44, p. 955–957.

Ham-Wong, J.M., 2007, Libreto Guía. Para el Proyecto de caracterización de sistemas de fracturas del Mesozoico del área Chiapas-Tabasco, México: Petróleos Mexicanos.

Hasebe, N., Barbarand, J., Jarvis, K., Carter, A., and Hurford, A.J., 2004, Apatite fission-track chronometry using laser ablation ICP-MS: Chemical Geology, v. 207, p. 135–145.

Hasebe, N., Carter, A., Hurford, A.J., and Arai, S., 2009, The effect of chemical etching on LA-ICP-MS analysis in determining uranium concentration for fission-track chronometry, *in* Lisker, F., Ventura, B., and Glasmacher, U.A., eds., Thermochronological methods: from palaeotemperature constraints to landscape evolution models: Geological Society of London, Special Publications, v. 324, p. 37–46.

Hasebe, N., Arai, S., 2007, LA-ICP-MS-FT dating of age standards: Fission Track News Lett., v. 20, p. 40–41 (in Japanese).

Hermann, J., 2002, Allanite: thorium and light rare earth element carrier in subducted crust: Chemical Geology, v. 192(3), p. 289–306.

Holden, N.E., and Hoffman, D.C., 2000, Spontaneous fission half-lives for ground-state nuclides (Technical report): Pure and Applied Chemistry, v. 72, p. 1525–1562.

Ketcham, R.A., Donelick, R.A., and Carlson, W.D., 1999, Variability of apatite fission-track annealing kinetics. III. Extrapolation to geological time scales: American Mineralogist, v. 84, p. 1235–1255.

Kowallis, B.J., Swisher, C.C., Carranza-Castañeda, O., Miller, W.D., and Tingey, D.G., 1998, Fission-track and single-crystal $^{40}Ar/^{39}Ar$ laser-fusion ages from volcanic ash layers in fossil-bearing Pliocene sediments in Central Mexico: Revista Mexicana de Ciencias Geológicas, v. 15 (2), p. 157–160.

Lee, J.K., Williams, I.S., and Ellis, D.J., 1997, Pb, U and Th diffusion in natural zircon: Nature, v. 390 (6656), 159–162.

Liu, W., Zhang, J., Sun, T., and Wang, J., 2014, Application of apatite U–Pb and fission-track double dating to determine the preservation potential of magnetite–apatite deposits in the Luzong and Ningwu volcanic basins, eastern China: Journal of Geochemical Exploration, v. 138, p. 22–32.

Mandujano Velásquez, J., 1996, Cuatro megasecuencias de evolución litoestratigráfica en la Sierra de Chiapas: Boletín de la Asociación Mexicana de Geólogos Petroleros, v. 45, p. 46–60.

Meneses-Rocha, J.J., 1985, Tectonic evolution of the Strike-slip Fault province of Chiapas, Mexico [M.S. thesis]: University of Texas at Austin, 315 p.

Meneses-Rocha, J.J., 1991, Tectonic development of the Ixtapa graben, Chiapas, Mexico [Ph.D. thesis]: University of Texas at Austin, 308 p.

Meneses-Rocha, J.J., 2001, Tectonic evolution of the Ixtapa Graben, an example of a strike-slip basin of southeastern Mexico: Implications for regional petroleum systems, *in* Bartolini, C., Buffler, R.T., and Cantú-Chapa, A., eds., The Western Gulf of Mexico Basin: Tectonics, Sedimentary Basins and Petroleum Systems: AAPG Memoir, v. 75, p. 183–216.

Molina-Garza, R.S., Geissman, J.W., Wawrzyniec, T.F., Peña Alonso, T.A., Iriondo, A., Weber, B., and Aranda-Gómez, J., 2015, Geology of the coastal Chiapas (Mexico) Miocene plutons and the Tonalá shear zone: Syntectonic emplacement and rapid exhumation during sinistral transpression: Lithosphere, v. 7, p. 257–274.

Mora, J. C., Layer, P.W., and James-Viera, M.D.C., 2012, New $^{40}Ar/^{39}Ar$ ages from the central part of the Chiapanecan Volcanic Arc, Chiapas, México. Geofísica Internacional, v. 51 (1), p. 39–49.

Moravec, D., 1983, Study of the Concordia Fault System near Jericó, Chiapas, Mexico [M.S. thesis]: University of Texas at Austin, 155 p.

Ortega-Rivera, A., Farrar, E., Hanes, J.A., Archibald, D.A., Gastil, R.G., Kimbrough, D.L., ... and Ruffet, G., 1997, Chronological constraints on the thermal and tilting history of the Sierra San Pedro Martir pluton, Baja California, Mexico, from U/Pb, $^{40}Ar/^{39}Ar$, and fission-track geochronology: Geological Society of America Bulletin, v. 109 (6), p. 728–745.

Ortega-Rivera, A., 2003, Geochronological constraints on the tectonic history of the Peninsular Ranges batholith of Alta and Baja California: Tectonic implications for western Mexico: Special papers, Geological Society of America, p. 297–336.

Padilla y Sánchez, R.J., 2007, Evolución geológica del sureste mexicano desde le Mesozoico al presente en el contexto regional del Golfo de México: Boletín de la Sociedad Geológica Mexicana, v. 59, p. 19–42.

Pi, T., Solé, J., and Taran, Y., 2005, (U-Th)/He dating of fluorite: application to the La Azul fluorspar deposit in the Taxco mining district, Mexico: Mineralium Deposita, v. 39, p. 976–982.

Price, P.B., and Walker, R.M., 1962, Observation of fossil particle tracks in natural micas: Nature, v. 196, p. 732–734.

Price, P.B., and Walker, R.M., 1963, Fossil tracks of charged particles in mica and the age of minerals: Journal of Geophysical Research, v. 68 (16), p. 4847–4862.

Quezada-Muñetón, J.M., 1983, Las Formaciones San Ricardo y Jericó del Jurásico Medio–Cretácico Inferior en el SE de México: Boletín de la Asociación Mexicana de Geólogos Petroleros, v. 35, p. 37–64.

Quezada-Muñetón, J.M., 1987, El Cretácico medio–Superior y el límite Cretácico Superior–Terciario inferior en la Sierra de Chiapas: Boletín de la Asociación Mexicana de Geólogos Petroleros, v. 39, p. 3–98.

Ratschbacher, L., Franz, L., Min, M., Bachmann, R., Martens, U., Stanek, K., Stübner, K., Nelson, B.K., Herrmann, U., Weber, B., López-Martínez, M., Jonckheere, R., Sperner, B., Tichomirowa, M., McWilliams, M.O., Gordon, M., Meschede, M., and Bock, P., 2009, The North American–Caribbean plate boundary in Mexico–Guatemala–Honduras, *in* James, K., Lorente, M., Pindell, J., eds., The Origin and Evolution of the Caribbean Plate: Geological Society of London, Special Publications, v. 328, p. 219–293.

Reiners, P., 2005, Zircon (U-Th)/He thermochronology: Reviews in Mineralogy and Geochemistry, v. 58, p. 151–179.

Rosales-Domínguez, M.D.C., Bermúdez-Santana, J.C., and Aguilar-Piña, M., 1997, Mid and Upper Cretaceous foraminiferal assemblages from the Sierra de Chiapas, southeastern Mexico: Cretaceous Research, v. 18, p. 697–712.

Rosales-Domínguez, M.D.C., 1998, Biohorizontes cronoestratigráficos en las facies carbonatadas de plataforma del Cretácico medio–superior de Chiapas, México: Revista Mexicana de Ciencias Geológicas, v. 15, p. 73–77.

Sánchez, M.O., Franco, N.A., Navarrete, S.F., and Martínez, M.G., 2004, Estratigrafía y evolución de facies del Cretácico Superior en el Sureste de México: Boletín de la Asociación Mexicana de Geólogos Petroleros, paper No. 697, p. 40–61.

Sánchez-Barreda, L.A., 1981, Geologica evolution of the continental margin of the Gulf of Tehuantepec in Southwestern Mexico: PhD Thesis, Department of Geological Sciences, The University of Texas at Austin.

Sánchez-Montes de Oca, R., 1979, Geología petrolera de la Sierra de Chiapas: Boletín de la Asociación Mexicana de Geólogos Petroleros, v. 31, p. 67–97.

Sánchez-Montes de Oca, R., 2006, Curso Cuenca del Sureste: México, Petróleos Mexicanos, 296 p.

Sassi, R., Harte, B., Carswell, D.A., and Yujing, H., 2000, Trace element distribution in Central Dabie eclogites: Contributions to Mineralogy and Petrology, v. 139(3), p. 298–315.

Schaaf, P., Weber, B., Weis, P., Groβ, A., Ortega-Gutiérrez, F., and Kohler, H., 2002, The Chiapas Massif (Mexico) revised: New geologic and isotopic data and basement characteristics, *in* Miller, H.E., ed., Contributions to Latin-American Geology: Neues Jahrbuch für Geologie und Paläontologie, Abhandlungen, v. 225, p. 1–23.

Schoene, B., and Bowring, S.A., 2007, Determining accurate temperature–time paths from U–Pb thermochronology: an example from the Kaapvaal craton, southern Africa: Geochimica et Cosmochimica Acta, v. 71 (1), p. 165–185.

Solé, J., and Pi, T., 2005, An empirical calibration for ^{4}He quantification in minerals and rocks by laser fusion and noble gas mass spectrometry using Cerro de Mercado (Durango, Mexico) fluorapatite as a standard: Analytica Chimica Acta, v. 535, p. 325–330.

Spandler, C., Hermann, J., Arculus, R., and Mavrogenes, J., 2003, Redistribution of trace elements during prograde metamorphism from lawsonite blueschist to eclogite facies; implications for deep subduction-zone processes: Contributions to Mineralogy and Petrology, v. 146, p. 205–222.

Wagner, G., and Van den Haute, P., 1992, Fission Track Dating: Dordrecht, Holland, Kluwer, Earth Sciences Library, 285 pp.

Weber, B., Cameron, K.L., Osorio, M., and Schaaf, P., 2005, A Late Permian tectonothermal event in Grenville crust of the southern Maya terrane: U-Pb zircon ages from the Chiapas Massif, southeastern Mexico: International Geology Review, v. 47, p. 509–529.

Weber, B., Iriondo, A., Premo, W.R., Hecht, L., and Schaaf, P., 2007, New insights into the history and origin of the southern Maya block, SE Mexico: U–Pb–SHRIMP zircon geochronology from metamorphic rocks of the Chiapas massif: International Journal of Earth Sciences, v. 96, p. 253–269.

Weber, B., Valencia, V.A., Schaaf, P., Pompa-Mera, V., and Ruiz, J., 2008, Significance of provenance ages from the Chiapas massif complex (Southeastern Mexico): redefining the Paleozoic basement of the Maya block and its evolution in a Peri-Gondwanan Realm: The Journal of Geology, v. 116, p. 619–639.

Weber, B., González Guzmean, R., Cisneros de León, A., Manjarrez Juárez, R., Martens, U., Estrada Carmona, J., Hecht, L., 2015, El Macizo de Chiapas – registro geológico de una evolución tectónica de 1000 Ma: Puerto Vallarta 2015, México, Reunión Anual de la Unión Geofísica Mexicana, SE05-2.

Witt, C., Brichau, S., and Carter, A., 2012, New constraints on the origin of the Sierra Madre de Chiapas (south Mexico) from sediment provenance and apatite thermochronometry: Tectonics, v. 31, TC6001, doi:10.1029/2012TC003141.

Yoshioka, T., Tsuruta, T., Iwano, H., Danhara, T., 2005, Spontaneous fission decay constant of ^{238}U determined by SSNTD method using CR-39 and DAP plates: Nuclear Instruments and Methods in Physics Research A, v. 555, p. 386–395.

APÉNDICES

Apéndice 1

Detalles de las dataciones de apatitos detríticos mediante trazas de fisión de cuatro areniscas de la Formación Todos Santos (ver también en Abdullin *et al*., 2016a).

Apéndice 2

Detalles de las dataciones de apatitos detríticos mediante trazas de fisión de dos areniscas de la Formación San Ricardo (ver también en Abdullin *et al*., 2016b).

Apéndice 3

Detalles de las dataciones de apatitos detríticos mediante trazas de fisión de cuatro areniscas de la Formación El Bosque.

Apéndice 4

Detalles de las dataciones de apatitos mediante trazas de fisión de cinco muestras del basamento cristalino (Macizo de Chiapas).

Apéndice 5

Composiciones geoquímicas de apatitos individuales obtenidas en todas las areniscas y en las muestras del Macizo de Chiapas (ver también en Abdullin *et al*., 2016b).

Apéndice 1

Supplementary Table A. LA-ICP-MS-based apatite fission track dating results of the standard Durango fluorapatite (DFA) and of the Todos Santos Formation sandstones (samples TS-1, TS-2, TS-3 and TS-4). Note: **^{238}U** is the uranium-238 concentration in ppm obtained by LA-ICP-MS technique. **± ^{238}Utot** represents the total uncertainty for ^{238}U content, including the analytical error of LA-ICP-MS measurement **(±1σ LA)** and an error generated by the common CaO variation (55 ± 2%) in apatites of different origin. ***A*** is the spontaneous fission track counting area in µm^2. **Ns** is the number of spontaneous fission tracks registered in the area ***A***. ***ps*** is the spontaneous fission track density (i.e. number of tracks expressed for 1 cm^2). **AFT age** corresponds to apatite fission track age in Ma with its absolute **±1σ** error.

SAMPLE: Standard DFA – Durango fluorapatite

Mean age = 31.8 ± 0.3 (1σ) Ma (n = 34; MSWD = 0.18; *P* = 1)

apatite	^{238}U (ppm)	±1σ LA	± ^{238}Utot	*A* (µm^2)	Ns	±Ns	*ps*	±*ps*	AFT age (Ma)	±1σ
CM 1-1	12.03	0.19	0.30	47040	92	2	195578	4252	31.7	1.6
CM 1-1	11.98	0.17	0.28	47040	92	2	195578	4252	31.8	1.6
CM 1-1	12.17	0.17	0.28	47040	92	2	195578	4252	31.3	1.5
CM 1-1	11.84	0.17	0.28	47040	92	2	195578	4252	32.2	1.6
CM 1-1	12.10	0.18	0.29	47040	92	2	195578	4252	31.5	1.6
CM-1-2	11.89	0.18	0.29	89340	173	3	193642	3358	31.8	1.5
CM 1-2	11.95	0.16	0.27	89340	173	3	193642	3358	31.6	1.5
CM 1-2	11.07	0.20	0.30	89340	173	3	193642	3358	34.1	1.7
CM 1-2	11.99	0.17	0.28	89340	173	3	193642	3358	31.5	1.5
CM 1-2	12.08	0.17	0.28	89340	173	3	193642	3358	31.3	1.5
CM 1-2	12.18	0.15	0.26	89340	173	3	193642	3358	31.0	1.4
CM 1-2	12.11	0.13	0.24	89340	173	3	193642	3358	31.2	1.4
CM 1-2	12.07	0.16	0.27	89340	173	3	193642	3358	31.3	1.5
CM 1-2	12.26	0.15	0.26	89340	173	3	193642	3358	30.8	1.4
CM 1-2	12.09	0.17	0.28	89340	173	3	193642	3358	31.2	1.5
CM 1-2	11.73	0.16	0.27	89340	173	3	193642	3358	32.2	1.5
CM 1-2	11.91	0.16	0.27	89340	173	3	193642	3358	31.7	1.5
CM 1-2	12.04	0.16	0.27	89340	173	3	193642	3358	31.4	1.5
CM 1-2	12.13	0.21	0.32	89340	173	3	193642	3358	31.1	1.5
CM 1-2	12.00	0.16	0.27	89340	173	3	193642	3358	31.5	1.5
CM 1-2	11.90	0.18	0.29	89340	173	3	193642	3358	31.7	1.5
CM 2	12.42	0.13	0.24	87750	172	3	196011	3419	30.8	1.4
CM 2	11.80	0.14	0.25	87750	172	3	196011	3419	32.4	1.5

Apéndice 1

CM 2	12.04	0.15	0.26	87750	172	3	196011	3419	31.8	1.5
CM 2	12.20	0.19	0.30	87750	172	3	196011	3419	31.3	1.5
CM 2	11.80	0.19	0.30	87750	172	3	196011	3419	32.4	1.6
CM 2	11.86	0.18	0.29	87750	172	3	196011	3419	32.2	1.5
CM 2	11.57	0.16	0.27	87750	172	3	196011	3419	33.0	1.6
CM 2	12.07	0.21	0.32	87750	172	3	196011	3419	31.7	1.6
CM 2	12.05	0.18	0.29	87750	172	3	196011	3419	31.7	1.5
CM 2	11.86	0.14	0.25	87750	172	3	196011	3419	32.2	1.5
CM 2	11.78	0.18	0.29	87750	172	3	196011	3419	32.5	1.6
CM 2	11.88	0.16	0.27	87750	172	3	196011	3419	32.2	1.5
CM 2	11.84	0.19	0.30	87750	172	3	196011	3419	32.3	1.6

SAMPLE: TS-1 (Toarcian–Oxfordian Todos Santos Formation, arkose)

16°42′30″ N; 93°38′47″ W; elevation = 564 m.a.s.l.

apatite	**^{238}U (ppm)**	**±1σ LA**	**± ^{238}Utot**	***A* (µm^2)**	**Ns**	**±Ns**	***ps***	**±*ps***	**AFT age (Ma)**	**±1σ**
1	35.87	0.63	1.94	4820	64	2	1327801	41494	72.0	5.2
2	7.05	0.11	0.37	4190	14	1	334129	23866	92.0	8.8
3	1.32	0.04	0.09	6960	4	1	57471	14368	84.8	22.1
4	28.70	0.41	1.45	5250	65	4	1238095	76190	83.8	7.4
5	5.36	0.09	0.28	5780	8	1	138408	17301	50.3	7.1
6	7.04	0.72	0.98	5900	11	1	186441	16949	51.6	8.8
7	27.60	2.00	3.00	6620	153	5	2311178	75529	161.7	19.2
8	29.60	2.70	3.78	5100	128	4	2509804	78431	163.7	22.2
9	28.20	2.30	3.33	3490	82	2	2349570	57307	160.9	20.2
10	6.11	0.09	0.31	7760	13	1	167526	12887	53.4	5.3
11	5.35	0.09	0.28	7680	11	1	143229	13021	52.1	5.8
12	5.39	0.19	0.39	6940	26	2	374640	28818	134.5	14.9
13	42.69	0.45	2.00	2850	36	2	1263158	70175	57.6	4.7
14	6.56	0.10	0.34	4340	7	1	161290	23041	47.9	7.5
15	8.47	0.15	0.46	5630	10	1	177620	17762	40.9	4.9
16	16.92	0.18	0.80	4660	21	1	450644	21459	51.9	4.0
17	45.12	0.96	2.60	3670	44	2	1198910	54496	51.7	4.3
18	26.80	0.80	1.78	3900	23	2	589744	51282	42.9	4.9
19	39.26	0.49	1.92	5910	48	2	812183	33841	40.3	3.0
20	33.11	0.79	2.00	3700	55	2	1486486	54054	87.2	6.9
21	13.17	0.15	0.63	4720	16	1	338983	21186	50.1	4.4
22	9.47	0.17	0.51	5120	41	2	800781	39063	163.3	13.3
23	9.89	0.22	0.58	5020	13	1	258964	19920	51.0	5.3
24	14.11	0.33	0.84	4460	20	2	448430	44843	61.8	7.6
25	38.20	1.60	2.99	3750	57	2	1520000	53333	77.3	7.2
26	1.19	0.04	0.09	7860	2	1	25445	12723	41.7	21.1
27	5.87	0.10	0.31	10420	18	1	172745	9597	57.3	4.9
28	5.68	0.11	0.32	5220	9	1	172414	19157	59.1	7.7

Apéndice 1

29	23.34	0.28	1.13	2550	21	2	823529	78431	68.6	7.7
30	6.86	0.48	0.73	4750	27	2	568421	42105	160.0	21.5
31	6.50	0.11	0.35	5030	9	1	178926	19881	53.6	6.9
32	29.76	0.59	1.67	7120	48	2	674157	28090	44.1	3.5
33	22.69	0.34	1.17	4620	23	1	497835	21645	42.8	3.3
34	16.90	0.19	0.81	5720	40	2	699301	34965	80.4	6.3
35	27.42	0.31	1.31	4080	44	3	1078431	73529	76.4	7.0
36	22.48	0.37	1.19	6580	41	2	623100	30395	54.0	4.4
37	57.72	0.76	2.86	4840	84	4	1735537	82645	58.5	4.6
38	133.60	2.30	7.16	3380	130	6	3846154	177515	56.0	4.5
39	58.27	0.82	2.94	4470	70	2	1565996	44743	52.3	3.6
40	1.75	0.05	0.11	4970	10	1	201207	20121	221.5	27.5
41	63.60	1.20	3.52	4000	103	4	2575000	100000	78.7	6.1
42	27.50	1.20	2.20	4180	41	2	980861	47847	69.4	7.0
43	13.43	0.19	0.68	4680	15	1	320513	21368	46.5	4.3
44	47.20	2.70	4.42	4550	70	3	1538462	65934	63.4	6.9
45	7.32	0.12	0.39	4660	26	1	557940	21459	147.3	11.0
46	89.30	1.10	4.35	4480	158	5	3526786	111607	76.8	5.3
47	19.92	0.28	1.01	6420	54	2	841121	31153	82.0	6.0
48	77.71	0.55	3.38	3980	127	5	3190955	125628	79.8	5.5
49	3.96	0.08	0.22	3500	5	1	142857	28571	70.1	14.8
50	4.34	0.09	0.25	4000	6	1	150000	25000	67.3	12.1
51	4.60	0.09	0.26	6900	10	1	144928	14493	61.4	7.4
52	24.70	0.68	1.58	2320	27	1	1163793	43103	91.5	7.6
53	19.77	0.32	1.04	4500	52	4	1155556	88889	113.3	11.3
54	2.46	0.13	0.22	8480	20	1	235849	11792	184.8	20.0

SAMPLE: TS-2 (Toarcian–Oxfordian Todos Santos Formation, arkose)

16°41′04″ N; 93°37′06″ W; elevation = 550 m.a.s.l.

apatite	**^{238}U (ppm)**	**±1σ LA**	**± ^{238}Utot**	***A* (µm^2)**	**Ns**	**±Ns**	***ps***	**±*ps***	**AFT age (Ma)**	**±1σ**
1	13.68	0.22	0.72	4670	22	1	471092	21413	67.0	5.3
2	11.52	0.14	0.56	4830	16	1	331263	20704	56.0	4.9
3	8.17	0.14	0.44	5080	12	1	236220	19685	56.3	5.9
4	139.80	1.00	6.09	2020	119	4	5891089	198020	81.9	5.4
5	14.79	0.66	1.20	5100	27	1	529412	19608	69.6	6.7
6	19.64	0.81	1.52	5150	39	2	757282	38835	75.0	7.5
7	2.49	0.08	0.17	5800	5	1	86207	17241	67.3	14.4
8	2.38	0.06	0.15	5850	5	1	85470	17094	69.7	14.8
9	52.70	1.20	3.12	3510	61	2	1737892	56980	64.2	5.0
10	1.77	0.05	0.11	4220	9	1	213270	23697	232.0	30.6
11	45.55	0.51	2.17	3470	121	6	3487032	172911	148.0	11.5
12	59.30	1.20	3.36	3230	82	2	2538700	61920	83.2	6.0
13	21.07	0.75	1.52	3290	22	1	668693	30395	61.8	5.7

Apéndice 1

14	35.69	0.64	1.94	4590	71	2	1546841	43573	84.2	6.0
15	5.80	0.10	0.31	5700	10	1	175439	17544	58.8	7.0
16	5.24	0.12	0.31	5340	8	1	149813	18727	55.7	8.0
17	4.60	0.09	0.26	5470	9	1	164534	18282	69.6	9.0
18	6.73	0.12	0.36	4670	30	2	642398	42827	184.0	17.1
19	7.21	0.14	0.40	4510	29	1	643016	22173	172.1	12.9
20	13.32	0.18	0.66	3480	17	1	488506	28736	71.3	6.1
21	12.31	0.29	0.74	3990	12	1	300752	25063	47.6	5.2
22	35.72	0.65	1.95	4790	70	2	1461378	41754	79.5	5.7
23	34.37	0.79	2.04	3580	52	2	1452514	55866	82.1	6.6
24	74.70	1.10	3.82	4400	118	2	2681818	45455	69.8	4.6
25	59.40	1.50	3.66	4910	107	3	2179226	61100	71.3	5.5
26	5.67	0.20	0.41	7180	11	1	153203	13928	52.6	6.4
27	7.54	0.53	0.80	6450	12	1	186047	15504	48.1	6.7
28	17.46	0.35	0.99	6130	34	2	554649	32626	61.8	5.5
29	20.63	0.29	1.04	5480	36	2	656934	36496	62.0	5.2
30	12.71	0.21	0.67	4060	56	3	1379310	73892	208.8	17.4
31	11.96	0.19	0.63	4050	52	2	1283951	49383	206.6	15.4
32	7.66	0.13	0.41	4950	32	1	646465	20202	162.9	11.7
33	6.99	0.15	0.40	4900	27	2	551020	40816	152.3	15.3
34	6.50	0.27	0.51	5120	26	1	507813	19531	151.0	14.2
35	36.43	0.98	2.31	4230	144	4	3404255	94563	180.2	14.1
36	31.79	0.67	1.83	3280	44	2	1341463	60976	82.0	6.7
37	6.57	0.27	0.51	2420	14	1	578512	41322	169.9	18.9
38	20.84	0.45	1.21	3120	30	1	961538	32051	89.6	6.8
39	16.46	0.58	1.18	2780	37	2	1330935	71942	156.2	15.1
40	4.38	0.11	0.27	3890	6	1	154242	25707	68.5	12.4
41	17.57	0.16	0.80	5020	25	2	498008	39841	55.2	5.5
42	15.70	0.18	0.75	5500	24	1	436364	18182	54.1	4.0
43	54.71	0.59	2.58	3960	58	3	1464646	75758	52.1	4.1
44	10.58	0.26	0.65	3330	15	1	450450	30030	82.7	8.1
45	9.84	0.42	0.78	4780	18	1	376569	20921	74.4	7.7
46	5.83	0.09	0.30	4030	6	1	148883	24814	49.8	8.9
47	19.48	0.45	1.16	5000	40	2	800000	40000	79.8	6.9
48	12.56	0.37	0.83	6350	32	1	503937	15748	78.0	6.4
49	27.16	0.60	1.59	3650	42	1	1150685	27397	82.3	6.0
50	19.75	0.73	1.45	3580	19	1	530726	27933	52.3	5.1
51	58.00	5.60	7.71	4320	92	3	2129630	69444	71.4	10.1
52	9.37	0.17	0.51	5890	17	2	288625	33956	60.0	8.1
53	7.88	0.13	0.42	6600	17	2	257576	30303	63.6	8.5
54	32.20	1.30	2.47	5300	62	2	1169811	37736	70.6	6.4
55	44.72	0.89	2.52	3810	63	4	1653543	104987	71.9	6.7
56	59.90	2.00	4.18	4920	180	7	3658537	142276	118.3	10.4
57	82.00	5.30	8.28	3290	120	4	3647416	121581	86.4	9.7
58	35.00	1.10	2.37	2780	110	6	3956835	215827	217.3	20.4
59	87.40	2.80	5.98	3330	138	4	4144144	120120	92.1	7.6
60	30.11	0.37	1.47	1950	24	1	1230769	51282	79.4	5.9
61	6.98	0.14	0.39	2500	7	1	280000	40000	78.0	12.3
62	13.44	0.49	0.98	5990	73	2	1218698	33389	174.9	15.0

Apéndice 1

63	33.86	0.31	1.54	2600	35	3	1346154	115385	77.3	8.0
64	14.76	0.30	0.84	3700	47	2	1270270	54054	166.1	13.2
65	34.50	1.40	2.66	2350	85	4	3617021	170213	201.8	19.6
66	15.14	1.70	2.25	4780	78	4	1631799	83682	207.4	33.3
67	6.10	0.07	0.29	2500	4	1	160000	40000	51.1	13.1
68	14.92	0.28	0.82	2500	11	1	440000	40000	57.4	6.5
69	6.06	0.07	0.29	2500	5	1	200000	40000	64.2	13.4
70	64.80	0.52	2.88	2500	74	2	2960000	80000	88.7	5.7
71	49.49	0.40	2.20	2500	41	2	1640000	80000	64.5	4.9
72	33.80	1.30	2.53	2500	37	1	1480000	40000	85.1	7.5
73	4.77	0.09	0.26	2500	5	1	200000	40000	81.4	17.1
74	16.30	0.22	0.81	2500	12	1	480000	40000	57.3	6.0
75	13.44	0.28	0.77	2500	14	2	560000	80000	81.0	12.8
76	6.41	0.06	0.29	2500	12	1	480000	40000	144.9	14.7
77	1.69	0.03	0.09	2500	4	1	160000	40000	182.4	46.8
78	80.25	0.60	3.52	2500	90	4	3600000	160000	87.1	6.3
79	2.52	0.04	0.13	2500	3	1	120000	40000	92.4	31.3
80	39.89	0.36	1.81	2500	35	2	1400000	80000	68.3	5.6
81	5.52	0.06	0.26	2500	12	1	480000	40000	167.8	17.1
82	45.33	0.40	2.05	2500	51	3	2040000	120000	87.4	7.2
83	48.93	0.75	2.53	2500	48	2	1920000	80000	76.3	5.8
84	4.12	0.14	0.29	2500	4	1	160000	40000	75.5	19.8
85	6.15	0.14	0.36	2500	4	1	160000	40000	50.7	13.1
86	17.65	0.29	0.93	2500	13	1	520000	40000	57.4	5.8
87	4.97	0.12	0.30	2500	5	1	200000	40000	78.2	16.6
88	29.59	0.40	1.48	2500	18	1	720000	40000	47.4	4.0
89	13.19	0.35	0.83	2500	14	1	560000	40000	82.5	8.4
90	6.49	0.07	0.31	2500	5	1	200000	40000	59.9	12.5
91	11.41	0.11	0.53	2500	11	1	440000	40000	75.0	8.1
92	21.65	0.44	1.23	2500	18	1	720000	40000	64.7	5.7
93	7.32	0.17	0.44	2500	5	1	200000	40000	53.2	11.3

SAMPLE: TS-3 (Toarcian–Oxfordian Todos Santos Formation, arkose)

16°39′03″ N; 93°34′20″ W; elevation = 538 m.a.s.l.

apatite	**^{238}U (ppm)**	**±1σ LA**	**± ^{238}Utot**	***A* (μm^2)**	**Ns**	**±Ns**	***ps***	**±*ps***	**AFT age (Ma)**	**±1σ**
1	4.34	0.10	0.25	7700	14	1	181818	12987	81.4	8.1
2	4.07	0.12	0.27	7200	12	1	166667	13889	79.6	8.9
3	7.33	0.31	0.58	6200	13	1	209677	16129	55.7	6.5
4	8.47	0.18	0.49	5270	16	1	303605	18975	69.7	6.5
5	6.17	0.66	0.88	5630	10	1	177620	17762	56.0	10.0
6	9.41	0.17	0.51	4470	20	1	447427	22371	92.3	7.6
7	48.46	0.79	2.55	2410	92	4	3817427	165975	152.2	11.8
8	51.30	1.10	2.97	2310	95	6	4112554	259740	154.9	14.4

Apéndice 1

9	23.74	0.38	1.24	3310	33	2	996979	60423	81.6	7.2
10	4.27	0.10	0.25	6850	9	1	131387	14599	59.9	7.8
11	28.11	0.40	1.42	6340	71	2	1119874	31546	77.4	5.3
12	12.81	0.41	0.88	3160	35	1	1107595	31646	166.9	13.8
13	2.13	0.07	0.15	6410	10	1	156006	15601	141.4	17.9
14	2.03	0.08	0.15	5680	9	1	158451	17606	150.6	20.7
15	5.07	0.13	0.31	5810	28	1	481928	17212	183.2	14.7
16	4.81	0.15	0.33	3000	14	1	466667	33333	187.0	19.5
17	2.13	0.09	0.17	5640	11	1	195035	17730	176.8	22.3
18	6.69	0.20	0.44	6980	38	2	544413	28653	157.2	14.5
19	14.29	0.22	0.74	3600	20	1	555556	27778	75.6	6.1
20	18.26	0.21	0.87	4110	36	2	875912	48662	93.1	7.6
21	11.36	0.71	1.12	4200	44	2	1047619	47619	177.8	20.3
22	5.26	0.23	0.42	3320	16	1	481928	30120	176.7	19.0
23	8.43	0.50	0.81	4600	14	1	304348	21739	70.2	8.8
24	7.26	0.21	0.47	2250	6	1	266667	44444	71.4	13.0
25	50.55	0.56	2.40	3200	56	2	1750000	62500	67.3	4.7
26	34.28	0.37	1.62	4820	59	3	1224066	62241	69.4	5.5
27	5.10	0.12	0.31	5330	9	1	168856	18762	64.4	8.5
28	75.70	1.30	4.06	4140	171	6	4130435	144928	105.8	7.8
29	5.03	0.13	0.31	7820	18	1	230179	12788	88.9	8.1
30	3.39	0.09	0.22	7820	13	1	166240	12788	95.1	10.1
31	9.24	0.15	0.49	3630	15	1	413223	27548	86.9	8.0
32	5.17	0.11	0.30	4870	8	1	164271	20534	61.8	8.8
33	10.03	0.43	0.80	5100	23	1	450980	19608	87.3	8.5
34	11.80	0.27	0.70	5200	27	2	519231	38462	85.5	8.7
35	7.19	0.13	0.39	4490	37	2	824053	44543	220.3	18.7
36	7.52	0.18	0.45	5160	43	2	833333	38760	213.1	18.0
37	5.80	0.17	0.38	5360	9	1	167910	18657	56.4	7.6
38	5.72	0.12	0.33	2960	5	1	168919	33784	57.5	12.1
39	8.52	0.17	0.48	6580	48	2	729483	30395	165.3	13.1
40	4.63	0.10	0.27	4440	22	1	495495	22523	205.9	16.9
41	36.22	0.35	1.67	5090	85	5	1669941	98232	89.5	7.5
42	10.00	0.24	0.60	7260	20	2	275482	27548	53.6	6.6
43	8.35	0.15	0.45	5510	41	1	744102	18149	171.9	12.0
44	9.54	0.18	0.53	5200	44	3	846154	57692	171.1	16.2
45	7.98	0.13	0.42	3380	24	1	710059	29586	171.7	13.1
46	5.98	0.11	0.33	7480	14	1	187166	13369	60.9	5.9
47	6.43	0.20	0.43	3700	8	1	216216	27027	65.4	9.6
48	7.84	0.16	0.45	4300	15	1	348837	23256	86.4	8.2
49	3.31	0.17	0.29	3780	15	1	396825	26455	230.3	26.6
50	4.71	0.12	0.29	6130	25	1	407830	16313	167.1	13.7
51	5.35	0.09	0.28	7470	17	1	227577	13387	82.7	7.2
52	7.09	0.14	0.40	3500	8	1	228571	28571	62.7	8.9
53	23.47	0.36	1.21	3600	95	3	2638889	83333	216.2	15.3
54	25.76	0.54	1.48	3250	86	2	2646154	61538	197.8	14.2
55	7.51	0.16	0.43	5350	10	1	186916	18692	48.5	5.9
56	4.45	0.08	0.24	2920	14	1	479452	34247	207.5	20.1
57	4.40	0.11	0.27	4330	12	1	277136	23095	122.0	13.4

Apéndice 1

58	3.36	0.08	0.20	4860	18	2	370370	41152	212.1	27.7
59	8.16	0.31	0.61	8640	30	2	347222	23148	82.7	8.8
60	5.71	0.64	0.85	5800	14	1	241379	17241	82.1	13.8
61	57.33	0.75	2.84	6840	166	7	2426901	102339	82.2	6.2
62	9.67	0.23	0.59	3480	13	1	373563	28736	75.1	7.9

SAMPLE: TS-4 (Toarcian–Oxfordian Todos Santos Formation, arkose)

16°37′13″ N; 93°32′13″ W; elevation = 590 m.a.s.l.

apatite	^{238}U (ppm)	±1σ LA	± ^{238}Utot	*A* (μm^2)	Ns	±Ns	*ps*	±*ps*	AFT age (Ma)	±1σ
1	7.87	0.16	0.45	6480	20	1	308642	15432	76.2	6.4
2	12.86	0.23	0.70	5080	26	1	511811	19685	77.4	5.9
3	10.44	0.15	0.53	5980	29	2	484950	33445	90.2	8.4
4	16.89	0.33	0.94	3420	27	1	789474	29240	90.8	7.0
5	10.53	0.26	0.64	8350	31	2	371257	23952	68.6	6.6
6	11.01	0.17	0.57	7300	27	1	369863	13699	65.4	4.8
7	10.09	0.16	0.53	4520	17	1	376106	22124	72.5	6.3
8	10.67	0.16	0.55	9500	36	3	378947	31579	69.1	7.2
9	2.88	0.06	0.17	8220	22	2	267640	24331	179.1	20.4
10	1.01	0.06	0.10	4200	4	1	95238	23810	181.3	48.6
11	2.39	0.14	0.23	6080	13	1	213816	16447	172.6	21.9
12	6.93	0.12	0.37	5080	15	1	295276	19685	82.8	7.7
13	4.59	0.11	0.28	6360	25	1	393082	15723	165.3	13.4
14	5.81	0.15	0.36	6500	11	1	169231	15385	56.7	6.6
15	5.57	0.14	0.34	8070	16	1	198265	12392	69.2	6.6
16	5.32	0.11	0.30	4030	8	1	198511	24814	72.6	10.3
17	5.29	0.13	0.32	6000	12	1	200000	16667	73.5	8.1
18	6.18	0.24	0.46	5590	15	1	268336	17889	84.3	9.0
19	5.54	0.13	0.33	6750	15	1	222222	14815	78.0	7.6
20	12.28	0.30	0.75	3400	16	1	470588	29412	74.5	7.1
21	10.95	0.61	1.01	8240	40	2	485437	24272	86.1	9.6
22	5.77	0.11	0.32	8140	22	1	270270	12285	90.9	7.3
23	4.39	0.10	0.26	3900	10	1	256410	25641	113.2	13.8
24	5.96	0.12	0.34	6510	18	2	276498	30722	90.1	11.7
25	6.97	0.16	0.41	6320	15	1	237342	15823	66.2	6.4
26	12.55	0.26	0.72	6050	32	2	528926	33058	81.9	7.6
27	5.32	0.15	0.34	5790	15	2	259067	34542	94.5	14.4
28	7.28	0.17	0.43	8830	28	1	317101	11325	84.6	6.7
29	7.24	0.12	0.38	4400	14	1	318182	22727	85.4	8.2
30	22.52	0.69	1.51	8430	40	2	474496	23725	41.1	3.8
31	19.16	0.51	1.21	4220	20	1	473934	23697	48.2	4.3
32	21.89	0.70	1.50	6420	31	3	482866	46729	43.0	5.3
33	24.83	0.51	1.41	4500	48	3	1066667	66667	83.5	7.7
34	9.01	0.32	0.65	4470	18	1	402685	22371	86.8	8.5

Apéndice 1

35	8.20	0.16	0.46	4480	30	1	669643	22321	157.7	11.8
36	11.44	0.82	1.24	3800	34	2	894737	52632	151.1	19.3
37	5.46	0.10	0.30	7920	14	2	176768	25253	63.0	9.9
38	4.60	0.11	0.28	7720	33	2	427461	25907	179.2	16.6
39	3.36	0.28	0.40	4100	13	1	317073	24390	181.9	26.6
40	4.45	0.10	0.26	6230	12	1	192616	16051	84.1	9.1
41	6.49	0.13	0.37	4950	15	1	303030	20202	90.7	8.6
42	6.92	0.12	0.37	8690	19	1	218642	11507	61.5	5.2
43	7.57	0.15	0.43	4500	11	1	244444	22222	62.8	7.1
44	13.52	0.20	0.69	4880	15	1	307377	20492	44.3	4.1
45	12.18	0.30	0.74	3980	21	1	527638	25126	84.2	7.2
46	6.55	0.12	0.36	5980	17	1	284281	16722	84.3	7.5
47	21.71	0.32	1.11	5250	44	2	838095	38095	75.0	5.8
48	23.81	0.63	1.50	2630	22	1	836502	38023	68.3	5.9
49	14.80	1.30	1.84	3540	48	2	1355932	56497	176.7	23.9
50	6.93	0.12	0.37	6510	45	2	691244	30722	192.1	15.1
51	7.62	0.17	0.45	3150	23	1	730159	31746	184.7	15.1
52	9.42	0.44	0.78	6630	53	3	799397	45249	163.8	17.5
53	15.74	1.70	2.27	2740	38	3	1386861	109489	170.0	28.5

Apéndice 2

Supplementary Table 3.

Fission-track dating results for unreset detrital apatites from the Berriasian to Aptian (?) member (samples SR-1 and SR-2) of the San Ricardo Formation (data presented in Abdullin *et al*. 2014). Apatite fission-track ages were calculated using ^{238}U contents determined *in-situ* by LA-ICP-MS at the Laboratorio de Estudios Isotópicos, Centro de Geociencias, UNAM (see details in Abdullin *et al*. 2016).

Note:

The reference number (e.g. SR2-17) indicate, in order, the rock sample name (SR-2) and the respective number of the individual apatite grain dated (17). **^{238}U** is the uranium-238 concentration in ppm obtained using LA-ICP-MS. **± ^{238}Utot** represents the total uncertainty for ^{238}U content, including the analytical error of LA-ICP-MS measurements (**±1σ LA**) and an error generated by the common CaO variation (55 ± 2 wt.%) in apatites of different origin. **A** is the spontaneous fission-track counting area in μm^2. **Ns** is the number of spontaneous fission-tracks registered within the area **A**. **Ps** is the spontaneous fission-track density (i.e. number of tracks expressed per 1 cm^2). **FT age** corresponds to apatite fission-track age in Ma with its absolute **±1σ** error. The geographic coordinates (latitude, longitude, and elevation in m.a.s.l.) of the studied rock samples are also given.

SAMPLE: SR-1 (Berriasian–Aptian? member of the San Ricardo Formation, fine-grained sandstone)

16°41′45″ N; 93°32′33″ W; elevation = 653 m.a.s.l.

apatite	^{238}U (ppm)	±1σ LA	± ^{238}Utot	A (μm^2)	Ns	±Ns	Ps	±Ps	FT age (Ma)	±1σ
SR1-1	30.75	0.26	1.38	3600	107	3	2972222	83333	186.3	12.0
SR1-2	15.68	0.22	0.79	12800	250	8	1953125	62500	239.1	16.7
SR1-3	23.54	0.23	1.09	8400	265	8	3154762	95238	256.9	17.0
SR1-4	22.20	1.60	2.41	8400	265	8	3154762	95238	272.0	31.9
SR1-5	23.02	0.46	1.30	3600	75	2	2083333	55556	174.6	12.6
SR1-6	33.99	0.43	1.67	4800	197	7	4104167	145833	231.9	16.4
SR1-7	43.14	0.61	2.18	4800	241	10	5020833	208333	223.6	16.7
SR1-8	25.12	0.31	1.22	6400	222	10	3468750	156250	264.5	20.0
SR1-9	20.05	0.24	0.97	8400	183	5	2178571	59524	209.0	13.9
SR1-10	22.66	0.30	1.12	8400	183	5	2178571	59524	185.3	12.5

Apéndice 2

SR1-11	20.22	0.36	1.10	8000	120	4	1500000	50000	143.4	10.5
SR1-12	20.95	0.34	1.10	4000	92	3	2300000	75000	211.2	15.2
SR1-13	11.24	0.26	0.67	9340	97	3	1038544	32120	178.2	13.6
SR1-14	10.27	0.31	0.68	8120	83	3	1022167	36946	191.7	16.1
SR1-15	9.67	0.15	0.50	4810	50	2	1039501	41580	206.8	15.5
SR1-16	35.22	0.37	1.65	3200	114	4	3562500	125000	194.8	13.5
SR1-17	46.50	1.20	2.89	3180	128	5	4025157	157233	167.1	13.7
SR1-18	12.85	0.27	0.74	5090	58	2	1139489	39293	171.1	13.0
SR1-19	24.01	0.56	1.43	3900	121	4	3102564	102564	247.8	19.1
SR1-20	14.91	0.47	1.01	5060	95	2	1877470	39526	241.6	19.2
SR1-21	21.08	0.26	1.03	9150	207	7	2262295	76503	206.5	14.4
SR1-22	19.67	0.57	1.29	4850	110	4	2268041	82474	221.6	18.4
SR1-23	24.98	0.32	1.23	3410	79	3	2316716	87977	178.8	12.9
SR1-24	15.83	0.25	0.83	4670	78	3	1670236	64240	203.1	15.1
SR1-25	11.61	0.24	0.66	4150	55	2	1325301	48193	219.4	16.8
SR1-26	23.19	0.36	1.20	7200	162	6	2250000	83333	187.0	13.7
SR1-27	16.90	0.29	0.91	7200	124	4	1722222	55556	196.2	14.2
SR1-28	15.61	0.68	1.25	5560	92	4	1654676	71942	204.0	19.9
SR1-29	26.24	0.51	1.47	2700	72	3	2666667	111111	195.7	15.4
SR1-30	11.82	0.17	0.60	5670	70	4	1234568	70547	201.1	17.0
SR1-31	12.56	0.20	0.66	3990	53	2	1328321	50125	203.5	15.1

SAMPLE: SR-2 (Berriasian–Aptian? member of the San Ricardo Formation, fine-grained sandstone)

16°39′47″ N; 93°31′27″ W; elevation = 872 m.a.s.l.

apatite	^{238}U (ppm)	±1σ LA	± ^{238}Utot	A (µm^2)	Ns	±Ns	Ps	±Ps	FT age (Ma)	±1σ
SR2-1	25.34	0.35	1.27	4800	129	4	2687500	83333	204.1	14.2
SR2-2	10.62	0.85	1.24	9600	116	3	1208333	31250	218.7	27.1
SR2-3	10.94	0.37	0.77	9600	116	3	1208333	31250	212.4	17.6
SR2-4	34.96	0.77	2.04	3600	114	3	3166667	83333	174.7	12.9
SR2-5	20.39	0.47	1.21	3600	92	4	2555556	111111	240.5	19.7
SR2-6	12.30	0.23	0.68	3600	52	2	1444444	55556	225.6	17.2
SR2-7	20.22	0.60	1.34	3600	62	2	1722222	55556	164.4	13.5
SR2-8	18.99	0.50	1.19	3600	61	3	1694444	83333	172.2	15.1
SR2-9	35.60	1.30	2.60	3600	85	4	2361111	111111	128.4	12.1

Apéndice 2

SR2-10	34.60	1.20	2.46	3600	142	6	3944444	166667	219.1	19.7
SR2-11	47.62	0.56	2.29	3600	189	8	5250000	222222	212.0	15.6
SR2-12	8.94	0.16	0.49	4100	50	2	1219512	48780	261.4	20.0
SR2-13	7.21	0.18	0.44	4200	31	1	738095	23810	197.1	15.4
SR2-14	10.93	0.26	0.66	4900	61	2	1244898	40816	218.9	17.0
SR2-15	11.95	0.33	0.76	3950	49	2	1240506	50633	199.8	16.8
SR2-16	10.89	0.15	0.55	3600	55	2	1527778	55556	268.6	19.3
SR2-17	2.73	0.23	0.33	7370	23	1	312076	13569	219.7	29.1
SR2-18	2.44	0.11	0.20	5470	17	1	310786	18282	244.4	26.0
SR2-19	49.20	1.20	2.99	2700	147	7	5444444	259259	212.8	18.1
SR2-20	27.70	1.50	2.51	3200	91	3	2843750	93750	197.7	20.3
SR2-21	10.90	0.42	0.82	5200	66	2	1269231	38462	223.8	19.8
SR2-22	12.87	0.36	0.83	5200	66	3	1269231	57692	190.0	16.5
SR2-23	22.45	0.61	1.43	4880	88	4	1803279	81967	155.2	13.4
SR2-24	28.44	0.33	1.37	4510	124	5	2749446	110865	186.3	13.5
SR2-25	19.30	0.39	1.09	5810	110	5	1893287	86059	189.0	15.3
SR2-26	14.51	0.25	0.78	10560	129	6	1221591	56818	162.6	13.0
SR2-27	12.56	0.18	0.64	4590	56	2	1220044	43573	187.2	13.5
SR2-28	13.77	0.23	0.73	8500	104	4	1223529	47059	171.4	12.9
SR2-29	23.63	0.31	1.17	7290	130	4	1783265	54870	145.9	10.1
SR2-30	36.09	0.59	1.90	2600	72	3	2769231	115385	148.3	11.4
SR2-31	40.67	0.76	2.24	4250	152	4	3576471	94118	169.7	12.1
SR2-32	36.70	0.99	2.33	5340	155	6	2902622	112360	152.8	12.6
SR2-33	32.02	0.75	1.92	3500	102	5	2914286	142857	175.6	15.0
SR2-34	13.59	0.30	0.79	4890	88	3	1799591	61350	253.9	19.5
SR2-35	25.75	0.53	1.47	6950	180	6	2589928	86331	193.7	14.6
SR2-36	21.13	0.55	1.32	4780	124	5	2594142	104603	235.7	19.4
SR2-37	14.53	0.37	0.90	8660	125	4	1443418	46189	191.4	15.0
SR2-38	14.20	0.31	0.83	4450	60	3	1348315	67416	183.0	15.5
SR2-39	15.71	0.26	0.83	8820	152	5	1723356	56689	211.0	15.2
SR2-40	22.60	1.10	1.92	5790	150	4	2590674	69085	220.3	21.1
SR2-41	12.53	0.26	0.72	8100	120	5	1481481	61728	227.1	18.0
SR2-42	3.48	0.15	0.28	4460	20	1	448430	22422	247.2	24.8

Apéndice 3

Fission-track dating results for detrital apatites from the Ypresian to Lutetian El Bosque Formation (samples BQ-1, BQ-2, BQ-4 and BQ-5). Fission-track ages were calculated using ^{238}U contents determined *in-situ* by LA-ICP-MS at the Laboratorio de Estudios Isotópicos, Centro de Geociencias, UNAM (see details in Abdullin *et al*. 2016a).

No of grain	238-U (ppm)	1SE (ppm)	total error for 238U	Area (micras2)	Ns	error Ns	ps	error ps	AFT age (Ma)	1SE (Ma)
BQ-1										
1	39,2	0,7	2,1	4800	38	2	791667	41667	39,4	3,3
2	10,4	0,1	0,5	4800	17	1	354167	20833	66,2	5,5
3	18,4	0,3	1,0	4800	22	1	458333	20833	48,5	3,8
4	2,8	0,1	0,2	4500	10	1	222222	22222	153,3	19,6
5	11,1	0,2	0,6	4800	24	2	500000	41667	87,5	9,3
6	26,6	0,4	1,4	4800	30	1	625000	20833	45,8	3,3
7	38,2	0,5	1,9	4800	64	3	1333333	62500	67,9	5,3
8	33,1	0,4	1,6	4800	42	2	875000	41667	51,5	4,0
9	0,5	0,1	0,1	10000	6	1	60000	10000	230,5	49,9
10	12,6	0,8	1,3	4800	19	1	395833	20833	61,1	7,3
11	20,6	0,2	0,9	4800	32	2	666667	41667	63,0	5,4
12	5,4	0,3	0,5	5000	10	1	200000	20000	72,0	10,1
13	12,9	0,2	0,7	4800	15	2	312500	41667	47,2	7,0
14	15,4	0,4	1,0	4800	28	2	583333	41667	73,6	7,5
15	5,8	0,1	0,3	4800	9	1	187500	20833	62,9	8,1
16	36,1	0,3	1,6	4800	66	3	1375000	62500	74,0	5,5
17	10,8	0,2	0,6	4800	15	1	312500	20833	56,3	5,3
18	2,8	0,1	0,2	4800	8	1	166667	20833	115,4	17,1
19	4,2	0,1	0,3	4800	18	1	375000	20833	172,3	15,4
20	7,5	0,1	0,4	4800	20	1	416667	20833	107,7	8,6
21	5,8	0,2	0,4	4800	17	2	354167	41667	118,3	16,8
22	28,2	0,3	1,3	4800	34	2	708333	41667	48,9	4,1

No of grain	238-U (ppm)	1SE (ppm)	total error for 238U	Area (micras2)	Ns	error Ns	ps	error ps	AFT age (Ma)	1SE (Ma)
BQ-2										
1	10,3	0,2	0,6	4800	12	1	250000	20833	47,3	5,1
2	15,2	0,2	0,8	4800	22	1	458333	20833	58,7	4,5
3	6,5	0,1	0,3	10000	4	1	40000	10000	12,0	3,1
4	9,1	0,1	0,4	4800	20	1	416667	20833	88,9	7,0
5	24,0	0,3	1,2	4800	26	2	541667	41667	44,0	4,3
6	0,8	0,1	0,1	4800	2	1	41667	20833	101,0	53,0
7	0,5	0,1	0,1	4800	2	1	41667	20833	160,9	88,7
8	2,9	0,1	0,2	5000	2	1	40000	20000	26,9	13,6
9	47,9	0,6	2,3	4000	42	2	1050000	50000	42,7	3,3
10	0,6	0,0	0,0	10000	8	1	80000	10000	255,6	35,7
11	5,8	0,4	0,6	4800	22	1	458333	20833	152,7	18,3
12	44,6	1,0	2,6	4800	56	2	1166667	41667	50,9	4,0
13	12,2	0,2	0,6	4000	9	1	225000	25000	36,0	4,6
14	20,8	0,5	1,3	5000	29	1	580000	20000	54,3	4,3
15	13,2	0,2	0,7	4800	20	1	416667	20833	61,4	5,0
16	3,8	0,2	0,3	4800	2	1	41667	20833	21,4	10,9
17	7,0	0,2	0,5	4000	8	1	200000	25000	55,6	8,1
18	2,4	0,1	0,2	4800	4	1	83333	20833	67,5	17,8
19	3,1	0,1	0,2	4800	8	1	166667	20833	104,3	15,3
20	2,8	0,1	0,2	4800	9	1	187500	20833	129,6	17,8
21	4,6	0,1	0,3	4800	10	1	208333	20833	88,0	10,7
22	5,4	0,1	0,3	4800	5	1	104167	20833	37,6	7,9
23	1,3	0,1	0,1	9600	4	1	41667	10417	62,4	17,2

Apéndice 3

No of grain	238-U (ppm)	1SE (ppm)	total error for 238U	Area (micras2)	Ns	error Ns	ps	error ps	AFT age (Ma)	1SE (Ma)
BQ-4										
1	18,7	2,5	3,2	4800	14	1	291667	20833	30,4	5,7
2	44,8	0,6	2,2	5000	84	3	1680000	60000	72,9	5,2
3	18,6	0,2	0,9	4000	16	1	400000	25000	41,9	3,6
4	5,8	0,1	0,3	4800	11	1	229167	20833	76,8	8,6
5	9,0	0,4	0,7	4000	20	1	500000	25000	107,7	11,0
6	11,0	0,1	0,5	4800	20	1	416667	20833	73,6	5,7
7	58,6	0,8	2,9	5000	74	3	1480000	60000	49,2	3,7
8	32,3	0,3	1,5	4800	34	1	708333	20833	42,7	2,8
9	4,4	0,1	0,3	4800	4	1	83333	20833	36,9	9,6
10	37,1	0,4	1,8	4000	48	2	1200000	50000	62,9	4,6
11	7,7	0,1	0,4	4000	17	1	425000	25000	107,0	9,1
12	1,7	0,1	0,2	4800	10	1	208333	20833	235,3	33,4
13	11,9	0,3	0,7	4800	18	1	375000	20833	61,3	5,6
14	5,8	0,1	0,3	4800	24	1	500000	20833	166,4	12,8
15	5,0	0,2	0,4	4800	7	1	145833	20833	56,8	9,4
16	16,6	0,3	0,9	4000	18	1	450000	25000	52,8	4,6
17	22,8	0,4	1,2	4000	25	1	625000	25000	53,4	4,1
18	35,7	0,4	1,7	4000	28	2	700000	50000	38,2	3,6
19	10,4	0,2	0,6	4800	14	1	291667	20833	54,6	5,3
20	154,7	1,5	7,1	4000	164	3	4100000	75000	51,6	3,2
21	10,9	0,1	0,5	4800	13	1	270833	20833	48,4	4,7
22	15,9	0,2	0,8	4800	14	1	291667	20833	35,8	3,4
23	53,7	0,4	2,4	4800	68	2	1416667	41667	51,4	3,3
24	2,5	0,1	0,2	9600	8	1	83333	10417	64,9	9,8
25	38,9	0,3	1,7	4800	52	2	1083333	41667	54,2	3,8
26	0,5	0,1	0,1	10000	6	1	60000	10000	230,5	49,9
27	5,1	0,1	0,3	5200	15	1	288462	19231	109,7	10,4
28	13,4	0,2	0,7	4800	18	1	375000	20833	54,5	4,6

No of grain	238-U (ppm)	1SE (ppm)	total error for 238U	Area (micras2)	Ns	error Ns	ps	error ps	AFT age (Ma)	1SE (Ma)
BQ-5										
1	3,6	0,1	0,2	3200	10	1	312500	31250	167,5	20,7
2	35,8	0,2	1,5	4800	60	2	1250000	41667	67,9	4,4
3	27,3	1,0	2,0	2000	45	2	2250000	100000	159,2	14,8
4	8,2	0,1	0,4	4800	4	1	83333	20833	19,8	5,1
5	4,7	0,1	0,3	4800	4	1	83333	20833	34,6	9,0
6	9,4	0,1	0,4	4800	4	1	83333	20833	17,3	4,4
7	3,2	0,2	0,3	4800	9	1	187500	20833	113,6	17,3
8	4,8	0,1	0,3	4800	9	1	187500	20833	75,9	9,9
9	3,6	0,1	0,2	4800	12	1	250000	20833	134,4	14,9
10	2,2	0,1	0,2	10000	4	1	40000	10000	35,5	9,4
11	5,7	0,1	0,3	4800	13	1	270833	20833	92,2	9,3
12	33,4	0,5	1,7	4000	29	2	725000	50000	42,3	4,0
13	7,1	0,1	0,4	5000	8	1	160000	20000	43,9	6,1
14	8,9	0,1	0,4	4000	30	2	750000	50000	162,7	14,6
15	3,9	0,1	0,2	4800	2	1	41667	20833	20,9	10,5
16	0,7	0,1	0,1	5000	2	1	40000	20000	110,8	58,7

Apéndice 4

Fission-track dating results for apatites from the Chiapas Massif samples (CM-1, CM-2, CM-3, CM-4, and CM-5). Apatite fission-track ages were calculated using ^{238}U contents determined *in-situ* by LA-ICP-MS at the Laboratorio de Estudios Isotópicos, Centro de Geociencias, UNAM (see details in Abdullin *et al*. 2016a).

Sample CM-1

apatite	^{238}U (ppm)	A (μm^2)	Ns	AFT age (Ma)
-1	12.6±0.7	10000	28±1	43.3±3.2
-2	12.0±0.9	10000	33±2	53.5±5.6
-3	13.3±0.6	5000	15±1	44.0±3.9
-4	14.9±0.8	5000	14±1	36.6±3.6
-5	12.1±0.6	10000	24±1	38.7±3.0
-6	11.6±0.6	10000	28±1	47.0±3.5
-7	7.8±0.4	10000	18±1	45.0±3.7
-8	9.7±0.5	5000	9±1	36.2±4.6
-9	5.5±0.3	10000	11±1	39.0±4.4
-10	7.2±0.7	10000	13±1	35.2±4.4
-11	5.8±0.3	10000	14±1	47.0±4.5
-12	5.6±0.3	10000	15±1	52.2±4.9
-13	7.3±0.4	5000	7±1	37.4±5.8
-14	9.1±0.5	10000	24±2	51.4±5.6
-15	8.3±0.4	10000	18±1	42.3±3.5
-16	6.0±0.3	5000	8±1	51.9±7.3
-17	12.0±0.6	5000	11±1	35.7±4.0
-18	13.1±0.7	5000	13±1	38.7±3.9
-19	9.3±0.5	10000	25±2	52.3±5.5
-20	11.4±0.6	10000	28±1	47.8±3.6
-21	12.1±0.6	10000	26±2	41.9±4.2
-22	10.3±0.6	10000	22±1	41.6±3.4
-23	8.3±0.4	5000	12±1	56.3±5.8

Apéndice 4

Sample CM-2

apatite	^{238}U (ppm)	A (μm^2)	Ns	AFT age (Ma)
·1	9.2±0.4	10000	19±2	40.3±4.9
·2	9.0±0.4	10000	16±1	34.7±3.0
·3	9.6±0.5	10000	18±2	36.6±4.8
·4	14.3±0.7	10000	19±2	25.9±3.2
·5	13.7±0.7	10000	20±1	28.5±2.3
·6	10.1±0.6	5000	10±1	38.6±4.7
·7	10.5±0.6	5000	9±1	33.4±4.3
·8	10.1±0.6	10000	17±1	32.8±2.9
·9	15.2±0.8	10000	21±2	27.0±3.1
·10	11.1±0.6	5000	10±1	35.1±4.2
·11	16.6±1.2	10000	22±1	25.9±2.4
·12	8.8±0.4	15000	20±1	29.6±2.3
·13	7.5±0.4	15000	22±1	38.1±2.9
·14	7.9±0.4	15000	20±2	32.9±3.9
·15	8.2±0.5	15000	22±2	34.9±4.0

Sample CM-3

apatite	^{238}U (ppm)	A (μm^2)	Ns	AFT age (Ma)
·1	8.9±0.5	6000	6±1	21.9±4.0
·2	7.4±0.4	7000	7±1	26.4±4.1
·3	7.6±0.4	10000	10±1	25.7±3.0
·4	10.3±0.5	5000	5±1	19.0±4.0
·5	7.8±0.4	10000	11±1	27.5±3.0
·6	9.1±0.4	10000	10±1	21.5±2.5
·7	8.8±0.4	5000	5±1	22.2±4.6
·8	8.4±0.4	5000	6±1	27.9±4.9
·9	9.1±0.5	10000	11±1	23.6±2.7
·10	8.6±0.4	10000	13±1	29.5±2.9
·11	8.8±0.5	10000	12±1	26.6±2.9
·12	8.1±0.4	10000	8±1	19.3±2.7
·13	8.9±0.4	10000	10±1	21.9±2.6
·14	8.5±0.4	10000	10±1	23.0±2.7
·15	9.5±0.4	10000	9±1	18.5±2.3

Apéndice 4

Sample CM-4

apatite	^{238}U (ppm)	A (μm^2)	Ns	AFT age (Ma)
·1	20.7±1.2	3600	6±1	15.7±2.8
·2	18.5±1.2	3600	5±1	14.7±3.1
·3	22.1±2.3	3600	7±1	17.2±3.1
·4	14.8±0.7	6400	7±1	14.4±2.2
·5	6.5±0.4	6400	4±1	18.8±4.9
·6	5.3±0.4	6400	3±1	17.3±5.9
·7	25.6±1.2	3600	4±1	8.5±2.2
·8	22.8±1.1	3600	6±1	14.3±2.5
·9	23.5±3.0	6400	13±1	16.9±2.6
·10	28.1±1.5	6400	13±1	14.1±1.4
·11	26.9±1.6	6400	15±1	17.0±1.6
·12	12.9±1.2	6400	5±1	11.8±2.6
·13	20.8±1.1	6400	11±1	16.1±1.8
·14	40.7±2.1	3600	8±1	10.7±1.5

Sample CM-5

apatite	^{238}U (ppm)	A (μm^2)	Ns	AFT age (Ma)
-1	48.5±2.9	10000	56±3	22.5±2.0
-2	38.6±1.9	10000	52±3	26.3±2.2
-3	11.1±0.6	10000	18±2	31.6±4.1
-4	17.4±0.9	10000	26±2	29.2±2.9
-5	9.5±0.5	6400	9±1	28.9±3.8
-6	14.4±0.7	6400	11±1	23.3±2.6
-7	12.5±1.0	12800	22±2	26.8±3.3
-8	16.2±0.8	6400	17±1	32.0±2.7
-9	38.3±3.5	3600	14±1	19.8±2.4
-10	27.5±3.2	6400	25±1	27.7±3.6
-11	9.1±0.4	10000	13±1	27.9±2.7
-12	13.6±0.8	10000	17±1	24.4±2.2
-13	23.2±1.3	6400	16±2	21.0±3.0
-14	10.7±0.6	6400	10±1	28.5±3.4
-15	14.8±0.7	6400	12±1	24.7±2.6
-16	15.9±1.5	3600	7±1	23.9±4.2
-17	9.6±0.4	6400	8±1	25.4±3.5
-18	10.1±0.6	6400	10±1	30.2±3.6

Apéndice 5

Supplementary Table 1.

LA-ICP-MS-based multi-elemental compositions (Sr, Y, Th, U, and ΣREE; in ppm) and corresponding geochemical parameters of the apatite populations analysed.

Note:

$(Eu/Eu^*)_{cn}$, the Eu anomaly; $(Ce/Yb)_{cn}$ (where cn denotes chondrite-normalised). REE are the rare earth elements (from La to Lu). LREE and HREE correspond to the light REE (La–Sm) and heavy REE (Eu–Lu), respectively. CM-(1–6), CMC igneous samples; TS-(1–4), the Todos Santos Formation sandstones; SR-(1 and 2), San Ricardo Formation sandstones; BQ-(1–6), the El Bosque Formation sandstones; min, minimum; avrg, average (shown in parentheses); max, maximum. Ng is the number of apatites. The full data set of apatite compositions is given in Supplementary Table 2.

Sample	Ng		Sr (ppm)	Y (ppm)	Th (ppm)	U (ppm)	ΣREE (ppm)	Th/U	La/Nd	(La–Pr)/ΣREE (%)	$(Eu/Eu^*)_{cn}$	$(Ce/Yb)_{cn}$	LREE/HREE
CM-1	37	min:	155	407	20.8	5.3	2138	2.2	0.8	62	0.62	5.9	6.6
		avrg:	(164)	(509)	(29.7)	(9.8)	(2798)	(3.3)	(1.0)	(65)	(0.69)	(7.1)	(7.7)
		max:	174	823	36.0	16.6	4288	5.8	1.2	68	0.74	9.4	9.1
CM-2	41	min:	280	51	20.0	7.4	1097	1.9	1.8	79	0.79	17.2	18.8
		avrg:	(348)	(87)	(27.1)	(9.6)	(1631)	(2.8)	(2.5)	(82)	(0.98)	(27.8)	(25.1)
		max:	392	204	88.6	26.9	3597	3.3	3.1	85	1.18	40.2	32.5
CM-3	6	min:	404	93	2.6	2.4	880	1.1	0.9	67	0.96	11.8	10.2
		avrg:	(413)	(173)	(8.2)	(5.4)	(1582)	(1.5)	(1.0)	(69)	(1.13)	(13.3)	(11.0)
		max:	420	281	12.6	6.6	2482	1.9	1.1	70	1.27	14.9	11.8
CM-4	7	min:	338	143	48.5	18.5	2167	2.5	2.3	80	0.80	20.3	19.6
		avrg:	(346)	(280)	(87.5)	(31.0)	(4648)	(2.7)	(2.4)	(81)	(0.88)	(22.6)	(21.6)
		max:	356	485	199.5	66.5	7435	3.0	2.7	82	0.97	25.9	24.7
CM-5	21	min:	372	34	6.6	9.1	386	0.4	0.9	67	0.69	16.8	11.2
		avrg:	(387)	(103)	(21.1)	(17.2)	(1260)	(1.2)	(1.1)	(70)	(0.90)	(20.0)	(13.2)
		max:	453	250	63.8	48.0	3060	2.5	1.3	73	1.00	32.3	16.2
CM-6	24	min:	506	300	10.6	2.9	3227	3.0	0.8	66	0.44	16.4	11.4
		avrg:	(574)	(359)	(18.9)	(5.1)	(3992)	(3.8)	(0.9)	(67)	(0.50)	(18.4)	(12.6)
		max:	598	434	30.5	9.0	5363	4.4	1.0	70	0.53	21.5	15.0

Apéndice 5

all CMC apatites	136	min:	155	34	2.6	2.4	386	0.4	0.8	62	0.44	5.9	6.6
		avrg:	(347)	(266)	(27.7)	(11.0)	(2461)	(2.8)	(1.5)	(72)	(0.81)	(18.4)	(15.5)
		max:	598	823	199.5	66.5	7435	5.8	3.1	85	1.27	40.2	32.5
TS-1	73	min:	132	58	3.1	1.2	529	0.3	0.3	43	0.20	2.8	3.3
		avrg:	(286)	(372)	(38.8)	(24.9)	(2960)	(2.3)	(1.3)	(68)	(0.66)	(14.2)	(12.3)
		max:	833	1544	142.9	132.3	7564	6.1	4.1	86	1.15	43.2	39.2
TS-2	102	min:	140	47	5.2	1.7	798	0.2	0.2	42	0.21	2.8	3.8
		avrg:	(306)	(344)	(38.9)	(23.5)	(3159)	(2.4)	(1.5)	(69)	(0.66)	(17.6)	(14.2)
		max:	582	993	177.0	138.5	8560	7.1	5.4	88	1.38	49.4	38.8
TS-3	70	min:	221	48	4.5	2.0	826	0.6	0.3	45	0.30	3.1	3.8
		avrg:	(400)	(276)	(28.2)	(13.1)	(2929)	(2.6)	(1.2)	(69)	(0.65)	(21.6)	(14.4)
		max:	865	932	147.4	74.9	6425	4.8	4.4	87	1.39	42.2	32.0
TS-4	80	min:	95	22	0.5	1.0	231	0.3	0.5	57	0.26	4.6	5.0
		avrg:	(343)	(275)	(24.2)	(12.8)	(2550)	(2.3)	(1.5)	(72)	(0.73)	(24.2)	(16.2)
		max:	563	1548	127.1	53.5	7396	5.2	5.3	89	1.77	61.2	42.4
all TS apatites	325	min:	95	22	0.5	1.0	231	0.2	0.2	42	0.20	2.8	3.3
		avrg:	(331)	(319)	(33.0)	(18.9)	(2915)	(2.4)	(1.4)	(69)	(0.67)	(19.3)	(14.3)
		max:	865	1548	177.0	138.5	8560	7.1	5.4	89	1.77	61.2	42.4
SR-1	77	min:	122	48	14.4	7.5	661	0.7	0.5	52	0.28	4.4	4.6
		avrg:	(327)	(318)	(88.1)	(36.4)	(4245)	(2.8)	(2.0)	(78)	(0.98)	(21.7)	(19.4)
		max:	451	937	268.9	172.6	8849	5.4	4.0	87	2.79	66.5	37.4
SR-2	47	min:	193	80	4	2	1366	0.7	1.0	68	0.33	4.2	7.3
		avrg:	(320)	(222)	(65)	(22)	(3975)	(3.0)	(2.3)	(80)	(0.97)	(26.7)	(23.3)
		max:	464	535	176	49	8475	4.9	4.9	89	1.95	49.4	40.1
all SR apatites	124	min:	122	48	4	2	661	0.7	0.5	52	0.28	4.2	4.6
		avrg:	(324)	(281)	(79)	(31)	(4143)	(2.9)	(2.1)	(79)	(0.98)	(23.6)	(20.8)
		max:	464	937	269	173	8849	5.4	4.9	89	2.79	66.5	40.1
BQ-1	74	min:	56	32	0.03	0.07	180	0.01	0.06	3	0.05	0.03	0.10
		avrg:	(2696)	(1748)	(24.3)	(11.5)	(4008)	(1.9)	(0.4)	(37)	(0.60)	(4.4)	(3.8)
		max:	12320	8344	269.6	55.0	15358	10.0	2.2	80	1.03	33.1	23.1
BQ-2	88	min:	74	74	0.01	0.10	198	0.01	0.05	7	0.10	0.06	0.21
		avrg:	(2822)	(1050)	(15.5)	(12.8)	(2262)	(1.4)	(0.3)	(31)	(0.60)	(2.8)	(2.4)
		max:	12276	4920	170.4	103.9	10644	13.0	1.1	73	1.06	15.9	14.0
BQ-3	54	min:	61	32	0.02	0.09	34	0.01	0.08	6	0.12	0.07	0.21
		avrg:	(2973)	(1418)	(20.1)	(12.6)	(3009)	(1.9)	(0.3)	(31)	(0.57)	(2.5)	(2.3)
		max:	9585	4983	163.6	84.4	17004	12.5	0.8	67	1.04	19.5	12.8
BQ-4	84	min:	54	56	0.01	0.05	93	0.01	0.07	4	0.09	0.06	0.19
		avrg:	(2272)	(1084)	(20.9)	(18.1)	(2624)	(1.1)	(0.4)	(36)	(0.59)	(4.3)	(3.5)
		max:	9181	4200	385.5	154.7	16828	5.0	2.8	83	1.33	44.2	22.2

Apéndice 5

BQ-5	29	min:	126	58	0.01	0.12	149	0.04	0.15	16	0.17	0.28	0.65
		avrg:	(2192)	(869)	(30.4)	(8.8)	(4073)	(1.9)	(0.5)	(47)	(0.60)	(9.2)	(6.3)
		max:	5760	3022	219.3	44.4	17336	7.5	1.4	77	0.92	46.3	24.3
BQ-6	52	min:	151	86	0.01	0.09	66	0.01	0.14	9	0.13	0.18	0.36
		avrg:	(1874)	(1261)	(29.6)	(9.9)	(5410)	(2.6)	(0.6)	(50)	(0.53)	(8.3)	(6.5)
		max:	7659	5935	286.1	70.9	18838	10.9	1.9	79	1.05	35.7	22.8
all BQ apatites	381	min:	54	32	0.01	0.05	34	0.01	0.05	3	0.05	0.03	0.10
		avrg:	(2520)	(1260)	(22.1)	(13.0)	(3354)	(1.7)	(0.4)	(37)	(0.58)	(4.6)	(3.8)
		max:	12320	8344	385.5	154.7	18838	13.0	2.8	83	1.33	46.3	24.3

Apéndice 5

Supplementary Table 2.

Trace element (Sr, Y, Th, and U) and rare earth element (from La to Lu) concentrations (in ppm) obtained on individual apatite grains using LA-ICP-MS at the Laboratorio de Estudios Isotópicos, Centro de Geociencias, Campus Juriquilla, UNAM.

Note:

The reference number (e.g. cm1-8) indicate, in order, the rock sample name (CM-1) and the corresponding number of the individual apatite crystal analysed (8). The geographic coordinates (latitude, longitude, and elevation in m.a.s.l.) of samples are also presented.

SAMPLE: CM-1 (Permo–Triassic Chiapas Massif Complex, granite)

16°34′11″ N; 93°38′31″ W; elevation = 568 m.a.s.l.

Apatite	Sr	Y	La	Ce	Pr	Nd	Sm	Eu	Gd	Tb	Dy	Ho	Er	Yb	Lu	Th	U
cm1-1	165.2	435.8	448.6	1009.0	117.1	489.7	87.6	20.5	88.2	10.7	65.7	13.6	40.1	36.6	6.6	29.84	12.47
cm1-2	167.8	434.9	434.2	976.0	115.1	480.8	86.1	20.3	86.7	10.8	64.8	13.7	40.1	36.8	6.7	27.98	12.49
cm1-3	161.2	551.0	548.3	1275.0	148.5	618.3	111.7	25.8	112.0	13.4	82.0	17.2	50.1	46.5	8.3	25.97	9.13
cm1-4	166.0	526.2	444.6	1023.0	124.2	533.3	100.8	22.0	99.5	12.5	76.9	16.3	48.2	45.3	8.1	32.63	12.60
cm1-5	157.5	462.6	411.8	967.0	114.8	493.0	90.3	20.6	93.6	11.5	68.9	14.8	43.6	39.1	7.1	27.76	12.02
cm1-6	164.9	435.4	378.5	856.7	103.9	445.7	82.2	18.8	83.2	10.5	63.2	13.1	39.1	37.0	6.5	28.85	13.30
cm1-7	161.1	530.2	429.7	1007.0	123.9	530.8	98.4	21.7	100.3	12.6	78.2	16.4	48.3	44.7	8.0	34.66	14.86
cm1-8	161.7	490.1	476.2	1037.8	124.7	538.8	97.0	21.4	96.1	11.9	71.9	15.1	44.9	41.5	7.7	31.85	12.06
cm1-9	157.6	657.5	563.4	1307.0	162.0	715.0	129.6	28.0	132.0	16.1	97.9	20.6	61.1	56.1	10.4	33.64	11.58
cm1-10	159.9	537.4	467.9	1078.1	135.7	589.0	108.7	22.6	109.1	13.7	81.2	17.1	50.1	46.2	8.4	32.68	11.92
cm1-11	162.2	455.6	421.7	946.2	117.6	505.6	93.1	19.9	90.0	11.4	67.7	14.2	41.9	38.9	6.9	32.15	11.66
cm1-12	162.6	499.1	578.8	1240.0	139.5	570.7	100.3	23.7	101.7	12.6	75.0	15.4	45.1	43.0	7.8	28.07	7.20
cm1-13	164.1	526.0	576.4	1238.0	143.6	596.4	108.0	24.4	106.8	13.1	79.3	16.4	48.2	44.4	8.1	29.49	7.82
cm1-14	168.8	480.3	524.6	1114.0	130.1	532.3	97.7	21.5	95.4	12.0	70.9	14.9	44.2	40.6	7.3	27.16	9.67
cm1-15	166.2	501.1	516.0	1116.0	131.4	546.7	99.9	22.3	100.0	12.5	74.9	15.5	45.9	42.0	7.6	27.75	10.56
cm1-16	157.9	622.8	548.9	1291.0	158.3	671.5	124.2	27.8	124.6	15.6	93.6	19.5	57.5	53.7	9.8	20.77	5.33
cm1-17	158.0	687.0	607.0	1423.0	174.7	744.0	135.9	31.0	135.6	17.1	101.1	21.2	62.3	58.8	11.0	35.95	16.55
cm1-18	157.5	822.7	768.9	1729.0	208.7	890.9	162.2	37.5	162.5	20.5	122.0	25.8	75.3	71.8	13.1	33.70	8.56
cm1-19	161.1	414.3	446.8	961.0	110.3	443.2	78.2	18.5	76.2	9.5	58.8	12.5	37.5	35.7	6.6	28.07	11.95
cm1-20	163.0	406.7	447.6	952.7	108.5	439.6	76.9	18.8	76.0	9.5	55.7	12.0	36.0	35.4	6.3	29.93	13.06
cm1-21	155.4	530.8	521.9	1203.0	141.2	570.9	103.3	23.0	102.1	12.9	77.8	16.3	47.5	45.1	8.1	25.48	7.82

Apéndice 5

cm1-22	160.5	517.8	561.0	1228.0	138.9	564.0	100.4	23.6	100.7	12.3	74.2	15.6	45.8	43.2	7.6	26.58	9.31
cm1-23	163.6	547.9	579.6	1210.0	143.1	600.1	105.8	24.6	104.3	13.2	79.9	16.8	50.5	46.7	8.1	28.09	7.77
cm1-24	167.4	457.0	476.1	1018.0	120.2	493.4	90.4	20.5	89.7	11.0	66.2	14.3	41.6	39.0	6.9	31.53	11.44
cm1-25	168.3	449.8	456.2	957.0	112.8	470.3	85.0	19.6	84.4	10.5	64.5	13.5	40.0	37.1	6.6	33.64	12.12
cm1-26	171.5	456.8	511.3	1022.6	118.3	487.7	85.9	20.7	86.1	10.8	65.3	13.7	41.2	38.3	6.8	31.64	12.17
cm1-27	170.2	478.2	616.8	1200.0	136.0	554.6	99.7	22.8	99.5	12.2	73.5	14.7	42.9	39.3	6.8	30.49	6.54
cm1-28	170.7	480.1	630.2	1217.0	136.6	561.6	102.3	22.8	100.2	12.2	73.1	14.9	43.2	38.8	6.8	31.81	5.50
cm1-29	164.0	476.5	569.2	1178.0	132.8	546.0	97.2	22.0	99.8	12.2	71.3	15.1	43.2	39.9	7.0	34.30	7.19
cm1-30	164.3	537.9	547.0	1164.0	136.6	573.5	103.9	24.0	104.8	13.2	78.7	16.4	48.5	45.2	7.8	25.14	7.80
cm1-31	160.2	538.8	502.3	1134.0	135.7	561.4	104.0	23.1	102.1	13.1	78.2	16.6	48.7	44.3	8.2	25.75	8.08
cm1-32	165.4	531.6	543.7	1173.0	136.8	562.8	102.1	23.4	101.5	12.8	76.5	16.1	47.6	43.1	7.9	31.28	10.27
cm1-33	167.5	535.8	534.0	1171.0	137.8	573.3	103.8	24.0	103.7	13.0	77.9	16.4	49.4	46.4	8.1	25.33	8.30
cm1-34	172.1	431.9	642.0	1246.0	136.6	546.1	97.1	22.3	95.9	11.8	68.0	13.7	39.8	34.8	6.0	28.73	5.75
cm1-35	171.9	442.9	616.5	1219.0	135.2	544.9	96.4	21.5	97.6	11.8	68.3	14.3	40.7	35.8	6.1	28.00	5.57
cm1-36	174.4	458.3	651.7	1252.0	140.0	561.0	101.0	22.7	98.0	12.3	72.3	14.5	42.0	36.5	6.4	27.29	5.56
cm1-37	173.0	465.9	663.3	1282.0	142.1	574.7	103.7	22.8	99.9	12.3	71.6	14.9	43.1	37.2	6.3	33.52	7.25

SAMPLE: CM-2 (Permo–Triassic Chiapas Massif Complex, granodiorite, slightly metamorphosed)

16°28′47″ N; 93°42′08″ W; elevation = 585 m.a.s.l.

Apatite	Sr	Y	La	Ce	Pr	Nd	Sm	Eu	Gd	Tb	Dy	Ho	Er	Yb	Lu	Th	U
cm2-1	303.8	183.6	717.0	1285.0	114.6	383.0	54.5	14.2	46.1	5.0	27.1	5.3	15.4	15.8	3.1	88.60	26.90
cm2-2	301.0	140.7	544.6	939.7	83.0	283.2	38.8	9.7	34.2	3.5	19.3	4.1	12.2	14.4	2.9	36.86	15.23
cm2-3	349.7	160.9	872.0	1389.0	116.0	369.4	49.8	14.8	42.3	4.3	23.6	4.8	14.0	14.9	2.8	30.49	11.11
cm2-4	337.0	203.5	1061.0	1720.0	144.7	460.8	60.7	17.0	53.3	5.3	28.0	5.8	17.1	19.7	4.0	44.30	16.62
cm2-5	363.5	92.3	508.6	801.3	65.8	212.3	27.1	8.3	24.1	2.5	13.5	2.6	7.6	8.7	1.7	26.04	8.35
cm2-6	368.7	74.8	470.6	704.6	56.7	182.0	22.9	7.1	20.2	2.1	10.8	2.1	6.1	6.4	1.3	22.74	7.67
cm2-7	360.0	77.4	434.9	696.1	57.4	186.0	23.4	6.8	20.5	2.1	11.1	2.2	6.5	6.7	1.3	22.38	7.77
cm2-8	390.7	85.6	539.8	798.9	63.2	201.4	25.3	7.9	22.6	2.2	12.1	2.4	7.2	7.9	1.5	25.96	7.81
cm2-9	392.0	86.2	524.2	772.5	61.1	196.7	25.6	7.7	22.4	2.3	11.6	2.4	7.3	8.0	1.5	26.34	7.87
cm2-10	385.8	93.5	558.2	835.5	66.2	214.0	26.6	8.3	23.4	2.4	13.0	2.7	7.8	8.6	1.7	26.55	8.27
cm2-11	306.6	89.4	393.0	682.0	59.9	197.2	25.5	7.5	21.3	2.3	12.3	2.5	7.7	8.4	1.6	23.40	8.63
cm2-12	303.5	92.2	405.6	714.9	61.8	197.7	26.4	7.6	21.6	2.3	12.9	2.6	7.8	8.3	1.6	23.69	8.77
cm2-13	300.6	85.7	356.4	634.2	56.2	186.3	24.8	6.9	21.0	2.2	11.9	2.4	7.3	7.8	1.5	22.44	8.13
cm2-14	311.0	85.6	390.6	686.8	59.7	196.6	25.5	7.7	21.5	2.2	11.7	2.3	7.0	7.4	1.4	25.75	8.90
cm2-15	332.0	89.4	426.4	731.3	62.5	201.7	25.7	7.8	21.5	2.2	12.3	2.5	7.5	8.2	1.6	26.98	9.49
cm2-16	326.1	97.4	459.6	795.0	67.2	214.7	27.4	8.3	24.4	2.4	13.1	2.6	7.6	8.7	1.7	26.14	9.22

Apéndice 5

cm2-17	293.9	96.0	385.9	692.7	62.1	203.2	25.7	7.2	23.3	2.3	13.1	2.7	7.7	8.6	1.7	22.68	9.06
cm2-18	285.4	97.9	392.8	712.3	63.8	212.0	28.6	7.6	23.7	2.4	12.8	2.8	8.1	8.9	1.8	25.20	9.58
cm2-19	280.2	118.0	435.7	794.0	70.9	240.8	31.9	8.2	28.3	2.9	15.8	3.3	10.1	10.8	2.2	34.21	14.28
cm2-20	378.9	80.9	501.2	759.5	60.8	193.6	25.2	7.6	22.2	2.2	11.4	2.3	6.4	7.1	1.4	27.75	10.30
cm2-21	348.1	79.1	334.7	587.4	51.6	171.3	23.6	6.2	20.8	2.2	11.2	2.2	6.5	6.8	1.2	26.54	13.70
cm2-22	324.9	68.1	308.0	524.3	45.0	149.0	20.5	5.8	18.6	1.8	9.7	2.0	5.7	6.0	1.1	22.56	10.10
cm2-23	340.9	67.9	361.1	582.0	48.3	155.5	20.6	6.2	17.6	1.8	9.5	1.8	5.4	5.3	1.1	24.45	10.52
cm2-24	310.1	74.4	315.0	548.2	48.1	161.6	23.0	6.1	20.0	2.0	10.7	2.2	6.2	6.5	1.3	23.73	10.05
cm2-25	382.6	78.0	568.9	823.6	62.5	192.8	24.1	8.0	20.7	2.1	10.4	2.1	6.2	6.8	1.4	26.80	8.91
cm2-26	392.4	68.4	532.1	761.9	57.9	177.6	21.3	7.4	19.2	1.8	9.3	1.9	5.3	6.0	1.3	23.24	7.44
cm2-27	380.4	78.6	480.0	734.3	58.7	182.5	23.5	7.7	20.6	2.1	10.7	2.2	6.0	6.9	1.4	23.19	7.61
cm2-28	329.7	60.5	462.6	712.4	56.0	172.9	20.3	7.1	17.5	1.7	8.7	1.8	5.1	5.1	1.1	25.98	8.84
cm2-29	345.2	50.9	418.1	619.2	47.5	143.9	17.3	6.2	15.5	1.4	7.7	1.4	4.0	4.2	0.9	20.00	7.45
cm2-30	370.2	50.9	455.8	653.5	48.6	146.5	16.8	6.3	15.1	1.4	7.3	1.4	3.9	4.3	0.9	21.40	7.90
cm2-31	357.6	55.3	399.0	606.8	47.4	149.0	17.9	6.0	15.3	1.5	8.1	1.6	4.5	4.7	1.0	20.91	8.15
cm2-32	378.6	78.6	472.6	712.4	57.3	182.6	22.7	7.3	20.3	2.1	11.5	2.3	6.6	7.6	1.4	22.76	7.81
cm2-33	375.1	77.2	516.5	756.1	59.0	184.8	23.0	7.6	21.0	2.0	11.2	2.1	6.5	6.8	1.4	25.82	9.09
cm2-34	363.0	85.2	553.5	830.0	64.5	206.3	25.5	8.1	22.7	2.2	12.0	2.4	7.2	7.9	1.5	27.16	8.83
cm2-35	367.4	62.1	527.7	753.3	56.9	177.3	20.9	7.4	18.7	1.8	9.5	1.7	5.0	5.2	1.1	23.16	7.62
cm2-36	364.2	70.3	533.7	782.5	60.6	187.0	22.7	7.6	19.7	2.0	9.9	2.0	5.5	5.7	1.2	24.77	8.10
cm2-37	382.1	85.6	537.4	809.0	64.7	203.2	25.3	8.1	23.2	2.2	12.1	2.5	6.9	7.9	1.5	23.68	7.87
cm2-38	373.3	60.9	519.2	759.1	57.7	178.0	21.2	7.2	19.1	1.8	9.0	1.6	5.1	5.3	1.1	24.17	7.53
cm2-39	364.2	62.2	492.7	746.5	58.7	180.2	20.5	7.3	19.0	1.7	8.8	1.7	5.1	5.6	1.1	24.49	7.96
cm2-40	368.2	58.3	514.8	759.4	57.1	171.0	19.4	6.9	17.6	1.7	8.3	1.7	4.8	5.0	1.1	23.69	7.66
cm2-41	372.2	61.4	512.6	745.5	56.6	173.6	20.7	7.1	18.3	1.7	8.8	1.7	4.8	5.5	1.0	23.41	7.51

SAMPLE: CM-3 (Permo–Triassic Chiapas Massif Complex, deformed granodiorite)

16°24′46″ N; 93°47′42″ W; elevation = 663 m.a.s.l.

Apatite	Sr	Y	La	Ce	Pr	Nd	Sm	Eu	Gd	Tb	Dy	Ho	Er	Yb	Lu	Th	U
cm3-1	419.5	128.3	243.7	517.3	58.5	234.9	36.9	13.7	33.7	3.5	20.8	4.1	11.6	9.8	1.8	9.42	5.88
cm3-2	408.8	92.8	180.9	378.2	42.7	175.4	27.3	10.4	26.4	2.6	15.1	3.1	9.2	7.4	1.3	2.58	2.42
cm3-3	403.8	149.1	283.2	615.5	67.6	261.1	39.6	13.8	35.2	3.9	21.2	4.6	14.0	12.8	2.3	12.57	6.51
cm3-4	414.8	281.2	454.6	1017.0	118.5	488.0	81.8	24.9	73.3	8.1	44.6	9.0	26.1	22.6	4.1	9.05	5.65
cm3-5	419.7	267.9	517.8	1084.0	119.6	477.9	75.1	27.7	70.4	7.6	42.8	8.6	24.7	21.9	4.3	8.39	5.26
cm3-6	412.8	121.2	251.1	524.7	57.2	229.3	35.8	14.5	32.5	3.5	18.4	3.8	11.2	9.2	1.8	7.22	6.61

Apéndice 5

SAMPLE: CM-4 (Permo–Triassic Chiapas Massif Complex, granodiorite, slightly metamorphosed)

16°22′22″ N; 93°51′31″ W; elevation = 687 m.a.s.l.

Apatite	Sr	Y	La	Ce	Pr	Nd	Sm	Eu	Gd	Tb	Dy	Ho	Er	Yb	Lu	Th	U
cm4-1	346.4	248.2	1342.0	1927.0	166.8	546.6	72.4	19.3	61.1	7.0	39.8	8.0	22.9	22.2	4.0	53.52	20.67
cm4-2	347.9	484.8	2279.0	3371.0	298.0	989.9	137.4	36.3	119.2	13.8	78.3	15.5	45.4	43.7	7.9	199.50	66.50
cm4-3	355.5	244.2	1184.0	1740.0	151.8	498.4	68.8	16.9	57.1	6.6	38.1	7.7	22.2	20.9	3.9	48.50	18.50
cm4-4	346.9	142.9	654.0	993.0	85.0	289.0	41.3	10.9	34.8	3.9	22.4	4.6	13.5	12.1	2.3	55.50	22.10
cm4-5	338.2	291.7	1658.0	2495.0	214.9	699.0	86.6	26.2	75.4	8.2	45.6	9.1	27.5	26.4	5.1	78.80	27.98
cm4-6	344.9	203.0	1329.0	1840.0	151.8	489.9	63.0	18.9	52.8	5.8	31.9	6.5	18.6	18.7	3.7	57.14	20.83
cm4-7	345.0	342.9	1693.0	2499.0	215.5	714.9	100.1	26.8	82.5	9.4	53.8	10.9	31.4	31.3	5.6	119.80	40.74

SAMPLE: CM-5 (Permo–Triassic Chiapas Massif Complex, deformed granodiorite)

16°48′52″ N; 93°49′24″ W; elevation = 630 m.a.s.l.

Apatite	Sr	Y	La	Ce	Pr	Nd	Sm	Eu	Gd	Tb	Dy	Ho	Er	Yb	Lu	Th	U
cm5-1	371.8	166.9	343.8	785.0	88.4	360.0	56.8	18.0	50.5	5.3	28.1	5.1	14.4	12.0	2.3	43.65	38.59
cm5-2	387.7	37.7	91.8	192.5	21.0	86.1	12.9	4.1	12.5	1.2	6.4	1.3	3.2	2.7	0.5	8.81	11.14
cm5-3	375.2	147.2	378.0	763.0	81.2	336.0	54.3	15.8	48.7	5.0	26.0	5.0	13.2	10.3	1.9	31.08	24.41
cm5-4	388.4	50.3	100.8	223.7	25.0	104.8	16.8	5.0	15.0	1.6	8.7	1.6	4.2	3.4	0.6	7.64	17.39
cm5-5	382.6	59.0	109.0	243.8	27.6	116.7	20.4	5.5	17.5	1.9	10.0	1.9	5.2	3.6	0.7	12.74	9.50
cm5-6	380.5	46.4	104.2	222.9	24.3	103.3	16.1	4.9	14.2	1.5	7.8	1.5	4.1	3.2	0.6	7.78	14.35
cm5-7	394.4	34.3	88.3	178.5	18.8	75.4	11.9	3.3	10.6	1.1	5.7	1.1	3.1	2.3	0.4	6.56	12.51
cm5-8	382.1	65.8	161.7	333.6	35.5	143.2	22.0	6.5	20.0	2.0	11.0	2.0	5.7	4.6	0.8	14.57	16.22
cm5-9	383.8	160.4	367.7	773.0	83.6	346.2	54.9	16.2	49.2	5.2	27.0	5.3	13.5	11.1	2.1	63.80	47.98
cm5-10	377.9	238.0	627.0	1302.0	141.3	567.0	87.1	25.1	79.0	8.3	41.6	8.0	20.8	17.4	3.2	45.00	27.50
cm5-11	385.4	107.0	318.4	633.7	65.7	262.5	39.8	11.0	35.5	3.6	18.4	3.4	9.1	7.8	1.5	18.52	9.06
cm5-12	408.5	58.5	121.2	256.5	28.7	120.3	20.0	5.2	17.2	1.9	9.9	1.9	5.0	4.0	0.7	10.30	12.46
cm5-13	380.5	186.2	571.2	1157.0	122.2	496.0	78.5	19.5	68.8	6.9	34.6	6.6	17.0	13.5	2.4	34.42	17.27
cm5-14	381.2	249.7	686.9	1365.0	145.9	575.1	86.7	25.4	74.3	7.8	42.4	7.9	21.4	18.3	3.5	39.78	19.51
cm5-15	379.0	49.1	131.2	268.5	28.4	114.2	17.3	5.2	15.7	1.6	8.5	1.6	4.1	3.2	0.6	8.06	13.57
cm5-16	375.0	36.2	75.9	167.9	19.0	80.2	13.0	3.8	10.9	1.2	6.3	1.2	3.3	2.5	0.5	7.08	10.71
cm5-17	374.2	98.1	252.5	531.2	57.0	231.9	36.1	10.1	30.3	3.3	17.0	3.2	8.5	6.7	1.3	17.99	14.83
cm5-18	397.6	168.7	461.3	928.0	97.5	390.3	60.1	15.5	50.0	5.3	28.8	5.4	14.5	12.0	2.3	25.94	15.89
cm5-19	452.6	125.3	529.0	1009.4	105.3	436.6	67.1	14.6	59.1	5.7	27.1	4.8	11.9	8.2	1.5	24.27	9.63

Apéndice 5

cm5-20	379.6	41.0	91.4	197.9	22.0	92.0	14.9	3.9	12.9	1.3	7.1	1.3	3.5	2.8	0.5	7.86	10.11
cm5-21	397.5	36.7	103.7	207.2	21.6	82.7	13.3	3.6	11.4	1.2	6.3	1.2	3.1	2.5	0.5	7.06	9.24

SAMPLE: CM-6 (Permo–Triassic Chiapas Massif Complex, granodiorite)

16°46′40″ N; 93°48′29″ W; elevation = 630 m.a.s.l.

Apatite	Sr	Y	La	Ce	Pr	Nd	Sm	Eu	Gd	Tb	Dy	Ho	Er	Yb	Lu	Th	U
cm6-1	570.6	351.2	666.6	1540.0	188.8	793.9	130.0	20.8	106.3	12.7	70.2	13.0	32.8	24.0	3.4	14.48	3.52
cm6-2	574.2	359.3	674.4	1552.0	193.5	812.7	136.0	21.2	108.4	13.0	72.0	13.2	33.9	23.8	3.4	14.71	3.58
cm6-3	575.0	365.2	832.7	1877.0	228.2	930.3	148.1	22.0	117.5	13.6	74.8	13.9	35.4	24.9	3.7	21.61	5.53
cm6-4	572.0	383.7	726.7	1670.0	206.1	865.0	142.8	23.1	117.1	14.1	76.7	14.4	37.1	26.2	3.7	29.19	8.16
cm6-5	574.9	359.9	648.6	1516.0	186.9	791.6	132.7	20.6	107.7	13.0	71.4	13.5	34.0	24.1	3.4	16.25	4.26
cm6-6	579.3	379.3	706.4	1608.0	200.1	835.0	139.5	22.8	113.9	14.0	76.8	14.0	35.9	25.8	3.6	17.43	4.48
cm6-7	533.7	352.4	900.0	2001.0	233.7	917.0	135.5	19.1	103.4	12.2	69.3	12.8	33.7	24.5	3.7	21.72	7.31
cm6-8	575.6	380.3	851.0	1912.0	233.5	950.0	151.4	22.1	115.9	13.9	75.1	14.2	36.4	26.0	3.7	16.17	4.22
cm6-9	591.1	364.4	748.5	1697.0	208.3	869.5	143.3	22.6	113.7	13.8	74.9	13.7	35.6	24.8	3.5	21.12	4.86
cm6-10	585.2	304.1	597.5	1390.0	171.7	704.0	118.1	18.7	92.6	10.9	60.1	11.0	28.4	20.7	3.0	11.52	2.94
cm6-11	580.3	388.4	781.0	1797.0	221.3	910.0	147.8	22.8	117.3	14.3	77.8	14.4	37.1	26.1	3.7	26.54	7.40
cm6-12	561.0	319.6	768.7	1726.0	208.4	832.8	128.9	19.0	98.9	12.0	63.5	12.0	30.7	22.2	3.2	10.55	3.02
cm6-13	562.2	312.2	737.7	1676.0	204.8	826.3	129.3	18.2	102.0	11.9	64.8	12.1	30.6	21.2	3.1	15.39	5.05
cm6-14	506.4	434.0	1058.0	2395.0	285.7	1109.0	167.3	22.3	130.8	15.3	84.7	16.1	41.9	32.0	4.7	30.53	9.01
cm6-15	581.8	333.2	665.8	1522.0	189.7	790.1	129.1	20.3	99.5	12.0	66.2	12.3	31.7	23.4	3.5	24.09	6.22
cm6-16	584.7	300.3	661.9	1502.0	182.3	741.2	118.8	19.2	94.5	11.1	62.0	11.3	28.9	19.7	2.8	11.82	3.27
cm6-17	588.1	351.2	728.9	1657.0	205.1	842.5	135.6	21.3	108.0	12.8	70.8	13.2	33.4	24.3	3.3	16.25	4.34
cm6-18	585.8	299.9	633.0	1457.0	177.0	726.6	118.5	18.1	93.2	11.1	59.4	11.2	28.7	20.0	2.9	11.09	2.95
cm6-19	598.0	424.0	847.5	1920.0	238.7	992.8	166.5	22.9	131.8	15.6	87.0	15.9	40.3	28.2	4.0	18.10	4.49
cm6-20	566.9	393.3	867.3	1974.0	244.0	989.0	158.6	23.2	124.2	14.3	79.2	14.7	37.8	28.1	4.1	23.37	5.70
cm6-21	576.5	383.5	824.6	1868.0	227.2	928.0	148.4	22.8	119.9	14.3	78.5	14.7	37.2	27.0	3.9	24.66	6.64
cm6-22	594.1	350.9	708.0	1627.0	201.5	838.0	137.2	22.0	109.7	13.0	72.0	13.2	34.3	24.0	3.5	16.57	3.89
cm6-23	576.2	370.9	843.0	1914.0	232.9	928.0	149.3	22.8	117.5	13.7	75.3	13.9	36.0	25.5	3.7	21.50	4.91
cm6-24	574.6	353.4	710.0	1623.0	199.6	819.0	136.6	21.6	107.0	12.7	70.7	13.3	34.2	24.7	3.5	19.55	5.52

Apéndice 5

SAMPLE: TS-1 (Toarcian–Oxfordian? Todos Santos Formation, coarse-grained arkose)

16°42′30″ N; 93°38′47″ W; elevation = 564 m.a.s.l.

Apatite	Sr	Y	La	Ce	Pr	Nd	Sm	Eu	Gd	Tb	Dy	Ho	Er	Yb	Lu	Th	U
ts1-1	264.6	498.8	714.8	1960.0	246.6	987.0	171.7	20.3	144.0	16.9	92.8	17.5	48.5	44.8	6.9	52.70	35.54
ts1-2	387.1	58.3	600.1	781.6	56.1	173.9	21.2	6.9	21.7	1.9	9.7	2.0	5.5	4.8	1.0	20.15	6.98
ts1-3	302.7	414.7	415.3	1179.0	139.6	534.5	86.2	17.7	76.8	9.0	52.1	11.1	34.5	40.4	7.1	3.14	1.31
ts1-4	266.9	371.9	382.2	1127.0	153.4	664.8	126.0	17.8	109.1	12.7	70.3	13.1	36.2	28.2	4.2	44.81	28.43
ts1-5	185.0	170.1	713.5	818.4	61.6	204.6	29.9	10.0	33.2	3.9	24.3	5.1	15.6	14.4	2.7	21.00	5.31
ts1-6	182.4	200.1	786.0	911.0	70.0	234.6	36.3	11.5	39.2	4.9	29.5	6.3	19.0	16.2	3.2	26.20	6.98
ts1-7	293.3	269.0	445.0	1163.0	148.2	619.0	100.9	15.3	83.8	9.5	50.7	9.5	25.1	21.6	3.3	65.20	27.30
ts1-8	293.4	282.0	486.0	1272.0	160.0	666.0	109.1	16.4	91.0	10.1	53.8	10.0	27.1	22.5	3.4	71.90	29.30
ts1-9	291.2	275.0	444.0	1206.0	154.0	641.0	105.6	15.7	87.5	9.6	50.9	9.6	26.3	22.0	3.3	64.30	27.90
ts1-10	344.9	194.6	189.2	502.9	63.1	266.1	47.6	10.9	45.1	5.3	29.2	6.4	18.4	17.1	2.9	6.79	10.43
ts1-11	249.6	514.4	225.3	757.8	119.7	594.6	132.5	18.8	126.7	16.1	90.8	18.1	50.0	41.3	6.1	6.27	6.05
ts1-12	247.0	555.2	244.7	818.8	128.0	648.8	147.6	19.6	136.9	17.4	98.7	20.3	53.7	43.8	6.4	7.09	5.30
ts1-13	428.2	389.2	783.0	1868.0	225.1	894.0	146.7	20.4	118.8	13.9	74.4	14.1	37.5	26.5	3.7	19.09	5.34
ts1-14	246.0	72.2	183.4	334.8	34.0	127.9	20.5	5.0	19.5	2.0	11.6	2.3	6.6	6.1	1.1	14.14	42.30
ts1-15	201.4	249.2	717.2	947.0	79.4	289.7	47.3	15.0	49.3	6.1	36.2	7.8	23.3	22.9	5.0	29.21	6.50
ts1-16	276.7	764.2	315.4	1275.0	228.8	1152.0	239.2	23.3	191.9	22.2	121.4	23.5	64.3	50.3	7.9	34.67	8.40
ts1-17	131.8	342.7	444.2	844.0	93.7	395.8	72.7	22.9	76.5	9.3	53.6	11.3	31.2	26.4	5.1	19.03	16.77
ts1-18	157.9	684.0	1068.0	1919.0	206.3	830.0	141.2	45.4	138.7	17.1	105.6	21.8	62.9	62.3	11.7	85.70	26.55
ts1-19	251.0	381.0	104.4	369.0	62.0	345.0	85.5	20.6	86.7	10.9	65.3	13.1	37.3	34.8	5.8	16.20	38.90
ts1-20	286.5	124.6	474.9	741.4	69.1	257.8	38.1	13.4	33.9	3.5	19.4	3.9	11.5	11.3	2.3	79.90	37.20
ts1-21	305.3	161.7	1015.0	1386.0	116.5	405.0	52.8	16.2	46.5	4.7	26.2	5.2	14.5	14.9	3.0	106.80	36.91
ts1-22	398.6	111.9	332.2	464.6	43.2	180.9	29.2	8.0	30.7	3.3	20.3	4.2	11.2	9.7	1.7	41.21	32.81
ts1-23	218.9	335.9	441.8	1060.8	126.5	531.0	91.9	13.0	87.1	10.4	61.8	12.3	34.0	29.0	4.4	42.02	40.64
ts1-24	274.1	97.7	1031.0	1480.0	113.9	328.5	30.0	10.0	27.9	2.4	12.6	2.7	8.5	9.9	2.0	55.33	13.04
ts1-25	486.5	495.3	771.5	2128.0	293.3	1372.0	246.6	15.2	203.5	21.0	107.3	18.6	45.3	27.1	3.7	19.22	9.38
ts1-26	207.3	584.1	399.6	1149.8	159.7	741.5	137.1	22.6	122.6	14.3	81.5	17.2	51.3	53.1	10.5	11.68	9.80
ts1-27	316.6	174.5	1039.2	1526.0	132.5	470.6	65.0	15.4	57.7	5.5	29.4	5.8	15.8	15.0	2.8	42.70	13.98
ts1-28	311.0	495.0	757.0	1965.0	254.5	1083.0	178.9	26.4	145.2	16.8	93.3	17.2	46.7	40.3	6.0	84.70	37.90
ts1-29	367.1	438.4	582.4	1408.5	177.0	795.6	138.7	23.4	126.9	13.5	73.6	14.0	38.4	40.3	7.0	3.44	1.18
ts1-30	150.2	532.7	1100.0	1945.0	190.5	707.0	115.6	22.5	110.0	13.8	83.3	17.1	49.2	45.3	7.9	35.54	5.82

Apéndice 5

ts1-31	147.8	632.1	1000.9	1917.0	196.3	762.4	130.1	25.1	124.6	16.2	99.2	20.3	57.1	54.6	9.8	31.92	5.62
ts1-32	338.4	145.4	774.0	1289.0	118.9	412.4	50.9	14.7	43.2	4.3	22.9	4.6	13.4	13.6	2.4	45.69	23.13
ts1-33	195.5	108.2	603.0	635.0	44.9	148.5	20.8	8.2	22.8	2.6	15.8	3.5	10.2	9.3	1.9	18.65	6.80
ts1-34	148.5	722.5	644.2	1637.0	188.0	749.7	132.5	32.8	130.2	17.9	111.3	23.7	73.0	81.4	13.5	95.60	107.20
ts1-35	294.0	185.5	158.3	438.3	58.1	255.5	44.8	9.2	41.2	5.1	29.0	6.0	17.4	18.2	2.9	9.62	6.44
ts1-36	157.1	352.5	367.6	927.1	108.3	419.4	64.7	14.0	63.0	7.6	47.4	10.6	33.2	36.1	6.6	33.18	29.49
ts1-37	157.0	309.7	290.9	763.7	91.4	357.5	57.7	13.0	54.2	6.6	41.6	9.4	29.4	31.8	6.0	24.41	22.48
ts1-38	217.4	202.9	69.2	183.0	29.2	170.8	46.3	10.2	51.3	6.2	37.5	7.4	20.2	15.6	2.6	11.39	16.74
ts1-39	218.8	500.0	159.2	454.9	74.4	433.8	116.7	21.6	123.1	15.6	90.2	18.2	49.5	39.1	6.3	27.82	27.17
ts1-40	322.7	275.2	709.2	1609.0	184.0	718.0	106.3	25.4	92.5	9.3	48.8	9.3	26.1	25.4	4.3	56.00	22.28
ts1-41	205.5	1167.0	820.9	2131.0	292.3	1301.0	256.6	29.2	258.6	32.9	194.4	40.0	115.2	95.2	15.4	46.89	57.19
ts1-42	206.2	1544.0	1128.8	2889.0	395.0	1754.0	340.0	39.9	341.2	44.1	265.6	54.1	157.4	133.6	21.3	125.70	132.30
ts1-43	300.5	69.2	94.8	222.3	26.7	111.4	19.8	6.5	18.3	2.1	11.9	2.3	6.6	5.8	1.1	14.78	57.74
ts1-44	832.6	409.7	706.1	1730.0	235.6	1038.2	176.8	28.9	141.0	15.9	84.6	15.2	39.4	26.5	3.7	5.41	1.73
ts1-45	211.9	408.0	309.6	928.0	127.9	557.6	101.1	26.4	88.4	11.4	67.4	13.4	39.4	40.7	6.7	104.40	63.10
ts1-46	304.4	82.3	650.5	804.2	65.7	239.8	33.2	8.8	32.4	3.1	14.5	2.9	7.4	5.1	1.0	46.08	15.19
ts1-47	304.1	70.4	501.7	640.1	54.2	199.5	28.8	6.7	26.4	2.5	13.1	2.4	6.5	4.6	0.9	31.71	11.22
ts1-48	242.4	735.0	979.0	2618.0	338.3	1394.0	240.2	24.3	193.2	23.1	127.7	24.1	68.0	61.3	9.1	89.80	27.30
ts1-49	317.1	82.8	395.7	656.7	64.1	252.6	37.3	7.2	34.2	3.3	15.9	2.9	7.3	6.0	1.1	32.68	13.31
ts1-50	268.2	537.0	714.0	1916.0	248.0	1059.0	186.5	18.8	157.2	18.0	100.3	18.6	51.7	42.7	6.2	33.90	46.70
ts1-51	491.4	358.7	760.9	1789.0	213.9	872.6	141.7	20.8	116.6	13.5	72.9	13.4	35.3	25.2	3.6	19.75	7.26
ts1-52	166.8	927.5	338.6	1140.0	168.0	806.0	179.1	20.8	178.9	25.1	155.4	32.1	93.7	86.0	12.9	71.40	88.50
ts1-53	293.2	422.6	627.5	1678.0	212.0	898.6	150.7	19.2	118.1	13.8	76.3	14.6	39.7	35.2	5.2	55.48	19.74
ts1-54	306.0	252.1	416.8	1277.0	169.1	731.2	123.4	30.8	92.7	10.0	50.9	9.1	22.2	17.3	2.6	36.16	77.00
ts1-55	284.1	59.1	226.2	353.1	31.5	112.3	15.7	4.9	13.4	1.5	8.4	1.8	5.3	4.9	0.9	13.47	39.51
ts1-56	283.8	70.8	269.8	417.5	36.7	129.8	18.1	5.4	16.7	1.7	10.2	2.1	6.3	5.8	1.1	12.38	39.97
ts1-57	182.5	213.3	695.3	943.6	76.9	261.2	40.3	9.8	39.4	4.8	30.1	6.4	18.7	18.4	3.5	18.61	3.93
ts1-58	185.9	218.5	709.3	948.9	77.2	261.2	40.8	9.9	39.0	4.9	30.1	6.5	19.6	19.0	3.5	18.88	4.30
ts1-59	183.0	226.8	693.1	964.8	79.8	274.3	42.5	10.3	41.6	5.4	32.1	6.9	20.0	18.4	3.5	19.76	4.56
ts1-60	540.7	435.9	787.6	1998.0	248.1	1033.4	173.2	22.3	136.1	15.7	84.8	16.1	40.6	29.6	4.0	13.72	4.80
ts1-61	552.9	452.0	820.3	2080.0	257.3	1076.5	183.8	23.1	140.5	16.5	86.7	16.6	42.4	29.9	4.3	14.68	5.39
ts1-62	548.3	444.0	808.5	2046.0	251.0	1058.5	182.5	23.3	135.9	15.8	85.9	16.1	41.2	28.7	4.2	14.03	5.07
ts1-63	393.4	226.0	406.0	855.5	97.2	418.9	73.9	19.8	66.0	7.4	38.2	7.9	20.4	15.6	2.9	38.00	34.73
ts1-64	379.8	235.3	417.1	862.0	97.8	421.7	74.6	20.6	69.1	7.8	41.0	8.4	21.2	16.4	3.1	38.60	49.80
ts1-65	185.2	274.2	1052.0	1399.0	111.7	368.9	53.7	18.9	54.5	6.5	38.7	8.5	25.0	23.8	5.0	29.17	5.10
ts1-66	180.5	315.0	1129.0	1544.0	122.4	416.0	61.2	21.9	63.0	7.4	44.2	9.8	28.2	28.2	5.7	35.44	6.77
ts1-67	428.4	451.6	204.2	766.0	120.3	597.0	119.7	23.1	104.9	13.8	80.8	15.9	43.0	34.4	5.1	6.08	3.89
ts1-68	275.4	749.2	1118.0	2809.0	346.1	1417.0	241.1	39.7	196.2	23.4	129.6	25.1	69.1	67.6	11.2	142.90	56.17

Apéndice 5

ts1-69	272.3	70.7	289.4	534.8	52.4	190.6	27.0	6.0	21.4	2.2	10.6	2.2	6.0	5.2	1.1	17.66	8.86
ts1-70	269.3	745.0	535.5	1457.0	196.3	846.0	168.7	26.9	148.0	19.7	120.7	24.2	70.5	64.6	9.8	53.30	24.47
ts1-71	255.1	618.3	430.5	1200.0	162.4	713.0	140.5	22.1	124.0	16.4	101.9	20.5	59.4	53.3	8.2	41.03	19.59
ts1-72	233.5	279.1	1210.0	2126.0	200.7	690.9	92.2	18.9	76.6	8.0	43.4	8.5	23.8	25.2	4.4	61.10	24.02
ts1-73	303.3	353.2	955.9	2083.0	236.0	899.2	133.8	16.0	105.7	11.6	63.2	11.9	31.5	28.2	4.0	44.35	19.81

SAMPLE: TS-2 (Toarcian–Oxfordian? Todos Santos Formation, coarse-grained arkose)

16°41′04″ N; 93°37′06″ W; elevation = 550 m.a.s.l.

Apatite	Sr	Y	La	Ce	Pr	Nd	Sm	Eu	Gd	Tb	Dy	Ho	Er	Yb	Lu	Th	U
ts2-1	177.1	702.4	420.5	1038.1	129.2	546.9	102.9	19.5	103.7	14.6	95.5	21.0	66.2	68.3	12.0	19.25	13.56
ts2-2	152.9	693.6	2396.0	3982.0	354.2	1194.0	156.8	30.0	151.8	16.8	97.7	21.1	65.8	78.5	15.6	62.74	11.41
ts2-3	165.3	493.1	1927.0	3122.0	275.7	927.0	116.9	19.9	114.6	12.4	71.8	15.2	46.7	49.9	9.6	52.42	8.10
ts2-4	232.5	463.8	132.6	628.1	119.2	680.1	153.7	35.7	129.2	15.9	86.0	16.2	43.6	36.8	5.8	46.42	138.50
ts2-5	350.1	342.9	657.2	1489.0	178.2	745.1	127.4	26.7	108.2	12.5	66.2	12.0	31.4	26.1	4.2	65.05	53.05
ts2-6	182.3	255.3	1078.0	1350.0	104.6	359.3	52.1	15.8	54.3	6.1	38.1	8.2	24.4	22.1	4.1	45.60	14.66
ts2-7	182.0	336.5	1370.0	1719.0	134.5	470.5	68.8	20.8	69.3	8.2	49.1	10.7	32.8	28.8	5.5	69.30	19.46
ts2-8	460.0	210.2	339.2	905.4	131.6	663.0	123.0	18.4	93.3	9.8	46.3	8.0	18.5	11.7	1.6	5.58	2.47
ts2-9	492.2	217.5	381.2	1044.9	148.5	733.0	131.0	19.7	97.7	9.9	48.2	8.1	19.8	12.1	1.7	5.50	2.36
ts2-10	285.9	939.6	266.6	1083.9	188.8	1020.4	234.2	38.2	214.4	28.3	165.4	34.0	94.3	79.4	12.2	102.70	50.38
ts2-11	311.4	483.0	894.2	1947.0	235.4	1037.9	181.3	24.7	154.5	17.5	91.4	16.9	45.4	38.8	6.0	111.50	52.30
ts2-12	471.0	817.8	534.8	1464.0	218.3	1115.0	250.1	25.7	245.9	30.6	174.0	32.8	78.0	47.3	6.0	8.07	1.75
ts2-13	256.1	494.6	472.4	1294.7	170.6	765.6	138.2	20.3	124.5	15.2	90.4	18.2	49.3	43.0	7.1	83.41	45.13
ts2-14	276.3	650.0	180.8	652.0	112.6	618.0	149.0	21.2	148.6	18.4	106.4	21.0	58.8	55.4	9.6	5.21	20.88
ts2-15	315.3	293.8	962.0	1921.0	214.8	889.0	139.4	21.6	121.4	12.3	61.0	11.1	27.7	22.2	3.7	67.70	35.36
ts2-16	139.8	554.5	753.6	1528.0	177.3	763.1	133.0	29.3	134.6	15.7	91.8	18.8	48.9	37.5	6.5	41.01	5.75
ts2-17	143.4	511.0	702.0	1434.0	165.7	695.4	120.6	27.4	122.9	14.5	85.4	17.1	45.9	35.2	5.8	32.22	5.19
ts2-18	379.7	183.2	303.1	668.5	94.1	478.0	95.6	15.4	82.2	8.6	42.6	7.3	16.8	11.0	1.7	7.02	4.56
ts2-19	505.0	393.7	752.4	1775.0	219.2	904.0	147.9	22.1	131.3	14.9	81.0	15.1	36.8	26.2	3.9	22.05	6.67
ts2-20	502.5	399.8	767.4	1812.0	222.8	916.3	150.6	22.7	131.3	14.8	82.6	15.3	37.5	27.1	3.8	22.61	7.14
ts2-21	382.2	184.4	1162.0	1894.0	175.9	653.5	94.7	18.4	85.1	7.8	38.8	6.7	17.2	14.5	2.7	43.28	13.20
ts2-22	279.6	148.6	698.8	1010.0	95.8	402.5	68.0	13.0	66.0	6.4	31.4	5.8	14.2	11.7	2.4	30.24	12.20
ts2-23	314.6	64.4	356.7	545.1	50.0	171.4	22.5	6.5	20.7	1.9	11.1	2.1	6.2	5.8	1.0	32.67	35.39
ts2-24	300.3	53.7	274.4	402.9	36.5	125.4	17.7	5.4	16.8	1.7	9.4	1.8	5.1	4.5	0.8	13.09	34.06
ts2-25	465.5	196.4	164.4	626.6	108.1	551.3	105.3	20.0	85.5	8.6	42.1	7.1	17.2	11.2	1.7	6.56	5.62
ts2-26	430.8	190.6	92.7	381.0	70.8	397.0	86.4	17.2	75.0	7.8	40.4	6.9	16.9	12.0	1.8	5.29	7.47
ts2-27	212.0	859.0	1179.0	2239.0	242.3	975.5	187.5	30.2	203.1	25.3	151.2	31.0	84.2	74.4	12.2	59.60	17.30

Apéndice 5

ts2-28	202.0	917.6	1084.0	2119.0	233.9	947.6	188.5	30.9	207.1	26.2	158.0	32.0	89.9	80.9	13.3	68.54	20.44
ts2-29	422.5	502.1	1136.9	2492.0	286.4	1129.2	179.5	22.2	157.4	17.8	100.1	18.7	47.7	34.4	4.9	47.38	12.59
ts2-30	423.2	469.9	1076.0	2373.0	270.3	1059.0	168.6	21.0	144.6	17.0	93.9	17.6	44.8	32.4	4.6	42.27	11.85
ts2-31	484.9	485.5	993.5	2320.0	280.6	1140.4	186.4	26.6	159.2	18.1	98.5	18.2	47.2	32.4	4.7	31.87	7.59
ts2-32	513.4	457.6	1068.0	2520.0	298.7	1193.0	189.1	27.1	151.7	17.2	90.9	16.7	43.0	30.9	4.6	24.40	6.93
ts2-33	524.5	432.7	1035.0	2445.0	288.0	1154.0	178.6	26.2	144.5	16.3	88.0	16.1	40.9	29.5	4.3	21.64	6.44
ts2-34	316.6	222.0	835.0	1698.0	188.1	742.0	112.0	7.8	92.5	9.5	47.5	8.6	20.6	14.8	2.6	71.60	36.09
ts2-35	249.3	338.3	285.6	815.0	112.5	524.7	99.8	21.2	90.6	10.3	56.6	11.2	31.3	29.9	5.7	45.41	31.50
ts2-36	425.8	342.0	809.0	1805.0	198.9	777.0	122.7	16.5	105.3	12.1	67.2	12.7	32.4	23.7	3.2	22.93	6.51
ts2-37	236.4	556.4	370.4	1066.0	145.3	685.0	136.7	17.4	130.9	16.6	94.4	19.2	52.5	46.1	7.3	14.50	16.31
ts2-38	403.6	132.1	594.6	1108.1	113.0	480.7	76.4	14.8	66.4	6.4	30.6	5.2	12.6	7.9	1.4	12.46	4.34
ts2-39	343.7	251.8	514.8	1013.3	100.1	373.2	53.5	9.0	51.6	6.0	35.6	7.8	23.6	23.9	4.4	20.47	17.41
ts2-40	330.7	228.5	424.3	853.9	86.7	326.5	49.7	7.9	46.9	5.4	32.3	7.0	21.6	20.7	4.0	18.08	15.55
ts2-41	324.5	583.4	936.1	1913.0	200.2	767.7	118.8	18.6	111.0	13.3	80.8	17.9	54.2	57.9	10.6	124.80	54.21
ts2-42	388.8	87.8	1469.0	1384.0	94.2	298.6	33.8	12.2	33.1	3.0	15.0	2.9	8.2	8.2	2.0	34.91	10.49
ts2-43	206.3	130.3	868.0	978.0	70.0	230.1	28.8	11.1	31.5	3.4	19.3	4.2	11.6	11.1	2.1	34.10	9.75
ts2-44	184.2	161.7	647.6	778.7	60.6	205.6	30.3	9.5	31.3	3.7	21.9	4.7	14.6	14.8	3.0	23.74	5.77
ts2-45	283.8	122.3	589.0	974.0	82.8	287.5	38.9	14.5	36.7	3.6	19.0	3.6	10.5	10.5	2.4	24.04	19.30
ts2-46	287.3	127.4	655.0	1055.0	90.1	313.2	43.3	13.6	39.8	4.0	20.6	4.0	11.1	10.8	2.4	18.96	12.44
ts2-47	194.0	601.0	1299.0	2455.0	248.5	969.0	152.5	15.0	156.5	17.2	100.5	20.6	58.7	53.1	9.6	51.05	26.91
ts2-48	284.7	121.5	442.7	763.0	69.8	264.1	39.1	13.0	36.1	3.6	19.6	3.9	10.2	10.6	2.1	24.74	19.57
ts2-49	288.5	173.0	413.0	1260.0	155.0	635.0	90.8	22.4	66.1	6.9	35.1	6.2	15.5	12.5	1.8	19.10	57.50
ts2-50	305.1	112.3	308.0	606.0	62.6	249.7	38.0	11.0	33.1	3.4	17.8	3.4	10.1	8.6	1.8	16.67	9.28
ts2-51	318.2	100.5	278.4	546.3	55.4	214.8	32.7	9.6	28.2	2.9	15.9	3.1	8.5	8.1	1.8	16.29	7.80
ts2-52	272.9	72.4	279.1	482.7	48.4	193.9	28.7	6.7	24.5	2.4	12.8	2.5	6.3	6.0	1.1	18.39	31.90
ts2-53	277.8	46.8	222.0	357.0	33.4	127.7	17.0	5.1	15.3	1.6	7.9	1.5	4.2	4.1	0.8	13.66	44.31
ts2-54	244.1	458.0	508.0	1488.0	206.2	919.0	159.1	13.5	136.0	16.0	88.0	16.8	44.9	32.7	4.6	31.70	59.30
ts2-55	236.4	601.0	584.0	1747.0	251.0	1157.0	203.4	17.4	174.5	21.1	116.6	21.5	58.0	41.0	5.9	47.50	81.30
ts2-56	227.4	506.0	647.0	1564.0	214.8	1014.0	176.0	17.9	158.4	17.9	95.4	17.8	44.8	29.2	4.6	31.60	34.70
ts2-57	312.7	802.0	494.0	1560.0	229.0	1101.0	230.0	26.8	203.0	26.0	146.7	28.0	77.5	65.2	10.3	73.00	82.40
ts2-58	332.9	552.0	913.0	2317.0	295.9	1277.0	218.2	25.6	176.1	20.4	109.3	20.0	52.2	42.3	6.3	177.00	86.60
ts2-59	272.5	139.0	928.0	1287.0	104.4	368.9	50.4	14.9	46.9	4.6	24.1	4.5	12.2	11.4	2.5	35.69	13.28
ts2-60	364.9	523.7	647.2	1442.0	180.5	794.3	151.9	21.3	123.6	15.6	91.2	17.0	47.1	38.4	5.8	70.60	29.84
ts2-61	174.8	97.9	443.1	537.3	41.1	138.7	19.9	6.8	20.9	2.4	14.0	3.2	9.4	8.4	1.7	22.99	9.98
ts2-62	181.2	152.3	599.0	758.0	59.1	201.1	28.1	10.3	29.4	3.6	21.8	4.6	14.1	13.6	2.6	28.58	6.91
ts2-63	300.8	218.2	703.7	1293.0	121.9	435.5	60.6	18.8	53.4	5.6	30.8	6.2	19.2	20.0	4.0	25.97	15.06
ts2-64	255.6	104.3	386.5	634.2	55.8	195.6	28.9	6.3	24.7	2.8	15.2	3.0	8.5	9.4	1.7	33.37	13.32
ts2-65	232.0	85.4	277.3	463.5	42.9	152.8	24.0	5.0	21.8	2.3	12.8	2.6	7.6	7.7	1.5	13.02	33.55

Apéndice 5

ts2-66	232.7	115.8	350.9	588.6	53.6	195.6	31.0	5.9	27.3	3.0	16.7	3.4	9.8	10.0	2.0	29.19	14.63
ts2-67	225.7	862.0	273.2	871.0	135.1	687.0	163.7	33.7	160.4	22.2	134.1	28.7	84.3	80.8	12.8	31.13	28.60
ts2-68	271.9	140.3	458.4	851.0	79.9	291.6	37.6	16.5	33.9	3.5	19.0	4.2	12.0	13.4	3.0	19.25	9.88
ts2-69	278.4	192.0	618.0	1158.0	114.1	404.0	51.6	19.5	46.9	4.9	27.8	5.7	16.5	18.1	3.8	17.28	5.28
ts2-70	279.0	142.6	463.6	879.0	83.9	301.1	39.9	14.5	35.2	3.6	20.3	4.2	12.2	13.5	3.0	13.59	4.41
ts2-71	577.9	763.4	304.0	947.6	147.3	732.4	189.1	26.2	176.8	23.8	141.3	27.5	71.9	55.4	7.6	13.30	13.26
ts2-72	582.3	673.7	287.4	893.8	136.1	674.3	171.2	23.8	160.3	21.1	126.8	24.6	64.8	48.2	6.5	10.75	11.07
ts2-73	260.0	269.0	122.5	517.9	87.1	446.9	97.0	28.1	81.7	9.4	51.4	9.5	24.8	20.5	3.1	24.72	71.25
ts2-74	209.1	625.9	418.4	1269.0	167.5	703.1	140.0	32.3	129.5	17.2	109.7	22.1	63.7	65.0	9.8	76.40	49.53
ts2-75	208.0	535.8	476.9	1389.0	176.8	715.8	132.6	34.5	118.4	15.4	92.3	18.5	54.1	56.9	8.6	72.44	46.74
ts2-76	283.3	311.2	256.0	613.0	74.1	334.9	68.1	16.2	63.9	7.7	45.0	9.0	26.7	28.9	5.3	21.16	11.46
ts2-77	162.9	63.9	725.0	696.0	43.9	133.2	17.2	3.9	18.2	1.7	9.5	1.9	5.7	5.4	1.1	13.40	20.01
ts2-78	164.1	75.2	835.0	802.0	50.5	154.7	20.9	4.2	21.6	2.2	11.3	2.3	6.5	6.4	1.4	15.63	23.64
ts2-79	359.8	202.6	1324.0	2114.0	174.6	631.3	88.2	14.0	78.8	7.5	36.6	6.6	16.8	13.3	2.3	24.99	6.10
ts2-80	164.4	992.5	503.5	1774.0	240.1	1097.0	213.4	20.2	196.1	24.7	144.2	29.8	85.2	81.7	15.7	31.29	14.92
ts2-81	320.3	86.4	446.0	757.0	62.6	216.5	28.5	8.3	25.5	2.5	12.6	2.5	6.9	6.8	1.4	16.23	6.06
ts2-82	332.6	340.8	809.5	2126.0	240.7	1008.8	158.5	21.3	124.0	13.2	68.2	12.2	30.8	24.8	3.8	119.60	64.80
ts2-83	235.0	746.3	423.3	1264.0	166.9	776.9	161.9	29.5	154.6	20.3	123.6	25.1	72.3	69.0	10.8	91.39	49.49
ts2-84	359.2	158.0	326.5	706.1	82.2	377.5	71.2	6.1	65.1	6.9	34.6	6.1	14.1	8.3	1.2	55.90	33.80
ts2-85	416.4	93.0	494.5	938.0	81.7	288.3	37.8	11.2	36.5	3.2	15.6	2.9	7.7	7.2	1.3	12.98	4.77
ts2-86	303.3	132.9	299.3	545.7	56.2	237.7	44.0	9.8	39.6	4.3	23.1	4.4	11.6	9.2	1.7	22.32	16.30
ts2-87	326.3	271.7	1210.0	2283.0	210.9	824.0	125.6	21.3	105.7	10.2	51.1	9.2	23.2	20.3	3.5	41.70	13.44
ts2-88	442.4	477.6	1121.9	2748.0	287.3	1134.1	171.8	20.5	139.7	15.9	87.7	16.7	43.5	32.7	4.6	35.40	6.41
ts2-89	500.3	495.2	1061.8	2523.0	273.6	1111.0	185.4	11.8	152.1	17.1	93.6	17.5	45.9	38.5	6.0	118.47	80.25
ts2-90	479.8	197.8	318.0	851.0	119.6	599.4	111.5	18.0	87.0	8.9	43.6	7.3	17.7	11.1	1.5	5.95	2.52
ts2-91	455.3	370.1	837.9	2015.0	209.9	835.1	132.8	18.0	108.8	12.6	70.6	13.0	33.6	24.7	3.5	22.19	5.52
ts2-92	262.4	412.2	722.8	1976.0	225.6	906.1	140.5	18.4	109.1	12.6	70.8	13.7	37.9	37.6	6.0	74.68	45.33
ts2-93	144.7	138.7	1685.0	1731.0	106.1	327.1	37.5	10.1	38.2	3.9	22.0	4.6	12.8	11.9	2.4	18.13	4.12
ts2-94	445.7	99.4	1046.0	1361.0	98.2	332.2	43.3	13.3	39.2	3.7	18.2	3.5	9.0	7.2	1.4	24.56	6.15
ts2-95	252.5	357.9	727.0	1447.0	138.0	540.0	84.2	19.6	81.6	8.9	51.5	10.8	31.4	32.7	6.2	56.60	17.65
ts2-96	283.3	139.2	1343.0	1780.0	120.8	370.8	44.1	10.5	40.2	3.8	20.3	4.1	11.9	13.7	2.9	23.44	4.97
ts2-97	316.3	215.9	1025.0	1706.0	149.8	553.0	75.9	19.6	63.0	6.6	35.3	6.8	18.5	16.7	2.9	82.80	31.54
ts2-98	272.6	332.5	845.7	1638.0	162.0	674.6	116.8	23.3	105.3	11.2	59.8	11.1	29.6	25.2	4.4	58.90	29.59
ts2-99	279.0	97.2	410.3	669.6	58.2	218.0	32.5	10.7	29.7	3.0	15.5	3.0	8.5	7.9	1.6	19.79	13.19
ts2-100	193.2	354.8	609.1	1020.9	97.9	388.8	69.6	10.8	71.0	9.0	55.0	11.4	32.2	26.4	4.6	21.89	6.49
ts2-101	202.9	294.0	1950.0	2558.0	163.1	482.0	54.3	23.6	59.8	6.1	36.1	8.4	26.4	30.4	6.5	93.30	21.65
ts2-102	184.6	147.2	542.2	666.3	52.9	191.4	29.7	9.2	30.5	3.6	21.8	4.6	13.2	12.1	2.3	22.42	7.32

Apéndice 5

SAMPLE: TS-3 (Toarcian–Oxfordian? Todos Santos Formation, coarse-grained arkose)

16°39′03″ N; 93°34′20″ W; elevation = 538 m.a.s.l.

Apatite	Sr	Y	La	Ce	Pr	Nd	Sm	Eu	Gd	Tb	Dy	Ho	Er	Yb	Lu	Th	U
ts3-1	396.0	76.2	540.7	889.5	75.7	264.3	34.2	10.8	32.5	2.9	13.9	2.6	7.2	5.5	1.1	12.03	4.30
ts3-2	370.0	66.5	450.0	743.0	63.2	220.6	29.1	9.4	26.5	2.5	11.5	2.3	6.1	4.9	1.0	10.46	4.03
ts3-3	446.6	172.5	376.0	836.0	100.1	442.0	71.4	17.5	60.7	6.5	34.2	6.4	17.0	12.5	2.1	17.03	7.26
ts3-4	372.3	118.2	540.3	1025.7	93.4	324.6	43.8	17.4	38.6	3.8	18.8	3.6	10.5	9.4	2.0	18.06	8.38
ts3-5	221.4	175.7	218.5	514.0	60.4	255.8	43.3	7.7	44.1	5.4	30.0	5.9	17.7	13.9	2.3	4.54	6.11
ts3-6	469.4	191.0	206.6	640.7	89.8	432.6	78.9	13.3	65.1	7.3	37.9	7.0	18.1	13.9	2.2	26.13	19.03
ts3-7	397.7	285.3	453.1	1397.0	200.2	921.7	157.6	13.9	119.7	12.5	59.9	10.2	25.6	15.8	2.2	15.08	7.62
ts3-8	417.7	386.0	632.4	1905.0	270.2	1245.0	213.7	20.8	159.8	16.8	82.1	13.8	34.7	22.2	3.0	27.09	9.32
ts3-9	245.4	441.2	533.8	1430.0	185.0	823.0	148.2	19.5	128.5	14.9	80.5	15.5	42.5	35.5	5.4	39.98	47.99
ts3-10	245.5	430.2	535.6	1421.0	184.0	818.0	148.0	19.6	126.7	14.5	78.1	14.8	40.7	33.9	5.4	39.59	50.80
ts3-11	301.4	235.5	479.1	946.4	101.1	403.2	66.1	14.7	60.5	7.2	40.1	7.8	22.6	19.1	3.2	46.22	23.51
ts3-12	441.9	126.5	679.4	1223.0	117.1	449.4	67.2	13.9	58.2	5.4	26.6	4.8	12.1	8.7	1.6	12.52	4.23
ts3-13	405.4	107.4	961.0	1174.0	81.3	251.1	36.6	9.2	35.1	3.5	17.9	3.5	9.8	8.5	1.7	60.40	27.84
ts3-14	411.4	103.9	983.0	1317.0	92.6	274.7	35.3	9.6	33.7	3.1	16.5	3.3	9.8	8.6	1.8	36.30	12.68
ts3-15	551.2	820.0	581.9	1582.0	219.3	1078.0	244.6	29.6	237.0	30.0	169.3	31.1	78.5	49.1	6.5	10.08	2.11
ts3-16	556.0	781.0	560.3	1506.0	212.4	1046.0	234.5	28.6	226.6	28.6	162.4	30.0	75.4	47.3	6.3	9.25	2.02
ts3-17	584.3	301.8	876.0	2020.0	233.3	915.0	142.2	20.2	106.6	11.5	61.4	11.0	28.5	20.6	2.9	18.12	5.02
ts3-18	584.5	297.3	858.6	1993.0	229.1	894.5	137.7	20.3	103.5	11.7	60.4	10.9	28.0	20.7	3.0	17.15	4.76
ts3-19	737.8	338.2	742.4	1753.0	219.6	914.0	149.2	25.2	113.7	12.9	65.9	12.3	32.7	23.3	3.5	6.99	2.11
ts3-20	229.5	421.1	547.0	1247.0	147.8	640.0	126.2	16.3	123.0	15.1	84.8	16.4	44.0	32.4	5.0	15.22	6.63
ts3-21	230.6	670.4	924.2	2029.0	237.0	1004.0	195.3	27.2	190.5	22.9	131.0	25.6	69.8	52.0	8.5	37.90	14.15
ts3-22	419.8	165.1	151.6	559.4	90.5	437.4	82.8	17.4	60.5	6.7	34.0	5.9	15.6	10.4	1.5	23.93	18.08
ts3-23	597.1	485.0	1160.0	2740.0	325.6	1314.0	213.8	32.7	165.4	18.5	98.0	18.1	47.3	34.3	5.2	48.40	11.25
ts3-24	594.3	327.0	829.0	1935.0	229.2	905.0	147.8	22.3	111.3	12.3	66.2	12.0	31.5	23.1	3.3	16.90	5.21
ts3-25	381.5	124.4	565.8	1070.0	97.8	342.0	44.6	19.3	37.9	3.7	20.0	3.6	10.6	10.9	2.3	22.70	8.35
ts3-26	380.0	117.5	535.5	1000.0	91.5	319.6	42.1	18.1	36.0	3.6	18.9	3.6	10.2	10.6	2.2	17.31	7.19
ts3-27	273.9	460.7	1532.0	2824.0	281.5	1067.0	171.5	29.5	143.7	15.7	85.1	16.4	44.0	36.7	6.1	147.40	50.06
ts3-28	269.1	296.5	1010.9	1832.0	182.0	680.1	109.4	18.9	92.4	9.9	53.7	10.3	28.4	23.1	3.8	88.56	33.95
ts3-29	430.3	109.0	472.9	1007.0	94.1	330.6	47.1	11.3	40.3	3.8	19.0	3.6	9.9	8.6	1.5	13.72	5.06
ts3-30	253.5	932.0	493.6	1551.0	223.4	1044.0	234.6	36.8	204.4	27.7	163.4	32.1	90.5	79.7	12.2	116.00	74.90
ts3-31	339.1	126.7	192.4	477.0	59.4	282.7	55.2	9.6	43.3	4.8	24.1	4.2	11.3	9.3	1.6	9.80	4.98
ts3-32	363.6	117.6	238.7	562.0	68.6	312.5	57.4	9.2	45.2	5.0	23.9	4.2	10.4	8.2	1.3	8.53	3.36
ts3-33	326.0	257.0	341.0	810.0	98.8	442.0	86.5	19.3	73.6	8.4	45.0	8.5	23.4	19.0	3.3	15.26	8.94

Apéndice 5

ts3-34	322.6	277.8	362.0	859.0	105.0	470.0	91.5	20.1	78.9	9.0	48.0	9.1	25.2	20.1	3.7	16.32	9.11
ts3-35	287.0	124.0	372.2	698.0	69.1	272.8	44.4	9.1	37.5	4.1	21.4	4.1	11.0	9.7	1.7	26.83	9.15
ts3-36	378.4	90.0	202.1	417.2	49.6	233.0	45.1	8.4	40.4	4.1	20.0	3.6	8.5	5.1	0.8	13.91	5.12
ts3-37	251.2	894.0	238.9	905.0	152.2	789.0	196.5	30.5	187.8	25.6	152.8	30.4	87.2	77.3	11.5	13.41	9.94
ts3-38	249.7	732.4	197.3	738.9	123.4	652.3	157.5	24.7	154.0	20.8	125.5	25.1	71.5	62.8	9.4	10.70	11.69
ts3-39	497.0	380.6	875.7	2045.0	238.1	947.4	151.7	21.5	121.4	13.8	74.4	14.3	35.9	25.9	3.7	24.65	7.12
ts3-40	575.9	359.6	1028.9	2381.0	275.8	1072.0	164.1	24.2	127.4	13.8	73.2	12.8	34.8	25.1	3.7	28.45	7.45
ts3-41	464.9	94.9	224.6	757.5	101.2	417.2	60.9	13.0	44.8	4.3	20.9	3.5	8.7	5.7	0.7	17.60	31.90
ts3-42	333.2	82.2	491.6	775.0	65.6	231.7	31.0	9.0	28.8	2.6	13.9	2.6	7.5	6.7	1.2	15.77	5.74
ts3-43	361.6	101.7	630.7	1015.9	86.2	296.5	40.1	10.8	34.1	3.3	16.2	3.1	8.9	7.5	1.5	16.56	5.67
ts3-44	391.3	210.0	121.2	374.0	57.7	309.6	70.1	11.8	62.3	7.4	40.8	7.7	20.0	14.7	2.4	12.23	8.44
ts3-45	396.7	197.9	116.3	358.2	54.7	293.6	63.1	11.1	60.3	7.1	38.0	7.3	18.7	14.0	2.3	12.28	11.72
ts3-46	581.7	351.5	820.4	2006.0	240.9	977.4	152.4	21.6	127.0	13.9	73.4	13.5	34.4	23.7	3.3	15.41	4.59
ts3-47	369.5	55.4	371.9	655.0	54.5	183.1	23.1	8.3	22.7	2.0	9.6	1.9	4.9	4.2	0.9	12.10	4.48
ts3-48	864.7	202.6	494.1	1268.0	158.2	650.3	103.3	19.7	73.9	7.9	40.0	7.3	18.6	13.5	2.0	9.61	3.88
ts3-49	323.3	354.2	645.2	1595.0	188.7	757.1	124.6	12.2	106.0	12.1	66.5	12.8	33.5	27.1	4.3	47.68	35.87
ts3-50	274.0	98.3	374.1	661.0	63.7	235.4	34.8	8.0	30.2	3.1	16.2	3.1	9.0	7.8	1.5	26.77	9.90
ts3-51	414.5	406.5	981.4	2175.0	241.4	938.2	148.2	18.4	130.5	14.5	80.2	15.0	39.0	27.2	3.9	29.91	8.27
ts3-52	420.1	429.7	1034.3	2287.0	252.8	996.0	157.9	19.8	135.1	15.4	83.9	15.5	40.4	29.4	4.0	33.48	9.45
ts3-53	419.6	392.6	954.6	2096.0	234.3	906.5	145.3	17.6	125.6	13.9	76.6	14.6	38.2	26.2	3.8	28.21	7.91
ts3-54	315.0	307.0	756.0	1520.0	158.0	604.0	90.0	22.8	84.0	9.3	51.8	10.6	30.0	28.3	4.8	83.00	31.90
ts3-55	309.6	460.0	1085.0	2180.0	228.0	880.0	133.0	33.4	126.0	13.9	78.2	15.9	45.7	42.0	7.4	146.00	45.80
ts3-56	419.5	127.8	137.1	351.3	46.8	229.6	43.6	8.4	39.0	4.7	24.8	4.7	11.9	9.1	1.4	6.47	9.15
ts3-57	223.8	81.8	773.5	892.2	60.2	174.0	18.4	7.0	21.2	1.8	11.1	2.6	7.7	7.3	1.6	20.41	5.92
ts3-58	228.8	88.6	831.0	969.0	65.0	187.9	20.1	7.8	22.4	2.1	11.9	2.7	8.5	7.5	1.8	23.71	6.36
ts3-59	537.9	303.6	898.1	2120.0	240.0	920.8	130.7	20.7	107.8	11.7	59.6	10.9	28.7	20.2	2.9	16.84	4.66
ts3-60	427.4	62.6	273.6	553.7	56.2	226.2	32.7	8.4	30.8	2.8	13.6	2.4	6.0	4.0	0.7	14.90	5.30
ts3-61	377.2	47.9	194.8	373.9	36.7	149.3	21.8	7.5	20.9	2.0	9.4	1.8	4.4	3.3	0.6	15.47	7.02
ts3-62	323.3	436.2	1132.0	2662.0	305.3	1189.0	177.6	24.3	148.9	16.4	85.3	15.7	41.8	32.4	4.9	56.95	23.25
ts3-63	335.7	463.9	1303.0	2938.0	329.9	1270.0	188.3	25.9	161.1	17.6	89.4	16.6	44.4	35.2	5.2	60.60	25.51
ts3-64	318.2	167.5	380.2	864.0	104.2	482.7	84.5	15.1	73.8	7.5	36.8	6.5	15.3	10.8	1.8	21.15	7.44
ts3-65	610.8	275.8	769.5	1850.0	211.5	829.7	120.7	19.2	99.4	10.8	55.7	10.3	26.7	19.3	2.8	15.20	4.40
ts3-66	465.7	116.8	315.5	656.1	76.2	340.0	58.0	11.0	51.3	5.2	25.8	4.5	10.7	6.5	0.9	12.52	4.35
ts3-67	600.5	240.9	739.1	1713.0	196.7	759.1	110.6	17.3	87.4	9.3	47.8	8.8	22.5	16.1	2.4	10.71	3.33
ts3-68	357.9	75.0	319.4	565.0	55.0	221.3	34.2	8.1	30.9	2.9	14.8	2.7	6.7	5.2	1.0	15.06	6.28
ts3-69	349.6	75.8	306.4	524.0	52.0	209.4	32.3	7.6	29.6	2.9	14.6	2.6	6.8	5.3	1.0	17.05	7.12
ts3-70	352.4	70.9	304.8	520.4	51.1	204.9	30.7	7.3	29.1	2.8	13.7	2.5	6.6	4.7	0.9	15.85	8.08

Apéndice 5

SAMPLE: TS-4 (Toarcian–Oxfordian? Todos Santos Formation, coarse-grained arkose)

16°37′13″ N; 93°32′13″ W; elevation = 590 m.a.s.l.

Apatite	Sr	Y	La	Ce	Pr	Nd	Sm	Eu	Gd	Tb	Dy	Ho	Er	Yb	Lu	Th	U
ts4-1	252.7	25.1	59.9	118.8	12.2	46.3	7.2	3.4	6.5	0.7	4.0	0.8	2.2	2.1	0.4	1.25	2.36
ts4-2	366.9	93.4	612.0	999.0	83.6	284.3	38.6	12.8	33.0	3.2	15.8	2.9	7.9	7.0	1.5	17.57	6.86
ts4-3	434.3	398.7	778.8	1923.0	231.2	958.8	163.2	20.5	128.8	15.0	81.6	15.4	38.3	25.8	3.5	15.60	4.54
ts4-4	287.5	539.9	709.0	1913.0	245.8	1038.0	182.0	22.9	145.5	17.8	97.0	18.8	51.5	43.5	6.6	49.17	48.48
ts4-5	277.4	537.0	635.0	1776.0	230.9	999.0	179.8	23.2	146.8	17.2	96.7	18.7	51.8	43.8	6.6	45.30	38.80
ts4-6	247.2	517.8	725.9	1730.0	200.1	808.7	141.9	11.5	127.7	15.7	91.8	18.0	50.7	44.7	7.5	50.88	35.38
ts4-7	417.5	106.6	617.4	1156.3	108.5	391.0	52.5	11.5	46.1	4.1	20.1	3.7	9.6	8.2	1.6	15.69	5.75
ts4-8	385.9	137.9	505.0	1030.0	111.0	482.0	81.5	13.5	64.7	6.5	31.2	5.4	12.9	8.2	1.2	14.65	5.52
ts4-9	365.1	149.4	598.9	1154.0	119.6	489.5	78.6	14.7	65.5	6.4	30.7	5.4	13.7	9.2	1.5	15.75	5.27
ts4-10	490.6	172.0	716.6	1437.0	155.8	643.0	106.9	17.5	83.0	8.3	38.1	6.6	16.2	10.7	1.5	15.66	5.24
ts4-11	360.6	35.3	529.6	530.3	34.8	109.9	12.3	4.8	12.8	1.1	6.0	1.1	3.3	2.9	0.6	21.12	7.79
ts4-12	354.6	31.5	471.5	446.4	28.6	91.8	10.6	4.3	10.5	1.0	4.9	0.9	2.8	2.4	0.5	27.42	12.74
ts4-13	322.9	94.6	393.2	716.0	69.3	258.6	36.9	7.9	33.4	3.3	16.4	3.1	8.7	6.9	1.3	24.85	10.34
ts4-14	284.7	73.9	248.6	447.0	42.2	159.1	23.8	8.4	21.5	2.4	12.2	2.4	6.7	6.3	1.3	25.55	16.72
ts4-15	94.7	1513.0	1135.0	3043.0	375.9	1449.0	248.2	25.2	227.1	31.5	202.7	44.3	140.4	151.2	25.8	36.10	10.42
ts4-16	95.4	1539.0	1131.7	3065.0	375.3	1464.0	248.9	24.9	230.3	32.3	205.5	45.3	142.5	153.9	26.0	36.87	10.90
ts4-17	94.9	1548.0	1216.0	3193.0	388.4	1492.0	252.1	26.2	224.8	31.7	204.7	45.2	141.9	153.1	27.1	42.37	9.99
ts4-18	95.7	1521.0	1205.2	3099.0	373.6	1464.0	244.3	25.9	222.3	31.5	198.7	44.7	141.0	153.3	26.5	39.37	10.57
ts4-19	253.8	35.3	86.3	166.5	16.6	64.8	10.6	4.9	9.2	1.1	5.7	1.1	3.5	3.0	0.6	1.25	2.86
ts4-20	251.2	22.4	53.8	104.9	10.5	39.1	6.1	3.0	5.1	0.6	3.2	0.6	1.9	1.9	0.4	0.51	1.00
ts4-21	413.8	87.5	349.0	684.0	63.6	223.1	29.7	8.7	24.3	2.6	12.5	2.5	7.4	7.1	1.4	15.72	6.12
ts4-22	452.8	92.1	636.6	1215.0	105.2	333.3	36.9	12.2	33.2	2.8	13.5	2.8	7.8	8.7	1.8	14.59	5.49
ts4-23	366.8	66.4	399.0	695.0	57.6	188.6	21.7	10.0	20.9	1.9	9.4	1.9	5.9	6.1	1.3	19.41	12.16
ts4-24	360.8	30.9	531.4	515.0	33.0	101.3	12.2	4.5	11.7	1.0	5.3	1.0	2.7	2.4	0.6	22.06	10.84
ts4-25	379.0	42.4	669.6	675.2	45.1	136.7	16.9	5.5	16.0	1.4	7.2	1.4	3.8	3.4	0.7	23.60	8.07
ts4-26	364.9	32.4	571.2	552.0	35.7	107.8	12.5	4.6	11.8	1.1	5.5	1.1	3.1	2.4	0.6	21.88	7.79
ts4-27	499.1	95.7	469.6	858.1	84.2	322.5	46.5	10.3	39.9	3.7	19.2	3.4	8.9	6.9	1.1	16.43	5.71
ts4-28	502.3	74.0	372.9	708.4	70.5	276.2	42.0	7.9	35.4	3.2	16.1	2.9	6.9	4.7	0.8	13.24	4.35
ts4-29	469.8	87.3	398.0	747.6	74.6	292.5	42.4	9.5	37.0	3.5	17.3	3.1	8.2	5.6	1.0	16.39	5.43
ts4-30	454.3	147.0	491.4	1059.0	117.5	503.6	82.4	16.6	71.7	7.1	34.1	5.9	14.5	9.1	1.5	16.76	5.90
ts4-31	414.1	191.4	637.0	1276.0	142.4	636.2	112.3	15.1	97.9	9.2	43.1	7.3	16.9	10.8	1.9	22.61	6.90
ts4-32	351.4	118.4	146.4	369.5	46.9	221.0	41.4	6.0	37.5	4.0	22.5	4.2	11.0	8.8	1.4	25.78	12.43
ts4-33	422.4	76.7	1003.0	1130.0	78.5	253.6	30.8	9.9	30.2	2.7	13.9	2.6	7.3	6.0	1.3	19.69	5.27

Apéndice 5

ts4-34	158.7	445.1	769.0	1308.0	139.1	579.4	102.9	21.5	104.2	12.7	73.8	15.0	40.7	32.8	5.3	30.15	7.21
ts4-35	155.6	523.3	777.3	1390.0	154.0	644.8	118.7	24.1	118.8	14.7	86.3	17.4	47.9	37.8	6.4	37.58	7.17
ts4-36	250.7	62.9	63.4	142.9	17.0	75.0	15.8	3.8	14.1	1.7	10.3	1.9	5.8	5.2	0.9	6.60	22.30
ts4-37	249.1	54.3	62.5	129.8	15.1	65.8	13.6	3.3	12.8	1.4	8.8	1.8	4.5	4.7	0.8	5.72	18.97
ts4-38	242.9	55.2	116.9	197.2	19.0	75.3	13.1	3.7	12.8	1.5	8.3	1.6	4.7	4.5	0.8	5.43	21.68
ts4-39	214.8	814.0	1042.0	2293.0	265.1	1099.0	198.5	30.7	194.2	23.5	141.0	28.2	80.1	65.3	10.9	37.75	24.59
ts4-40	215.7	1035.0	1124.0	2623.0	321.2	1411.0	268.0	33.1	267.7	32.2	188.8	37.0	102.4	81.5	13.2	23.10	8.92
ts4-41	430.8	352.4	1013.7	2230.0	238.5	896.6	132.1	16.7	111.9	12.6	68.3	12.7	33.4	24.8	3.6	24.99	8.12
ts4-42	428.9	420.0	1166.0	2531.0	275.8	1048.0	158.0	19.9	132.7	15.0	80.3	15.2	39.9	30.1	4.3	37.60	11.33
ts4-43	384.5	108.6	726.3	1186.0	98.5	324.2	41.2	11.5	36.4	3.4	18.0	3.3	9.3	9.1	1.8	15.30	5.40
ts4-44	394.3	69.2	492.0	892.0	79.9	280.4	34.8	8.4	32.8	2.9	14.5	2.5	6.2	5.5	1.0	13.02	4.55
ts4-45	381.8	44.2	320.0	572.0	50.0	183.0	22.9	5.9	21.4	1.9	8.5	1.7	4.3	3.3	0.7	9.26	3.33
ts4-46	416.7	104.3	586.4	1037.0	94.7	344.3	44.6	10.9	41.4	3.8	19.1	3.4	9.4	7.4	1.4	13.17	4.41
ts4-47	429.1	145.9	826.0	1463.0	134.5	480.6	62.5	14.8	56.9	5.4	26.4	4.8	12.4	10.7	1.8	17.90	6.43
ts4-48	296.8	47.5	206.9	363.9	32.8	121.5	17.7	5.1	16.5	1.7	8.2	1.5	4.3	3.5	0.7	16.04	6.86
ts4-49	290.9	38.9	165.7	291.3	26.6	101.1	15.1	4.7	15.2	1.3	6.6	1.2	3.6	2.9	0.7	14.85	7.49
ts4-50	517.2	411.9	864.0	2057.0	243.2	984.0	159.3	24.3	135.4	15.0	82.2	15.2	38.9	28.4	4.3	26.15	7.96
ts4-51	352.6	140.6	728.1	1338.0	119.8	444.6	63.0	17.7	60.0	5.4	26.6	5.0	12.6	11.1	2.5	27.92	13.39
ts4-52	255.8	337.6	636.0	1370.0	155.8	672.0	130.6	12.5	119.0	13.3	70.7	12.7	31.6	21.7	3.2	29.03	12.06
ts4-53	404.6	65.4	207.9	405.3	41.9	170.6	27.2	6.5	24.7	2.4	12.4	2.2	6.1	4.4	0.8	17.03	6.49
ts4-54	252.6	204.3	235.2	536.4	62.6	265.7	46.2	7.7	44.1	5.4	31.2	6.4	18.6	16.9	3.0	37.66	21.50
ts4-55	239.9	206.4	208.4	487.4	59.4	258.2	47.7	7.3	47.6	5.7	33.3	6.7	19.2	16.1	2.9	32.90	23.58
ts4-56	368.6	57.4	300.0	541.0	45.9	152.0	19.4	8.5	17.7	1.7	8.9	1.6	5.1	4.5	1.0	20.85	14.60
ts4-57	432.6	116.0	190.3	507.9	67.6	319.2	57.9	11.7	50.2	4.9	25.0	4.4	10.9	7.2	1.2	10.30	6.41
ts4-58	396.7	90.5	277.9	459.4	44.7	182.5	31.6	7.5	30.1	3.3	17.2	3.6	9.2	6.6	1.2	17.37	20.90
ts4-59	337.8	153.9	383.0	772.0	77.0	306.0	51.9	12.8	48.5	5.1	27.0	4.9	13.2	11.3	2.3	20.00	11.43
ts4-60	489.4	270.4	587.6	1376.0	173.8	787.0	147.9	22.9	117.5	12.0	58.9	10.0	23.9	14.4	2.1	16.49	5.44
ts4-61	522.7	267.1	614.0	1414.0	178.4	804.0	148.6	24.0	120.3	12.0	58.9	10.0	23.7	14.5	2.1	17.02	5.83
ts4-62	306.3	544.0	338.0	835.0	106.3	490.0	111.4	28.0	115.4	15.2	92.3	18.8	51.6	47.5	7.6	77.10	39.80
ts4-63	309.7	603.0	594.0	1423.0	172.8	734.8	144.0	33.8	135.6	17.0	101.7	19.9	55.9	53.8	8.7	127.10	53.50
ts4-64	562.7	359.5	646.8	1602.0	193.3	801.0	141.4	21.9	117.1	13.4	73.0	13.5	34.9	25.3	3.5	23.25	6.86
ts4-65	559.4	363.1	676.0	1650.0	197.6	819.0	146.7	21.7	120.0	13.5	75.2	13.5	35.1	25.1	3.5	24.30	7.54
ts4-66	363.1	51.1	244.6	393.0	34.8	134.1	20.6	6.1	19.1	1.9	9.4	1.9	4.6	3.6	0.7	14.17	9.33
ts4-67	360.6	106.7	498.2	815.0	75.1	284.9	46.9	11.3	39.4	3.8	19.8	3.8	9.3	7.6	1.4	16.34	19.87
ts4-68	333.5	69.8	339.6	522.6	43.7	162.5	23.6	13.7	23.1	2.1	11.2	2.3	5.7	5.5	1.1	32.93	28.46
ts4-69	329.0	93.9	738.2	1079.3	83.5	291.8	42.9	13.9	42.1	3.6	17.7	3.4	8.3	7.8	1.7	18.35	7.22
ts4-70	335.8	80.3	664.0	949.0	72.4	247.0	36.4	12.1	33.0	2.9	13.9	2.6	7.1	6.4	1.4	15.99	6.91
ts4-71	335.8	77.2	628.4	923.0	72.2	253.0	36.7	11.7	34.1	3.0	14.5	2.7	7.0	5.9	1.4	15.15	5.86

Apéndice 5

ts4-72	417.5	177.9	283.3	698.0	94.7	495.0	110.6	14.8	89.5	9.4	46.7	7.4	16.3	8.4	1.2	12.29	4.53
ts4-73	489.1	266.2	420.6	1062.5	146.5	739.1	160.0	22.4	126.5	13.1	67.2	10.8	24.8	12.9	1.8	13.92	4.82
ts4-74	435.8	144.6	914.5	1547.0	143.7	556.2	87.6	16.1	73.1	6.5	31.8	5.6	13.2	9.8	1.7	25.00	7.73
ts4-75	253.0	537.0	418.1	1228.0	171.3	795.0	167.5	16.1	146.1	16.9	97.9	18.9	49.9	42.9	6.3	29.95	18.50
ts4-76	251.5	562.0	437.0	1301.0	182.1	848.0	176.0	17.4	153.9	18.3	105.3	20.0	55.0	44.2	6.7	44.80	24.40
ts4-77	253.5	178.5	555.6	1193.0	124.9	458.2	62.0	11.1	51.1	5.7	32.9	6.2	17.0	13.8	2.1	26.92	27.52
ts4-78	228.5	182.8	366.2	980.0	112.8	432.1	60.3	11.5	49.7	5.6	32.1	6.3	17.0	15.6	2.4	16.88	32.26
ts4-79	269.3	133.4	317.0	730.0	74.9	269.0	41.9	11.1	34.7	3.8	22.6	4.2	11.5	11.1	1.9	46.60	35.79
ts4-80	340.0	557.0	611.0	1543.0	183.0	783.0	143.0	19.2	149.0	16.6	113.7	21.8	56.8	50.9	7.5	30.80	15.50

SAMPLE: SR-1 (Berriasian–Aptian? member of the San Ricardo Formation, fine-grained sandstone)

16°41′45″ N; 93°32′33″ W; elevation = 653 m.a.s.l.

Apatite	Sr	Y	La	Ce	Pr	Nd	Sm	Eu	Gd	Tb	Dy	Ho	Er	Yb	Lu	Th	U
sr1-1	338.4	549.0	968.2	1940.0	183.1	609.4	85.1	22.9	80.5	9.7	60.1	13.8	47.2	62.8	11.7	87.20	30.75
sr1-2	346.8	87.4	651.0	956.0	76.1	240.6	28.5	9.1	26.7	2.5	13.6	2.7	8.3	7.4	1.5	36.81	12.88
sr1-3	360.4	260.4	2080.0	2986.0	236.3	738.8	82.7	26.6	82.0	7.4	38.7	8.2	24.3	24.2	4.7	105.20	29.33
sr1-4	375.1	211.2	1726.0	2449.0	193.1	603.4	66.9	21.7	64.5	5.9	32.0	6.5	19.9	19.7	3.8	58.22	15.68
sr1-5	281.9	125.4	1747.0	2400.0	179.3	540.5	51.0	29.2	52.3	4.2	19.2	4.0	11.1	9.5	2.1	60.22	23.54
sr1-6	275.8	48.4	819.0	1016.0	71.1	204.0	19.2	18.5	21.1	1.6	7.2	1.5	4.4	4.1	0.9	37.70	22.20
sr1-7	278.8	67.6	1062.0	1363.0	98.1	286.0	28.0	20.8	28.9	2.2	10.2	2.2	6.2	5.4	1.2	46.30	19.17
sr1-8	391.7	346.1	1268.0	2261.0	200.2	646.5	82.3	23.5	73.0	7.9	44.3	9.5	30.0	33.7	6.5	70.40	23.02
sr1-9	351.0	202.8	1086.0	1666.0	124.0	371.4	47.2	16.5	48.7	4.7	27.8	6.1	19.1	22.2	4.7	99.30	33.99
sr1-10	355.7	242.6	1325.0	2008.0	146.3	444.9	55.0	19.6	55.7	5.7	33.0	7.0	21.7	26.4	5.6	125.70	43.14
sr1-11	435.6	280.8	1926.0	2937.0	254.2	836.2	97.6	27.8	92.9	8.8	46.1	9.2	25.9	24.0	5.0	72.74	25.00
sr1-12	264.2	157.9	663.7	1122.5	101.0	343.7	45.7	11.9	45.0	4.7	25.5	5.1	15.0	13.9	2.8	56.27	20.05
sr1-13	262.7	187.4	656.5	1166.0	107.6	372.6	51.5	13.3	49.6	5.3	28.4	5.9	17.1	16.9	3.4	63.80	22.66
sr1-14	352.4	161.5	347.7	705.0	73.1	266.3	39.8	10.6	36.2	4.2	23.6	5.0	15.2	14.7	2.7	32.53	20.22
sr1-15	345.6	376.9	1058.9	1914.0	177.8	592.4	82.4	24.2	75.6	8.5	50.0	10.5	32.3	36.2	7.0	63.31	20.95
sr1-16	416.1	240.5	948.0	1631.0	152.8	531.2	72.5	20.9	63.1	7.0	38.3	7.4	21.0	18.2	3.1	40.40	11.24

Apéndice 5

sr1-17	413.1	214.9	919.0	1557.0	144.6	493.0	65.7	19.0	57.0	6.2	33.0	6.5	18.7	17.3	2.9	39.20	10.27
sr1-18	431.2	220.5	1067.0	1692.0	153.5	508.0	66.2	20.4	58.8	6.2	34.2	6.8	19.3	18.0	3.0	36.66	9.67
sr1-19	226.8	549.0	1760.0	2999.0	269.9	869.0	117.7	31.6	118.1	13.3	77.1	16.5	50.5	47.8	8.9	120.94	35.22
sr1-20	302.5	108.9	737.0	1004.0	75.1	226.1	28.2	9.2	28.8	2.8	15.8	3.4	10.4	13.7	3.4	72.30	46.50
sr1-21	399.0	356.0	1355.0	2348.0	221.6	770.1	105.5	32.1	94.9	10.5	57.6	11.2	32.0	30.4	5.2	53.86	12.85
sr1-22	291.3	563.6	902.0	1819.0	194.0	712.0	113.8	27.7	107.2	12.9	79.5	16.6	50.7	55.7	10.3	71.40	24.01
sr1-23	287.5	601.0	1032.0	2025.0	209.1	751.0	119.3	29.6	108.7	13.4	83.1	16.7	53.3	60.4	11.1	57.20	14.91
sr1-24	399.2	318.2	1186.5	2002.0	194.2	668.8	91.1	24.4	79.9	8.8	49.8	9.9	28.8	27.2	4.6	69.69	21.08
sr1-25	389.7	312.7	1074.0	1870.0	187.0	664.0	94.2	23.4	81.7	9.0	50.6	9.8	28.9	26.2	4.5	69.50	19.67
sr1-26	389.8	365.8	1215.0	2109.0	209.7	747.0	106.0	27.5	93.8	10.3	58.8	11.5	32.9	31.1	5.2	85.40	24.98
sr1-27	352.9	236.7	857.6	1513.0	145.0	513.2	73.6	20.4	70.5	7.3	42.4	8.3	23.1	21.7	4.0	45.88	15.83
sr1-28	374.9	245.7	829.9	1517.0	149.8	540.8	80.9	19.5	74.9	8.0	44.6	8.6	24.1	21.3	3.8	37.20	11.61
sr1-29	309.1	269.8	2400.0	3688.0	302.8	917.0	96.6	34.7	93.3	8.0	42.3	8.5	24.9	23.3	4.7	85.07	23.19
sr1-30	313.2	283.6	2450.0	3789.0	311.5	952.0	100.9	34.4	99.2	8.7	44.5	8.9	26.5	24.7	4.9	69.90	16.90
sr1-31	450.5	250.6	979.0	1829.0	170.2	553.0	67.7	29.1	58.3	6.0	36.4	7.3	21.7	22.2	4.1	43.60	15.61
sr1-32	436.4	418.9	1263.0	2429.0	236.8	792.0	103.9	45.9	90.4	10.1	61.2	12.4	38.2	39.1	6.9	75.50	26.24
sr1-33	415.4	216.0	919.0	1629.0	153.1	528.7	68.6	27.9	61.6	6.5	34.9	6.9	20.6	18.2	3.2	36.01	11.82
sr1-34	294.9	200.4	1428.0	2108.0	167.4	511.0	57.0	20.5	55.8	5.2	28.5	5.9	17.2	19.0	3.9	51.54	12.56
sr1-35	239.5	336.0	1170.0	1940.0	164.0	532.0	65.2	20.4	63.2	7.1	42.3	9.5	31.2	38.9	8.4	109.00	40.45
sr1-36	267.4	211.5	1411.0	1965.0	144.5	442.0	48.5	24.6	49.1	4.9	28.1	6.3	20.0	24.1	5.8	194.60	97.10
sr1-37	214.8	838.5	2271.0	4060.0	376.8	1288.0	172.2	48.7	166.9	18.3	113.0	25.1	82.5	94.6	20.0	201.10	72.23
sr1-38	356.9	155.4	1118.0	1512.0	120.7	395.8	47.6	12.6	44.5	4.3	24.5	4.9	14.6	14.9	3.0	80.90	34.07
sr1-39	370.4	273.4	953.0	1730.0	166.8	603.7	79.7	28.3	70.6	7.8	43.5	8.7	25.9	25.2	4.6	69.80	32.68
sr1-40	358.4	325.0	1047.0	1800.0	167.3	607.0	84.1	24.7	78.2	8.7	50.5	10.2	30.6	31.2	6.1	116.60	41.10
sr1-41	389.2	87.6	622.0	997.0	82.6	278.1	29.8	15.3	26.7	2.5	13.5	2.6	7.9	7.5	1.6	78.30	33.00
sr1-42	305.3	937.4	1405.0	3621.0	486.9	2187.0	389.7	33.1	309.1	36.1	196.4	34.7	86.3	56.1	7.3	70.36	17.15
sr1-43	265.8	463.7	394.4	931.8	114.7	521.1	104.1	11.7	104.4	12.9	77.1	15.3	42.3	33.2	5.3	27.31	24.73
sr1-44	421.9	232.2	2259.0	3161.0	246.6	786.9	80.2	39.4	76.1	6.7	35.5	7.2	21.2	20.4	4.2	197.50	78.76
sr1-45	323.8	387.4	1208.0	2096.0	192.6	681.4	92.4	26.0	84.9	9.4	56.1	11.8	36.1	38.5	7.5	128.60	52.56
sr1-46	257.5	314.2	1930.0	3085.0	254.8	807.0	86.7	35.2	79.8	7.8	44.3	9.5	29.3	33.0	6.5	76.06	21.09
sr1-47	329.3	359.7	1835.0	2712.0	213.7	688.7	88.0	23.6	79.8	8.9	51.7	10.7	33.3	37.9	7.5	159.20	50.90
sr1-48	297.2	55.5	172.9	294.9	27.6	106.6	15.6	3.3	16.2	1.7	9.5	1.9	5.2	4.8	0.9	14.49	22.23
sr1-49	286.2	129.5	1260.0	1861.0	155.1	517.5	55.1	15.5	51.0	4.4	22.7	4.5	12.7	10.4	2.0	38.15	12.51
sr1-50	400.2	148.5	1006.0	1468.0	122.1	420.6	50.7	16.2	47.3	4.4	24.0	4.8	13.8	12.3	2.3	41.91	13.12
sr1-51	306.7	114.0	540.1	903.4	74.6	248.0	28.7	12.4	27.6	2.7	15.8	3.5	10.4	11.9	2.5	52.24	19.74
sr1-52	322.3	323.1	1223.8	2004.0	164.7	545.8	72.9	23.6	69.9	7.7	45.7	9.7	29.8	33.7	7.6	223.60	105.00
sr1-53	251.8	383.5	1639.0	2589.0	219.9	732.0	96.8	25.0	86.4	9.6	55.4	11.4	34.6	37.6	7.2	116.70	49.73
sr1-54	349.0	521.4	1149.0	2194.0	232.2	933.6	148.2	36.2	139.7	15.5	87.4	17.8	51.2	44.1	7.8	173.00	72.39

Apéndice 5

sr1-55	312.5	339.0	2018.0	3048.0	256.4	835.0	91.6	35.8	83.3	8.5	46.8	9.9	29.4	34.7	7.2	67.10	23.99
sr1-56	275.5	335.7	1112.0	1805.0	164.5	588.0	83.0	22.4	79.0	8.9	51.6	10.8	32.3	32.9	6.8	120.90	51.75
sr1-57	345.5	712.6	1401.0	2593.0	264.1	1074.0	180.9	43.4	170.8	20.2	119.9	23.4	67.0	60.8	10.9	268.90	122.20
sr1-58	321.4	208.8	1018.0	1657.0	136.1	446.0	55.3	18.1	51.0	5.3	30.3	6.1	19.3	20.8	4.3	59.80	18.83
sr1-59	293.5	615.3	1789.0	3169.0	281.6	930.0	121.7	25.7	117.9	12.8	80.4	18.3	60.1	71.7	15.0	183.80	57.30
sr1-60	323.8	155.4	467.0	813.0	73.3	258.2	35.6	10.9	34.3	3.9	23.1	4.8	14.2	14.2	2.9	62.70	30.66
sr1-61	300.0	294.0	1404.0	2330.0	206.0	681.0	77.7	23.3	71.4	7.6	42.7	9.0	26.7	26.9	5.6	74.60	25.06
sr1-62	355.9	111.2	862.0	1183.0	82.7	239.5	26.2	9.8	27.9	2.6	15.2	3.3	10.6	11.5	2.6	108.50	53.96
sr1-63	415.7	98.2	257.6	498.0	49.0	190.3	27.5	10.5	25.7	2.9	16.4	3.3	9.1	7.8	1.4	28.56	19.81
sr1-64	320.3	323.0	1007.0	1860.0	170.0	579.0	76.6	28.0	69.9	7.8	44.7	9.3	29.6	33.6	6.8	110.50	59.10
sr1-65	315.9	342.3	1578.0	2454.0	201.1	668.8	85.6	26.5	81.5	8.7	50.3	10.6	32.1	35.0	7.6	235.90	84.80
sr1-66	377.1	245.8	900.9	1580.0	149.6	543.0	75.8	19.3	68.0	7.5	41.0	8.4	24.0	20.8	3.7	48.73	38.39
sr1-67	230.3	559.9	937.0	1942.0	204.5	753.8	113.3	24.2	101.3	12.3	74.8	15.9	50.4	60.0	11.6	57.05	22.18
sr1-68	187.9	526.0	411.2	960.0	127.1	615.0	137.6	19.1	139.9	17.2	100.7	20.0	53.9	36.1	6.1	43.82	45.30
sr1-69	270.6	464.1	1707.0	2694.0	239.2	834.5	109.6	29.2	101.2	11.0	65.6	14.2	44.1	44.6	8.5	149.50	40.44
sr1-70	320.6	414.2	776.0	1601.0	171.3	665.0	101.5	24.7	94.2	11.1	65.8	13.6	39.5	37.8	6.9	102.90	145.30
sr1-71	317.6	252.6	1041.0	1810.0	159.1	543.0	65.8	30.6	61.5	6.4	36.9	7.8	24.1	25.0	5.3	211.10	172.60
sr1-72	340.5	396.7	1669.0	3023.0	264.5	817.0	91.5	27.8	84.1	8.9	52.6	11.8	36.8	39.7	7.6	121.70	37.30
sr1-73	121.8	825.0	986.0	2494.0	306.0	1254.0	209.7	27.7	188.6	23.6	141.4	28.4	78.6	61.0	10.0	40.90	7.53
sr1-74	312.7	447.5	1285.0	2430.0	232.8	772.0	95.3	22.6	82.9	9.5	57.9	13.2	42.5	47.4	9.4	162.10	54.10
sr1-75	249.4	334.0	164.0	446.0	60.9	314.0	71.0	9.6	77.0	9.8	60.2	11.8	32.9	26.5	4.3	14.40	13.40
sr1-76	345.6	455.4	855.0	1840.0	206.8	834.0	140.8	25.3	122.0	14.1	79.6	15.2	41.5	35.6	5.4	89.50	29.80
sr1-77	291.2	136.6	1233.0	1553.0	115.8	365.8	40.2	18.9	38.0	3.6	19.3	4.2	12.1	11.9	2.4	73.70	28.57

SAMPLE: SR-2 (Berriasian–Aptian? member of the San Ricardo Formation, fine-grained sandstone)

16°39′47″ N; 93°31′27″ W; elevation = 872 m.a.s.l.

Apatite	Sr	Y	La	Ce	Pr	Nd	Sm	Eu	Gd	Tb	Dy	Ho	Er	Yb	Lu	Th	U
sr2-1	396.0	209.9	2038.0	2805.0	223.5	703.0	75.2	27.5	73.2	6.8	34.8	7.0	20.0	18.1	3.8	110.10	25.34
sr2-2	361.1	153.0	1570.0	1920.0	141.0	438.0	49.3	17.2	50.4	4.6	24.2	4.7	13.9	12.7	2.6	42.10	10.62
sr2-3	356.7	111.8	1249.0	1441.0	103.1	313.4	34.1	14.2	33.6	3.1	16.7	3.4	9.8	9.0	2.0	33.58	10.94
sr2-4	265.0	374.4	2177.0	3001.0	245.8	775.8	95.9	30.1	95.6	10.0	56.7	11.9	35.4	37.4	8.2	129.40	34.96
sr2-5	379.6	233.8	1976.0	2846.0	228.4	703.0	77.5	24.2	73.7	6.8	36.2	7.2	21.7	21.6	4.4	69.40	20.39
sr2-6	383.9	143.3	1398.0	2023.0	163.9	509.6	54.5	21.0	54.0	4.6	24.3	4.6	13.8	11.7	2.4	44.68	12.30
sr2-7	293.5	163.2	433.3	783.1	78.4	295.9	44.5	9.5	40.7	4.6	27.1	5.4	15.4	14.3	2.6	40.06	19.71
sr2-8	288.0	123.5	630.0	982.0	85.4	289.0	35.9	9.5	35.4	3.5	19.9	3.9	10.9	10.4	1.9	48.20	20.22
sr2-9	259.9	159.5	1923.0	2546.0	184.3	541.0	53.5	34.8	53.9	4.6	23.1	4.8	14.2	13.5	2.9	89.90	18.99

Apéndice 5

sr2-10	244.0	180.1	508.0	947.0	84.8	274.9	36.5	9.5	34.0	3.8	22.8	5.0	17.1	22.7	4.7	31.60	35.60
sr2-11	230.2	234.8	1132.0	1735.0	134.9	403.7	47.2	19.7	44.1	4.7	28.3	6.5	21.5	30.2	6.5	109.80	34.60
sr2-12	226.9	362.6	1789.0	2732.0	209.9	617.5	70.9	29.4	68.9	7.6	44.0	9.7	33.5	46.9	10.1	142.20	47.62
sr2-13	463.8	336.9	1246.0	2150.0	205.9	719.5	101.0	22.5	86.3	10.0	54.1	10.5	28.9	26.0	4.1	32.50	8.94
sr2-14	285.6	167.9	665.7	1228.0	113.1	387.7	52.8	16.0	44.6	4.8	27.3	5.1	14.2	13.7	2.3	19.30	7.21
sr2-15	215.9	214.2	328.0	728.0	76.7	282.5	43.6	6.6	40.6	4.9	30.3	6.4	20.9	23.2	4.6	30.45	10.93
sr2-16	215.4	223.1	376.0	823.0	83.5	299.8	44.9	7.0	43.5	5.1	30.7	6.7	21.6	23.8	4.8	33.10	11.95
sr2-17	400.5	188.8	1128.0	1793.0	155.1	518.2	61.3	16.9	58.2	5.8	29.3	6.0	17.3	15.2	3.1	42.16	10.89
sr2-18	408.3	125.4	295.2	621.0	66.9	260.3	40.0	7.4	35.1	3.9	21.8	4.1	11.5	8.8	1.4	4.98	2.73
sr2-19	418.6	123.5	300.8	630.0	67.5	260.7	39.8	7.7	33.7	3.9	21.7	4.1	10.8	8.7	1.4	4.24	2.44
sr2-20	272.2	155.7	2173.0	2480.0	160.6	442.0	41.2	23.3	44.9	3.7	21.0	4.5	15.0	17.1	3.7	176.30	49.20
sr2-21	264.6	105.5	1430.0	1730.0	111.4	311.0	29.4	14.7	31.6	2.7	14.0	3.1	10.0	11.5	2.5	104.40	27.70
sr2-22	393.8	102.8	851.0	1196.0	92.2	289.0	34.1	11.5	31.5	3.1	15.6	3.3	9.4	8.5	1.7	40.70	10.90
sr2-23	392.1	151.3	1210.0	1664.0	129.7	410.0	46.0	16.5	44.8	4.3	23.4	4.6	14.1	13.0	2.5	56.00	12.87
sr2-24	321.1	238.6	532.0	1123.0	113.5	410.7	62.6	13.6	52.5	6.4	37.2	7.5	21.8	22.4	4.0	50.85	22.45
sr2-25	316.9	235.7	490.0	1062.0	108.9	404.4	62.1	13.3	55.7	6.5	36.6	7.4	22.3	21.6	3.8	46.05	27.98
sr2-26	192.7	303.9	256.2	604.5	65.0	238.2	36.1	9.8	37.9	4.9	30.7	7.5	27.8	38.2	8.6	22.42	32.59
sr2-27	325.4	341.2	606.0	1329.0	142.0	548.0	87.8	32.6	85.9	9.6	52.6	10.9	29.7	26.3	4.8	52.53	28.44
sr2-28	320.8	236.0	380.1	847.0	91.4	368.3	59.9	21.5	60.0	6.6	37.2	7.7	21.6	18.8	3.2	33.72	19.30
sr2-29	272.1	141.3	1062.0	1617.0	129.0	397.7	42.7	17.6	41.6	3.9	20.2	4.2	12.7	13.5	2.7	46.29	14.51
sr2-30	278.5	158.2	1258.0	1889.0	149.1	455.8	50.0	19.9	46.9	4.2	22.3	4.6	13.7	14.5	2.8	37.06	12.56
sr2-31	277.2	148.9	1167.0	1757.0	137.9	419.0	44.9	18.3	42.7	3.9	20.8	4.4	12.5	13.4	2.7	39.70	13.77
sr2-32	268.8	142.4	989.0	1498.0	118.0	366.6	40.3	18.2	37.9	3.6	20.1	4.3	12.6	13.4	2.6	57.11	21.83
sr2-33	308.5	274.6	1610.0	2456.0	192.1	571.2	62.8	16.0	60.5	6.5	36.8	8.1	25.6	29.4	5.9	86.00	23.63
sr2-34	304.6	394.0	2225.0	3480.0	278.0	827.0	93.0	21.7	86.1	9.0	52.1	11.5	37.4	43.7	8.6	158.20	37.20
sr2-35	346.7	288.6	1059.0	1873.0	158.7	518.2	69.4	23.9	65.8	7.2	41.0	8.7	25.8	28.7	5.5	102.10	36.09
sr2-36	381.2	336.0	1402.0	2348.0	194.8	680.5	96.1	24.4	92.7	9.9	55.6	11.2	30.7	27.4	4.8	144.80	40.67
sr2-37	297.2	534.5	1787.0	4250.0	400.9	1389.0	205.9	21.5	176.1	19.4	104.5	20.2	52.8	41.5	6.0	114.70	36.70
sr2-38	300.2	475.2	1565.0	3930.0	353.4	1228.0	181.9	18.6	151.0	16.8	91.4	17.7	46.4	34.6	5.2	97.00	32.02
sr2-39	357.0	213.6	858.0	1758.0	140.6	430.2	58.6	17.6	53.0	5.5	32.6	6.6	19.7	20.8	4.0	30.52	13.59
sr2-40	251.0	283.9	1745.0	3680.0	258.0	727.0	80.6	29.2	79.9	7.4	39.6	8.4	24.8	28.0	5.5	91.20	25.75
sr2-41	253.0	260.6	1696.0	3210.0	236.4	665.0	74.4	26.5	72.3	6.8	36.8	7.7	23.5	25.5	5.0	87.80	21.13
sr2-42	390.9	202.2	1782.0	2585.0	189.5	566.3	64.6	20.8	62.1	5.9	31.2	6.5	19.5	20.2	4.1	57.40	14.53
sr2-43	391.7	225.4	1982.0	2811.0	209.8	619.6	70.3	23.5	67.1	6.2	33.4	7.2	21.6	22.2	4.6	79.50	24.73
sr2-44	254.5	258.9	1211.0	2197.0	192.6	605.0	75.7	25.0	64.7	6.7	36.7	7.6	23.4	24.8	5.0	69.68	14.20
sr2-45	425.8	175.6	1317.0	2298.0	179.7	558.7	63.9	17.8	58.2	5.3	26.7	5.5	15.7	14.3	2.7	41.15	15.71
sr2-46	386.1	124.4	771.0	1441.0	119.6	375.0	44.7	12.5	39.7	3.8	18.9	4.0	11.0	10.5	2.0	39.00	22.60
sr2-47	399.4	79.6	494.9	953.0	76.4	239.9	27.7	8.3	26.1	2.4	12.1	2.5	7.5	6.7	1.2	22.26	12.53

Apéndice 5

SAMPLE: BQ-1 (Ypresian-Lutetian El Bosque Formation, micaceous sandstone with abundant detrital muscovite grains)

17°22′28″ N; 91°59′23″ W; elevation = 390 m.a.s.l.

Apatite	Sr	Y	La	Ce	Pr	Nd	Sm	Eu	Gd	Tb	Dy	Ho	Er	Yb	Lu	Th	U
bq1-1	80.0	1943.0	247.1	891.9	146.3	758.6	362.8	6.4	442.8	77.9	432.0	65.7	153.9	100.4	11.7	2.47	39.66
bq1-2	784.0	1311.0	305.4	1150.0	201.7	1170.0	307.6	67.0	312.7	42.9	257.6	48.7	123.9	89.3	12.6	18.21	9.35
bq1-3	3610.0	338.0	43.0	127.0	18.5	109.0	37.9	9.5	57.9	10.5	66.3	11.7	29.0	21.9	2.9	2.25	0.60
bq1-4	2337.0	1210.0	4.9	19.9	4.3	33.0	21.1	7.8	54.7	14.2	146.7	42.6	155.1	175.2	25.9	8.74	7.19
bq1-5	7463.0	5226.0	505.3	1675.0	279.1	1469.0	514.2	121.1	676.0	125.8	854.0	185.4	518.8	432.5	53.9	4.27	39.24
bq1-6	12320.0	4446.0	248.6	877.0	163.7	1027.0	502.4	103.0	814.3	150.7	944.8	179.7	411.6	218.9	24.3	2.94	10.39
bq1-7	220.0	6982.0	1060.2	3708.0	633.6	3426.0	1134.8	43.1	1233.1	193.7	1219.3	241.6	668.1	501.1	68.8	257.80	55.02
bq1-8	3927.0	1091.0	48.8	168.1	30.6	187.0	80.1	21.3	131.7	23.6	162.7	37.1	108.1	101.6	15.9	0.11	2.83
bq1-9	311.2	626.0	1351.0	3034.0	339.2	1362.0	225.9	11.9	215.6	23.4	119.0	23.1	58.2	45.0	6.9	23.70	11.08
bq1-10	4699.0	4780.0	372.6	1288.0	220.9	1273.0	467.3	112.3	697.3	123.9	798.3	171.3	449.5	341.5	44.2	4.32	26.60
bq1-11	5193.0	5479.0	605.5	2056.0	331.3	1697.0	554.9	136.3	688.7	126.6	850.5	185.9	539.8	502.1	64.4	5.17	38.17
bq1-12	9441.0	8344.0	559.3	1990.0	339.6	1842.0	714.1	152.6	1011.0	202.1	1402.0	301.0	821.7	657.8	81.3	2.53	33.11
bq1-13	4536.0	192.5	19.4	68.6	12.6	79.0	26.4	8.4	36.3	5.4	32.0	6.7	18.3	13.6	2.1	0.04	0.44
bq1-14	6209.0	929.0	337.0	983.0	145.4	713.0	174.0	51.8	177.0	24.3	142.1	30.1	83.8	69.7	10.0	24.30	12.60
bq1-15	2892.0	4139.0	600.8	2031.0	320.1	1634.0	535.7	114.3	660.7	116.5	736.6	151.0	404.7	326.7	43.3	7.36	20.59
bq1-16	2490.0	596.0	142.7	516.5	98.6	642.9	288.6	64.4	378.4	43.3	160.7	21.0	39.1	28.5	3.7	0.23	5.41
bq1-17	2450.0	3905.0	339.7	1198.9	238.3	1549.0	636.8	256.7	899.7	149.7	901.2	170.4	403.9	242.2	27.7	0.24	12.90
bq1-18	3554.0	4190.0	503.8	1483.0	216.1	1029.0	320.8	81.2	436.7	86.7	607.0	137.9	400.0	375.0	49.7	6.07	15.43
bq1-19	802.3	486.6	921.0	2013.0	255.8	1062.0	173.9	26.1	150.3	17.2	88.8	17.1	44.1	34.8	5.2	14.56	5.77
bq1-20	2102.0	206.9	151.9	365.9	44.6	184.5	30.3	9.1	38.4	4.5	27.5	6.8	22.4	30.0	6.1	16.03	10.80
bq1-21	2961.0	1088.0	24.0	91.1	19.3	137.3	73.8	26.5	148.7	28.9	192.4	39.3	101.6	72.0	9.5	0.03	0.61
bq1-22	892.2	209.5	750.2	1585.0	186.0	729.8	104.2	18.3	89.0	8.7	43.2	7.9	18.5	12.6	1.8	7.18	2.79
bq1-23	797.2	461.8	305.5	770.6	120.7	624.1	141.7	22.4	144.9	17.4	90.7	16.8	39.3	25.0	3.4	6.54	4.25
bq1-24	1231.0	1294.0	116.9	404.8	71.8	410.0	133.7	29.6	174.2	25.9	155.9	35.7	106.9	107.3	17.6	4.04	7.48
bq1-25	2769.0	610.7	25.8	101.3	19.8	130.3	57.6	16.4	85.9	14.5	93.7	20.0	54.5	45.6	6.0	1.36	5.75

Apéndice 5

bq1-26	4892.0	3180.0	591.0	1976.0	320.2	1611.0	476.6	116.3	532.1	90.2	571.5	116.2	309.7	247.3	30.3	2.99	28.18
bq1-27	4372.0	1481.0	153.9	527.5	93.4	542.6	201.1	52.5	251.1	41.9	265.5	52.9	136.8	108.8	12.7	3.15	23.94
bq1-28	453.2	974.5	1665.0	4063.0	467.1	1967.0	362.2	41.1	336.3	39.2	195.6	34.9	81.1	53.9	7.3	85.28	18.35
bq1-29	2393.0	31.8	42.1	74.5	7.5	31.4	4.7	1.0	4.5	0.6	4.1	1.0	3.7	4.5	0.8	2.87	0.65
bq1-30	2124.0	5483.0	582.9	1769.0	281.1	1494.0	531.1	86.2	694.1	132.1	948.6	194.7	567.6	505.1	71.2	267.40	38.47
bq1-31	2442.0	512.0	15.8	55.2	11.3	81.2	34.4	10.3	59.3	10.4	77.5	17.8	56.7	53.3	7.8	40.70	14.53
bq1-32	6424.0	326.3	103.0	335.0	57.2	349.0	104.3	23.1	121.2	14.4	73.6	12.2	25.6	12.0	1.4	3.69	1.89
bq1-33	733.0	1726.0	1716.0	4320.0	559.0	2420.0	463.0	22.4	410.2	53.1	314.1	61.1	166.7	129.2	17.9	269.60	36.30
bq1-34	2953.0	1594.0	32.1	125.7	25.7	188.3	100.4	33.2	190.6	38.1	288.9	60.1	168.9	134.5	17.0	0.03	0.98
bq1-35	666.4	1709.0	312.9	996.7	169.3	901.4	269.0	78.0	319.9	51.9	346.9	69.4	194.9	155.0	20.6	0.99	1.97
bq1-36	1754.0	1298.0	68.1	246.6	45.6	292.4	127.3	36.3	181.5	31.4	214.5	43.5	124.5	105.7	14.9	0.18	9.97
bq1-37	56.4	221.5	34.0	115.4	20.2	118.5	40.0	9.3	49.0	7.4	46.4	9.1	25.6	21.4	3.2	0.21	0.53
bq1-38	3805.0	134.2	60.3	184.3	27.0	141.2	29.2	6.2	25.5	3.1	18.0	3.9	12.4	13.6	2.5	0.77	2.69
bq1-39	4057.0	556.1	106.9	390.4	71.1	432.0	129.4	36.3	126.6	16.8	101.2	19.1	51.1	38.7	5.5	0.10	1.92
bq1-40	271.1	2981.0	1219.0	3286.0	453.0	2108.0	431.0	40.7	420.0	64.4	453.4	101.0	322.8	382.9	55.2	113.20	22.31
bq1-41	4305.0	2500.0	84.2	352.0	68.0	465.0	179.8	55.5	315.0	58.5	436.0	93.5	266.4	213.2	30.9	15.05	14.87
bq1-42	3224.0	604.2	2990.0	5094.0	457.0	1500.0	180.6	28.2	156.8	16.4	95.0	19.6	58.2	58.1	10.6	78.24	9.58
bq1-43	1167.0	1087.0	20.3	164.6	46.6	357.0	210.2	62.3	305.2	50.5	288.4	46.0	107.3	67.4	7.4	2.92	0.29
bq1-44	2511.0	648.0	180.2	499.0	70.9	347.0	78.5	15.1	82.1	12.3	87.0	20.5	68.9	76.2	13.2	22.80	11.85
bq1-45	3377.0	2197.0	75.1	311.9	64.9	470.3	217.9	88.0	373.9	64.5	442.8	88.6	231.7	161.7	22.3	22.95	7.10
bq1-46	4769.0	106.1	16.6	53.7	9.1	58.8	22.8	7.9	37.2	4.9	24.9	4.1	9.1	5.6	0.9	1.27	1.06
bq1-47	3732.0	2216.0	81.9	268.4	43.3	247.4	109.3	37.4	192.4	39.6	324.7	78.0	250.7	222.6	30.4	0.14	0.48
bq1-48	3099.0	952.4	15.2	59.5	12.8	97.5	56.3	20.6	119.9	23.0	168.1	33.9	90.8	62.9	7.8	0.04	0.89
bq1-49	266.4	388.0	3.9	17.4	4.7	44.7	31.8	9.9	67.5	9.7	61.4	13.3	33.1	13.4	1.4	0.28	0.07
bq1-50	651.3	767.0	977.0	2374.0	296.1	1255.0	225.8	24.5	181.7	22.8	134.4	25.3	71.0	61.8	8.9	35.50	13.32
bq1-51	125.1	1213.0	125.5	500.0	97.2	644.6	227.0	32.0	288.8	41.4	252.9	48.1	119.7	68.6	8.6	0.62	0.30
bq1-52	1551.0	2299.0	54.0	187.6	34.5	223.9	105.5	27.5	196.9	40.0	323.0	78.0	249.8	242.5	37.3	21.81	21.40
bq1-53	2780.0	1646.0	29.0	107.4	21.7	163.0	102.3	44.6	216.3	42.8	309.7	60.9	156.0	85.9	8.9	0.91	0.42
bq1-54	508.1	661.6	1260.0	2867.0	346.5	1453.0	255.2	15.0	217.6	25.1	138.3	25.4	65.7	45.3	6.0	14.98	5.18
bq1-55	2442.0	2274.0	648.5	1952.0	297.1	1442.0	346.1	60.6	329.2	49.0	325.3	69.4	218.0	216.8	30.3	11.50	4.72
bq1-56	438.4	467.6	1931.0	3686.0	366.4	1283.0	172.6	10.9	136.3	14.8	82.6	15.6	45.2	40.7	6.1	14.59	6.45
bq1-57	906.0	1109.1	154.0	442.0	70.4	401.0	115.3	24.9	154.8	25.9	175.7	38.1	113.2	99.5	15.9	10.16	3.07
bq1-58	4644.0	1791.0	323.6	942.0	146.4	798.0	234.4	47.7	313.8	53.1	348.3	67.2	179.7	145.7	22.3	36.75	8.42
bq1-59	4225.0	85.5	98.2	344.2	55.1	292.8	58.5	12.6	44.2	4.4	21.3	3.4	7.5	3.6	0.5	1.15	9.06
bq1-60	443.5	333.6	1279.0	1907.0	166.1	590.6	86.2	16.8	82.3	8.8	51.4	10.6	31.4	31.8	6.3	43.45	40.82
bq1-61	3565.0	1935.0	120.7	444.2	78.4	457.8	169.8	40.4	238.7	43.3	319.0	67.8	202.4	171.0	23.6	0.51	4.19
bq1-62	5232.0	3332.0	595.2	2149.0	396.9	2305.0	784.9	197.3	843.2	132.1	805.1	145.0	358.0	206.3	23.9	0.14	2.24
bq1-63	3795.0	1709.0	104.4	379.0	68.6	437.0	164.4	44.3	249.6	41.8	284.3	61.7	190.2	195.1	31.7	38.10	22.01

Apéndice 5

bq1-64	2043.0	2085.0	5.7	21.9	4.8	37.4	24.0	10.3	78.6	23.5	265.0	78.6	259.7	186.9	25.7	0.21	2.19
bq1-65	1004.0	1324.0	125.7	472.0	94.2	647.0	256.2	78.7	321.9	46.4	269.0	48.3	118.4	72.7	10.2	0.22	19.92
bq1-66	1526.0	1406.7	220.0	813.9	137.0	711.4	220.8	59.6	225.9	37.9	253.3	50.6	143.0	116.1	16.6	0.04	1.53
bq1-67	4898.0	508.0	18.4	69.8	13.1	85.9	31.5	10.5	49.7	9.6	75.8	18.1	57.2	54.8	8.1	3.18	1.68
bq1-68	592.1	1183.0	21.1	74.9	14.0	96.5	48.6	8.6	113.9	23.4	175.0	39.5	113.8	90.4	12.5	8.47	5.12
bq1-69	412.0	2337.0	1232.0	3113.0	432.8	2066.0	500.8	77.9	514.7	74.9	461.4	87.3	235.1	192.2	28.4	59.60	8.22
bq1-70	255.2	2934.0	1619.0	5179.0	764.5	3680.0	828.9	61.2	750.7	101.5	598.8	110.4	291.4	216.7	29.8	89.26	30.15
bq1-71	1025.0	733.3	77.8	360.5	72.9	452.4	145.2	38.8	155.2	22.7	136.1	25.8	69.1	51.4	7.6	0.30	5.86
bq1-72	4202.0	1235.4	37.8	155.4	32.2	229.0	122.1	34.5	200.9	36.8	240.4	43.5	109.3	76.1	10.2	0.30	0.72
bq1-73	3835.0	453.5	39.3	151.5	27.7	166.8	61.5	13.8	77.0	11.2	72.4	15.1	43.8	35.6	5.5	0.23	1.23
bq1-74	509.0	2543.0	2399.0	6120.0	795.0	3508.0	700.5	38.9	620.7	84.0	502.8	95.4	261.4	204.2	28.1	50.34	7.88

SAMPLE: BQ-2 (Ypresian-Lutetian El Bosque Formation, micaceous sandstone with abundant detrital muscovite grains)

17°09′01″ N; 92°07′23″ W; elevation = 836 m.a.s.l.

Apatite	Sr	Y	La	Ce	Pr	Nd	Sm	Eu	Gd	Tb	Dy	Ho	Er	Yb	Lu	Th	U
bq2-1	2894.0	818.9	125.0	448.3	87.4	591.7	277.3	70.3	400.9	57.6	255.3	30.3	37.8	7.4	0.7	0.17	3.81
bq2-2	2315.0	775.6	197.2	715.0	136.4	880.0	316.0	62.6	346.2	44.5	214.1	30.0	57.7	23.8	2.7	0.13	2.74
bq2-3	844.3	1151.0	10.1	37.8	8.4	65.2	41.8	13.8	106.9	22.4	184.9	43.8	128.0	79.0	11.1	0.04	1.74
bq2-4	73.5	2306.0	214.9	744.7	121.2	600.0	309.9	12.0	411.7	80.6	484.3	80.4	199.1	150.5	18.2	4.65	103.90
bq2-5	1819.0	1782.0	43.5	154.2	29.5	204.2	97.4	22.8	219.4	41.4	303.3	72.9	189.8	125.5	17.8	3.26	9.13
bq2-6	3003.0	1855.0	44.0	181.9	39.4	294.9	141.2	40.1	266.3	49.7	336.6	68.5	155.8	83.4	9.6	114.30	24.04
bq2-7	2932.0	301.4	6.5	25.6	5.4	39.8	19.6	5.9	40.7	7.1	46.7	10.2	28.7	26.8	4.7	0.21	0.83
bq2-8	4843.0	240.8	17.4	57.2	10.3	70.6	24.8	7.4	38.0	5.6	35.9	8.3	23.7	21.3	3.5	0.06	0.43
bq2-9	1575.0	1289.0	17.0	71.9	16.4	135.8	77.8	13.6	165.2	31.8	222.1	47.5	120.2	78.5	9.2	38.10	2.93
bq2-10	10199.0	1324.0	177.8	593.0	105.5	648.0	236.2	52.1	302.7	46.5	268.9	51.8	128.6	93.8	12.1	10.20	47.92
bq2-11	1187.1	1083.0	7.2	27.6	5.7	38.6	21.2	5.3	52.9	13.1	122.3	35.4	118.8	113.3	15.3	0.03	0.59
bq2-12	942.5	817.8	156.6	570.3	85.5	502.7	189.7	46.4	256.8	39.0	197.4	28.3	46.8	21.9	2.3	0.29	5.84
bq2-13	3501.0	2328.0	393.1	1294.0	212.1	1210.0	417.7	83.7	501.3	79.7	464.8	90.7	228.7	170.5	21.4	21.30	44.60
bq2-14	2739.0	345.0	3.8	13.7	2.6	17.4	9.3	3.1	21.9	5.2	44.7	11.7	33.3	27.2	3.7	0.02	0.10
bq2-15	6026.0	219.8	26.3	85.2	15.4	91.5	31.2	7.9	43.7	6.4	38.8	7.8	19.2	13.5	2.1	0.01	0.25
bq2-16	1104.0	338.4	332.3	867.0	116.6	555.4	101.5	25.3	101.6	10.9	56.9	11.5	29.3	24.2	4.3	1.69	12.26
bq2-17	83.7	2009.0	214.7	687.4	109.3	558.3	243.2	23.4	321.4	60.9	365.5	67.3	167.2	150.9	19.7	1.47	20.82
bq2-18	373.6	770.9	18.6	128.6	39.4	362.7	182.7	28.5	270.1	35.9	178.3	30.0	61.9	33.7	4.7	0.10	13.21
bq2-19	1097.0	1999.0	68.5	213.9	38.6	254.6	120.2	30.9	232.2	43.6	310.6	71.0	193.5	142.9	18.0	0.65	7.01
bq2-20	589.2	1792.0	42.6	140.9	24.3	151.5	72.3	19.4	144.7	32.4	253.0	60.2	170.7	128.2	16.2	0.19	2.42
bq2-21	4130.0	231.5	21.4	84.9	17.1	114.5	37.0	8.4	48.6	6.9	39.9	9.3	24.5	17.1	3.0	0.38	3.11

Apéndice 5

bq2-22	5690.0	2090.0	203.0	841.0	179.1	1247.0	447.0	86.1	531.0	71.1	384.0	73.0	169.4	106.7	14.5	19.65	2.78
bq2-23	1250.0	439.8	380.5	839.0	107.7	530.5	105.9	15.5	126.9	14.7	74.4	15.5	37.6	26.7	5.0	0.58	4.62
bq2-24	732.8	452.8	243.2	621.5	96.6	526.7	128.1	26.6	141.4	17.4	92.8	17.7	40.3	24.4	3.4	14.36	5.43
bq2-25	3741.0	270.0	18.9	61.4	11.2	77.4	30.7	11.9	50.8	7.4	42.5	9.2	23.8	18.8	3.0	0.31	1.33
bq2-26	216.3	747.2	142.7	563.3	105.3	646.1	176.0	16.6	173.1	22.3	131.6	26.6	71.8	60.4	9.6	51.34	45.12
bq2-27	243.2	774.0	52.5	264.0	60.6	427.0	145.1	43.5	156.1	22.1	135.3	26.5	71.1	64.3	9.9	38.50	59.30
bq2-28	249.5	734.8	152.5	560.7	103.0	604.1	172.6	51.8	180.9	23.1	134.5	25.9	70.4	59.0	9.4	74.50	67.05
bq2-29	2909.0	539.0	9.0	46.1	11.1	90.8	47.9	15.4	81.6	13.8	93.9	19.4	52.0	34.4	4.5	7.50	4.47
bq2-30	4447.0	290.0	40.3	137.5	24.8	162.8	55.5	13.5	67.5	8.7	50.9	10.2	27.1	19.4	3.3	0.13	0.99
bq2-31	4542.0	94.0	21.2	55.4	8.4	46.0	13.0	3.7	15.7	2.3	15.9	3.3	9.7	8.3	1.3	17.11	2.13
bq2-32	2934.0	2041.0	1162.0	2988.0	412.4	1965.0	413.0	25.9	398.5	53.9	333.8	65.7	178.5	128.2	17.6	72.40	20.35
bq2-33	485.1	205.8	8.1	30.6	6.3	44.2	16.8	4.9	26.0	4.4	30.4	7.2	21.0	14.0	1.8	0.74	0.52
bq2-34	196.0	1315.0	73.1	318.2	64.8	424.8	223.2	20.7	294.4	49.8	302.3	51.1	126.5	89.4	11.3	0.41	38.24
bq2-35	345.1	2049.0	937.5	2475.0	338.0	1566.0	348.9	24.6	353.7	54.2	349.8	72.7	213.1	188.9	29.7	16.15	4.61
bq2-36	3710.0	193.2	146.2	441.0	61.8	281.0	47.5	7.4	41.0	5.0	30.8	6.8	20.5	20.6	3.3	10.28	5.68
bq2-37	3748.0	539.3	42.8	154.6	30.1	209.1	99.8	41.8	144.4	22.1	122.0	19.5	42.5	21.5	2.7	0.13	0.96
bq2-38	4877.0	1977.0	1449.0	3638.0	458.6	2091.0	440.9	33.8	411.3	54.1	316.9	60.5	164.9	129.1	19.9	70.70	17.83
bq2-39	3036.0	695.2	7.3	29.2	6.1	45.4	25.4	9.1	55.9	11.9	99.6	23.3	68.8	54.3	7.4	0.03	0.29
bq2-40	434.9	73.5	31.5	102.0	16.0	86.8	20.2	5.0	19.8	2.2	11.6	2.3	6.9	5.2	1.0	0.12	0.18
bq2-41	1227.0	664.9	10.8	41.8	8.1	54.7	29.7	6.4	59.8	12.6	101.2	23.2	65.8	44.2	5.7	0.05	0.95
bq2-42	1998.0	1725.0	826.3	2283.0	336.6	1583.0	435.8	68.9	440.6	64.2	374.0	65.6	161.0	88.2	10.4	18.60	60.00
bq2-43	5673.0	666.0	81.4	253.0	38.5	203.0	56.2	9.8	76.0	14.0	106.5	23.4	65.8	51.0	7.4	9.12	2.70
bq2-44	1051.0	929.0	32.5	109.0	21.2	125.3	54.2	21.8	84.9	17.2	138.3	32.8	106.1	96.2	13.4	0.09	1.07
bq2-45	1106.0	667.9	76.0	257.9	44.6	275.4	99.2	35.2	123.4	18.8	121.6	24.2	65.5	46.0	6.7	0.27	1.26
bq2-46	12276.0	277.0	47.3	159.7	28.9	196.2	79.4	26.9	105.9	12.6	60.3	10.2	25.7	18.3	2.7	7.30	16.44
bq2-47	7342.0	1681.0	402.0	1174.0	187.8	1075.0	356.6	66.2	385.3	55.7	340.6	65.7	182.1	145.0	20.2	31.30	37.19
bq2-48	6678.0	371.0	29.1	112.4	21.4	144.2	58.4	16.4	82.9	13.0	74.6	12.8	28.7	16.1	2.1	0.02	0.27
bq2-49	1500.0	254.7	224.9	584.0	86.3	399.7	73.4	22.1	71.2	8.4	47.4	9.3	25.0	16.2	2.3	1.12	2.46
bq2-50	767.0	1090.9	51.6	199.0	36.6	252.9	115.1	29.3	169.8	29.3	206.6	43.1	123.9	104.1	13.7	0.76	9.35
bq2-51	1347.0	513.0	148.3	439.0	75.4	402.1	107.9	33.5	118.8	15.5	92.9	19.0	54.1	39.6	6.2	1.25	3.43
bq2-52	4617.0	4920.0	641.7	2777.0	490.3	2571.0	814.4	121.9	855.1	140.4	938.6	185.0	540.9	502.8	64.8	170.40	98.20
bq2-53	1365.0	120.6	5.9	32.4	7.3	56.1	18.1	4.9	25.2	3.4	21.7	4.5	12.4	9.8	1.7	0.03	2.79
bq2-54	723.7	952.2	180.0	605.7	109.8	633.8	274.2	58.5	366.2	57.0	281.7	35.9	65.8	34.0	4.0	0.64	16.55
bq2-55	2323.0	1740.0	467.2	1305.0	199.6	1072.0	285.8	54.3	341.0	49.5	319.4	65.8	184.0	145.4	21.9	32.00	6.32
bq2-56	1712.0	489.0	16.5	61.9	12.9	95.1	50.2	17.1	95.8	16.8	101.0	17.8	45.7	33.4	4.6	1.25	1.75
bq2-57	125.3	2343.0	184.3	700.8	126.9	745.4	302.3	35.3	372.4	64.2	433.5	86.8	250.0	230.4	31.0	11.60	16.81
bq2-58	2601.0	353.6	76.8	260.0	46.5	292.0	83.8	10.9	102.3	12.6	72.0	13.8	35.3	21.2	3.4	0.02	0.71
bq2-59	2222.0	1345.0	1136.0	2820.0	403.1	1955.0	438.3	71.1	435.9	56.3	313.1	53.9	127.2	76.6	9.5	10.82	4.84

Apéndice 5

bq2-60	623.1	1338.0	42.8	170.1	35.4	251.6	127.5	19.7	247.5	38.8	248.8	51.2	135.4	95.3	15.5	0.52	6.44
bq2-61	2517.0	1910.0	26.8	108.6	23.3	187.0	124.7	43.8	293.0	58.5	412.0	71.3	149.1	63.5	7.2	14.00	8.37
bq2-62	8716.0	1404.0	329.8	1096.0	190.3	1103.0	342.2	67.0	362.7	49.8	290.0	54.4	144.7	109.4	14.0	10.23	22.96
bq2-63	2129.0	634.0	23.1	70.0	11.5	69.9	30.2	8.7	54.9	9.6	80.7	22.9	81.8	86.5	14.7	23.40	10.85
bq2-64	1430.0	435.4	307.7	674.0	88.8	380.4	74.9	20.2	82.4	11.6	77.7	16.5	46.4	32.7	4.2	2.55	2.10
bq2-65	7569.0	2794.0	301.0	1080.9	200.3	1267.0	502.7	106.9	607.9	91.2	568.5	109.8	300.0	238.3	30.7	51.53	53.04
bq2-66	129.4	1709.0	176.9	699.3	135.5	861.0	293.4	31.8	372.4	55.1	346.3	66.5	168.1	101.9	12.9	0.67	0.31
bq2-67	108.0	1285.0	1950.0	4815.0	526.3	1779.0	239.1	16.8	204.5	24.6	149.5	33.7	105.9	111.5	18.6	25.38	3.20
bq2-68	1135.0	383.9	30.1	110.6	21.0	139.2	67.7	17.9	114.6	19.0	104.4	14.8	27.8	10.9	1.2	0.01	0.20
bq2-69	173.0	171.4	44.2	131.2	21.7	109.5	30.6	7.1	33.5	4.5	27.8	5.8	16.3	11.3	2.0	0.13	1.40
bq2-70	747.8	246.1	8.0	28.3	5.2	31.7	13.0	4.0	21.2	4.5	37.0	8.7	30.6	29.2	3.7	0.51	0.14
bq2-71	3942.0	1437.0	94.5	320.0	59.2	395.5	153.8	40.5	244.6	39.8	264.1	54.3	143.6	102.7	14.1	103.80	28.13
bq2-72	4240.0	367.0	22.3	86.3	15.9	102.9	45.0	11.5	63.7	9.5	62.3	12.3	30.0	19.1	2.5	0.33	0.31
bq2-73	644.0	1148.0	508.0	1624.0	261.3	1280.0	294.8	55.9	245.4	32.8	193.7	37.5	107.9	104.1	17.4	123.40	31.35
bq2-74	5269.0	1491.0	224.5	617.1	107.7	629.0	203.9	50.9	277.5	44.4	286.8	56.6	155.1	131.2	19.9	36.20	10.47
bq2-75	10374.0	154.5	25.6	97.2	19.5	126.9	47.8	11.8	62.4	7.7	37.7	5.6	10.1	3.9	0.4	0.16	0.23
bq2-76	1008.0	501.1	9.6	32.7	6.2	41.2	21.8	9.6	47.3	10.6	82.6	17.9	47.4	31.6	4.0	0.04	0.36
bq2-77	2108.0	189.0	156.8	438.4	66.4	313.6	63.0	18.2	57.3	6.7	37.2	7.1	18.2	11.4	1.6	3.21	4.34
bq2-78	578.0	297.2	47.6	164.8	31.0	197.5	99.5	22.0	137.5	19.4	83.5	11.3	27.8	29.8	4.5	0.22	3.42
bq2-79	4897.0	1778.0	53.0	269.1	64.0	520.1	289.0	75.2	479.9	81.7	455.6	69.8	156.2	102.4	13.8	30.89	12.50
bq2-80	5226.0	143.5	63.9	169.1	25.0	135.4	39.1	13.0	50.5	6.7	35.0	5.6	13.5	8.9	1.4	4.14	1.10
bq2-81	5230.0	459.0	11.1	65.4	18.6	166.5	85.0	22.1	114.6	16.4	97.2	17.5	43.1	24.8	3.3	0.03	1.83
bq2-82	3486.0	1531.0	45.2	184.1	43.7	333.9	166.0	23.7	260.9	44.3	290.0	60.4	150.2	78.0	9.9	0.27	2.72
bq2-83	4721.0	1088.0	765.0	1700.0	227.0	1026.0	263.0	56.9	309.0	48.4	271.1	41.6	83.4	40.0	4.3	27.60	7.43
bq2-84	7453.0	702.0	52.5	186.2	33.7	213.6	85.2	27.4	121.9	19.8	133.6	27.1	73.9	52.5	7.1	7.10	4.40
bq2-85	5187.0	2040.0	26.5	107.7	23.0	170.2	97.1	20.1	208.1	43.3	322.9	74.8	204.9	150.9	19.5	0.01	0.15
bq2-86	2685.0	4490.0	372.9	969.0	193.2	1214.0	464.4	124.2	712.8	113.1	701.1	147.1	380.6	300.4	40.8	3.42	10.29
bq2-87	1169.0	746.4	428.0	1087.0	164.3	761.4	181.6	49.7	194.7	27.7	159.3	31.0	78.1	49.0	6.0	4.54	15.19
bq2-88	2108.0	1117.0	117.4	240.0	68.8	423.5	169.8	20.1	266.2	39.6	221.3	42.1	95.5	53.5	7.2	2.46	6.50

SAMPLE: BQ-3 (Ypresian-Lutetian El Bosque Formation, micaceous sandstone with abundant detrital muscovite grains)

17°01′10″ N; 92°08′04″ W; elevation = 967 m.a.s.l.

Apatite	Sr	Y	La	Ce	Pr	Nd	Sm	Eu	Gd	Tb	Dy	Ho	Er	Yb	Lu	Th	U
bq3-1	3863.0	616.0	3.9	15.7	3.3	25.2	15.3	6.1	39.8	9.5	88.4	22.1	70.2	60.4	8.5	1.32	0.99
bq3-2	61.3	2399.0	237.2	828.5	138.8	717.3	345.3	14.3	404.1	74.9	474.5	85.7	229.2	194.5	24.2	1.69	33.50
bq3-3	6075.0	886.9	251.1	1043.0	220.0	1458.0	536.0	143.3	553.9	59.9	259.4	34.5	62.7	28.5	3.8	2.27	6.95

Apéndice 5

bq3-4	209.4	1773.0	1296.0	3372.0	460.1	2102.0	431.6	37.9	402.2	53.1	319.1	61.9	171.4	152.7	23.7	44.39	3.55
bq3-5	457.7	2758.0	2332.0	6395.0	911.4	4294.0	913.0	42.5	810.6	105.9	610.6	110.4	277.3	179.1	22.7	54.37	16.52
bq3-6	4523.0	180.3	21.7	75.1	12.8	76.9	23.9	6.8	28.8	4.2	27.7	5.9	17.1	14.9	2.3	1.17	0.58
bq3-7	4397.0	1268.0	77.0	345.0	72.5	518.0	193.6	41.7	266.0	39.2	245.8	48.0	129.0	94.8	14.0	12.53	16.90
bq3-8	3733.0	103.1	2.3	10.0	1.9	12.7	5.7	1.9	9.9	1.8	14.5	3.6	12.0	10.1	1.8	0.06	0.09
bq3-9	3036.0	2380.0	107.3	502.0	122.3	954.0	392.6	148.6	482.9	70.8	446.1	90.1	248.5	186.5	26.8	6.86	25.83
bq3-10	3087.0	1334.0	277.4	874.0	132.9	708.0	211.5	48.1	224.5	34.4	220.1	44.9	127.6	101.6	13.0	22.85	5.93
bq3-11	2491.0	1239.0	53.0	201.4	39.3	259.5	117.4	20.5	183.3	29.7	189.9	39.4	102.6	57.3	7.6	0.06	0.77
bq3-12	5423.0	1679.0	33.2	124.5	23.4	147.0	67.5	16.7	127.3	28.5	248.8	62.7	200.7	161.2	21.7	0.21	2.40
bq3-13	2824.0	1721.0	168.0	628.0	111.9	686.0	227.5	64.4	294.4	44.5	290.5	60.8	172.9	137.5	19.8	12.43	35.97
bq3-14	4442.0	843.4	94.5	416.0	83.8	506.0	156.3	25.8	164.0	22.1	137.4	28.0	79.7	59.9	9.3	1.13	4.80
bq3-15	1606.0	1843.0	519.0	1418.0	198.9	934.0	255.9	59.5	274.7	43.8	293.8	61.6	181.7	155.2	22.1	18.81	5.03
bq3-16	4527.0	1653.0	122.0	482.4	92.1	605.0	260.9	70.1	364.1	61.3	387.4	63.2	136.2	80.2	10.3	6.55	8.35
bq3-17	1027.0	588.1	28.3	194.4	48.3	350.5	125.6	24.5	147.1	20.4	117.8	22.1	55.0	34.2	4.9	0.11	9.62
bq3-18	9585.0	606.5	17.4	86.3	18.7	125.3	57.8	11.8	85.5	14.5	99.7	21.7	61.5	47.8	7.1	0.02	0.79
bq3-19	3350.0	2310.0	222.0	630.0	97.0	550.0	206.0	42.0	330.0	63.3	453.0	89.0	238.0	180.0	23.3	52.00	13.20
bq3-20	425.4	1801.0	60.0	274.7	59.2	414.4	174.9	37.3	250.6	43.7	311.9	66.6	197.8	174.3	26.6	19.37	6.75
bq3-21	859.0	223.0	399.0	922.0	115.1	505.0	93.1	18.4	77.9	8.9	46.7	8.5	20.8	13.8	1.9	14.72	6.14
bq3-22	6626.0	3080.0	659.0	1792.0	265.9	1392.0	410.2	87.1	495.0	76.9	510.1	106.9	315.6	268.7	41.5	98.00	25.25
bq3-23	1138.0	497.0	67.0	202.0	30.8	164.0	52.3	9.1	70.6	12.5	86.8	17.6	47.9	32.6	4.2	1.62	0.62
bq3-24	730.0	417.8	850.7	2062.0	253.6	1034.9	173.0	12.8	141.2	15.8	85.0	15.6	40.6	27.8	4.0	94.70	59.15
bq3-25	2049.0	450.0	26.6	132.8	20.9	128.4	46.6	13.2	63.9	9.9	69.6	15.9	48.8	37.6	5.0	0.21	1.04
bq3-26	3753.0	2452.0	613.0	1766.0	268.0	1388.0	369.9	46.1	439.7	68.7	449.2	89.5	251.8	202.9	30.0	21.70	5.40
bq3-27	5486.0	603.8	120.7	519.6	104.6	677.2	221.4	63.9	208.2	25.9	137.3	22.7	53.0	30.3	4.1	0.33	2.77
bq3-28	2115.0	1680.0	55.4	212.0	43.5	321.1	156.0	41.7	252.0	41.6	284.2	63.7	191.5	168.7	29.2	23.30	12.63
bq3-29	5015.0	639.0	30.8	114.9	20.7	125.6	49.8	15.0	78.2	13.7	100.0	22.6	67.3	52.8	8.1	0.09	1.61
bq3-30	1848.0	146.0	1.9	6.3	1.0	6.5	3.5	1.4	8.9	2.3	20.5	4.4	12.0	6.9	0.9	0.05	1.14
bq3-31	6029.0	391.0	66.7	217.3	36.3	207.4	73.4	21.3	84.3	12.2	75.1	14.5	37.4	26.9	3.5	2.58	4.96
bq3-32	1348.0	406.4	43.9	145.1	25.8	161.3	78.3	13.8	121.3	19.1	104.8	16.1	35.7	22.4	3.0	0.20	0.17
bq3-33	115.6	32.2	1.9	6.1	1.1	6.2	2.1	0.5	2.6	0.5	3.8	1.0	3.4	3.8	0.7	0.04	0.44
bq3-34	4792.0	593.0	67.0	200.0	32.4	206.0	74.0	16.6	107.0	15.6	102.0	21.3	60.7	51.1	7.3	60.00	6.70
bq3-35	902.0	721.0	57.6	235.3	42.9	277.7	109.7	32.2	138.6	21.1	136.9	26.5	71.9	51.3	6.9	0.19	5.42
bq3-36	285.6	2583.0	282.2	1037.0	196.6	1173.0	442.1	35.9	492.2	75.1	478.1	93.0	255.0	232.5	31.4	19.47	8.71
bq3-37	3443.0	837.0	56.8	219.2	42.6	275.9	112.9	32.3	160.6	23.6	151.7	31.0	81.2	57.4	7.5	9.86	5.31
bq3-38	4096.0	3028.0	295.0	871.0	130.4	688.0	204.6	33.1	310.5	59.2	475.5	109.9	324.1	264.6	34.5	9.58	3.22
bq3-39	418.4	227.6	241.7	617.4	81.6	374.9	72.8	12.4	66.7	7.5	41.0	8.1	22.3	18.5	3.1	15.61	8.11
bq3-40	2676.0	544.7	45.3	126.3	19.2	114.1	34.8	5.0	54.3	9.4	75.5	19.4	66.5	74.6	12.5	64.10	7.56
bq3-41	1227.0	2945.0	420.6	1440.0	243.2	1292.0	436.0	110.0	539.6	85.4	565.8	110.0	284.1	191.3	22.7	6.85	36.83

Apéndice 5

bq3-42	325.9	4983.0	111.3	584.3	155.9	1349.0	745.3	79.2	1077.0	164.1	1025.0	192.9	481.6	275.3	34.1	18.13	12.77
bq3-43	3498.0	267.0	10.8	38.8	7.2	48.5	19.1	5.6	34.1	5.4	40.4	9.3	28.2	24.7	4.1	4.24	1.98
bq3-44	3449.0	2501.0	945.6	3076.0	493.7	2394.0	698.5	123.1	661.0	95.0	575.2	104.4	280.1	211.0	26.2	66.60	84.40
bq3-45	8062.0	233.0	26.4	109.5	23.2	161.4	75.0	24.4	109.0	13.2	61.2	8.9	18.7	9.3	1.2	0.07	2.27
bq3-46	4490.0	1160.0	98.0	317.0	53.4	316.0	116.3	23.1	175.9	28.5	195.9	41.4	115.7	97.6	14.7	28.20	5.56
bq3-47	1242.0	412.9	6.1	42.7	5.6	38.1	26.2	7.7	61.7	11.3	81.2	16.7	42.7	26.6	3.1	0.08	0.17
bq3-48	125.2	3147.0	274.9	1041.0	177.7	976.0	448.3	29.3	637.5	108.7	668.1	118.9	303.5	242.8	32.6	19.63	37.16
bq3-49	336.5	4512.0	388.3	1247.0	189.7	981.0	351.1	65.5	523.1	101.7	756.2	165.5	479.9	403.3	58.9	163.60	82.50
bq3-50	3507.0	2590.0	611.0	2010.0	360.0	2050.0	584.0	108.0	587.0	75.0	446.0	90.0	247.0	190.0	27.7	9.10	7.10
bq3-51	4686.0	1577.0	65.0	246.8	47.1	299.2	139.2	42.8	218.0	39.6	283.2	59.0	159.4	108.1	12.7	0.17	0.53
bq3-52	4948.0	664.0	258.5	814.0	133.0	733.0	191.2	40.9	190.2	23.0	128.3	24.8	65.8	48.2	7.1	11.70	29.13
bq3-53	2348.0	765.0	16.5	86.3	23.1	207.5	120.5	32.5	192.8	26.0	155.2	29.8	81.0	69.2	11.4	2.61	5.73
bq3-54	3418.0	3268.0	380.2	1655.0	333.9	2012.0	640.2	165.7	721.1	104.1	643.5	128.8	339.9	182.5	18.7	60.26	9.95

SAMPLE: BQ-4 (Ypresian-Lutetian El Bosque Formation, micaceous sandstone with abundant detrital muscovite grains)

16°48′51″ N; 92°11′48″ W; elevation = 1237 m.a.s.l.

Apatite	Sr	Y	La	Ce	Pr	Nd	Sm	Eu	Gd	Tb	Dy	Ho	Er	Yb	Lu	Th	U
bq4-1	1319.0	1223.0	17.9	66.5	13.0	90.6	48.4	9.5	100.0	22.1	178.7	41.8	123.9	93.5	12.3	0.11	1.70
bq4-2	82.1	2050.0	184.2	650.6	106.5	544.2	269.9	9.5	360.1	71.6	420.8	70.5	174.2	126.6	14.8	1.86	69.30
bq4-3	868.0	56.2	12.6	42.5	7.8	53.9	15.0	2.6	18.6	2.1	12.2	2.4	5.8	3.5	0.5	0.02	0.07
bq4-4	1145.4	411.6	79.2	357.7	53.8	329.1	162.1	39.5	218.2	30.6	134.1	16.2	29.6	14.7	1.8	0.50	2.99
bq4-5	54.5	2428.0	221.2	790.7	128.4	671.7	316.9	12.3	378.6	69.1	435.6	78.2	207.5	177.5	22.3	1.54	35.68
bq4-6	3077.0	599.0	74.1	283.0	53.4	330.0	124.6	31.1	146.1	22.3	134.1	24.6	63.5	43.8	5.4	5.00	18.70
bq4-7	5019.0	2111.0	619.3	2152.0	300.2	1403.0	388.8	74.8	392.1	62.0	393.7	77.0	214.8	171.6	21.9	16.80	44.80
bq4-8	643.5	486.3	104.7	492.8	99.1	604.4	165.7	22.5	160.2	19.2	100.4	17.7	42.4	27.7	4.0	0.39	18.55
bq4-9	3908.0	473.2	12.1	47.2	9.5	69.8	35.0	11.9	69.1	12.2	82.0	16.3	44.5	37.2	5.1	0.01	0.29
bq4-10	3233.0	351.1	51.7	225.0	46.3	314.0	99.3	22.7	113.9	14.1	74.7	12.6	28.5	17.1	2.2	4.11	5.81
bq4-11	284.2	502.0	1284.0	3100.0	358.0	1476.0	241.6	25.2	182.6	20.4	105.6	18.9	46.4	30.4	3.9	31.20	9.04
bq4-12	165.7	1371.7	109.9	405.8	75.3	469.7	158.9	8.9	204.2	30.7	200.6	41.8	123.7	108.9	16.2	7.18	5.83
bq4-13	2085.0	1700.0	776.0	2351.0	317.1	1482.0	393.4	64.0	406.0	59.0	347.4	61.4	148.1	86.3	9.7	22.80	58.63
bq4-14	1657.0	1516.0	602.1	1953.0	256.5	1137.7	297.1	56.8	299.7	45.8	290.0	56.6	158.8	125.8	15.5	10.79	32.25
bq4-15	2257.0	1008.0	102.1	341.0	55.1	316.0	89.9	15.5	127.2	21.9	163.5	35.0	94.3	59.2	7.1	9.09	4.35
bq4-16	9181.0	2298.0	433.4	1578.0	243.0	1334.0	439.4	98.6	497.8	74.3	452.4	85.4	227.2	177.0	22.3	7.74	37.08
bq4-17	902.4	924.4	86.3	325.0	56.1	359.5	139.7	34.5	178.9	27.6	177.4	34.9	96.3	79.9	10.4	0.68	7.70
bq4-18	1229.0	633.0	60.5	245.9	50.8	362.2	161.3	31.1	224.6	31.5	159.9	23.5	47.5	22.0	2.6	0.05	1.68
bq4-19	1564.0	2132.0	26.3	97.3	19.7	148.3	88.0	21.9	193.4	36.8	275.7	62.3	183.7	164.0	25.6	0.81	11.88

Apéndice 5

bq4-20	1271.7	545.1	173.3	500.7	81.7	426.1	110.8	35.5	124.6	16.3	100.1	20.5	56.5	42.4	6.5	1.96	5.79
bq4-21	1270.0	344.1	297.7	688.1	88.0	377.9	73.1	22.0	73.9	9.3	55.7	11.8	32.7	24.8	4.0	2.60	5.03
bq4-22	342.1	285.5	313.3	834.0	101.9	425.7	75.0	13.4	68.2	7.6	43.6	8.9	25.9	25.8	4.5	17.66	16.61
bq4-23	6736.0	697.2	267.2	899.3	144.3	799.3	232.3	40.8	232.2	30.1	168.6	29.0	69.8	41.8	4.9	6.27	22.78
bq4-24	4859.0	1838.0	33.7	135.2	25.7	165.8	79.7	22.8	155.9	32.9	274.1	65.4	192.4	144.1	19.1	18.11	10.35
bq4-25	1811.0	2184.0	1713.0	4666.0	589.8	2493.0	501.1	40.7	464.1	63.0	385.0	74.7	205.4	168.0	23.4	385.50	154.70
bq4-26	4653.0	935.0	52.0	210.0	41.1	277.6	108.8	29.5	161.6	24.7	161.1	31.8	83.4	56.8	7.6	33.85	10.85
bq4-27	1535.0	646.7	434.1	1179.3	157.5	717.6	177.7	77.0	171.3	25.2	148.0	24.9	59.7	36.3	3.9	3.84	15.85
bq4-28	1152.4	3009.0	559.1	1897.0	277.6	1399.0	416.4	111.1	495.0	79.6	527.2	102.1	267.3	182.0	21.4	8.10	53.73
bq4-29	699.5	388.2	137.0	381.3	60.9	344.4	95.1	23.1	107.0	13.6	79.4	14.9	36.5	22.6	2.8	5.70	2.54
bq4-30	5368.0	1485.0	565.5	1941.0	281.8	1439.0	387.1	78.6	370.1	51.2	303.4	54.6	142.0	102.6	12.5	7.94	38.85
bq4-31	639.5	645.0	193.0	717.0	129.4	731.0	187.6	20.7	170.2	22.2	130.3	23.8	60.9	45.4	5.7	3.52	5.12
bq4-32	2662.0	2135.0	150.5	696.3	108.7	616.2	197.4	34.7	253.2	44.6	330.3	73.1	225.0	214.9	29.7	8.51	13.59
bq4-33	336.6	400.8	49.5	268.5	59.6	396.8	134.0	22.0	141.4	17.3	87.6	14.4	32.0	18.8	2.4	0.41	10.95
bq4-34	4011.0	1625.0	78.5	285.7	56.2	380.2	178.4	46.1	291.4	51.2	321.2	60.3	158.9	130.0	18.2	24.43	9.05
bq4-35	3262.0	293.1	7.6	32.1	7.0	51.8	26.6	6.5	44.4	7.2	48.3	9.9	29.0	25.3	4.2	0.21	0.89
bq4-36	1167.0	1179.0	3.4	17.0	4.6	45.6	40.8	5.5	102.1	23.1	191.0	42.5	118.5	80.5	9.1	0.23	0.47
bq4-37	4559.0	2356.0	84.3	327.0	59.4	364.0	142.8	31.3	236.3	48.2	380.3	85.0	249.9	202.3	26.0	6.85	2.17
bq4-38	239.1	114.7	2.2	7.7	1.6	10.4	5.4	2.4	9.7	2.1	16.6	3.9	12.9	15.8	2.2	0.03	0.05
bq4-39	1125.0	883.0	520.5	1324.0	199.7	900.0	218.7	56.6	212.4	31.7	195.2	37.2	97.9	61.9	7.0	5.74	19.35
bq4-40	1676.0	995.0	79.3	172.0	48.9	300.1	121.4	13.5	186.8	30.1	189.4	37.1	92.3	53.1	7.2	1.39	3.29
bq4-41	1699.0	3212.0	58.5	238.5	47.9	319.2	166.6	35.9	329.8	66.7	536.8	130.8	381.0	284.3	41.4	12.94	37.20
bq4-42	2789.0	4170.0	370.7	998.6	200.2	1203.0	472.6	118.9	655.1	103.9	681.5	137.8	377.3	288.1	38.9	3.20	11.07
bq4-43	3722.0	1767.0	236.5	726.0	113.9	615.0	194.2	34.9	256.0	45.8	314.6	63.8	174.7	144.0	21.0	32.24	6.69
bq4-44	4152.0	2571.0	76.2	336.0	73.1	529.0	263.5	71.7	424.0	77.3	510.9	95.7	232.4	142.7	17.6	70.10	37.27
bq4-45	505.1	1684.0	203.8	863.0	159.8	920.0	280.9	33.2	317.1	51.6	335.9	66.5	182.6	137.7	17.9	9.61	3.42
bq4-46	4159.0	102.9	16.1	50.3	8.5	53.3	17.5	5.4	22.9	3.1	19.0	4.0	10.3	8.3	1.5	0.05	0.43
bq4-47	314.6	287.8	782.4	1432.0	182.5	877.0	171.2	17.2	141.8	15.0	73.5	12.5	28.2	15.8	2.4	32.45	10.87
bq4-48	196.9	419.0	571.0	1318.0	166.7	703.0	129.8	19.2	109.5	13.8	77.2	15.2	40.9	32.1	4.9	45.60	23.70
bq4-49	272.5	139.8	777.0	1124.0	86.3	277.0	35.8	11.7	32.2	3.4	19.0	4.2	12.8	16.9	3.7	24.80	6.41
bq4-50	313.1	192.4	985.0	1507.0	132.7	446.2	59.0	17.5	47.0	5.3	28.6	5.8	17.4	19.7	3.7	40.00	15.09
bq4-51	280.2	221.6	1123.0	1692.0	156.4	578.0	83.2	23.4	70.9	7.4	38.0	7.2	19.6	18.1	3.7	85.10	67.80
bq4-52	258.0	495.5	120.1	480.0	90.3	521.5	136.4	32.3	119.6	15.9	90.8	17.1	46.6	40.5	6.2	32.63	43.00
bq4-53	395.7	516.4	448.0	1281.0	179.3	798.0	152.4	15.5	130.2	16.0	90.2	17.4	48.4	40.7	6.3	29.87	45.63
bq4-54	505.3	2584.0	278.3	936.0	148.5	749.0	232.2	39.5	250.2	53.6	423.1	90.3	276.6	278.4	36.0	15.59	17.61
bq4-55	1402.0	217.8	14.2	56.0	11.1	75.3	27.0	6.3	37.5	5.8	37.4	7.8	22.3	23.0	3.2	0.66	0.99
bq4-56	1360.0	431.4	52.2	184.6	36.4	262.2	103.4	10.4	150.3	20.5	116.0	21.1	45.9	19.7	2.6	0.15	2.38
bq4-57	544.0	4200.0	2254.0	6266.0	870.0	3748.0	806.5	70.9	745.2	112.1	714.7	146.1	447.9	555.3	91.6	263.50	99.90

Apéndice 5

bq4-58	4882.0	508.0	49.1	162.4	29.4	189.1	69.6	18.8	99.8	15.2	96.6	18.2	44.0	25.6	3.1	16.59	4.35
bq4-59	4085.0	706.0	25.1	92.6	18.6	122.2	62.0	20.5	114.1	22.5	150.9	25.9	58.8	35.7	4.4	0.02	0.17
bq4-60	1820.0	247.2	11.1	38.3	7.1	44.4	19.1	7.2	31.9	6.3	44.1	7.8	17.3	9.0	1.1	0.03	0.31
bq4-61	4632.0	310.0	13.3	49.0	10.8	78.7	36.7	9.0	69.4	10.5	62.4	11.3	28.7	24.5	3.7	0.04	0.28
bq4-62	2475.0	327.2	50.6	190.1	34.4	207.2	62.6	8.3	74.0	9.6	57.4	11.8	31.6	24.0	3.9	0.24	2.60
bq4-63	3924.0	99.1	321.0	822.0	105.2	462.0	62.6	20.2	48.3	4.6	20.7	3.6	8.4	4.9	0.7	3.46	2.72
bq4-64	285.0	473.5	233.9	591.6	78.2	360.7	75.2	13.9	72.0	10.4	66.6	14.2	46.2	44.1	7.9	35.66	46.95
bq4-65	2219.0	350.4	4.9	19.7	4.4	32.9	16.1	5.2	31.9	5.6	43.5	11.7	43.1	50.5	9.3	46.48	12.32
bq4-66	4721.0	774.0	56.2	198.1	38.9	260.0	98.8	26.9	146.6	22.8	141.3	28.2	75.4	52.4	6.8	22.30	7.32
bq4-67	529.5	2541.0	731.0	2207.0	356.2	1853.0	530.2	56.7	557.7	84.0	511.3	96.9	258.4	200.2	26.9	176.90	35.67
bq4-68	5128.0	436.0	178.0	480.0	63.0	300.0	73.8	18.3	91.3	13.4	81.8	16.4	47.2	39.6	6.4	5.30	2.36
bq4-69	321.2	286.7	322.0	936.0	144.4	685.7	126.3	14.7	92.8	10.7	57.6	10.3	26.6	20.8	3.1	1.34	1.36
bq4-70	5446.0	2191.0	462.1	1579.0	295.2	1747.0	521.3	103.2	573.6	79.3	463.9	85.7	207.1	116.6	13.9	21.95	4.95
bq4-71	630.9	1252.0	162.3	501.0	84.1	483.3	175.1	40.8	239.6	41.0	273.4	52.4	141.2	105.4	13.8	21.60	17.37
bq4-72	1167.0	1199.0	11.9	45.3	9.6	76.6	42.8	7.5	94.2	19.9	162.9	38.1	114.8	103.3	15.0	1.71	1.75
bq4-73	6484.0	202.6	43.5	134.7	21.4	121.0	39.0	13.2	53.1	7.7	44.1	7.9	18.1	10.1	1.4	0.16	1.06
bq4-74	3335.0	194.2	1.9	6.9	1.5	11.6	6.1	2.3	13.6	2.9	24.0	6.8	21.2	18.5	2.8	1.34	0.85
bq4-75	3461.0	1494.0	36.0	132.5	26.5	184.5	99.7	33.9	187.1	37.5	266.8	54.7	142.6	94.2	11.7	0.04	0.37
bq4-76	917.0	816.7	139.5	533.7	83.3	494.5	191.1	44.3	241.5	37.0	203.0	28.7	52.6	24.3	2.8	0.41	4.10
bq4-77	1186.0	1171.3	13.8	50.2	9.9	64.5	34.6	7.2	71.4	15.8	142.8	38.7	133.6	122.8	16.1	0.15	0.37
bq4-78	3847.0	2141.0	557.0	1787.0	295.8	1546.0	491.0	88.7	489.4	75.5	462.8	86.7	229.4	167.6	20.4	16.16	67.89
bq4-79	4038.0	2207.0	661.5	2120.0	338.2	1707.0	516.8	93.0	505.4	76.7	464.7	87.2	231.2	168.2	20.6	15.89	77.04
bq4-80	1043.0	418.8	42.2	235.2	53.4	349.4	101.4	20.2	100.8	13.1	80.7	15.2	40.7	30.5	4.3	0.34	10.41
bq4-81	441.0	620.0	38.8	214.0	58.3	508.0	251.0	50.4	305.0	35.5	164.0	24.8	50.0	28.0	4.4	0.15	19.10
bq4-82	6391.0	606.9	29.3	107.3	20.7	143.4	73.5	28.5	120.4	20.0	122.5	21.6	50.8	27.3	3.2	0.11	0.83
bq4-83	2668.0	331.8	4.0	15.4	3.2	20.9	11.4	3.2	22.4	5.2	45.4	11.1	33.6	25.7	3.4	0.14	0.09
bq4-84	3822.0	670.0	13.9	53.4	13.1	101.2	61.5	22.5	112.3	21.6	138.7	23.8	53.9	32.4	4.0	6.20	2.60

SAMPLE: BQ-5 (Ypresian-Lutetian El Bosque Formation, micaceous sandstone with abundant detrital muscovite grains)

16°44′07″ N; 92°25′38″ W; elevation = 2167 m.a.s.l.

Apatite	Sr	Y	La	Ce	Pr	Nd	Sm	Eu	Gd	Tb	Dy	Ho	Er	Yb	Lu	Th	U
bq5-1	2072.0	223.5	63.4	219.1	39.6	241.2	101.6	26.3	134.3	17.1	74.1	8.6	13.9	4.4	0.5	0.32	8.18
bq5-2	5760.0	129.1	9.0	31.0	5.6	32.9	11.4	3.5	16.4	2.6	18.7	4.4	13.1	11.2	1.7	0.03	0.47
bq5-3	3628.0	503.6	13.5	54.8	11.4	80.8	39.9	13.0	73.3	12.7	90.7	18.8	49.8	33.7	4.7	0.01	0.15
bq5-4	703.8	169.0	352.5	756.7	91.6	376.8	65.7	14.1	53.4	6.1	33.5	6.3	16.2	12.1	1.8	8.61	3.64
bq5-5	125.7	2802.0	2606.0	6955.0	894.8	3964.0	812.9	43.7	724.7	94.7	555.3	100.0	256.6	174.1	22.2	103.94	35.76

Apéndice 5

bq5-6	1295.0	298.7	944.1	2204.0	248.0	1010.4	155.4	27.7	119.7	12.4	67.5	11.8	30.1	20.8	2.9	21.93	7.09
bq5-7	4028.0	1299.0	41.1	156.2	30.5	207.1	103.5	35.5	176.1	32.3	241.8	49.6	140.4	106.8	13.6	0.57	0.70
bq5-8	382.4	1434.0	2622.0	6180.0	726.0	2973.0	532.9	52.3	433.5	53.2	291.1	50.8	127.9	90.5	12.1	116.50	27.30
bq5-9	947.0	210.0	497.0	1205.0	143.4	596.0	99.4	16.9	75.3	8.0	42.9	7.6	19.6	14.3	2.0	7.13	3.17
bq5-10	677.1	569.9	816.8	2047.0	249.5	1106.0	207.3	28.6	171.7	20.8	117.9	21.4	53.4	35.4	4.4	6.28	4.76
bq5-11	1014.3	239.3	220.7	514.6	71.2	345.0	78.3	19.8	75.2	8.8	49.7	8.9	21.8	13.9	1.8	10.57	3.59
bq5-12	792.9	188.2	529.9	1270.0	147.5	595.6	89.5	15.2	65.8	6.9	36.1	6.3	16.7	12.4	1.8	3.38	2.25
bq5-13	1184.0	186.6	1139.0	2327.0	225.5	825.3	111.0	20.1	81.1	7.9	40.8	7.1	18.0	13.2	1.9	15.57	5.68
bq5-14	341.3	2627.0	2075.0	6864.0	973.0	4384.0	919.0	118.9	790.2	99.0	566.8	98.5	248.6	176.6	22.9	134.10	33.37
bq5-15	450.6	893.2	857.4	2119.0	273.7	1295.0	285.1	19.9	273.0	33.2	190.5	34.1	86.5	56.0	7.2	18.86	8.90
bq5-16	529.2	523.0	468.7	1052.0	127.8	525.1	96.7	26.2	101.9	12.1	75.2	16.7	53.5	55.8	11.1	2.33	3.93
bq5-17	313.1	3022.0	2374.0	6321.0	890.4	4104.0	870.6	65.8	777.9	105.1	616.0	116.3	310.0	228.6	30.9	219.30	44.35
bq5-18	4806.0	198.7	4.2	19.5	4.2	27.4	11.4	4.3	18.2	3.6	27.6	6.5	21.1	18.5	2.7	0.01	0.12
bq5-19	2543.0	900.0	480.0	1260.0	177.0	840.0	191.0	17.5	191.0	28.7	180.0	33.7	86.1	55.7	7.5	24.40	8.20
bq5-20	3155.0	589.0	72.0	221.0	34.6	201.0	66.0	14.7	91.0	15.0	100.0	21.1	59.8	48.3	7.2	6.70	3.62
bq5-21	5087.0	1114.0	172.0	500.0	83.8	499.0	161.4	45.9	192.0	28.5	185.0	39.2	115.9	101.1	16.3	1.55	4.28
bq5-22	2080.0	2602.0	225.3	871.6	151.3	849.8	297.0	45.2	379.2	64.3	436.0	90.1	265.0	229.2	35.4	154.90	20.60
bq5-23	1069.0	58.4	10.5	36.5	6.7	39.3	12.2	2.8	15.3	1.9	10.4	2.3	6.1	4.7	1.0	0.10	2.42
bq5-24	3654.0	1310.0	43.9	179.0	37.7	269.0	129.0	40.3	213.0	36.2	249.0	52.2	141.0	98.0	13.9	1.79	1.51
bq5-25	3745.0	1201.2	107.5	363.6	63.7	381.7	148.3	42.8	199.9	31.2	204.9	43.1	121.3	90.4	12.7	0.20	3.10
bq5-26	2924.0	1225.0	45.4	161.0	29.0	177.1	72.5	24.1	117.7	22.8	178.4	41.7	127.0	109.7	16.0	0.15	3.77
bq5-27	2757.0	198.6	430.0	830.0	87.8	352.0	49.3	7.9	40.1	4.8	29.1	6.5	20.5	19.7	3.5	21.77	6.61
bq5-28	4499.0	337.4	70.3	228.3	35.2	176.9	48.2	15.4	53.5	7.7	49.1	10.8	33.0	32.4	5.2	1.02	7.90
bq5-29	3012.0	140.1	15.5	54.5	9.4	59.3	18.1	4.7	25.4	3.2	21.7	4.8	14.4	13.1	2.4	0.07	0.89

SAMPLE: BQ-6 (Ypresian-Lutetian El Bosque Formation, micaceous sandstone with abundant detrital muscovite grains)

16°50′40″ N; 92°55′54″ W; elevation = 1078 m.a.s.l.

Apatite	Sr	Y	La	Ce	Pr	Nd	Sm	Eu	Gd	Tb	Dy	Ho	Er	Yb	Lu	Th	U
bq6-1	383.2	157.1	4.3	15.5	3.4	23.1	10.6	3.7	18.2	3.2	25.1	5.8	17.8	18.9	2.6	0.04	0.09
bq6-2	3688.0	195.0	24.3	87.0	14.8	87.0	29.0	8.6	39.2	5.9	37.8	7.7	20.3	12.1	1.9	0.74	2.00
bq6-3	942.0	976.0	1069.9	2280.0	288.2	1204.5	225.3	28.1	208.2	27.5	167.7	33.5	91.6	70.4	9.6	32.35	5.89
bq6-4	5934.0	3615.0	1324.0	3594.0	542.1	2675.0	694.8	96.3	707.5	102.2	643.6	130.5	374.2	342.0	50.4	22.96	7.59
bq6-5	7659.0	264.3	741.6	1549.0	204.0	887.4	168.3	36.6	130.0	13.4	63.4	9.8	21.0	11.4	1.4	25.41	5.46
bq6-6	269.3	280.3	1464.0	2359.0	232.8	790.4	98.1	10.4	79.5	8.4	46.5	9.3	28.1	29.0	5.3	20.58	6.40
bq6-7	346.9	1966.0	1735.0	4678.0	657.0	2996.0	625.2	36.5	566.6	73.5	416.6	75.7	192.9	130.7	16.6	71.22	18.64
bq6-8	558.1	189.3	640.9	1004.0	94.9	332.8	54.0	11.4	55.1	6.4	36.7	7.3	19.2	13.8	2.0	1.28	1.47

Apéndice 5

bq6-9	1695.0	392.6	265.2	578.0	77.9	354.8	84.6	21.4	79.5	11.0	67.7	13.5	37.5	30.5	4.1	3.92	3.05
bq6-10	2375.0	1931.0	980.8	2891.0	458.7	2238.0	514.0	60.9	495.3	67.7	411.8	78.7	205.8	130.0	16.6	4.27	3.97
bq6-11	693.0	4541.0	1947.0	6312.0	1021.0	5054.0	1180.0	50.4	1118.8	158.5	957.9	180.8	471.8	340.7	45.2	9.69	9.28
bq6-12	1045.3	260.6	241.5	544.5	77.4	378.9	88.5	21.3	79.5	9.9	54.3	9.9	24.1	16.2	2.0	12.38	4.05
bq6-13	1165.0	187.4	612.6	1037.4	109.8	417.1	62.5	12.9	50.7	5.6	31.8	6.3	17.0	13.7	2.1	6.97	2.36
bq6-14	5124.0	279.0	34.1	108.2	18.2	111.8	41.8	16.9	57.5	8.2	49.9	9.9	25.8	18.3	2.5	0.57	0.49
bq6-15	1589.0	111.7	82.3	212.2	32.6	168.7	40.6	12.4	36.3	4.4	23.0	4.0	9.9	6.5	0.9	0.63	0.47
bq6-16	1663.0	470.0	315.0	807.0	114.0	547.0	114.0	13.1	111.0	15.3	92.3	17.2	44.0	27.5	3.7	3.58	1.35
bq6-17	324.9	2407.0	2596.0	6600.0	891.7	3890.0	751.9	68.0	636.2	83.3	483.8	91.4	250.7	217.6	29.9	286.10	70.92
bq6-18	191.6	2652.0	2902.0	7279.0	992.0	4337.0	876.9	42.4	757.6	98.5	559.3	101.1	255.8	170.0	21.5	88.57	23.51
bq6-19	385.4	1054.0	1819.0	4530.0	559.2	2194.0	364.3	18.8	282.0	34.2	189.2	36.0	102.5	91.5	13.3	51.98	25.10
bq6-20	423.6	641.0	1236.0	2818.0	333.9	1281.0	206.1	12.6	167.6	19.8	109.9	21.4	61.2	57.5	8.9	20.92	10.08
bq6-21	837.0	1042.0	775.6	2017.0	271.0	1149.0	215.5	19.9	200.2	26.1	159.3	32.8	96.7	102.7	18.1	27.83	7.23
bq6-22	4903.0	1841.0	158.0	493.0	81.3	475.0	177.2	38.4	252.6	44.6	312.7	65.4	189.1	155.0	21.3	34.82	7.56
bq6-23	206.2	949.0	912.0	2100.0	279.0	1200.0	240.0	22.7	216.0	28.0	165.0	32.4	88.4	63.9	9.1	82.50	13.60
bq6-24	301.0	1695.0	2626.0	6398.0	846.0	3685.0	715.2	52.3	582.0	71.3	382.9	65.8	156.2	90.7	11.6	58.50	14.32
bq6-25	151.1	995.0	904.0	2650.0	342.0	1432.0	262.0	17.9	227.8	28.5	166.4	33.3	90.6	67.8	9.6	84.80	30.00
bq6-26	3807.0	589.8	46.9	181.2	34.6	217.5	82.7	16.8	109.7	15.8	99.0	20.3	55.1	39.7	5.7	0.17	1.94
bq6-27	302.6	524.8	159.7	404.2	62.9	348.9	104.1	23.3	123.7	15.6	91.6	18.4	47.2	25.6	3.0	7.10	0.65
bq6-28	348.7	1834.0	2337.0	5673.0	743.8	3206.0	631.9	46.4	534.2	66.7	371.4	67.6	174.0	119.4	16.0	119.20	30.92
bq6-29	1316.0	90.9	118.3	303.4	46.3	241.8	54.2	14.6	42.4	4.6	21.4	3.6	8.3	5.3	0.7	0.90	0.26
bq6-30	820.0	810.0	131.0	350.0	56.0	275.0	72.0	29.0	98.0	18.1	128.0	36.0	87.0	63.0	4.9	67.00	43.90
bq6-31	414.7	245.3	25.2	90.7	16.6	102.7	37.3	7.7	50.7	6.9	43.3	8.7	21.9	14.3	2.3	0.08	0.10
bq6-32	1282.0	968.0	175.5	633.2	112.7	667.8	235.6	69.8	280.9	40.9	238.6	40.7	91.6	41.4	4.3	0.41	2.72
bq6-33	715.2	241.1	633.6	1417.0	176.1	737.3	117.0	17.9	89.6	9.6	50.8	9.2	23.5	15.8	2.2	8.47	4.14
bq6-34	509.0	330.6	378.0	921.0	123.8	561.0	104.8	15.6	91.4	11.2	62.0	12.2	31.6	21.2	3.0	3.74	0.54
bq6-35	762.8	249.6	751.0	1438.0	158.2	601.7	86.6	16.2	67.9	7.3	40.2	8.1	23.2	21.7	3.3	4.82	2.50
bq6-36	882.0	306.1	557.4	1255.0	163.5	708.8	120.6	17.1	93.0	10.6	59.1	11.1	30.0	21.6	3.1	9.83	3.90
bq6-37	192.3	1457.0	16.9	67.9	14.7	114.9	73.0	26.4	160.4	34.4	269.1	55.9	151.7	97.3	10.8	0.08	0.17
bq6-38	1969.0	107.2	88.2	213.0	28.1	131.7	24.0	5.8	20.1	2.6	16.2	3.4	11.4	10.9	1.8	5.86	2.32
bq6-39	1066.0	479.2	1664.0	3454.0	361.2	1304.0	192.2	11.0	155.9	17.0	89.7	17.3	47.7	38.9	5.4	21.65	16.67
bq6-40	4393.0	1279.0	109.7	393.9	72.6	448.9	179.9	56.4	231.3	36.5	231.4	45.9	123.0	95.1	13.5	0.41	9.38
bq6-41	3355.0	184.9	3.8	14.7	3.2	27.1	14.4	6.2	33.4	5.9	38.0	6.8	15.9	9.8	1.7	0.04	0.10
bq6-42	2514.0	2237.0	293.7	1110.0	203.3	1164.0	363.7	69.9	397.1	58.2	373.9	76.9	224.0	175.9	22.9	3.25	7.94
bq6-43	4423.0	1312.0	888.0	2457.0	364.2	1714.0	372.6	41.5	351.7	46.2	260.7	48.1	127.8	95.0	13.1	105.90	27.70
bq6-44	1516.0	5227.0	499.0	1533.0	231.4	1134.0	393.8	69.6	506.7	97.3	732.7	168.7	553.8	544.7	77.3	6.17	17.25
bq6-45	3961.0	4686.0	1675.0	4876.0	673.1	2974.0	749.0	106.0	786.3	129.1	860.1	173.5	499.3	438.0	61.2	57.01	16.86
bq6-46	3420.0	993.9	302.5	1112.0	195.8	1116.3	308.5	54.7	308.2	39.6	219.0	39.7	96.9	56.8	7.8	1.00	5.45

Apéndice 5

bq6-47	2972.0	334.7	89.9	287.4	46.5	245.1	63.7	15.7	62.4	8.4	50.9	10.7	31.2	26.5	4.6	0.54	2.63
bq6-48	303.5	2869.0	2042.0	5789.0	836.3	3889.0	849.9	41.6	769.3	103.8	605.6	110.1	285.3	190.6	24.1	76.04	16.64
bq6-49	4880.0	5935.0	372.0	1273.0	208.4	1094.1	442.0	107.4	603.0	130.6	986.8	209.3	607.4	480.4	57.1	2.85	4.27
bq6-50	3579.0	1869.0	1047.0	2488.0	338.8	1553.0	364.7	55.8	403.6	64.1	395.2	68.8	172.9	125.9	16.1	53.45	15.28
bq6-51	4553.0	85.6	2.3	8.2	1.5	9.1	3.8	1.5	6.6	1.2	9.6	2.5	8.5	9.9	1.8	0.01	0.92
bq6-52	348.9	1235.0	917.0	2579.0	381.7	1818.0	394.3	27.0	349.7	45.7	255.5	46.0	115.1	75.3	9.4	30.11	2.87